Acta Oceanologica Sinica

Vol. 39 No. 4 **April 2020**

CONTENTS

Articles

Research Notes

Marine Biology

Acta Oceanol. Sin., 2020, Vol. 39, No. 4, P. 1–8
https://doi.org/10.1007/s13131-020-1542-z
http://www.hyxb.org.cn
E-mail: hyxbe@263.net

Validation and application of soil moisture active passive sea surface salinity observation over the Changjiang River Estuary

Qiong Wu[1], Xiaochun Wang[2, 3*], Wenhao Liang[2], Wenjun Zhang[1]

[1] School of Atmospheric Science, Nanjing University of Information Science and Technology, Nanjing 210044, China

[2] School of Marine Science, Nanjing University of Information Science and Technology, Nanjing 210044, China

[3] Joint Institute for Regional Earth System Science and Engineering, University of California at Los Angeles, Los Angeles 90095, USA

Received 19 April 2019; accepted 27 May 2019

Abstract

Using sea surface salinity (SSS) observation from the soil moisture active passive (SMAP) mission, we analyzed the spatial distribution and seasonal variation of SSS around Changjiang River (Yangtze River) Estuary for the period of September 2015 to August 2018. First, we found that the SSS from SMAP is more accurate than soil moisture and ocean salinity (SMOS) mission observation when comparing with the *in situ* observations. Then, the SSS signature of the Changjiang River freshwater was analyzed using SMAP data and the river discharge data from the Datong hydrological station. The results show that the SSS around the Changjiang River Estuary is significantly lower than that of the open ocean, and shows significant seasonal variation. The minimum value of SSS appears in July and maximum SSS in December. The root mean square difference of daily SSS between SMAP observation and *in situ* observation is around 3 in both summer and winter, which is much lower than the annual range of SSS variation. In summer, the diffusion direction of the Changjiang River freshwater depicted by SSS from SMAP is consistent with the path of freshwater from *in situ* observation, suggesting that SMAP observation may be used in coastal seas in monitoring the diffusion and advection of freshwater discharge.

Key words: soil moisture active passive mission, in situ observation, soil moisture and ocean salinity mission, sea surface salinity, Changjiang River (Yangtze River) Estuary, freshwater plume

Citation: Wu Qiong, Wang Xiaochun, Liang Wenhao, Zhang Wenjun. 2020. Validation and application of soil moisture active passive sea surface salinity observation over the Changjiang River Estuary. Acta Oceanologica Sinica, 39(4): 1–8, doi: 10.1007/s13131-020-1542-z

1 Introduction

Sea surface salinity (SSS) can be considered as an indicator of the water cycle and the flux of freshwater across the air sea interface (Bingham et al., 2011). The low SSS areas are usually occupied by precipitation, freshwater and melting glaciers (Dickson et al., 1988; Durack and Wijffels, 2010). Currently, the main methods for obtaining SSS are *in situ* observation and satellite remote sensing (Bai et al., 2013, 2014).

In situ observations are widely used for scientific researches and ocean operational monitoring. The temperature and salinity from Argo profiles are often utilized to address the seasonal and interannual variability of SSS of many regions, such as the eastern Equatorial Indian Ocean and Southeastern Arabian Sea (Subrahmanyam et al., 2011). Liu and Feng (2012) studied the salinity data, which were collected on two zonal sections near the Jeju Island, to analyze the impact of wind on the transport of the Changjiang River freshwater plume in August. However, the *in situ* observation cannot describe the variations of SSS at finer spatial and temporal scales. Increasing availability of the satellite observations of SSS data will undoubtedly provide us with more accurate method to observe SSS. At present, several satellites such as AQUARIUS, SMOS and SMAP have been launched for observing SSS. SMOS is the first satellite mission to address the challenge of measuring SSS from space by the European Space Agency in 2009 (Berger et al., 2002; Font et al., 2010). Hasson et al. (2018) and Guimbard et al. (2017) analyzed the 2015–2016 El Niño event with SSS from SMOS, found that the SSS is strong anomalies in the tropical Pacific. AQUARIUS is lunched for observing the SSS from space with a combined passive/active L-band microwave instrument in 2011. The SSS data supports us to investigate the coupling relationships between ocean circulation, global water cycle, and climate (Le Vine et al., 2007; Lagerloef et al., 2008; Yueh et al., 2014). The SMAP mission is one of the first Earth observation satellites of National Aeronautics and Space Administration (NASA) to detect soil moisture from January of 2015. The SMAP can distinguish frozen from thawed land surfaces, it improving the estimates of water, energy, and carbon transfers between the land and the atmosphere. The SMAP mission provides high resolution and high accuracy soil moisture and frozen/thaw state data using L-band radar and radiometer instruments (Entekhabi et al., 2010, 2014; Das et al., 2011; Yueh et al., 2016). The SMAP can directly exhibit the flood assessment and drought monitoring of many large rivers through the distributions of SSS observations, such as the Niger River, the Amazon River, the Nujiang River, the Mississippi River and the Gangs River (Yueh et al., 2016). The SSS from SMAP was used to focus

Foundation item: The National Key Research and Development Program of China under contract No. 2016YFC1401600; the Public Science and Technology Research Fund Projects for Ocean Research under contract No. 201505003; the 2015 Jiangsu Program of Entrepreneurship and Innovation Group under contract No. 2191061503801/002.
*Corresponding author, E-mail: xcwang@nuist.edu.cn

on the May 2015 severe flooding in Texas (Fournier et al., 2016).

SSS satellite missions provide new opportunities to study SSS variation and their potential applications in terms ocean monitoring and forecasting need to be explored, especially in coastal regions where the riverine freshwater discharge plays a significant role in oceanic processes and in situ salinity observation is often sparse in space. In present research, the SSS observation from SMAP mission is used to study SSS variation around Changjiang River Estuary. Section 2 introduces the materials we used in the study. Section 3 validates SMAP and SMOS observations using *in situ* observation and analyzes SSS variability of SMAP on seasonal and sub-seasonal time scales. In section 4, we summarize results.

2 Data

In present study, the SMAP data we used is from September 1, 2015 to August 31, 2018 while the SMOS data is from September 1, 2015 to August 31, 2016. The SMAP is a gridded product with 1-day temporal resolution and 0.25° horizontal resolution while the temporal resolution of SMOS is 4-day and the spatial resolution is 0.26°.

The *in situ* measurement of sea-bird SBE CTD used for all measurements is from the R/V *Rongjiang No. 1*. The two observation time periods are from December 20 to 30, 2015 and August 3 to 13, 2016. For each station, the CTD instrument is put in the water for 3–5 min, and descends with a speed around 1 m/s. The procedure was repeated 1–2 times to measure temperature and salinity. Our data quality control procedure includes two steps. First, we removed all the data with the pressures smaller than 0. Second, the temperature and salinity with variability larger than 3 standard deviations are removed.

The daily freshwater discharge data of the Datong hydrological station over the Changjiang River from September 2015 to August 2018 is used in this study (http://xxfb.hydroinfo.gov.cn).

3 Results

3.1 *Comparisons of SSS from satellite datasets with in situ observations*

In this study, the SSS obtained from SMAP and SMOS satellite datasets were used to validate against *in situ* SSS observations over the Changjiang River Estuary. The scatter plot of Fig. 1 shows the SSS of SMAP observation (Figs 1a, b) and *in situ* observation between winter, 2015 (Figs 1a, c) and summer, 2016 (Figs 1b, d) while the SMOS observations are shown in Figs 1c and d. The RMSD between the *in situ* observation and SMAP is 3.15, with the bias of –1.36 in winter 2015. The RMSD is 2.79 with –0.63 bias between *in situ* observation and SMOS. From above comparisons, we found that both the SMAP and SMOS overestimated SSS. However, the quality of SMOS SSS is slightly better than SMAP in winter. The RMSD between the *in situ* observation and SMAP is 3.02, with the bias of 0.47 in summer. The RMSD of the *in situ* observation and SMOS is 3.95 with the bias of 0.54, which means that the SMAP mission and SMOS mission both overestimated SSS during summer. However, the error of SMAP observation is smaller than SMOS.

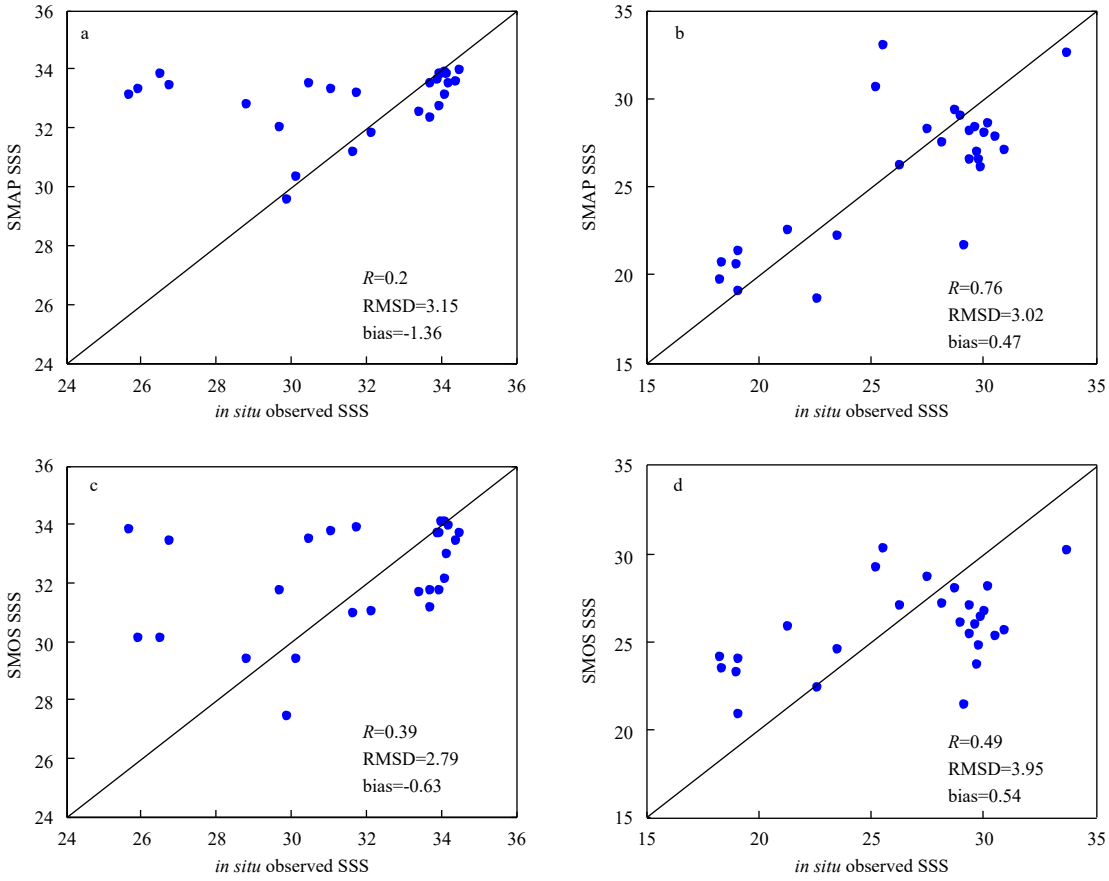

Fig. 1. Comparison of SSS data from SMAP and SMOS missions against *in situ* observations. a. The correlation coefficient (R), root mean square difference (RMSD) and bias between SMAP data and *in situ* observation in winter of 2015, b. the same as a but for summer of 2016, c. the same as a but for SMOS dataset, and d. the same as b but for SMOS dataset.

Though there is large bias of SMAP SSS observation during the winter of 2015, it is encouraging to note the similarity between SSS spatial distribution from SMAP (Fig. 2a) and *in situ* measurement (Fig. 2b). For instance, gradual increase of SSS from around 29 to 31 along 32°N is visible in both SMAP and *in situ* SSS observation. Figures 2c and d present the distribution of SMAP and *in situ* CTD observation for the summer of 2016. The major feature in both SMAP and *in situ* SSS observation is the northeastward extension of Changjiang River freshwater plume, similar to the observations of Kim et al. (1991) and Xuan et al. (2012). Though the RMSDs in SMAP SSS observation are as large as 3, it is encouraging to note that the SMAP SSS observation has great potential to monitor the spreading of freshwater plume from the Changjiang River.

Similar to the validation of SMAP SSS against *in situ* observation, the SSS spatial distribution derived from SMOS data also shows consistent distribution with that of the *in situ* SSS observation (Fig. 3). Along 32°N, the SSS from both SMOS and *in situ* observation increase from around 29 to 31. Figures 3c and d present the spatial distributions of the SMOS SSS and *in situ* observation in summer of 2016. Although the SSS of the SMOS observation reproduces the main characteristics of the Changjiang River freshwater that extends to the northeast, the value of the SMOS SSS is larger than that of the *in situ* SSS observation, especially over the stations (C1 to C7) region. During summer of 2016, SMOS SSS has a larger bias and RMSD than those of SMAP SSS (Figs 1b, d). Thus, in the following analysis, we only use SMAP SSS.

3.2 *Annual mean and variation of SSS*

Due to the sparseness of *in situ* observations, the fine spatial SSS distribution is still unclear over the Changjiang River Estuary according to previous studies. However, the SSS observations from satellites have shown great potential based on the validation of SSS from satellites (SMAP and SMOS) against *in situ* observation in this study. The SMAP SSS observation can better represent the spatial distribution of SSS over the Changjiang River Estuary. Figure 4a shows annual mean SMAP SSS averaged from previous September to next August during the period of 2015–

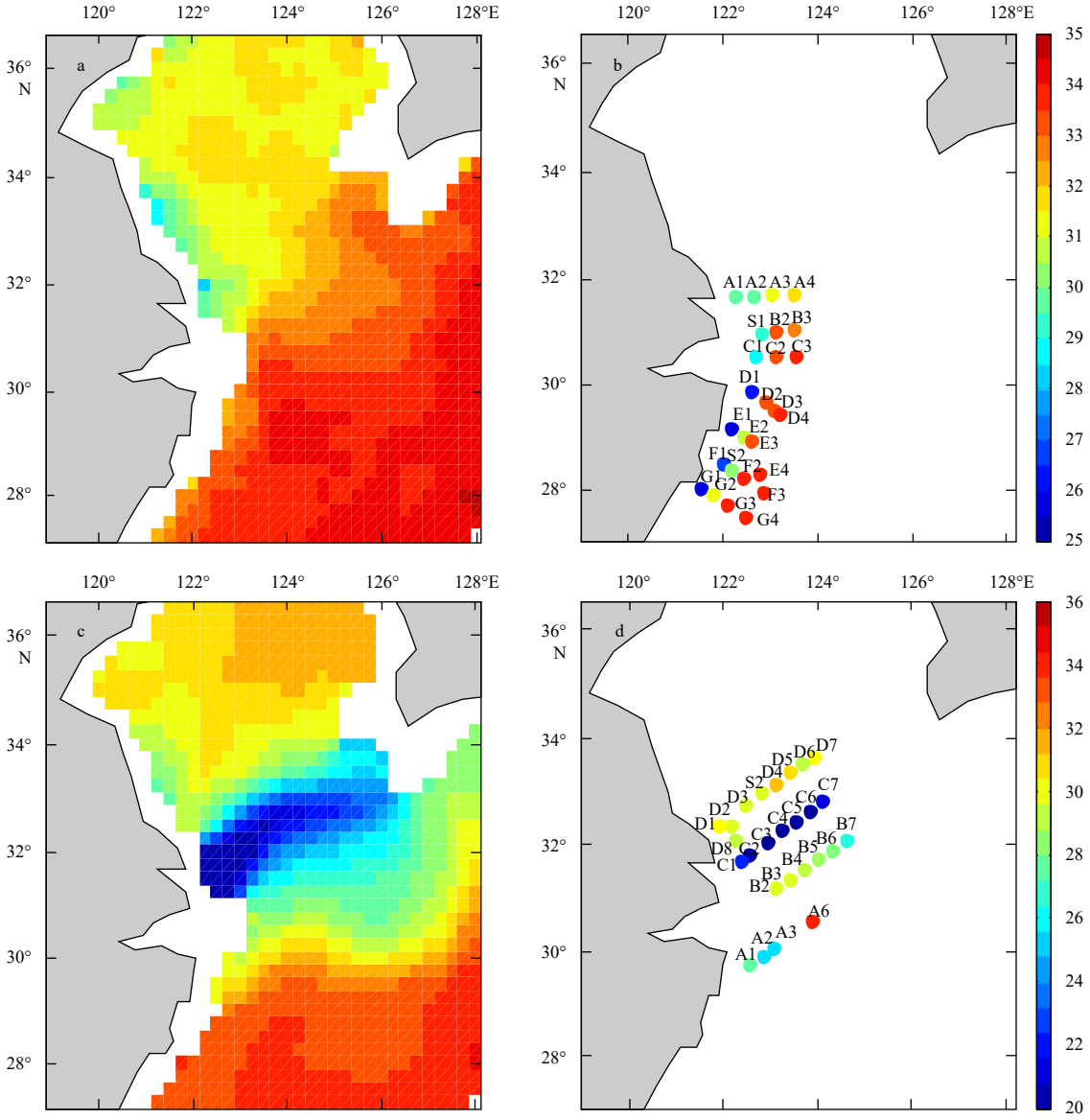

Fig. 2. SSS of SMAP during December 20–30, 2015 (a); SSS of *in situ* CTD observation during December 20–30, 2015 (b); SSS of SMAP during August 3–13, 2016 (c); and SSS of *in situ* CTD observation during August 3–13, 2016 (d).

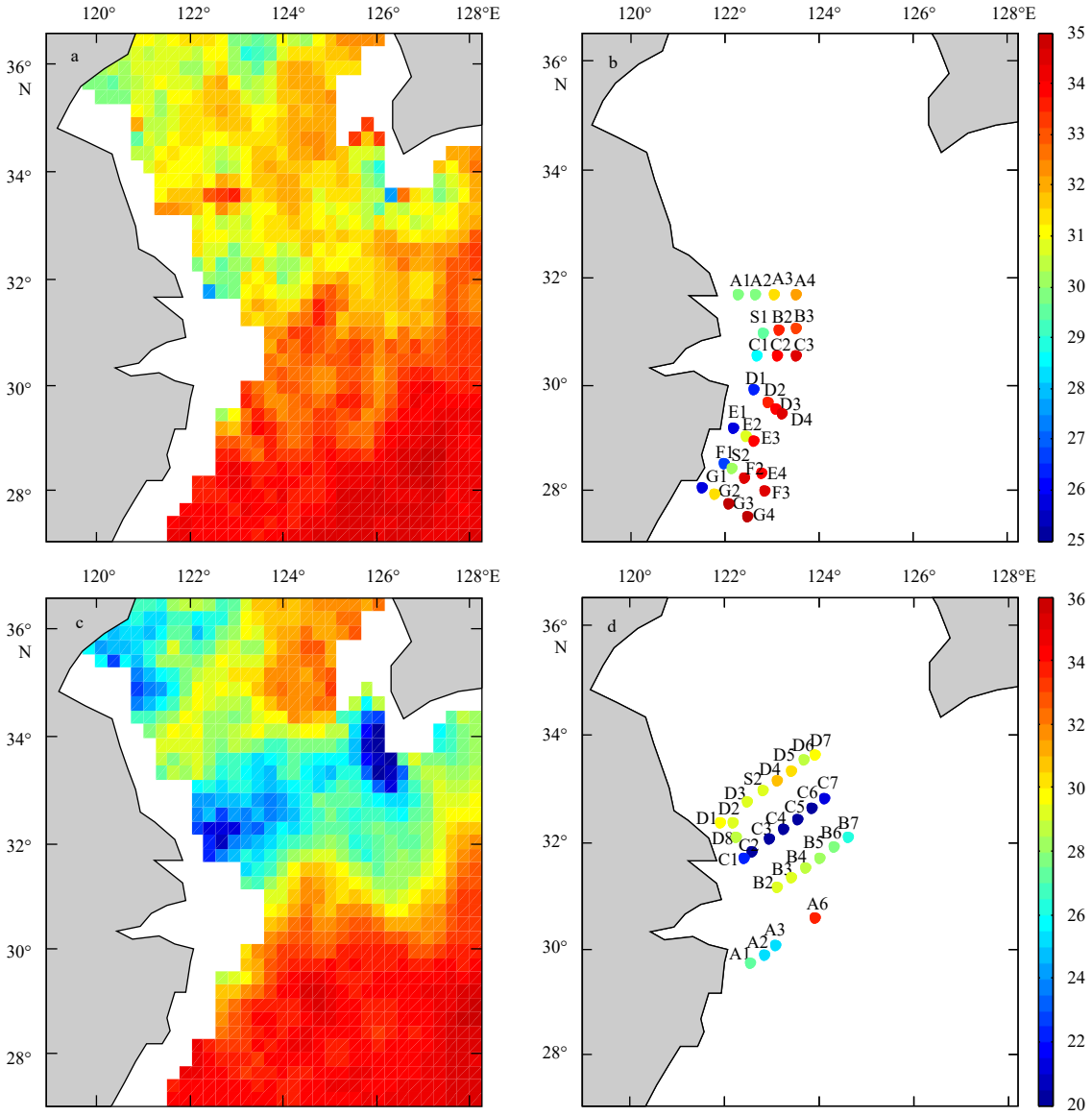

Fig. 3. SSS from SMOS observation in December 20–30, 2015 (a); SSS from *in situ* observation in December 20–30, 2015 (b); SMOS SSS observation in August 4–12, 2016 (c); and *in situ* SSS observation in August 3–13, 2016 (d).

2018 over the Changjiang River Estuary. Owing to the effect of large freshwater, the minimum value of annual mean SSS around the Changjiang River Estuary is close to 25. We further describe the spatial variation of the SSS value over the Changjiang River Estuary by calculating the difference between the highest and lowest values of the SSS at each grid point, as shown in Fig. 4b. An important characteristic of the SSS is that it decreased sharply from the near shore area to the offshore area. The range of SSS around the Changjiang River Estuary can reach as high as 16.

3.3 *Seasonal variation*

Figures 5a–l show seasonal evolutions of SSS during the period of 2015–2018. The value of the SSS ranges from 29 to 34 from previous September to next August over the Changjiang River Estuary. Figures 5a–d display that the low SSS region over the Changjiang River Estuary gradually decays from September to December. Figures 5e–l indicate that the low value SSS region gradually extends from coastal regions to outer sea from January to August. Because of the gradual increase of precipitation over the middle and lower reaches of the Changjiang River from previous winter to next summer, the SSS reaches the maximum in December (Fig. 5d) while it reaches the minimum in July (Fig. 5k).

The averaged SSS over the region (32°–33°N, 122°–124°E) is used as an indicator of the Changjiang River Estuary for analyzing the relationship between SSS variation and hydrological cycle. Figure 6 displays the time series of mean SSS and mean freshwater discharge during the same period. The freshwater discharge ranges from 2×10^4 to 3×10^4 m^3/s from September to February, and the SSS gradually increases from 30 to around 32. The SSS sharply decreased from May to August, reaching a minimum value of 26 in August, while the discharge value increased gradually and reached peak (7×10^4 m^3/s) in July. In general, the averaged SSS and freshwater discharge has a significant negative correlation. Large freshwater discharge corresponds to the low SSS and the small freshwater discharge is consistent with the high SSS over the Changjiang River Estuary. The correlation coefficient between mean SSS and freshwater discharge is –0.89 which is significant at the 95% confidence level.

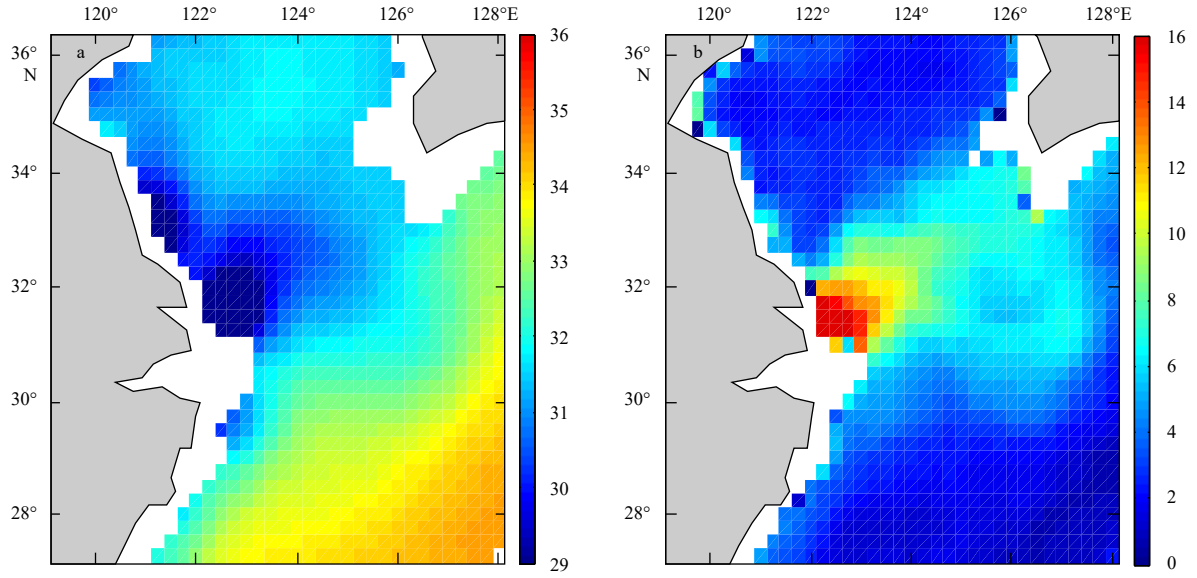

Fig. 4. Annual mean SMAP SSS averaged from previous September to next August during the period of 2015–2018 over the Changjiang River Estuary (a); and the spatial distribution of the range of SSS, the difference between the highest and the lowest SSS for each point (b).

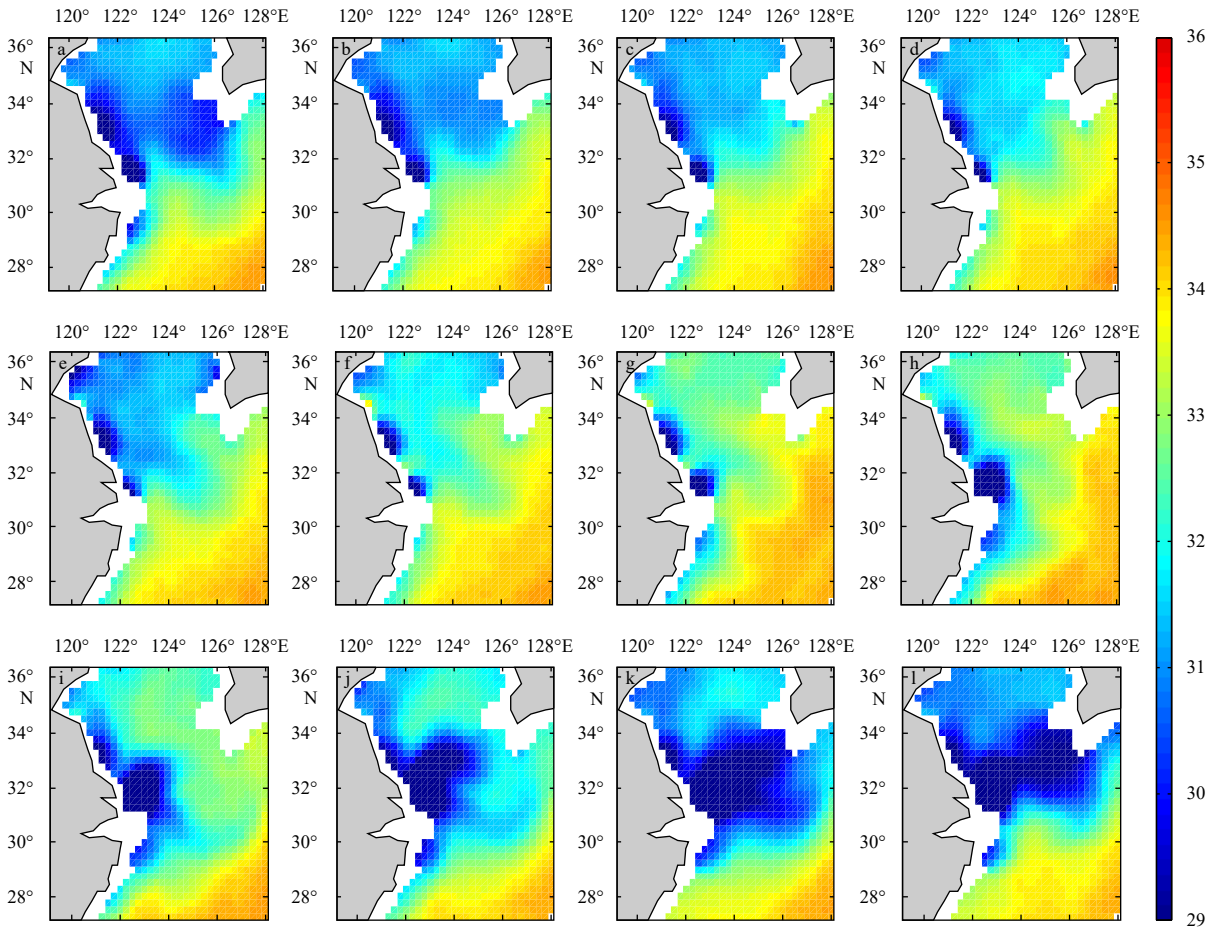

Fig. 5. Seasonal evolutions of SSS from previous September to next August (3-year averaged from 2015–2018) of the Changjiang River Estuary.

3.4 *Path of the Changjiang River freshwater discharge*

Owing to the advantages of SMAP data in terms of high spatial and temporal resolution, we can investigate the spread of river plume from the near shore area to the offshore area. A signi-

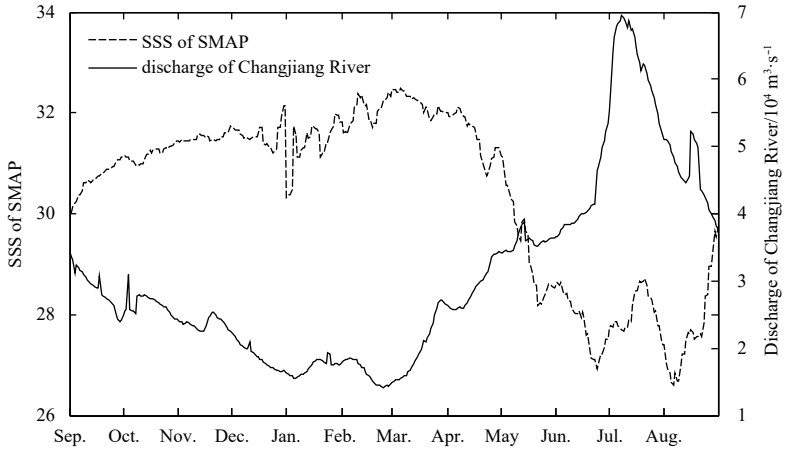

Fig. 6. The time series of SSS averaged over the region (32°–33°N, 122°–124°E) and the freshwater discharge of the Datong hydrological station from previous September to next August (3-year averaged from 2015–2018). The unit of discharge is m^3/s.

ficant characteristic of the diffusion of the Changjiang River discharge is that it spreads northeastward from May to July while this trend of northeastward extension weakens in August (Fig. 5l). Figures 7a–f show the SSS spatial evolution from May to July with 15-day interval averaged from 2015 to 2018. The low SSS area expands northeastward gradually, with the increasing freshwater discharge of the Changjiang River from May to July.

The diffusion path of the Changjiang River freshwater during winter is completely different from that during summer. Figures 8a–f show the evolution of SSS from December to February with 15-day temporal interval. The SSS gradually increases along the coastal area from 30°N to the south (Mao et al., 1963), indicating that the freshwater plume is weak and spreads southward along the coast. The diffusion path may be related to the north wind in winter. Overall, the area of freshwater diffusion in winter is much smaller than that in summer. Besides the discharge, wind is also an important factor that cannot be ignored. Due to the influence of monsoon system, the southwesterly wind prevails in summer, leading to the extension of the low SSS area northeastward. However, the winter is dominated by the northeasterly wind, and the low SSS region extends to the southwest. Based on Figs 7 and 8, we can draw a conclusion that due to the different value of discharge and the direction of wind, the scope and direction of the Changjiang River freshwater diffusion are far different at seasonal time scales. Though these features were analyzed using *in situ* data in previous studies, our analysis demonstrates the potential to use satellite SSS data to study and even monitor the spreading of the Changjiang River freshwater.

4 Conclusions

In this study, we compare SSS from SMAP and SMOS missions, with *in situ* observation, and find that the RMSDs between

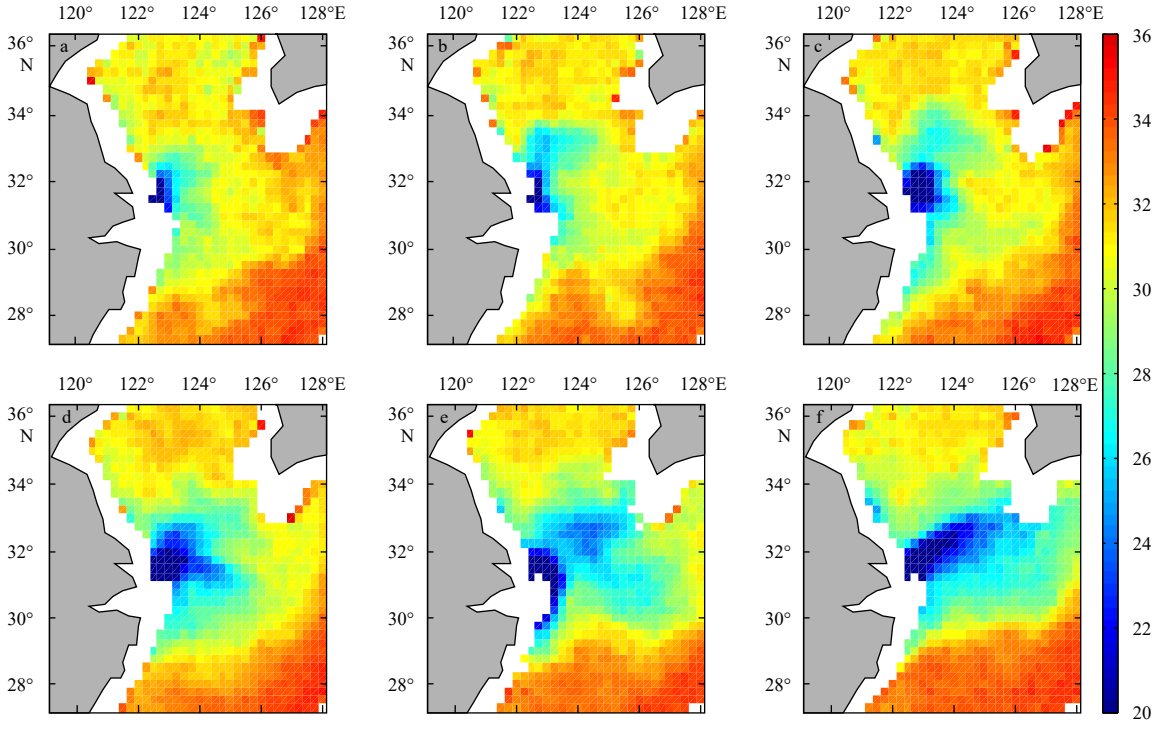

Fig. 7. The SSS evolutions from May to July with 15-day intervals over the Changjiang River Estuary averaged from 2015–2018.

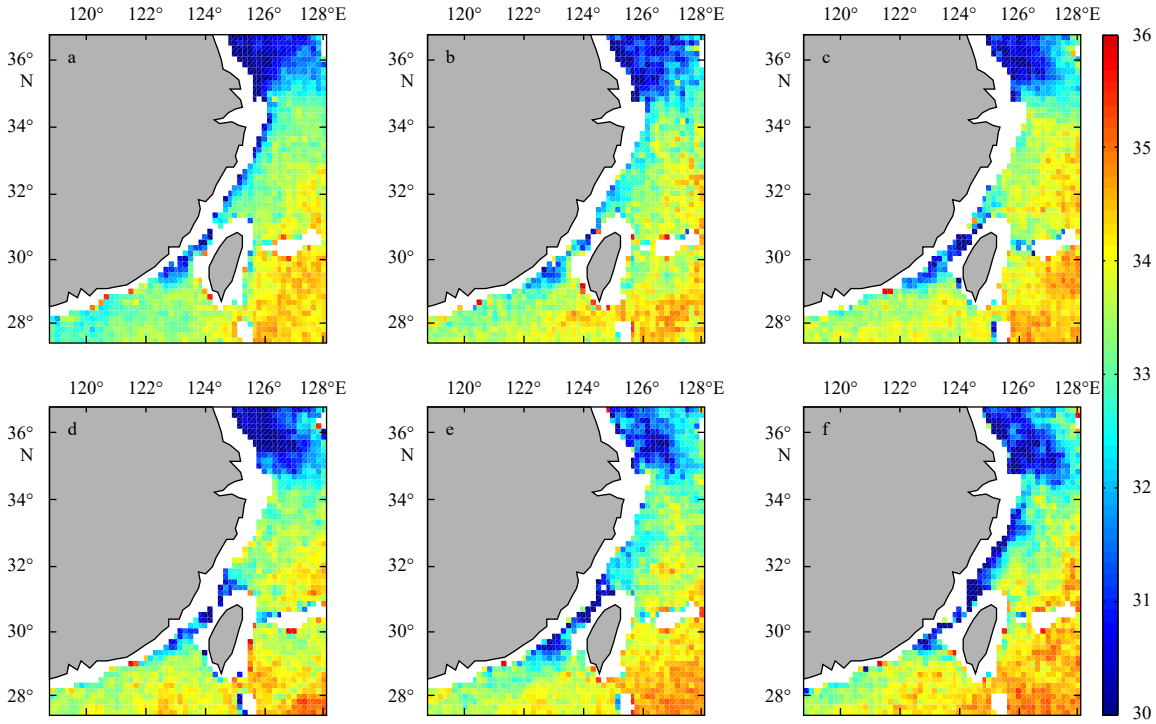

Fig. 8. The SSS evolution from previous December to February of next year with 15-day intervals for the Changjiang River Estuary averaged from 2015–2018.

satellite SSS and *in situ* observations are about 3. However, the SSS derived from SMAP mission may be more suitable for describing the spreading of the freshwater plume from the Changjiang River than SMOS, especially in summer, since SMOS SSS has a larger bias and RMSD than that of SMAP. In addition, we also analyze the spatial distribution and temporal evolutions of SSS around the Changjiang River Estuary using SMAP data. The results show that the SMAP SSS has obvious seasonal cycle. The annual range of SSS, the difference between the maximum value in winter and minimum value in summer, exceeds 16. The averaged SSS over the region (32°–33°N, 122°–124°E) is negatively related with freshwater discharge from the Changjiang River. The Changjiang River freshwater spreads northeastward during summer time and southwestward during winter time. Our analysis demonstrates the potential of satellite SSS for studying and monitoring the Changjiang River freshwater plume in the East China Sea.

Acknowledgements

We thank Xianqiang He and the crew member of R/V *Rongjiang No. 1* for making *in situ* CTD observations in the winter of 2015, and summer of 2016. The SMAP data are downloaded from the National Snow and Ice Data Center (NSIDC, http://nsidc.org/the-drift/data-set/smap/).

References

Bai Yan, He Xianqiang, Pan Delu, et al. 2014. Summertime Changjiang River plume variation during 1998–2010. Journal of Geophysical Research: Oceans, 119(9): 6238–6257, doi: 10.1002/2014JC009866

Bai Yan, Pan Delu, Cai Wenjun, et al. 2013. Remote sensing of salinity from satellite-derived CDOM in the Changjiang River dominated East China Sea. Journal of Geophysical Research: Oceans, 118(1): 227–243, doi: 10.1029/2012JC008467

Berger M, Camps A, Font J, et al. 2002. Measuring ocean salinity with ESA's SMOS mission- advancing the science. ESA Bulletin-European Space Agency, (111): 113–121

Bingham F M, Foltz G R, McPhaden M J. 2011. Characteristics of the seasonal cycle of surface layer salinity in the global ocean. Ocean Science Discussions, 8(6): 2377–2415, doi: 10.5194/osd-8-2377-2011

Das N N, Entekhabi D, Njoku E G. 2011. An algorithm for merging SMAP radiometer and radar data for high-resolution soil-moisture retrieval. IEEE Transactions on Geoscience and Remote Sensing, 49(5): 1504–1512, doi: 10.1109/TGRS.2010.2089526

Dickson R R, Meincke J, Malmberg S A, et al. 1988. The "great salinity anomaly" in the northern North Atlantic 1968–1982. Progress in Oceanography, 20(2): 103–151, doi: 10.1016/0079-6611(88)90049-3

Durack P J, Wijffels S E. 2010. Fifty-year trends in global ocean salinities and their relationship to broad-scale warming. Journal of Climate, 23(16): 4342–4362, doi: 10.1175/2010JCLI3377.1

Entekhabi D, Das N, Yueh S, et al. 2014. SMAP Handbook Soil Moisture Active Passive: Mapping Soil Moisture and Freeze/Thaw from Space. Pasadena, CA: JPL Publication, 31–46

Entekhabi D, Njoku E G, O'Neill P E, et al. 2010. The soil moisture active passive (SMAP) mission. Proceedings of the IEEE, 98(5): 704–716, doi: 10.1109/JPROC.2010.2043918

Font J, Camps A, Borges A, et al. 2010. SMOS: the challenging sea surface salinity measurement from space. Proceedings of the IEEE, 98(5): 649–665, doi: 10.1109/JPROC.2009.2033096

Fournier S, Reager J T, Lee T, et al. 2016. SMAP observes flooding from land to sea: the Texas event of 2015. Geophysical Research Letters, 43(19): 10338–10346, doi: 10.1002/2016GL070821

Guimbard S, Reul N, Chapron B, et al. 2017. Seasonal and interannual variability of the Eastern Tropical Pacific Fresh Pool. Journal of Geophysical Research: Oceans, 122(3): 1749–1771, doi: 10.1002/2016JC012130

Hasson A, Puy M, Boutin J, et al. 2018. Northward pathway across the tropical North Pacific Ocean revealed by surface salinity: how do El Niño anomalies reach Hawaii?. Journal of Geophysical Research: Oceans, 123(4): 2697–2715, doi: 10.1002/2017JC013423

Kim K, Kim K R, Rhee T S, et al. 1991. Identification of water masses in the Yellow Sea and the East China Sea by cluster analysis. Elsevier Oceanography Series, 54: 253–267, doi: 10.1016/S0422-9894(08)70100-4

Lagerloef G, Colomb F R, Le Vine D, et al. 2008. The Aquarius/SAC-D mission: designed to meet the salinity remote-sensing challenge. Oceanography, 21(1): 68–81, doi: 10.5670/oceanog.2008.68

Le Vine D M, Lagerloef G S E, Colomb F R, et al. 2007. Aquarius: an instrument to monitor sea surface salinity from space. IEEE Transactions on Geoscience and Remote Sensing, 45(7): 2040–2050, doi: 10.1109/TGRS.2007.898092

Liu Baochao, Feng Licheng. 2012. An observational analysis of the relationship between wind and the expansion of the Changjiang River diluted water during summer. Atmospheric and Oceanic Science Letters, 5(5): 384–388, doi: 10.1080/16742834.2012.11447027

Mao H L, Kan T C, Lan Shufang. 1963. A preliminary study of the Yangtze diluted water and its mixing processes. Oceanologia et Limnologia Sinica (in Chinese), 5(3): 183–206

Subrahmanyam B, Murty V S N, Heffner D M. 2011. Sea surface salinity variability in the tropical Indian Ocean. Remote Sensing of Environment, 115(3): 944–956, doi: 10.1016/j.rse.2010.12.004

Xuan Jiliang, Huang Daji, Zhou Feng, et al. 2012. The role of wind on the detachment of low salinity water in the Changjiang Estuary in summer. Journal of Geophysical Research: Oceans, 117(C10): C10004, doi: 10.1029/2012jc008121

Yueh S, Fore A, Tang Wenqing, et al. 2016. Applications of SMAP data to retrieval of ocean surface wind and salinity. In: Proceedings of SPIE 9999, Remote Sensing of the Ocean, Sea Ice, Coastal Waters, and Large Water Regions 2016. Edinburgh, United Kingdom: SPIE, doi: 10.1117/12.2240710

Yueh S, Tang Wenqing, Fore A, et al. 2014. Aquarius geophysical model function and combined active passive algorithm for ocean surface salinity and wind retrieval. Journal of Geophysical Research: Oceans, 119(8): 5360–5379, doi: 10.1002/2014JC009939

Acta Oceanol. Sin., 2020, Vol. 39, No. 4, P. 9–17
https://doi.org/10.1007/s13131-020-1541-0
http://www.hyxb.org.cn
E-mail: hyxbe@263.net

Difference of planktonic ciliate communities of the tropical West Pacific, the Bering Sea and the Arctic Ocean

Chaofeng Wang[1, 2, 3, 4†], Haibo Li[1, 2, 4†], Zhiqiang Xu[4, 5], Shan Zheng[4, 5], Qiang Hao[6, 7], Yi Dong[1, 2, 4], Li Zhao[1, 2, 4], Wuchang Zhang[1, 2, 4*], Yuan Zhao[1, 2, 4*], Gérald Grégori[8], Tian Xiao[1, 2, 4]

[1] CAS Key Laboratory of Marine Ecology and Environmental Sciences, Institute of Oceanology, Chinese Academy of Sciences, Qingdao 266071, China

[2] Laboratory for Marine Ecology and Environmental Science, Pilot National Laboratory for Marine Science and Technology (Qingdao), Qingdao 266237, China

[3] University of Chinese Academy of Sciences, Beijing 100049, China

[4] Center for Ocean Mega-Science, Chinese Academy of Sciences, Qingdao 266071, China

[5] Jiaozhou Bay Marine Ecosystem Research Station, Institute of Oceanology, Chinese Academy of Sciences, Qingdao 266071, China

[6] State Key Laboratory of Satellite Ocean Environment Dynamics, Hangzhou 310012, China

[7] Second Institute of Oceanography, Ministry of Natural Resources, Hangzhou 310012, China

[8] Aix-Marseille University, Toulon University, CNRS, IRD, Mediterranean Institute of Oceanology UM110, Marseille 13288, France

Received 2 January 2019; accepted 6 March 2019

Abstract

Ciliates are important components in planktonic food webs, but our understanding of their community structures in different oceanic water masses is limited. We report pelagic ciliate community characteristics in three seas: the tropical West Pacific, the Bering Sea and the Arctic Ocean. Planktonic ciliate abundance had "bimodal-peak", "surface-peak" and "DCM (deep chlorophyll *a* maximum layer)-peak" vertical distribution patterns in the tropical West Pacific, the Bering Sea and the Arctic Ocean, respectively. The abundance proportion of tintinnid to total ciliate in the Bering Sea (42.6%) was higher than both the tropical West Pacific (7.8%) and the Arctic Ocean (2.0%). The abundance proportion of small aloricate ciliates (10–20 μm size-fraction) in the tropical West Pacific was highest in these three seas. The Arctic Ocean had higher abundance proportion of tintinnids in larger LOD (lorica oral diameter) size-class. Proportion of redundant species increased from the Arctic Ocean to the tropical West Pacific. Our result provided useful data to further understand ecology roles of planktonic ciliates in different marine habitats.

Key words: planktonic ciliates, vertical distribution, community structure, tropical West Pacific, Bering Sea, Arctic Ocean

Citation: Wang Chaofeng, Li Haibo, Xu Zhiqiang, Zheng Shan, Hao Qiang, Dong Yi, Zhao Li, Zhang Wuchang, Zhao Yuan, Grégori Gérald, Xiao Tian. 2020. Difference of planktonic ciliate communities of the tropical West Pacific, the Bering Sea and the Arctic Ocean. Acta Oceanologica Sinica, 39(4): 9–17, doi: 10.1007/s13131-020-1541-0

1 Introduction

Oceanic environments varied from the equator to high latitudes. In addition to the obvious decrease in surface water temperature with a progression northward to the pole, the stratification type varied from alpha oceans (subtropical seas stratified by temperature) to beta oceans (high-latitude seas stratified by salinity) (Carmack, 2007). The deep chlorophyll *a* maximum layer (DCM) became shallow in the area between the alpha and beta oceans. It ultimately changed into surface chlorophyll *a* maximum layer as in the Bering Sea (Wolf and Woods, 1988; Sohrin et al., 2010; Arrigo and van Dijken, 2011; Jiang et al., 2015; Burridge et al., 2017).

Biogeographically, plankton distribution can be determined by large gyres (Longhurst, 2007), of which three exist from the northern Pacific Ocean to the Arctic Ocean: the North Pacific Gyre, the Subarctic Gyre, and the Beaufort Gyre (Springer et al., 1996; Longhurst, 2007; Steele et al., 2004, 2011; Hu et al., 2015; Li et al., 2016). In addition to the difference in species composition and abundance in these different habitats, the structure and function of planktonic ecosystems were different (Megrey et al., 2009; Legendre and Niquil, 2013).

Planktonic ciliates belong to the phylum Ciliophora, class

Foundation item: The National Natural Science Foundation of China under contract No. 41706192; the Science & Technology Basic Resources Investigation Program of China under contract No. 2017FY100803; the National Natural Science Foundation of China-Shandong Joint Fund for Marine Science Research Centers under contract No. U1606404; the CNRS-NSFC Joint Research Projects Program under contract No. NSFC 41711530149; the 2017–2019 Sino-French Cai Yuanpei Programme; the National Natural Science Foundation of China under contract No. 41706217.

*Corresponding author, E-mail: wuchangzhang@qdio.ac.cn; yuanzhao@qdio.ac.cn

†These authors contributed equally to this work.

Spirotrichea, and subclasses Oligotrichia and Choreotrichia (Lynn, 2008). They comprise tintinnids with lorica, and aloricate ciliates without lorica. These ciliates are primary consumers of pico-(0.2–2 μm) and nano-(2–20 μm) sized producers, and are important food source for metazoan and fish larvae (Gómez, 2007). Accordingly, ciliates play an important role in material circulation and energy flow, from microbial food webs to the traditional food chain (Azam et al., 1983; Pierce and Turner, 1992; Calbet and Saiz, 2005).

It has been established that different tintinnid taxa dominate each of these gyres (Taniguchi, 1984; Dolan et al., 2014; Li et al., 2016; Wang et al., 2019). There was no study on other community characteristics of ciliates in addition to the taxonomic difference. In this study, we examined community characteristics of ciliates in the tropical West Pacific, the Bering Sea and the Arctic Ocean. The three study areas belong to the three gyres (the North Pacific Gyre, the Subarctic Gyre and the Beaufort Gyre), respectively. We hypothesize that ciliates characteristics differ due to the influence of each gyre. We examine following characteristics of ciliate community: (1) distribution patterns in their vertical direction, (2) abundance proportions of tintinnids to total ciliates, (3) the abundance proportion of aloricate ciliate size-fractions, and (4) tintinnid abundance proportion of different lorica oral diameter (LOD) size-classes and proportions of tintinnid redundant species in total tintinnids. Our results will assist in understanding differences in vertical distributions of ciliate communities in these three seas, exploit considerable mechanism that how pelagic ciliates structured in water column, and enable prediction of variation in tintinnid community species richness and LOD size-class composition in world oceans.

2 Materials and methods

Planktonic ciliates were sampled during two cruises: one to the tropical West Pacific (12 stations, deeper than 3 000 m) from 28 November to 31 December, 2015 aboard R/V *Kexue* (Fig. 1), and the other to the Bering Sea (5 stations, deeper than 500 m) and the Arctic Ocean (13 stations, deeper than 2 000 m) from 18 July to 10 September, 2016, during the 7th Chinese National Arctic Research Expedition aboard R/V *Xuelong* (Fig. 1).

At each station, temperature and salinity profiles were obtained from the surface to 200 m using a conductivity-temperature-pressure (CTD) sensor (Sea-Bird Electronics, Bellevue, WA,

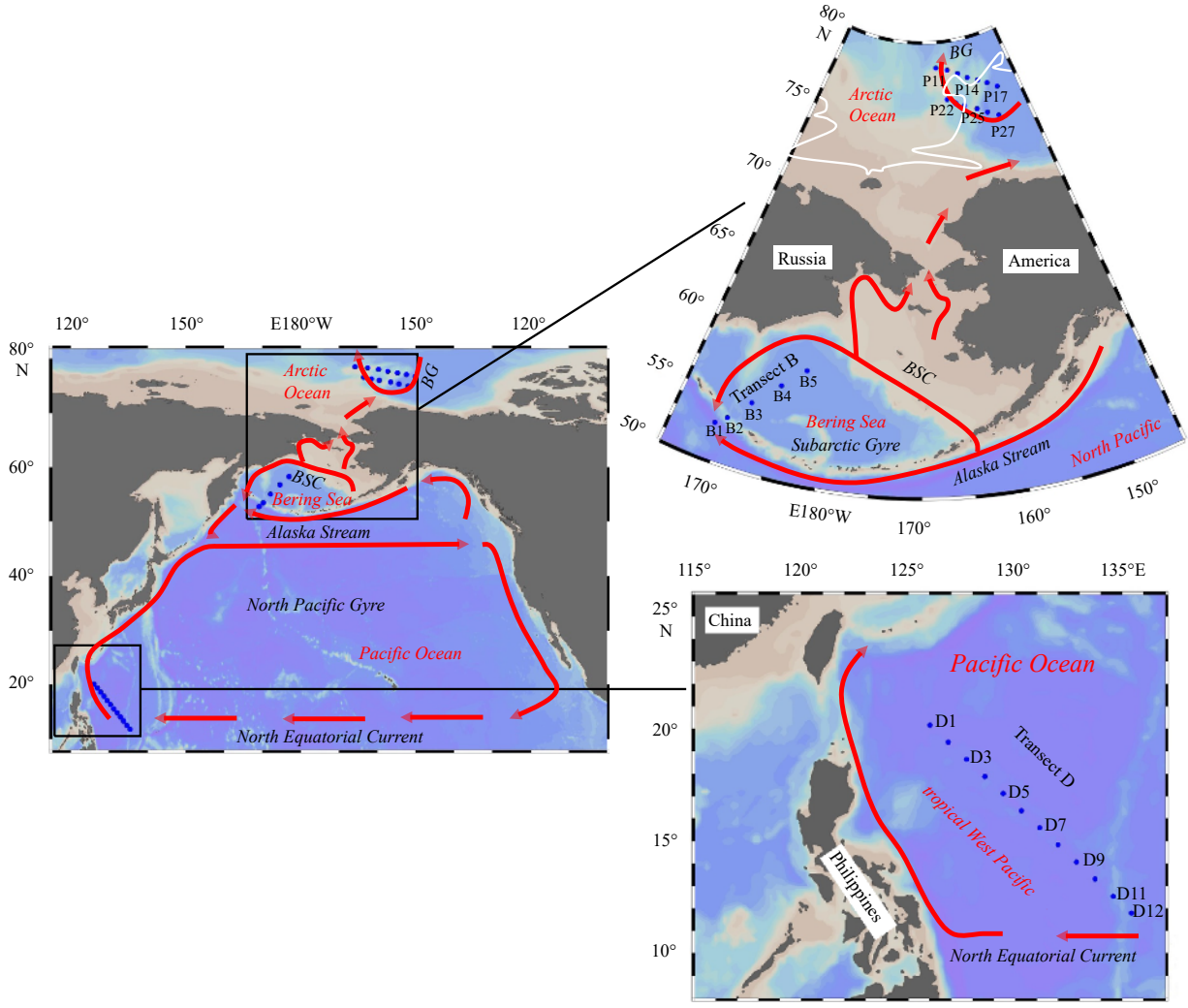

Fig. 1. Survey stations: tropical West Pacific, Bering Sea and Arctic Ocean. White line: 80% sea ice concentrations, 15th August, 2016, according to Sea Ice Remote Sensing at the University of Bremen (https://seaice.uni-bremen.de/sea-ice-concentration/). Arrows depict currents according to Springer et al. (1996), Steele et al. (2004), Longhurst (2007), and Hu et al. (2015). BSC: Bering Sea Current; BG: Beaufort Gyre.

USA). Water samples were collected at seven depths (sampling points) using 12-L Niskin bottles attached to a rosette wheel. Most sampling occurred at the surface (5 m), 30 m, 50 m, 75 m, 100 m, 150 m and 200 m in each station, but sampling within the DCM necessitated some variation in sampling depth.

Chlorophyll *a* (Chl *a*) concentration was determined by filtering 250 mL of seawater through a Whatman GF/F glass fiber filter. Plankton retained on the filter was extracted in 90% (v/v) acetone, and its fluorescence measured according to the JGOFS protocol (Knap et al., 1996) using a Turner Trilogy fluorometer Model 10.

Water samples (1 L) collected from each depth for ciliate enumeration were fixed with 1% acid Lugol's iodine and stored below 4°C in darkness. In the laboratory, samples were concentrated to about 100 mL by gently siphoning off supernatant after settling for at least 48 h. This settling and siphoning processes was repeated until a final concentrated volume of 50 mL was achieved, which was then settled in two Utermöhl counting chambers (25 mL per chamber) (Utermöhl, 1958) for at least 24 h.

The samples in the two chambers was examined using an Olympus IX 71 inverted microscope (100× or 400×). Less-abundant species were counted in two chambers, while high abundance species were counted in one chamber. Because mechanical and chemical disturbance associated with collection and fixation may have provoked detachment of the protoplasma from the lorica (Paranjape and Gold, 1982; Alder, 1999), empty tintinnid loricae were counted as living cells. We acknowledge the possibility that some lorica might have been empty at collection (Kato and Taniguchi, 1993; Dolan and Yang, 2017), and that our abundances might be overestimates.

For each species, size (length, width, according to shape) of the cell (aloricate ciliate) or lorica (tintinnid, especially length and oral diameter) were measured for at least 20 individuals if possible. Aloricate ciliates were categorized into size-fractions in increments of 10 μm for maximum body length for each individual. According to lorica morphology and size, tintinnids were identified to species following Kofoid and Campbell (1929, 1939), Lynn (2008) and Zhang et al. (2012). Ciliate volumes were estimated using appropriate geometric shapes (cone, ball, and cylinder). Tintinnid carbon biomass was estimated using the equation: carbon = lorica volume (μm^3) × 0.053 + 444.5 (Verity and Lagdon, 1984). We used a conversion factor of carbon biomass for aloricate ciliates of 0.19 pg/μm^3 (Putt and Stoecker, 1989).

There was no existing standardized reference to aloricate ciliate size-fraction. Though Marquis et al. (2011) suggested using equivalent spherical diameter (ESD) to calculate microzooplankton communities, but this method does not reveal the exact length of each aloricate ciliate. We categorized aloricate ciliate size-fractions based on measurement of their longest cell length, following Lessard and Murrell (1996), Taylor et al. (2011) and Liang et al. (2018).

Tintinnid lorica length at different life stages might differ greatly (Gold and Morales, 1976), while the lorica oral diameter (LOD) variation was low for the same tintinnid species (Dolan, 2010). Therefore, LOD was used as a proxy for tintinnid size in this study. The tintinnids were divided into different LOD size-classes which were 4 μm apart (12–16 μm, 16–20 μm and so on). Redundant tintinnid species were defined as these species in the same LOD size-classes. If one LOD size-class has species number (n) larger than one, redundant species number of this LOD size-class was n–1. For a tintinnid assemblage, redundant species number is the sum of that in every LOD size-class. Methematically, redundant species number of a tintinnid assemblage could be calculated as the number of species minus the number of LOD size-classes (Dolan et al., 2016). The proportion of redundant tintinnid species was calculated as the percentage of redundant species number in total species number.

3 Results

3.1 *Hydrographic features*

Surface temperature and salinity decreased from the tropical West Pacific (27.2–28.6°C, 33.8–34.7) to the Bering Sea (10.1–10.5°C, 32.7–33.0), then to the Arctic Ocean (–1.2–0.7°C, 26.5–28.3). Surface average Chl *a* was highest in the Bering Sea ((0.8±0.5) μg/L), and values in the tropical West Pacific and the Arctic Ocean were (0.1±0.0) μg/L and (0.0±0.0) μg/L, respectively (Fig. 2).

Vertical temperature, salinity and Chl *a* concentration profiles differed in the three seas. The thermocline in the tropical West Pacific occurred at about 100 m, much deeper than in the Bering Sea (about 30 m) and the Arctic Ocean (about 5 m). In the Arctic Ocean, a second temperature peak occurred between 50 and 75 m (Fig. 2).

Salinity was stratified with depth, with lower salinity in surface waters of each sea. The magnitude of differences in temperature and salinity between surface waters and those at 200 m differed in the three seas: temperature ranges in the tropical West Pacific (13.9–28.6°C, difference 14.7°C) and the Bering Sea (1.5–11.3°C, difference 9.8°C) were larger than in the Arctic Ocean (–1.6–1.2°C, difference 2.8°C); salinity ranges in the tropical West Pacific (34.3–35.1, difference 0.8) and the Bering Sea (32.8–33.4, difference 0.6) were smaller than in the Arctic Ocean (27.4–33.4, difference 6.0) (Fig. 2).

Chl *a* concentration differed significantly among the three seas. DCM occurred in both the tropical West Pacific ((101±17) m) and the Arctic Ocean ((66±7) m), but not the Bering Sea, where high Chl *a* concentration occurred in the surface (Fig. 2).

3.2 *Ciliate abundance, biomass and vertical distribution*

Basically ciliate abundance and biomass (calculated by carbon) in the Bering Sea (152–3 267 ind./L, 0.3–11.6 μg/L) was larger than in the tropical West Pacific (35–443 ind./L, 0–0.7 μg/L) and the Arctic Ocean (12–1 615 ind./L, 0–4.5 μg/L) (Fig. 3). In the surface layer, average abundances in the Bering Sea ((1 830±1 046) ind./L) were 5.7 times and 12.0 times higher than those in the tropical West Pacific ((320±88) ind./L) and Arctic Ocean ((153±94) ind./L), respectively (Fig. 4).

Vertical distribution trend of average abundances of ciliates for each depth in the tropical West Pacific, the Bering Sea and the Arctic Ocean differed (Fig. 4). Average abundance had a "bimodal-peak" (high abundance in both surface and DCM layers), "surface-peak" (high abundance in surface layers), and "DCM-peak" (high abundance in DCM layers), in the tropical West Pacific, the Bering Sea, and the Arctic Ocean, respectively (Fig. 4).

3.3 *Abundance proportion of tintinnid to total ciliate*

Generally, tintinnids were not the dominant (abundance proportion >50%) group of planktonic ciliates. However, tintinnids were the dominant group at layers of 50 m and 100 m (abundance proportion 51.7% and 57.0%, respectively) in the Bering Sea. In terms of average abundance proportion in different layers, tintinnids represented 0.0%–18.3% (average 7.8%±3.1%), 3.9%–75.1% (average 42.6%±20.9%), and 0.0%–9.7% (average 2.0%±2.2%) of all ciliates in the tropical West Pacific, the Bering Sea and the Arctic Ocean, respectively (Fig. 5).

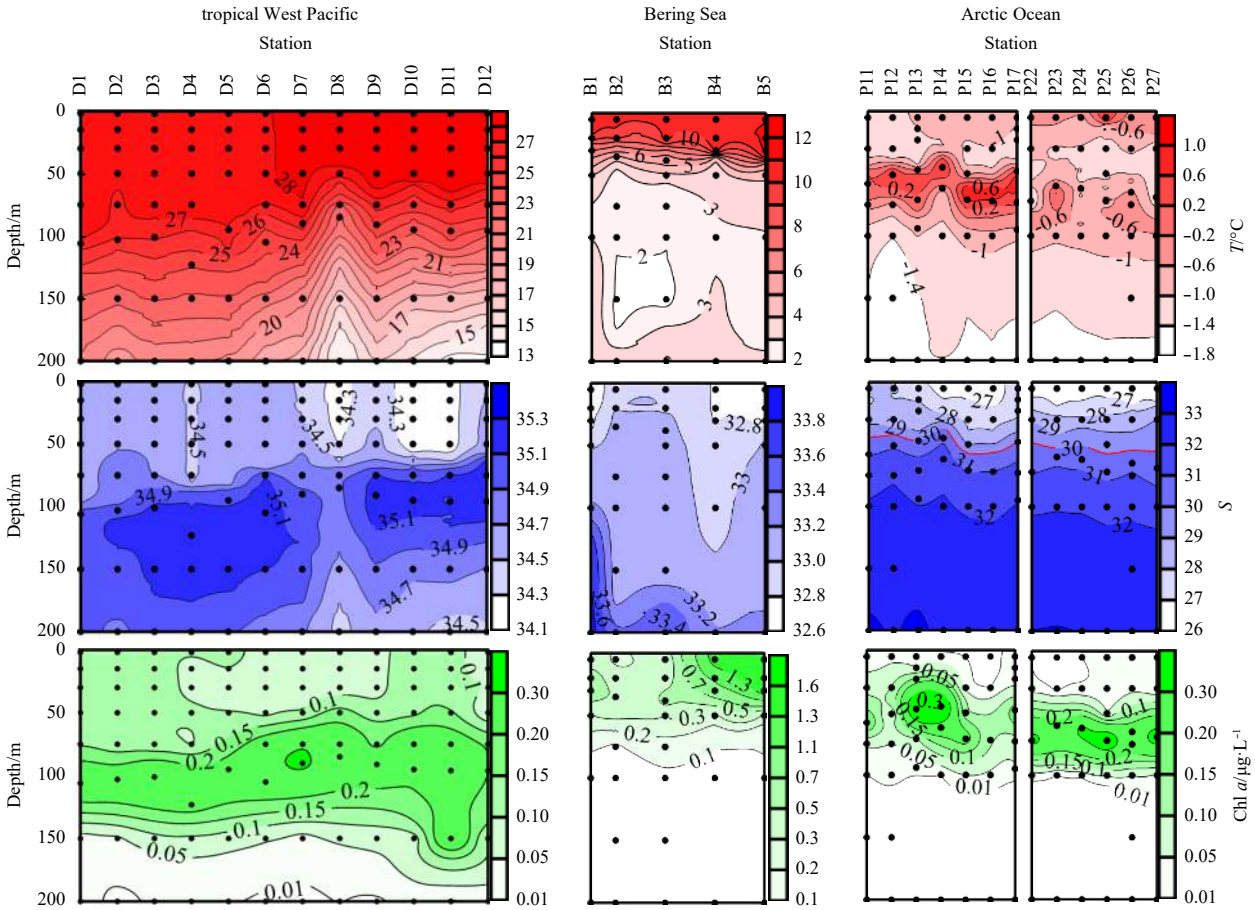

Fig. 2. Vertical distributions of temperature (T), salinity (S) and Chl *a* concentration from the surface to 200 m in the tropical West Pacific, the Bering Sea and the Arctic Ocean. Black circles: sampling points. Vertical distribution of temperature and salinity in the tropical West Pacific from Wang et al. (2019).

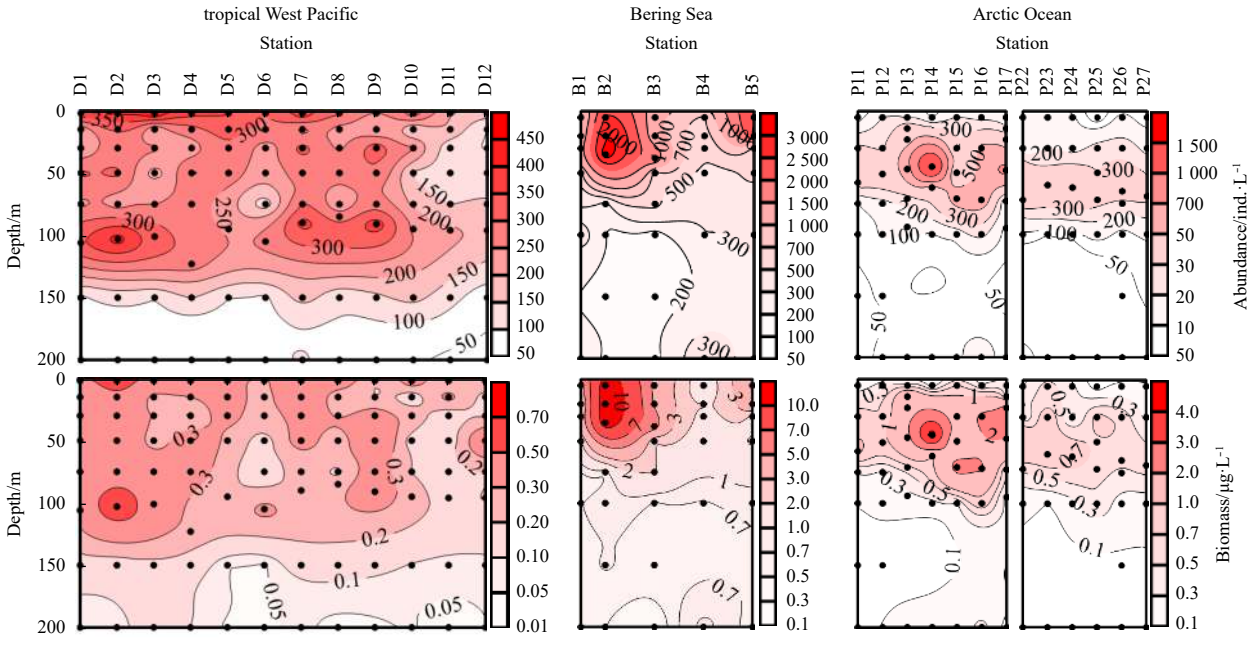

Fig. 3. Vertical distribution of ciliate abundance and biomass from the surface to 200 m in the tropical West Pacific, the Bering Sea and the Arctic Ocean. Black circles: sampling points. Vertical distributions of ciliate abundance and biomass in the tropical West Pacific from Wang et al. (2019).

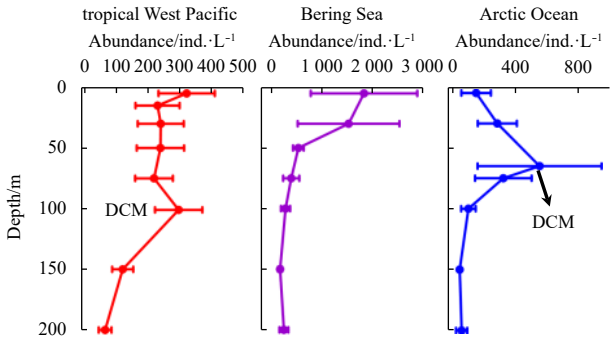

Fig. 4. Vertical distributions of ciliate (total of aloricate and tintinnid ciliates) average abundance for sampling layers in three study areas. DCM: deep chlorophyll *a* maximum layer. Vertical distribution of average ciliate abundance in the tropical West Pacific from Wang et al. (2019).

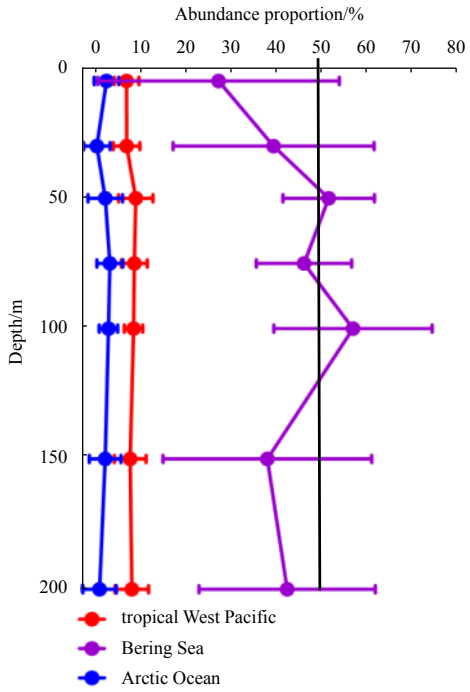

Fig. 5. Average abundance proportion of tintinnids to total ciliates from the surface to 200 m depth in the tropical West Pacific, the Bering Sea and the Arctic Ocean.

3.4 *Aloricate ciliate size-fraction difference*

Abundance proportions of different size-fractions of aloricate ciliates revealed individuals of 10–30 μm size-fractions were more abundant at each depth in the tropical West Pacific than in the Bering Sea and Arctic Ocean (Fig. 6). The 10–30 μm size-fraction in surface waters represented 76.5%±6.8% of aloricate ciliates in the tropical West Pacific, about 20% higher than in both the Bering Sea (54.6%±7.5%) and the Arctic Ocean (56.7%±7.8%). Aloricate ciliates >30 μm size-fraction in surface waters represented less than 30% of all aloricate ciliates in the tropical West Pacific, but more than 40% in both the Bering Sea and the Arctic Ocean (Fig. 6). From surface waters to 200 m depth, aloricate ciliates abundance proportion of 10–20 μm size-fraction were most abundant in the tropical West Pacific, representing more than 40% of all aloricate ciliates. In the Bering Sea and the Arctic Ocean, aloricate ciliates >30 μm size-fraction were the dominant size-fraction component from surface waters to 150 m depth, but at 200 m the 10–20 μm size-fraction predominated (>40% of all aloricate ciliates) (Fig. 6).

In all three gyres, the abundance proportion of aloricate ciliates in the 10–20 μm size-fraction decreased from surface layers to 75 m (in both the tropical West Pacific and Bering Sea) or 50 m (in the Arctic Ocean), then increased to 200 m depth, while that of the 20–30 μm size-fraction was relatively constant throughout the water column to depths of 200 m. The abundance proportion of aloricate ciliates >30 μm size-fraction first increased from surface waters to 75 m (in both the tropical West Pacific and Bering Sea) or 30 m (in the Arctic Ocean), but then decreased to 200 m in all three water masses. In the layers of 30–75 m, the average abundance proportions of aloricate ciliates >30 μm size-fraction were about 4.4%, 4.9% and 3.8% higher than in surface layers in the tropical West Pacific, the Bering Sea and the Arctic Ocean, respectively (Fig. 6).

3.5 *Lorica oral diameter size-classes and proportion of redundant tintinnid species*

From the tropical West Pacific to the Arctic Ocean, abundance proportion of tintinnids with larger lorica oral diameter (LOD) became higher (Fig. 7). Tintinnid species with LOD ranging 12–16 μm and 24–28 μm size-classes were proportionally most abundant (26.7% and 59.5%) in the tropical West Pacific and the Bering Sea, respectively, while in the Arctic Ocean, tintinnids of LOD 60–64 μm size-class was proportionally most abundant (50.0%) (Fig. 7).

Different seas had different tintinnid species richness patterns in LOD size-classes, and proportions of redundant species. Tintinnids ranging 28–32 μm and 32–36 μm LOD size-classes were the two most species rich size-classes, with 9 and 8 tintinnid species, respectively, in the tropical West Pacific (Fig. 7). Tintinnids of LOD ranging 60–64 μm size-class was the most species rich (3 species) in the Bering Sea. In the tropical West Pacific and Bering Sea there were 48 and 4 redundant species, with the proportion of redundant species being 72.4% and 28.6%, respectively. In the Arctic Ocean, four species were equally distributed in four LOD size-classes, and there were no redundant species.

4 Discussion

4.1 *Planktonic ciliate vertical distribution*

In our study, the distributions of planktonic ciliates in the oceanic area through the water column in the Bering Sea and the Arctic Ocean were revealed to be “surface-peak” and “DCM-peak” patterns, respectively. Though previous studies have not specifically described the patterns in the vertical distribution of planktonic ciliates in either of these two areas, their data revealed that comparable patterns existed: high abundances were reported from surface layers in the Bering Sea (Taniguchi, 1984), and in the Arctic Ocean DCM at 40–80 m (Yang et al., 2015); while a “bimodal-peak” pattern was reported from the Bering Strait to the western Arctic Ocean based on average values (Xu et al., 2018a). The surface peak in Xu et al. (2018a) might be due to high values at shelf stations in the Bering Strait (Matsuno et al., 2014; Yang et al., 2015; our unpublished data), so results of Xu et al. (2018a) may be not representative for the oceanic Arctic Ocean.

Planktonic ciliate vertical distributions have been reported for oceanic waters of the Pacific Ocean (Strom et al., 1993; Leakey et al., 1996; Yang et al., 2004; Gómez, 2007; Sohrin et al., 2010; Zhao et al., 2017; Wang et al., 2016, 2019). However, only Wang et al.

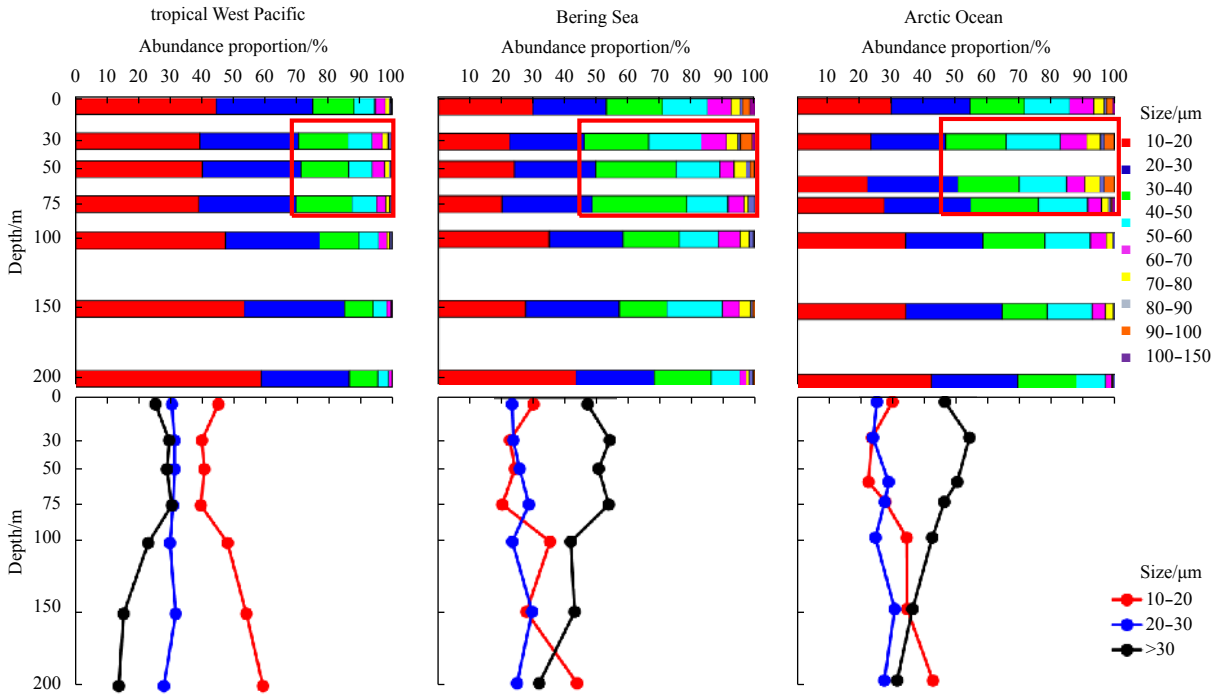

Fig. 6. The abundance proportion of aloricate ciliates different size-class composition (upper) and average abundance (lower) by each layers in the tropical West Pacific, the Bering Sea and the Arctic Ocean. The red dashed box depicts the abundance proportions of aloricate ciliates >30 μm size was greater than those in surface layers.

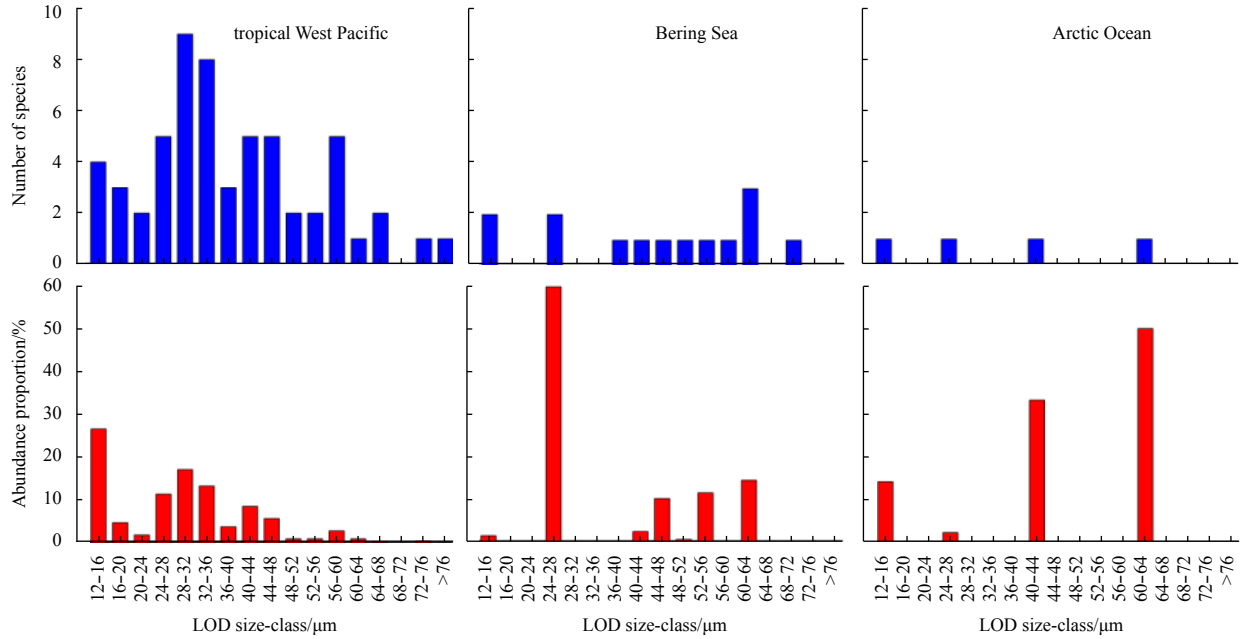

Fig. 7. Number of species and the abundance proportion of each tintinnid LOD (lorica oral diameter, μm) size-class in the tropical West Pacific, the Bering Sea and the Arctic Ocean.

(2019) explicitly described ciliate vertical distribution patterns as having a "bimodal-peak" in the tropical West Pacific.

Several studies have shown ciliate abundance to be positively correlated with Chl *a* concentration (Dolan and Marrasé, 1995; Yu et al., 2013; Jiang et al., 2015; Xu et al., 2018a, b). Our studies showed that there were ciliate peaks in the maximum Chl *a* layer, no matter it is in the subsurface (DCM) or surface layer. Although the tropical West Pacific and the Arctic Ocean had low Chl *a* concentration in the surface, but there was no surface ciliate peak in the Arctic Ocean as in the tropical West Pacific. We do not know the reasons of this phenomenon because there were differences in surface temperature and salinity between the two areas.

Low salinity in the Arctic Ocean might not be a decisive factor for the low ciliate abundance in the surface layer. In the estuaries such as Changjiang River Estuary, fresh water river discharge

causes low salinity (<30) as well as high Chl *a* and nutrient concentrations in the surface waters (Wang et al., 2013; Zhang et al., 2015). In this case, ciliate in the surface freshwater was higher than in the subsurface layer (Yu et al., 2015).

4.2 *Abundance proportion of tintinnid to total ciliate*

Abundance proportion of tintinnid to total ciliate have been described for tropical and subtropical waters (Fig. 8) (Yang et al., 2004; Gómez, 2007; Sohrin et al., 2010; Wang et al., 2016, 2019). In the tropical West Pacific, average tintinnid abundance proportions varied from 20% (Yang et al., 2004) to less than 10% (Wang et al., 2016, 2019), and in other studies, abundance proportions about 10% in surface equatorial waters to 5% in waters from 10°–15°N (Sohrin et al., 2010). Our result of 7.8% for the tropical West Pacific is comparable to that of Wang et al. (2016) and Sohrin et al. (2010).

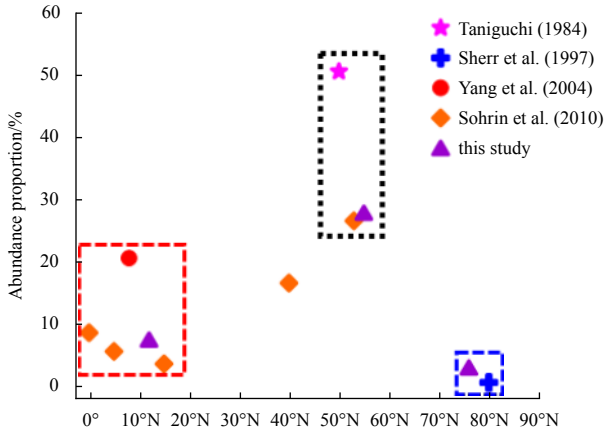

Fig. 8. Abundance proportions of tintinnids to total ciliates in surface layers by latitude. Red dashed box: the tropical Pacific; black dashed box: the Bering Sea; and blue dashed box: the Arctic Ocean.

Abundance proportion of tintinnid to total ciliates were unknown for the Bering Sea and the Arctic Ocean. The abundance proportion (42.6%) in the Bering Sea waters (52°–58°N) in our study was higher than that (25%) for the same latitude (53°N) along 160°W in the subarctic Pacific (Sohrin et al., 2010). We estimate previous abundance proportion (from the surface to 160 m depth) for the Bering Sea based on values in Fig. 2 of Taniguchi (1984) to be about 50%, which is close to our result from this region. The very low value (2.0%) we report for the Arctic Ocean is consistent with Sherr et al. (1997), where tintinnids were reported to be rarely observed from 70°–90°N.

Our data and previous studies showed that the Bering Sea and the Arctic Ocean had the highest and lowest abundance proportion of tintinnids to total ciliates. Until now, environmental factors responsible for these differences were unknown. Loricate ciliates are adapted to high Chl *a* environment where food is sufficient (Suzuki and Taniguchi, 1998). High Chl *a* concentration in the Bering Sea might contribute to the high tintinnid abundance proportion (Fig. 2).

4.3 *Difference in aloricate ciliate size-fractions*

The bathymetric distributions of different size-fractions of aloricate ciliates have been rarely reported from oceanic environments. Ours is the first report of the vertical distribution of aloricate ciliate size-fractions in these three gyres. Our results reveal aloricate ciliates <20 μm size-fraction comprise about 45% of all ciliates in surface waters of the tropical West Pacific. This result is consistent with that reported for the northeast equatorial Pacific (5°–11°N), where the average abundance proportion of aloricate <20 μm to total ciliates in the surface was about 50% (Yang et al., 2004), and the Red Sea (29.5°N, depth 650 m), where it was >50% in surface water (Claessens et al., 2008).

No reports of the size-fraction composition of aloricate ciliates in the Bering Sea and the Arctic Ocean are known. In the Prydz Bay (65°–68°S, Southern Ocean), the aloricate ciliates <20 μm size-fraction represented about 40% of the total numbers of aloricate ciliate (Liang et al., 2018), which is both higher than in the Bering Sea and the Arctic Ocean.

We found abundance proportion of aloricate ciliate >30 μm size-fraction in each depth increased from the tropical West Pacific to the Arctic Ocean. The Arctic Ocean has a lower percentage of smaller size-fraction aloricate ciliates. This result supports Bergmann's rule, that, in general, larger-bodied animals tend to live further north than their smaller-bodied relatives (Bergmann, 1847). Some subarctic and subantarctic zooplankton tend to be larger than their relatives in subtropical species (Reid et al., 1978; Martin et al., 2006; Gallienne et al., 2001). For example, species in genus *Euphausia* is 20 mm in body length in subarctic, while it is only 8 mm in subtropical area (Reid et al., 1978).

Why proportionally more larger-sized aloricate ciliates occur in subsurface layers, and more smaller-sized aloricate ciliates occur in deeper waters in all the three areas is unknown in vertical direction. As maximum Chl *a* concentration layers occurred at different depths in the three areas, we speculate that Chl *a* concentration might not be the reason.

4.4 *Variation of dominant lorica oral diameter size-class and proportion of tintinnid redundant species*

Tintinnid LOD (lorica oral diameter) size-class in these three seas has not been previously compared. Dominant tintinnid LOD size-classes have been reported for the Bering Sea (Li et al., 2016) and the Jiaozhou Bay (Feng et al., 2018). Our result that the dominant LOD size-class (24–28 μm) in the Bering Sea is similar to that (22–26 μm) of Li et al. (2016). The space difference in our study that the dominant LOD size-class is large in the cold Arctic Ocean, but small in the warm tropical West Pacific is similar to seasonal changes in dominant LOD size-classes in the Jiaozhou Bay (Feng et al., 2018), where it is larger (48–52 μm) in winter than summer (24–32 μm). Thus, we speculate dominant LOD size-class might be large in cold areas, which might be another aspect of the Bergman's Rule in tintinnids.

Proportions of redundant species in tintinnid assemblages increased markedly from polar to low latitude areas in the northern hemisphere. From 83°N to 37°N, this proportion increased from 0% to 57% (Dolan et al., 2016), while in the Jiaozhou Bay (36°N), this value was 50% all year round (Feng et al., 2018). We found this value to continue increasing with progression from the Arctic Ocean to 15°N, in a linear manner (Fig. 9). Further study is needed to support whether this value will continue to increase southward to equatorial waters.

5 Conclusions

We report changes in ciliate community characteristics in some transects influenced by three gyres (the North Pacific Gyre, the Subarctic Gyre and the Beaufort Gyre). Planktonic ciliates manifest "bimodal-peak", "surface-peak" and "DCM-peak" patterns of bathymetric distribution in the tropical West Pacific, the Bering Sea and the Arctic Ocean, respectively. The abundance

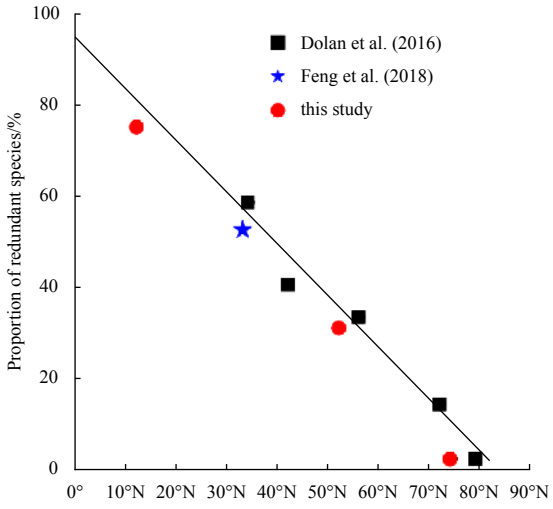

Fig. 9. Relationship between latitude and proportion of redundant species.

proportion of tintinnid to total ciliate increased from the tropical West Pacific to the Bering Sea, then decreased to the Arctic Ocean. Abundance proportion of aloricate ciliate in larger size-fraction increased from tropical West Pacific waters to the Arctic Ocean. Finally, the dominant LOD size-class was small in the tropical West Pacific waters, but large in the Arctic Ocean, with the proportion of redundant species decreasing from the former to the latter. Our results represent a snapshot of ciliate community structure in each gyre, which constitute a baseline for further comparative study on temporal and spatial variation of ciliate communities in the three gyres.

Acknowledgements

Special thanks to the great efforts of the crew of R/V *Kexue* during the cruise in the tropical West Pacific, and R/V *Xuelong* during the cruise in the Bering Sea and the Arctic Ocean, respectively. We thank Steve O'Shea of the Edanz Group (www.edanzediting.com/ac) for editing a draft of this manuscript.

References

Alder V A. 1999. Tintinnoinea. In: Boltovskoy D, ed. South Atlantic Zooplankton. Leiden: Backhuys, 321–384

Arrigo K R, van Dijken G L. 2011. Secular trends in Arctic Ocean net primary production. Journal of Geophysical Research, 116(C9): C09011

Azam F, Fenchel T, Field J G, et al. 1983. The ecological role of water-column microbes in the sea. Marine Ecology Progress Series, 10: 257–263, doi: 10.3354/meps010257

Bergmann C. 1847. Über die verhältnisse der wärmeökonomie der thiere zu ihrer größe. Göttinger Studien (in German), 3: 595–708

Burridge A K, Goetze E, Wall-Palmer D, et al. 2017. Diversity and abundance of pteropods and heteropods along a latitudinal gradient across the Atlantic Ocean. Progress in Oceanography, 158: 213–223, doi: 10.1016/j.pocean.2016.10.001

Calbet A, Saiz E. 2005. The ciliate-copepod link in marine ecosystems. Aquatic Microbial Ecology, 38(2): 157–167

Carmack E C. 2007. The alpha/beta ocean distinction: a perspective on freshwater fluxes, convection, nutrients and productivity in high-latitude seas. Deep Sea Research Part II: Topical Studies in Oceanography, 54(23–26): 2578–2598, doi: 10.1016/j.dsr2.2007.08.018

Claessens M, Wickham S A, Post A F, et al. 2008. Ciliate community in the oligotrophic Gulf of Aqaba, Red Sea. Aquatic Microbial Ecology, 53(2): 181–190

Dolan J R. 2010. Morphology and ecology in tintinnid ciliates of the marine plankton: correlates of lorica dimensions. Acta Protozoologica, 49: 235–244

Dolan J R, Marrasé C. 1995. Planktonic ciliate distribution relative to a deep chlorophyll maximum: Catalan Sea, N. Mediterranean, June 1993. Deep Sea Research Part I: Oceanographic Research Papers, 42(11–12): 1965–1987, doi: 10.1016/0967-0637(95)00092-5

Dolan J R, Yang E J. 2017. Observations of apparent lorica variability in *Salpingacantha* (Ciliophora: tintinnida) in the Northern Pacific and Arctic Oceans. Acta Protozoologica, 56(3): 217–220

Dolan J R, Yang E J, Kang S H, et al. 2016. Declines in both redundant and trace species characterize the latitudinal diversity gradient in tintinnid ciliates. The ISME Journal, 10(9): 2174–2183, doi: 10.1038/ismej.2016.19

Dolan J R, Yang E J, Kim T W, et al. 2014. Microzooplankton in a warming Arctic: a comparison of tintinnids and radiolarians from summer 2011 and 2012 in the Chukchi Sea. Acta Protozoologica, 53(1): 101–113

Feng Meiping, Wang Chaofeng, Zhang Wuchang, et al. 2018. Annual variation of species richness and lorica oral diameter characteristics of tintinnids in a semi-enclosed bay of western Pacific. Estuarine, Coastal and Shelf Science, 207: 164–174, doi: 10.1016/j.ecss.2018.04.003

Gallienne C P, Robins D B, Woodd-Walker R S. 2001. Abundance, distribution and size structure of zooplankton along a 20° west meridional transect of the northeast Atlantic Ocean in July. Deep Sea Research Part II: Topical Studies in Oceanography, 48(4–5): 925–949, doi: 10.1016/S0967-0645(00)00114-4

Gold K, Morales E A. 1976. Observations on the nature and significance of the particles used by Tintinnida during lorica-building. Transactions of the American Microscopical Society, 95(1): 69–72, doi: 10.2307/3225353

Gómez F. 2007. Trends on the distribution of ciliates in the open Pacific Ocean. Acta Oecologica, 32(2): 188–202, doi: 10.1016/j.actao.2007.04.002

Hu Dunxin, Wu Lixin, Cai Wenju, et al. 2015. Pacific western boundary currents and their roles in climate. Nature, 522(7556): 299–308, doi: 10.1038/nature14504

Jiang Yong, Yang E J, Min J O, et al. 2015. Vertical variation of pelagic ciliate communities in the western Arctic Ocean. Deep Sea Research Part II: Topical Studies in Oceanography, 120: 103–113, doi: 10.1016/j.dsr2.2014.09.005

Kato S, Taniguchi A. 1993. Tintinnid ciliates as indicator species of different water masses in the western North Pacific Polar Front. Fisheries Oceanography, 2(3–4): 166–174, doi: 10.1111/j.1365-2419.1993.tb00132.x

Knap A H, Michaels A, Close A R, et al. 1996. Protocols for the joint global ocean flux study (JGOFS) core measurements. Bergen, Norway: JGOFS Core Project Office, Centre for Studies of Environment and Resources, University of Bergen, 155–162

Kofoid C A, Campbell A S. 1929. A conspectus of the marine and fresh-water ciliata belonging to the suborder tintinnoinea, with descriptions of new species principally from the Agassiz expedition to the Eastern Tropical Pacific 1904–1905. University of California, Publications in Zoology, 34: 1–403

Kofoid C A, Campbell A S. 1939. The ciliata: the tintinnoinea. Reports on the scientific results of the expedition to the eastern tropical Pacific, 1904–1905. Cambridge: Museum of Comparative Zoology at Harvard College, 1–473

Leakey R J G, Burkill P H, Sleigh M A. 1996. Planktonic ciliates in the northwestern Indian Ocean: their abundance and biomass in waters of contrasting productivity. Journal of Plankton Research, 18(6): 1063–1071, doi: 10.1093/plankt/18.6.1063

Legendre L, Niquil N. 2013. Large-scale regional comparisons of ecosystem processes: methods and approaches. Journal of Marine System, 109-110: 4–21, doi: 10.1016/j.jmarsys.2011.11.021

Lessard E J, Murrell M C. 1996. Distribution, abundance and size composition of heterotrophic dinoflagellates and ciliates in the Sargasso Sea near Bermuda. Deep Sea Research Part I: Oceano-

graphic Research Papers, 43(7): 1045–1065, doi: 10.1016/0967-0637(96)00052-0

Li Haibo, Xu Zhiqiang, Zhang Wuchang, et al. 2016. Boreal tintinnid assemblage in the Northwest Pacific and its connection with the Japan Sea in summer 2014. PLoS One, 11(4): e0153379, doi: 10.1371/journal.pone.0153379

Liang Chen, Li Haibo, Dong Yi, et al. 2018. Planktonic ciliates in different water masses in open waters near Prydz Bay (East Antarctica) during austral summer, with an emphasis on tintinnid assemblages. Polar Biology, 41(11): 2355–2371, doi: 10.1007/s00300-018-2375-5

Longhurst A R. 2007. Ecological Geography of the Sea. 2nd ed. Amsterdam: Academic Press

Lynn D H. 2008. The Ciliated Protozoa: Characterization, Classification, and Guide to the Literature. New York: Springer, 1–455

Marquis E, Niquil N, Dupuy C. 2011. Does the study of microzooplankton community size structure effectively define their dynamics? Investigation in the Bay of Biscay (France). Journal of Plankton Research, 33(7): 1104–1118, doi: 10.1093/plankt/fbr009

Martin E S, Harris R P, Irigoien X. 2006. Latitudinal variation in plankton size spectra in the Atlantic Ocean. Deep Sea Research Part II: Topical Studies in Oceanography, 53(14–16): 1560–1572, doi: 10.1016/j.dsr2.2006.05.006

Matsuno K, Ichinomiya M, Yamaguchi A, et al. 2014. Horizontal distribution of microprotist community structure in the western Arctic Ocean during late summer and early fall of 2010. Polar Biology, 37(8): 1185–1195, doi: 10.1007/s00300-014-1512-z

Megrey B A, Link J S, Hunt G L Jr, et al. 2009. Comparative marine ecosystem analysis: applications, opportunities, and lessons learned. Progress in Oceanography, 81(1–4): 2–9, doi: 10.1016/j.pocean.2009.04.002

Paranjape M A, Gold K. 1982. Cultivation of marine pelagic protozoa. Annales de L'institut Océanographique, Paris, 58(S): 143–150

Pierce R W, Turner J T. 1992. Ecology of planktonic ciliates in marine food webs. Reviews in Aquatic Sciences, 6(2): 139–181

Putt M, Stoecker D K. 1989. An experimentally determined carbon: volume ratio for marine "oligotrichous" ciliates from estuarine and coastal waters. Limnology and Oceanography, 34(6): 1097–1103, doi: 10.4319/lo.1989.34.6.1097

Reid J L, Brinton E, Fleminger A, et al. 1978. Ocean circulation and marine life. In: Charnock H, Deacon G, eds. Advances in Oceanography. Boston: Springer, 65–130

Sherr E B, Sherr B F, Fessenden L. 1997. Heterotrophic protists in the Central Arctic Ocean. Deep Sea Research Part II: Topical Studies in Oceanography, 44(8): 1665–1673, doi: 10.1016/S0967-0645(97)00050-7

Sohrin R, Imazawa M, Fukuda H, et al. 2010. Full-depth profiles of prokaryotes, heterotrophic nanoflagellates, and ciliates along a transect from the equatorial to the subarctic central Pacific Ocean. Deep Sea Research Part II: Topical Studies in Oceanography, 57(16): 1537–1550, doi: 10.1016/j.dsr2.2010.02.020

Springer A M, Mcroy C P, Flint M V. 1996. The Bering Sea green belt: shelf-edge processes and ecosystem production. Fisheries Oceanography, 5(3–4): 205–223, doi: 10.1111/j.1365-2419.1996.tb00118.x

Steele M, Ermold W, Zhang Jinlun. 2011. Modeling the formation and fate of the near-surface temperature maximum in the Canadian Basin of the Arctic Ocean. Journal of Geophysical Research, 116(C11): C11015, doi: 10.1029/2010JC006803

Steele M, Morison J, Ermold W, et al. 2004. Circulation of summer Pacific halocline water in the Arctic Ocean. Journal of Geophysical Research, 109(C2): C02027

Strom S L, Postel J R, Booth B C. 1993. Abundance, variability, and potential grazing impact of planktonic ciliates in the open subaratic Pacific Ocean. Progress in Oceanography, 32(1–4): 185–203, doi: 10.1016/0079-6611(93)90013-4

Suzuki T, Taniguchi A. 1998. Standing crops and vertical distribution of four groups of marine planktonic ciliates in relation to phytoplankton chlorophyll *a*. Marine Biology, 132(3): 375–382, doi: 10.1007/s002270050404

Taniguchi A. 1984. Microzooplankton biomass in the Arctic and subarctic Pacific Ocean in summer. Memoris of the National Institute of Polar Research, Special Issue, 32: 63–76

Taylor A G, Landry M R, Selph K E, et al. 2011. Biomass, size structure and depth distributions of the microbial community in the eastern equatorial Pacific. Deep Sea Research Part II: Topical Studies in Oceanography, 58(3–4): 342–357, doi: 10.1016/j.dsr2.2010.08.017

Utermöhl H. 1958. Zur vervollkommnung der quantitativen phytoplankton-Methodik: mit 1 tabelle und 15 abbildungen im text und auf 1 tafel. Internationale Vereinigung für Theoretische und Angewandte Limnologie: Mitteilungen, 9(1): 1–38

Verity P G, Lagdon C. 1984. Relationships between lorica volume, carbon, nitrogen, and ATP content of tintinnids in Narragansett Bay. Journal of Plankton Research, 6(5): 859–868, doi: 10.1093/plankt/6.5.859

Wang Kui, Chen Jianfang, Jin Haiyan, et al. 2013. Nutrient structure and limitation in Changjiang River Estuary and adjacent East China Sea. Haiyang Xuebao (in Chinese), 35(3): 128–136

Wang Chaofeng, Li Haibo, Zhao Li, et al. 2019. Vertical distribution of planktonic ciliates in the oceanic and slope areas of the western Pacific Ocean. Deep Sea Research Part II: Topical Studies in Oceanography, 167: 70–78, doi: 10.1016/j.dsr2.2018.08.002

Wang Chaofeng, Zhao Li, Zhao Yuan, et al. 2016. Vertical distribution of planktonic ciliates in tropical western Pacific. Oceanologia et Limnologia Sinica (in Chinese), 47(2): 429–437

Wolf K U, Woods J D. 1988. Lagrangian simulation of primary production in the physical environment-the deep Chlorophyll maximum and nutricline. In: Rothschild B J, ed. Toward a Theory on Biological-Physical Interactions in the World Ocean. Dordrecht: Springer, 51–70

Xu Guangjian, Yang E J, Jiang Yong, et al. 2018a. Can pelagic ciliates indicate vertical variation in the water quality status of western Arctic pelagic ecosystems?. Marine Pollution Bulletin, 133: 182–190, doi: 10.1016/j.marpolbul.2018.05.017

Xu Guangjian, Yang E J, Lee Y, et al. 2018b. Vertical shift in ciliate body-size spectrum and its environmental drivers in western Arctic pelagic ecosystems. Environmental Science and Pollution Research, 25(19): 19082–19091, doi: 10.1007/s11356-018-2094-z

Yang E J, Choi J K, Hyun J H. 2004. Distribution and structure of heterotrophic protist communities in the northeast equatorial Pacific Ocean. Marine Biology, 146(1): 1–15, doi: 10.1007/s00227-004-1412-9

Yang E J, Ha H K, Kang S H. 2015. Microzooplankton community structure and grazing impact on major phytoplankton in the Chukchi Sea and the western Canada Basin, Arctic Ocean. Deep Sea Research Part II: Topical Studies in Oceanography, 120: 91–102, doi: 10.1016/j.dsr2.2014.05.020

Yu Ying, Luo Xuan, Zhang Cuixia, et al. 2015. Distribution of tintinnids (Ciliophora, Tintinnida) in the Changjiang Estuary and adjacent areas in spring. Advances in Marine Sciences (in Chinese), 2(3): 45–52, doi: 10.12677/AMS.2015.23007

Yu Ying, Zhang Wuchang, Wang Shiwei, et al. 2013. Abundance and biomass of planktonic ciliates in the sea area around Zhangzi Island, Northern Yellow Sea. Acta Ecologica Sinica, 33(1): 45–51

Zhang Wuchang, Feng Meiping, Yu Ying, et al. 2012. Illustrated Guide to Contemporary Tintinnids in the World (in Chinese). Beijing: Science Press

Zhang Cuixia, Zhang Wuchang, Ni Xiaobo, et al. 2015. Influence of different water masses on planktonic ciliate distribution on the East China Sea shelf. Journal of Marine System, 141: 98–111, doi: 10.1016/j.jmarsys.2014.09.003

Zhao Li, Zhao Yanchu, Wang Chaofeng, et al. 2017. Comparison in the distribution of microbial food web components in the Y3 and M2 seamounts in the tropical western Pacific. Oceanologia et Limnologia Sinica (in Chinese), 48(6): 1446–1455

Acta Oceanol. Sin., 2020, Vol. 39, No. 4, P. 18–32
https://doi.org/10.1007/s13131-020-1544-x
http://www.hyxb.org.cn
E-mail: hyxbe@263.net

Sources and implications of particulate organic matter from a small tropical river—Zuari River, India

Dearlyn Fernandes[1]*, Ying Wu[1], Prabhaker Vasant Shirodkar[2], Umesh Kumar Pradhan[3], Jing Zhang[1]

[1] State Key Laboratory of Estuarine and Coastal Research, East China Normal University, Shanghai 200062, China

[2] National Institute of Oceanography (Council of Scientific and Industrial Research), Dona Paula, Goa 403004, India

[3] National Institute of Oceanography (Council of Scientific and Industrial Research), Regional Centre, 4 Bungalows, Andheri (West) 400053, Mumbai, India

Received 1 July 2019; accepted 10 October 2019

Abstract

Transitional ecosystems, estuaries and the coastal seas, are distinctively affected by natural and anthropogenic factors. Organic matter (OM) originating from terrestrial sources is exported by rivers and forms a key component of the global biogeochemical cycles. Most previous studies focused on the bulk biochemical and anthropogenic aspects affecting these ecosystems. In the present study, we examined the sources and fate of OM entrained within suspended particulate matter (SPM) of the Zuari River and its estuary, west coast of India. Besides using amino acid (AA) enantiomers (L- and D-forms) as biomarkers, other bulk biochemical parameters viz. particulate organic carbon (POC), δ^{13}C, particulate nitrogen (PN), δ^{15}N and chlorophyll *a* were analyzed. Surprisingly no significant temporal variations were observed in the parameters analyzed; nonetheless, salinity, POC, δ^{13}C, PN, δ^{15}N, glutamic acid, serine, alanine, tyrosine, leucine and D-aspartic acid exhibited significant spatial variability suggesting source differentiation. The POC content displayed weak temporal variability with low values observed during the post-monsoon season attributed to inputs from mixed sources. Estuarine samples were less depleted than the riverine samples suggesting contributions from marine plankton in addition to contributions from river plankton and terrestrial C_3 plants detritus. Labile OM was observed during the monsoon and post-monsoon seasons in the estuarine region. More degraded OM was noticed during the pre-monsoon season. Principal component analysis was used to ascertain the sources and factors influencing OM. Principally five factors were extracted explaining 84.52% of the total variance. The first component accounted for 27.10% of the variance suggesting the dominance of tidal influence whereas, the second component accounted for heterotrophic bacteria and their remnants associated with the particulate matter, contributing primarily to the AA pool. Based on this study we ascertained the role of the estuarine turbidity maximum (ETM) controlling the sources of POM and its implications to small tropical rivers. Thus, changes in temporal and regional settings are more likely to affect the natural biogeochemical cycles of small tropical rivers.

Key words: Zuari River, estuarine turbidity maximum (ETM), suspended particulate matter (SPM), organic matter (OM), amino acids (AA), degradation index (DI)

Citation: Fernandes Dearlyn, Wu Ying, Shirodkar Prabhaker Vasant, Pradhan Umesh Kumar, Zhang Jing. 2020. Sources and implications of particulate organic matter from a small tropical river—Zuari River, India. Acta Oceanologica Sinica, 39(4): 18–32, doi: 10.1007/s13131-020-1544-x

1 Introduction

Continental margins are dominated by inputs from rivers which play an important role in influencing the global biogeochemical cycles as they receive significant amounts of terrigenous and marine materials. These regions are characterized by highly dynamic physical, chemical and biological processes (Hedges et al., 1997; Bianchi and Allison, 2009). Pathway of the transport of organic matter (OM) from the land to the sea provides valuable insights into the natural processes and anthropogenic disturbances occurring within the drainage basin (Ke et al., 2017; Ni et al., 2016; Mai-Thi et al., 2017). In this regard, small tropical rivers are very sensitive and vulnerable to significant environmental changes and socio-economic problems, thus acting as indicators of change on spatial and temporal scales (Syvitski et al., 2014). Small tropical rivers transport the same or nearly the same amounts of solutes, suspended particulates and sediments as large rivers in response to extreme catastrophic events such as cyclones, floods, or earthquakes (Hilton et al., 2008; Milliman et al., 2017). Additionally, these rivers possess unique characteristics as they are predominantly seasonal and dynamic in nature. The factors controlling the sources composition, distribution and transport of solutes, particulates and sediments in these rivers is governed by the seasonal (Jennerjahn et al., 2008; Wu et al., 2013) and geomorphological features (meandering river loops) (Fernandes et al., 2019) along with tides, rainfall and river discharge (Goldsmith et al., 2015).

Estuaries are transition zones acting as conduits for transferring both dissolved solutes and particulate matter from the terrestrial environs to the marine regions (Abril and Borges, 2005; Abril et al., 2007). Freshwater discharge, tidal forcing coupled with physical processes such as gravitational circulation and salinity stratification forms the estuarine turbidity maxima (ETM)

Foundation item: The National Natural Science Foundation of China under contract No. 41530960.
*Corresponding author, E-mail: dearlynfernandes@qq.com

within estuaries. The distribution and concentration of suspended particulate matter (SPM) within the ETM can be directly related to its location and physical processes (Geyer, 1993). The ETM behave differently as they have dual characteristics. Both the allochthonous and autochthonous sources of OM exist due to the hydrodynamic function of the tidal pumping and estuarine circulation (Suzuki et al., 2010; Uncles et al., 2006). The ETM is an important feature as it influences primary productivity, pollutant flushing, fish migration, and anthropogenic activities (dredging) (Mitchell et al., 1999). Additionally, the ETM are important sites where mineralization of particulate organic nitrogen (PON) takes place (Abril et al., 2000). The non-conservative mixing behavior of the particulate components and their active transport by the estuary influences the quality and quantity of OM. The OM entrained within SPM plays a vital role in the lateral and vertical transport of material from the river to the sea. Therefore, in the recent years the estuarine systems have received considerable attention as they are impacted by nutrients influx and pollutants from agricultural, industrial sources, and waste water runoff from their watersheds (Rao et al., 2011).

The origin and diagenetic state of OM entrained within suspended particles has been studied using number of techniques mainly taking into consideration the bulk parameters (C:N ratio and stable isotope composition) and organic biomarkers (pigments, lipids, lignin phenols and amino acids) (Cowie and Hedges, 1994; Wu et al., 2007; Veuger et al., 2012; Pradhan et al., 2014). Most conventional studies have taken into consideration the C:N ratio coupled with stable isotopes in order to distinguish between the terrestrial and marine sources of OM (Gordon and Goñi, 2003). Components used as biomarkers are derived from terrestrial plants, marine plankton and bacteria provide specific and complementary data to trace the origins of OM (Zhang et al., 2014). Amino acids (AA) are the basic building blocks of all organisms, and are often used as biomarkers. They act as a promising tool as they have specific biological sources and are relatively well preserved during diagenesis (Eglinton and Eglinton, 2008). Being ubiquitous in the environment, they are often used to provide insights about OM sources and diagenetic alterations (Dauwe and Middelburg, 1998; Kaiser and Benner, 2008). Additionally, the D-enantiomers of some AA are used as tracers to identify sources and degradation status of organic nitrogen (ON) (Wu et al., 2007). The AA such as alanine, glutamic acid, aspartic acid, serine and arginine provide information about bacterial sources (Lomstein et al., 2009; Wu et al., 2007).

Previously, most studies focused on the bulk characteristics of OM in relation to the origin, distribution and its role in affecting the environment (Gupta et al., 1997; Jørgensen et al., 2014; Ke et al., 2017). The Zuari River system (ZRS) is a small tropical river located on west coast of India which is affected by natural (rainfall, tides) and anthropogenic (agriculture, aquaculture, mining, land reclamation, sewage discharge) stressors. The occurrence of ETM is a consistent feature of this river and it persists throughout the year at the mouth of the estuary. However, most studies conducted in this river distinguished between the sources of organic carbon (OC), geochemistry of major and trace metals (Kessarkar et al., 2013), and bacterial production (Bhaskar and Bhosle, 2008) from SPM. The distribution and speciation of trace metals in surface sediments was investigated by Dessai and Nayak (2009). Number of biomarkers have been used to study various aspects of riverine and estuarine environment, however there are limited studies focusing on the use of AA as the biomarker approach to explain the composition and diagenetic status of OM from this river. Considering the importance of the ETM in influencing the distribution and transformation of OM, we conducted this study to understand the sources, contributions, quality and factors controlling POM within this small tropical river. Detailed investigations were carried out for the AA biomarkers (L- and D- enantiomers) entrained within particulate matter along with the ancillary parameters so as to determine the provenance, contributions, and the controlling factors such as seasons, zone, and geomorphological settings (wide mouth of the estuary). We hypothesize the composition and diagenetic status of POM trapped within the estuarine region is influenced by the ETM.

2 Materials and methods

2.1 *Study area*

The ZRS is located in the state of Goa, India between the latitudes 15°20′N and 15°30′N, and longitudes 73°45′E and 74°10′E (Fig. 1a) and has a catchment area of approximately 550 km^2 (Bardhan et al., 2015). It is a highly seasonal river originating at Hemad–Barshem hills in the Western Ghats escarpments. The river flows approximately 145 km before draining into the Arabian Sea at Mormugao. The Zuari River and its basin experience a humid tropical monsoon type of climate. The Ghats presents a topographical barrier to the southwest monsoon (SWM) winds and thus creates one of the world's highest orographic gradients (Hibbert et al., 2015). Approximately 85% of the seasonal precipitation and runoff occurs during the monsoon months (June–September). The maximum rainfall that the region experiences during the monsoon season for any day could range from 70 to 200 mm/d (India Meteorological Department (IMD), 2013). The fresh water discharge of ZRS is regulated by a dam (Selaulim dam) in the upstream that has a storage capacity of 227×10^6 m^3/a (i.e., ~10% of total annual runoff: 2 190×10^6 m^3/a; Suprit and Sankar, 2008). Most of the river discharge is during the monsoon with negligible discharge during the other (post- and pre-monsoon) seasons (Kessarkar et al., 2013). The runoff measured in the upstream for the monsoon, post-monsoon and pre-monsoon were ~147, 7.3 and 0.8 m^3/s, respectively (Kessarkar et al., 2013). The river flows steeply down the Western Ghats across the low-lying coastal plains, which are mainly composed of heavily weathered rocks and covered by laterites. Due to low elevation of the coastal plains, the tidal effect are observed ~45 km inland and it is forced out seawards during the monsoons by high amounts of river discharge (Shetye et al., 2007). The tides are of mixed semi-diurnal type and the river experiences a meso-tidal range of about ~2.3 and 1.5 m during the spring and neap tides as it is situated along the central west coast of India (Sundar and Shetye, 2005; Shetye et al., 2007). The river experiences vertical mixing of the water column due to strong flood and ebb tides (Manoj and Unnikrishnan, 2009). The river forms an estuarine system at the mouth (Shetye et al., 1995) and is classified as a "monsoonal estuary" (Vijith et al., 2009). A characteristic feature of this estuary is the occurrence of ETM in the channel during the monsoon and post-monsoon season and it moves to the bay region near to the mouth during the pre-monsoon season. The formation of the ETM results from the interaction of tidal currents, river flow and wind induced currents (Rao et al., 2011). The estuarine region of the Zuari River is fringed with mangroves along its banks serving as nursery grounds to organisms such as prawn, fish and many other invertebrate species thereby supporting diverse flora and fauna (Bhosle, 2007). The sediments of the river are primarily composed of sand (58.6%±34.7%) while silt+clay fractions account for 42%±34.1% (Rao et al., 2015). Dominant land use practices include plantations within the degraded forest lands (jack-

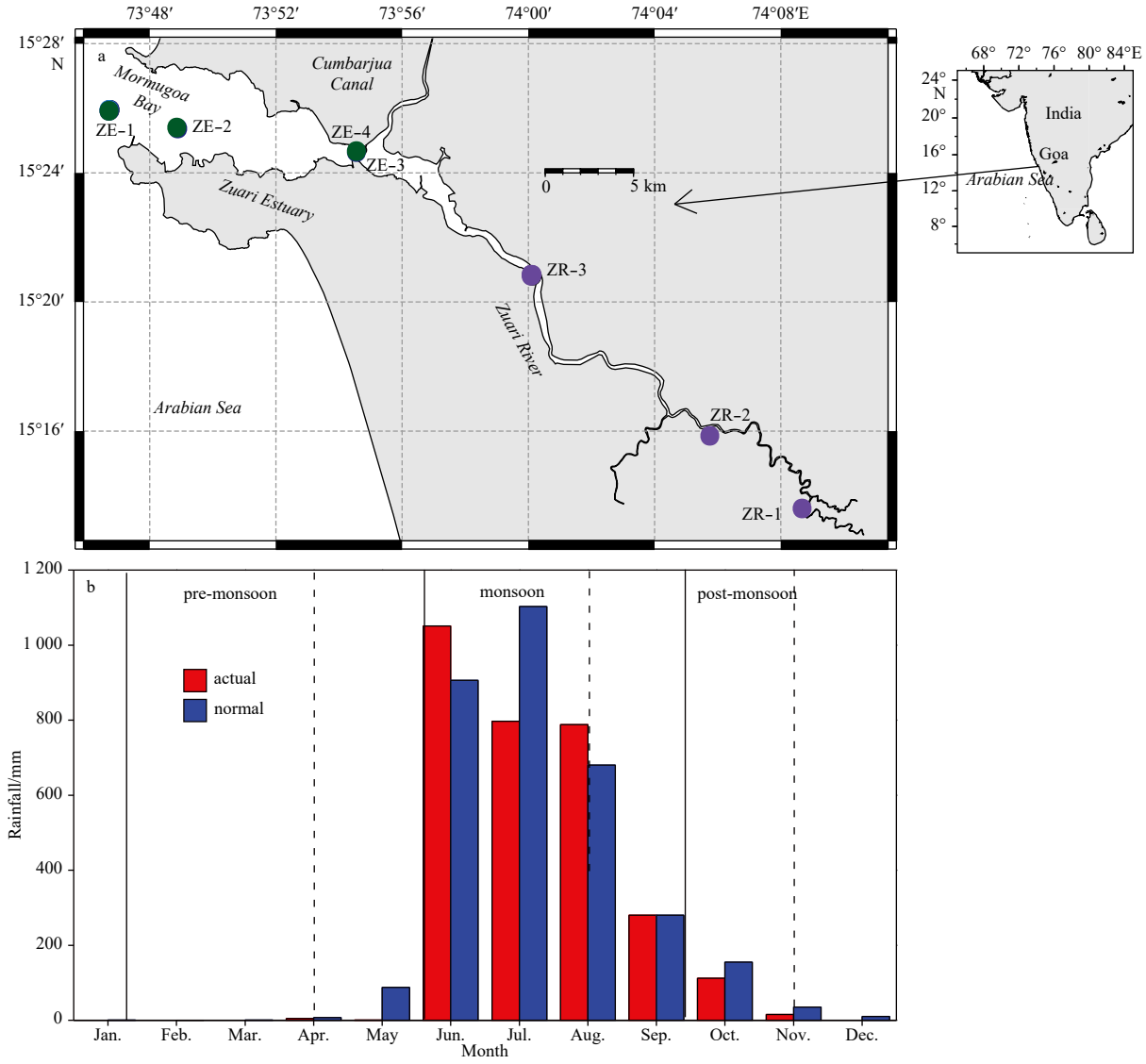

Fig. 1. The location of sampling stations within the Zuari River (station marked in dark green are the estuarine stations and the ones in violet are the riverine stations) (a), and average monthly rainfall (mm) for the year 2011–2012 (the red color columns indicate actual rainfall and the blue color the predicted rainfall) (b). Source is from the India Meteorological Department (IMD, 2013). The solid lines demarcate the three seasons and the dashed lines the sampling period.

fruit and coconut) and areas of mineral ore mining. This area is associated with moderately dense human settlements over the basin (population density of Goa is 394 inhabitants per km^2; Census Organization of India, 2011). A major shipping port is located in close proximity to the river mouth and is affected by anthropogenic activities such as mine tailings, discharge of partially treated or untreated sewage from municipal sources (Bardhan et al., 2015).

2.2 *Sampling sites and sample collection*

Surface water samples were collected from the riverine and estuarine region from predetermined locations along the Zuari River during the SWM of 2011 (August–September), post-monsoon season of 2011 (November–December) and pre-monsoon season of 2012 (April–May) (Figs 1a, b). The sampling stations Zuari River 1 and 2 (ZR-1 and ZR-2) are located in the main channel of the river, whereas the stations Zuari Estuary 1, 2, 3 and 4 (ZE-1, ZE-2, ZE-3 and ZE-4) were positioned within the estuarine region of the river. River water was collected using a clean bucket lowered from the top of a bridge into the river channel. Surface water samples from the estuarine region were collected using a 5 L Niskin water sampler (General Oceanic, USA) from a mechanized boat. The collected water samples were transferred to acid cleaned polyethylene carboys and were preserved with ice in an icebox and transported to the local laboratory (National Institute of Oceanography, Goa, India) for preliminary analyses and subsampling. The water samples were then sub-sampled, processed and preserved at –20°C before shipping them to SKLEC, ECNU, Shanghai for further analyses.

2.3 *Hydrographic measurements*

In-situ measurements of temperature, pH, and salinity were done using a multi-parameter system provided with a probe (Inolab multi-720). The average precision for temperature, salinity, and pH measured by the probe system was 0.01°C, 0.01 and 0.01 pH units, respectively.

2.4 *Suspended particulate matter (SPM), chlorophyll a and dissolved organic carbon (DOC)*

Water samples were filtered through pre-combusted (450°C, 5 h) GF/F fiber filters (nominal pore size 0.7 μm; 47 mm diameter; Whatman) under moderate vacuum for analyses of bulk and trace level contents from SPM. The filters were stored in pre-combusted aluminum foils (450°C, 5 h) at –20°C until further analysis of the contents was done for the isotopic measurements of the stable isotope of carbon (δ^{13}C), nitrogen (δ^{15}N) (Krishna et al., 2018), chlorophyll *a* and AA. The SPM was measured as the difference of weight after drying the filters at 40°C for 48 h. Chlorophyll *a* concentration was determined using Whatman 47 mm Ø GF/F fiber filters (0.7 μm nominal pore size). The contents were extracted using 90% acetone, refrigerated (4°C) in dark for 20–24 h, centrifuged and the absorbance was measured at 750, 664, 647 and 630 nm using a spectrophotometer (Shimadzu UV 1800) according to Strickland and Parsons (1972). Analysis of DOC from filtered water samples was done using the high-temperature catalytic oxidation (HTCO) method [Shimadzu TOC analyzer (model: TOC-CPH)]. The relative standard deviation of the method was less than 2% (Wu et al., 2013).

2.5 *Elemental and stable isotope analyses*

About one quarter of the dried filter membrane containing SPM was weighed, cut and acidified with excess 1 mol/L HCl for 24 h in order to completely remove the inorganic carbon. These filters were then dried at 45°C in an oven for 24–36 h to remove the traces of acid and moisture, and were later packed in tin cups for analyses. The content of particulate organic carbon (POC) and δ^{13}C were measured by an elemental analyzer (Finnigan EA1112) interfaced with a continuous flow isotope ratio mass spectrometer (Finnigan Delta plus XP). The results are expressed as per mille (‰) deviation relative to the Vienna–Pee Dee Belemnite (V-PDB) standard calculated using the equation below:

$$\delta^{13}\mathrm{C}\ (‰) = \left[\left(\left(^{13}\mathrm{C}/^{12}\mathrm{C}\right)_{\mathrm{sample}}/\left(^{13}\mathrm{C}/^{12}\mathrm{C}\right)_{\mathrm{PDB}}\right) - 1\right] \times 1\,000. \quad (1)$$

Particulate nitrogen (PN) and nitrogen isotope composition (δ^{15}N) were measured form un-acidified filter membranes. The δ^{15}N was determined using a Thermo Finnigan Delta plus XP gas isotope ratio mass spectrometer (IRMS) after high temperature combustion in a Flash 1112EA elemental analyzer. The δ^{15}N values are presented as per mille (‰) deviation from atmospheric N_2 isotope composition and were calculated using the equation below:

$$\delta^{15}\mathrm{N}\,(‰) = \left[\left(\left(^{15}\mathrm{N}/^{14}\mathrm{N}\right)_{\mathrm{sample}}/\left(^{15}\mathrm{N}/^{14}\mathrm{N}\right)_{\mathrm{atmospheric\ N2}}\right) - 1\right] \times 1\,000. \quad (2)$$

The standard deviations based on replicate analyses of laboratory standard was <10% for OC content, <1% for N content, ±0.3‰ for δ^{13}C and ±0.2‰ for δ^{15}N. Standards were analyzed every ten samples and had a mean analytical error of 0.05%.

2.6 *Amino acid analyses*

Digestion of OM (proteins) to its monomers (AA) was done by acid hydrolysis, as it is an ideal method (Nunn and Keil, 2005). Total hydrolysable amino acids (THAA) were analyzed according to Fitznar et al. (1999) and Wu et al. (2007). In brief, approximately one quarter of the filter membranes were hydrolyzed with HCl (16%, 10 mL) in pre-combusted glass ampoules (450°C, 5 h), sealed in a nitrogen (N_2) environment and incubated in an oven for 22–24 h at 110°C. The samples were cooled and neutralized with boric acid buffer. The pH was adjusted to pH 8.5 by adding NaOH solution. Samples were analyzed using a slightly modified method that incorporated a Phenomenex™ Hyperclone column (5 μm particle diameter, BDS C18, 250 mm length, 4 mm inner diameter) with a guard column (4 mm×2 mm). The mobile phases were: (A) 125 mmol/L sodium acetate with 2% methanol (pH 6.8, adjusted with acetic acid), and (B) HPLC grade 100% methanol. The gradient began at 99% A and 1% B and was gradually changed to 100% B at 110 min (held for 3 min), before being shifted back to the initial conditions. External AA enantiomer standards (Fluka, Switzerland; Aldrich, USA; Sigma, USA) were used for calibration. Deamination reaction results in the degradation of glutamine (Gln) and asparagines (Asn) during hydrolysis. Therefore in the results we represent Asx and Glx as the sum of aspartic acid (Asp) + asparagines (Asn) = (Asx) and glutamic acid (Glu) + glutamine (Gln) = (Glx), respectively. The L- and D-enantiomers of the individual amino acids in the hydrolyzates were determined fluorometrically by a high performance liquid chromatography (HPLC) system (Agilent 1100 series). The relative standard deviation for the individual amino acids for triplicate analysis was <3.5% (Wu et al., 2007). The contribution of racemerized D-amino acid content during hydrolysis is very small as compared to the naturally occurring D-amino acid as discussed in study conducted by Dittmar et al. (2001). The relative abundance of individual AA was used to calculate the degradation index (DI) of the samples following the equation based on Dauwe and Middelburg (1998) and Dauwe et al. (1999), given below as follows:

$$\mathrm{DI} = \sum_i \left[\frac{\mathrm{var}_i - \mathrm{AVGvar}_i}{\mathrm{STDvar}_i}\right] \times \mathrm{fac.coef.}_i \quad (3)$$

where var_i is the molar percentage of AA i in the sample, $\mathrm{fac.coef.}_i$, AVGvar_i and STDvar_i are the principal component analysis factor coefficient, mean molar percentage and standard deviation of AA i in the dataset of Dauwe et al. (1999).

2.7 *Statistical analyses*

Data were tested for normality using Shapiro–Wilk test and homogeneity of variance using Levene's test. One way analysis of variance (ANOVA) followed by Tukey's post hoc test and the independent *t* test were applied to the temporal and spatial data, respectively so as to determine the significant differences. Pearson's correlation coefficient was calculated to assess the inter-relationships and associations among the parameters investigated. A p value of $\leqslant 0.05$ was considered statistically significant for all the statistical tests, unless otherwise stated. The R-mode factor analysis (FA) with Varimax-normalized rotation by means of principal components extraction method (Kara, 2009) was applied to the physical and bio-chemical variables of the data set. The data were normalized by subtracting the mean of all values and dividing each variable by its standard deviation (Unger et al., 2013). All statistical analyses were done using the IBM SPSS 20 software (IBM, Armonk, NY, USA).

3 Results

3.1 *Physical, biological and ancillary parameters*

The highest average rainfall was recorded during the mon-

soon season ((730±280) mm) followed by the post-monsoon ((30±45) mm) and pre-monsoon ((1±2) mm) seasons, respectively during the period of this study (IMD, 2013). Rainfall during the monsoon was significantly higher than the other two seasons (post- and pre-monsoon) (p<0.05). No significant difference was observed between the recorded actual rainfall and the predicted normal rainfall (p>0.05, Fig. 1b). Surface water temperature and pH values varied from 28.0°C to 33°C and 6.6 to 8.2 with an average of 30.6°C and 7.7, respectively. Significantly lower temperatures (p<0.05) were observed during the monsoon season as compared to the post- and pre-monsoon season. Significantly higher pH (p<0.05) was observed in the estuarine region as compared to the riverine region. Salinity values measured ranged from 0 to 35, with the highest value recorded during the pre-monsoon season in the estuarine region (Table 1). Significantly higher salinities (p<0.05) were recorded in the estuarine region as compared to the riverine region. The SPM values varied from 1.3 to 165.6 mg/L (Table 1, Fig. 2a), with no significant spatial or temporal variations (p>0.05). Chlorophyll *a* values ranged from 2.0 to 9.5 mg/m^3 with an average of 4.1 mg/m^3. The highest values were observed in the riverine region during the pre-monsoon season (Table 1) with no significant spatial or temporal variations (p>0.05). Although higher values of DOC are observed in the riverine region, no significant differences were observed spatially and temporally (p>0.05, Table 1).

3.2 *Bulk geochemical parameters*

The POC and PN content expressed on the basis of the whole weight varied from 1.4% to 38.8% and from 0.1% to 5.2% with an average of 6.7% and 0.9%, respectively with no significant temporal differences in both the estuarine and riverine regions (p>0.05, Table 1). The POC and PN content of the riverine stations were significantly higher than that of the estuarine stations (p<0.05). The C:N_{atomic} ratio and N:C_{atomic} ratio varied from 1.9 to 19.8 and 0.05 to 0.53 with an average of 11.0 and 0.12, respectively with no significant temporal or spatial variation (p>0.05). The δ^{13}C values of SPM varied from –34.1‰ to –20.4‰ with an average of –26.4‰ and the values were significantly different spatially with more depleted values in the riverine region (p<0.05, Fig. 2b). The δ^{15}N values of SPM varied from 1.0‰ to 9.3‰ with an average of 5.6‰ (Table 1). Significantly higher δ^{15}N values were measured in the estuarine region as compared to the riverine region (p<0.05). Furthermore, the POC:Chl *a* ratio and DOC:POC ratio varied from 49.4 to 610.6 and 0.4 to 3.5 with an average of 182.7 and 1.8, respectively (Table 1). Apparently these ratios did not show any significant variability spatial or temporal (p>0.05).

3.3 *Biomarkers and allied indices*

The THAA content varied from 0.1 to 0.5 μmol/g with an average of 0.2 μmol/g with no significant differences spatially and temporally (p>0.05). Highest values were measured in the estuarine region during the pre-monsoon season (Table 2). The contribution of THAA to carbon (AA-C%) varied from 0.1% to 10.0% with an average of 2.4% and was significantly different for the two regions, with higher values in the estuarine region (p<0.05). The contribution of THAA to nitrogen (AA-N%) varied from 0.5% to 51.2% with an average of 10.7% with no significant spatial or temporal differences (p>0.05). Based on functional groups, neutral AA was the most abundant ones and varied from 73.4% to 81.4% with an average of 77.7%. Acidic AA accounted for almost 27.1% to 30.9% with an average of 29.8%. Significantly lower amounts of acidic AA were found in the riverine region as compared to the estuarine region (p<0.05). Hydroxylic AA accounted for about ~16% (Table 2). Aromatic and basic AA accounted for about 5.7% to 7.5% and 3.7% to 4.9% with an average of 6.4% and 4.4%, respectively with no significant spatial and temporal differences (p>0.05, Table 2).

A total of 18 monomers of AA were detected from SPM for the three seasons (Table 3). The average mol percentage (mol%) composition of individual AA from SPM for the two regions with significant differences is presented in Fig. 3a. The most abundant AA were Gly, Ala, Glx, Asx, Ser and Val. The basic AA—Arg varied from 2.7% (mole pencentage) to 3.6% with an average of 3.3%. No significant differences were observed between the AA data collected for the three seasons. Hence the data was analyzed spatially (estuarine and riverine samples). Glx, Ser, Ala, Tyr and Leu displayed significant spatial differences (p<0.05) with higher values of Glx and Tyr were observed in the estuarine region as compared to the riverine region. Likewise, higher values of Ser, Ala and Leu were observed in the riverine region as compared to the estuarine region. The contribution from non protein AA—gamma (γ)-aminobutyric acid (GABA) was low and varied from 0.4% to 1.2% with an average of 0.6% for the three seasons with no significant spatial or temporal variations. The contribution from Tyr+Phe was slightly above 5% (Table 3).

Furthermore, the contributions from the D-enantiomers of AA, namely, D-Asx, D-Glx, D-Ser and D-Ala, varied between 2.2% to 9.6% with an average of 6.6% for the three seasons (Table 3). The percentage contribution of D-Arg was higher as compared to the other D-AA and accounted for more than 13% with no significant spatial or temporal differences (p>0.05). The percentage contributions from D-AA were comparatively higher in the estuarine region as compared to the riverine region (Fig. 3b). Only D-Asx showed significant differences (p<0.05) with higher values observed in the estuarine region as compared to the riverine region. The D/(D+L)AA ratio varied from 2.9 to 7.2 with an average of 4.3 and was significantly different for the two regions (p<0.05) with higher ratios observed in the estuarine region as compared to the riverine region. The DI values varied from –0.23 during the monsoon season to 0.19 during the post-monsoon season with an average of –0.03. The Glx:GABA ratio varied from 8.5 to 28.9 with an average of 18.7 (Fig. 4). No significant spatial or temporal differences were observed with DI and Glx:GABA ratio (p<0.05).

3.4 *Correlation and principal component analyses (PCA)*

Correlation analyses indicated contrasting results with some parameters depicting positive correlations while others presented negative correlations (Table S1). Significant positive correlation was observed between salinity and δ^{13}C (r=0.89, p<0.01), acidic AA (r=0.72, p<0.01) and D-Asx (r=0.57, p<0.05). Similarly, strong positive correlations were observed between SPM with THAA, D-Asx (r=0.84, p<0.01; Fig. 5), D-Glx, D/(D+L)AA ratio, D-Ala, and GABA. D/(D+L) ratio and GABA were strongly positively correlated with the individual monomers of D-AA (Table S1). Likewise, D-Asx correlated positively with all the other D-AA, namely, D-Ala, D-Arg, D-Glx (p<0.01) and D-Ser (p<0.05), suggesting a common source of D-AA (Table S1). Furthermore, significantly strong negative correlation was observed between OC and δ^{13}C (r=–0.72, p<0.01). Strong negative correlations were observed between acidic AA and chlorophyll *a* (r=–0.75, p=0.01) and between hydroxylic AA and DI (r=–0.78, p=0.01) (Table S1).

Unbiased variables from the data set were subjected to principal components (PC) analyses. Five leading PC were extracted based on the Eigen values (>1) and accounted for 85.5% of the total variance. The PC analyses showed that the first principal

Table 1. Station locations, physical and bulk biochemical parameters of water and suspended particulates of the Zuari River, west coast of India

Season /station name	Distance from estuary/km	North latitude	East longitude	Temperature /°C	pH	Salinity	SPM /mg·L^{-1}	Chl *a* /mg·m^{-3}	POC /%	PN /%	δ^{13}C/ ‰	δ^{15}N/ ‰	C:N atomic	N:C atomic	POC:Chl *a*	DOC /μmol·L^{-1}	DOC:POC
Monsoon																	
ZE-1	–4	15.43°	73.78°	29.4	8.1	18.9	13.6	2.2	3.3	0.3	–22.8	7.7	11.4	0.09	204.4	60.1	1.6
ZE-2	0	15.42°	73.82°	29.3	8.1	18.4	17.7	3.5	2.8	0.3	–22.8	7.8	12.9	0.08	143.1	58.9	1.4
ZE-3	13	15.41°	73.91°	29.2	7.5	7.5	10.9	2.0	3.2	0.4	–28.4	6.4	9.1	0.11	175.6	43.9	1.5
ZR-2	46	15.35°	74.00°	28.0	7.0	0.0	9.7	4.3	8.5	5.2	–28.5	1.0	1.9	0.53	191.6	50.7	0.7
ZR-1	56	15.23°	74.14°	29.2	6.6	0.0	1.3	3.0	38.8	2.3	–34.1	2.5	19.8	0.05	172.3	39.7	0.9
Average				29.0	7.5	9.0	10.7	3.0	11.3	1.7	–27.3	5.1	11.0	0.17	177.4	50.7	1.2
SD				0.6	0.7	9.4	6.0	0.9	15.5	2.1	4.7	3.2	6.5	0.20	23.1	9.0	0.4
Post-monsoon																	
ZE-1	–4	15.42°	73.82°	30.4	8.2	33.7	16.5	3.8	1.9	0.2	–20.4	8.1	9.4	0.11	82.6	65.9	2.5
ZE-2	0	15.43°	73.78°	30.5	8.1	33.7	18.5	2.7	1.5	0.2	–21.0	9.3	10.6	0.09	105.9	69.9	2.9
ZE-4	12	15.41°	73.91°	31.7	7.8	24.8	27.5	3.6	1.4	0.2	–24.7	4.9	9.5	0.11	104.3	75.3	2.4
ZE-3	13	15.41°	73.91°	31.1	8.0	31.1	44.4	3.5	1.4	0.1	–23.0	5.6	11.8	0.08	177.6	85.4	1.6
ZR-2	46	15.35°	74.00°	30.6	7.0	10.4	27.3	4.8	2.8	0.2	–27.3	5.4	13.7	0.07	156.7	149.0	2.4
ZR-1	56	15.23°	74.14°	29.1	6.9	0.0	11.0	3.7	9.4	0.8	–29.4	4.3	13.7	0.07	278.2	138.9	1.6
Average				30.6	7.7	22.3	24.2	3.7	3.1	0.3	–24.3	6.3	11.5	0.09	150.9	97.4	2.3
SD				0.9	0.6	14.0	11.8	0.7	3.1	0.3	3.5	2.0	1.9	0.01	71.8	36.8	0.5
Pre-monsoon																	
ZE-1	–4	15.43°	73.78°	31.0	8.1	35.0	165.6	5.6	2.1	0.2	–23.4	6.2	13.6	0.07	610.6	124.8	0.4
ZE-2	0	15.42°	73.82°	31.3	7.9	35.0	14.4	3.2	1.9	0.2	–21.3	8.2	10.9	0.09	84.9	78.3	3.5
ZR-3	27	15.27°	74.11°	33.0	7.6	17.6	22.1	3.4	3.6	0.5	–29.6	5.6	9.0	0.11	231.2	45.5	0.7
ZR-2	46	15.35°	74.00°	33.0	7.2	0.0	8.3	6.3	11.7	1.5	–31.5	3.0	9.4	0.11	155.0	55.4	0.7
ZR-1	56	15.23°	74.14°	32.2	7.0	0.0	3.5	9.5	13.4	1.7	–33.6	3.8	9.4	0.11	49.4	119.8	3.1
Averege				32.1	7.6	17.5	42.8	5.6	6.5	0.8	–27.9	5.4	10.5	0.10	226.2	84.8	1.7
SD				0.9	0.5	17.5	69.0	2.6	5.6	0.7	5.3	2.0	1.9	0.02	225.9	36.3	1.5

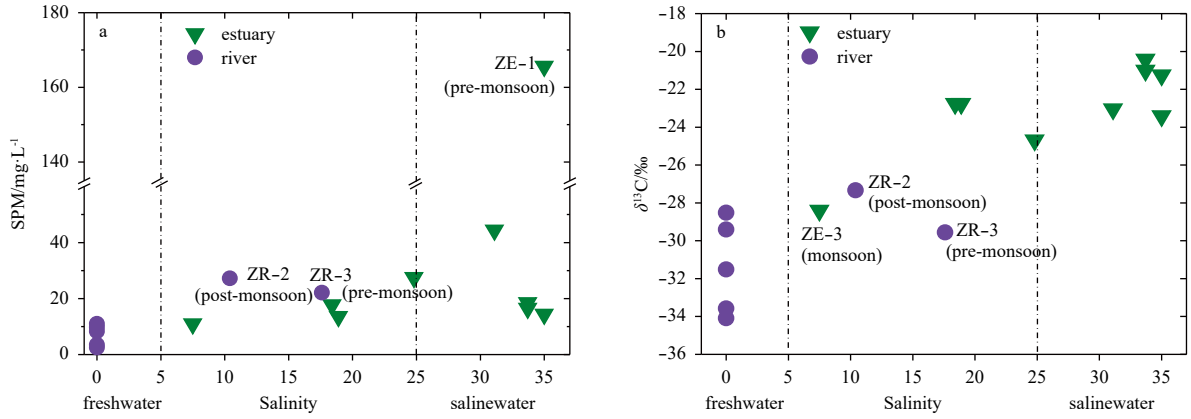

Fig. 2. Plots of suspended particulate matter (SPM, mg/L) with salinity (a), and δ^{13}C (‰) with salinity (b) of the Zuari River and estuary.

Table 2. Bulk concentrations of amino acids (AA) from suspended particulates of the Zuari River, west coast of India

Season/station name	THAA/μmol·g^{-1}	AA-C/%	AA-N/%	Neutral/%	Acidic/%	Hydroxylic/%	Aromatic/%	Basic/%	D/(D+L)AA
Monsoon									
ZE-1	0.2	1.8	7.8	79.8	30.9	16.0	6.2	3.7	4.5
ZE-2	0.2	2.2	10.5	80.3	29.9	16.2	6.7	3.9	3.4
ZE-3	0.1	1.5	5.3	77.8	30.3	16.6	6.2	4.4	3.8
ZR-2	0.1	0.6	0.5	81.4	28.7	17.7	5.9	4.6	4.4
ZR-1	0.1	0.1	0.8	74.7	28.6	17.2	6.1	4.8	4.2
Average	0.1	1.2	5.0	78.8	29.7	16.7	6.2	4.3	4.1
SD	0.0	0.9	4.4	2.6	1.0	0.7	0.3	0.5	0.5
Post-monsoon									
ZE-1	0.1	2.5	8.8	75.2	30.7	16.1	6.7	4.2	3.8
ZE-2	0.1	2.9	11.6	75.1	29.9	16.0	7.5	4.3	3.7
ZE-4	0.1	3.6	13.1	76.0	29.9	16.5	6.1	4.6	5.0
ZE-3	0.2	4.7	21.5	79.0	30.1	17.4	5.8	4.4	4.9
ZR-2	0.2	2.8	14.7	78.6	29.3	17.0	5.7	4.4	4.4
ZR-1	0.2	1.0	5.2	73.4	29.0	17.4	6.0	4.6	5.2
Average	0.2	2.9	12.5	76.2	29.8	16.7	6.3	4.4	4.5
SD	0.1	1.2	5.5	2.2	0.6	0.6	0.7	0.2	0.6
Pre-monsoon									
ZE-1	0.5	10.0	51.2	79.1	29.8	17.2	7.1	4.6	7.2
ZE-2	0.1	1.8	7.6	77.4	30.4	16.2	6.4	4.9	5.1
ZR-3	0.2	2.2	7.5	78.0	28.7	16.2	6.2	4.5	2.9
ZR-2	0.2	0.8	2.9	80.1	27.6	16.3	6.9	4.5	3.0
ZR-1	0.1	0.4	1.5	77.8	27.1	15.9	6.3	4.5	3.8
Average	0.2	3.0	14.1	78.5	28.7	16.4	6.6	4.6	4.4
SD	0.2	3.9	20.9	1.1	1.4	0.5	0.4	0.2	1.8

component represents up to 27.1% of the total variance of the observations with strong positive loading of acidic AA, δ^{13}C and salinity with negative loading of chlorophyll *a*. The positive values on component one corresponds to important inputs and the negative values to low inputs. The first component can be characterized as the tidal factor. The second component accounted for 19.6% of the variance, with strong positive loading of GABA, D-Asx and SPM, together with moderate positive loading of hydroxylic AA (Fig. 6; Table S2). The second component favors the characterization of microbial inputs attached to SPM. The third component accounts for 14.1% of the variance with positive loading of pH and moderate positive loading of POC and PN, and strong negative loading of DOC. The variances accounted by component four and five were 13.3% and 10.4%, respectively (Table S2).

4 Discussion

4.1 *The sources of OM in the Zuari River and estuary*

In our study, the POC and PN values of the estuarine region were significantly lower than the values found in the riverine region, whereas the C:N $_{atomic}$ ratio was >9 for most stations except Sta. ZR-2 (monsoon season) displayed a very low value (Table 1). These values are within the range of values observed for terrestrial (plant detritus and soils) and marine sources. Terrigenous plants are rich in lignin whereas, phytoplankton are rich in protein and thus have a C:N$_{atomic}$ ratio of >15 and 4–10, respectively and this ratio is often used to distinguish sources arising from

Table 3. Concentration of L-enantiomer of AA in mole percentage, percentage contribution of D-AA and diagenetic indices of suspended particulates of the Zuari River, west coast of India

Season /station name	Asx /%	Glx /%	Ser /%	Thr /%	Gly /%	Arg /%	Ala /%	GABA /%	Tyr /%	Val /%	Phe /%	Ile /%	Leu /%	D-Asx /%	D-Glx /%	D-Ser /%	D-Ala /%	D-Arg /%	DI (Dauwe)	Glx: GABA
Monsoon																				
ZE-1	11.1	11.3	6.6	5.1	26.5	2.7	12.9	0.8	0.5	7.7	4.0	5.5	5.1	6.3	4.6	5.5	5.7	23.9	–0.04	15.11
ZE-2	10.3	11.3	6.8	4.9	26.8	2.9	12.7	0.6	0.6	7.4	4.3	5.5	5.5	4.8	3.8	5.1	3.7	15.4	0.11	19.09
ZE-3	10.9	11.3	7.1	5.1	25.9	3.2	13.1	0.7	0.6	7.3	3.9	5.3	5.4	5.1	4.5	4.9	4.7	18.7	–0.03	16.91
ZR-2	10.6	10.0	7.7	5.0	27.5	3.3	13.5	0.7	0.2	7.1	4.0	4.8	5.4	4.6	6.1	3.4	6.2	23.8	–0.23	14.39
ZR-1	10.8	10.8	7.5	5.5	23.7	3.6	14.4	0.7	0.4	7.4	4.3	4.9	5.6	4.6	5.9	4.6	4.1	20.2	–0.13	15.08
Average	10.8	11.0	7.1	5.1	26.1	3.1	13.3	0.7	0.5	7.4	4.1	5.2	5.4	5.1	5.0	4.7	4.9	20.4	–0.1	16.1
SD	0.3	0.6	0.5	0.2	1.4	0.4	0.7	0.1	0.2	0.2	0.2	0.3	0.2	0.7	1.0	0.8	1.0	3.6	0.1	1.9
Post-monsoon																				
ZE-1	11.0	12.0	7.1	4.9	24.6	3.1	13.4	0.5	1.0	7.2	4.1	5.2	5.6	4.5	4.7	7.5	3.4	15.6	0.11	26.72
ZE-2	11.1	11.4	7.1	4.9	24.6	3.2	13.3	0.4	1.3	7.2	4.4	5.3	5.7	4.7	4.9	4.9	4.2	14.5	0.19	28.91
ZE-4	10.7	11.5	7.4	4.9	24.6	3.5	14.3	0.9	0.6	7.2	4.0	4.8	5.4	5.7	5.8	7.7	5.9	21.4	–0.11	13.28
ZE-3	11.3	10.6	7.7	4.9	26.7	3.2	13.3	0.6	0.4	7.2	3.9	4.8	5.2	6.0	6.5	6.4	4.9	23.7	–0.21	17.10
ZR-2	10.9	10.6	7.5	5.0	25.8	3.2	13.4	0.7	0.2	7.4	4.0	5.2	5.6	5.1	5.1	5.0	5.1	21.5	–0.09	15.59
ZR-1	11.0	11.0	7.9	5.3	23.1	3.5	14.2	0.9	0.5	7.2	4.0	4.9	5.7	4.5	5.7	8.4	4.9	25.4	–0.07	12.38
Average	11.0	11.2	7.5	5.0	24.9	3.3	13.7	0.7	0.7	7.2	4.1	5.0	5.5	5.1	5.4	6.7	4.7	20.3	0	19.0
SD	0.2	0.6	0.3	0.2	1.2	0.2	0.5	0.2	0.4	0.1	0.2	0.2	0.2	0.6	0.7	1.5	0.9	4.4	0.1	7.1
Pre-monsoon																				
ZE-1	11.3	10.1	7.2	5.2	27.1	3.3	12.6	1.2	1.4	7.0	3.7	4.7	4.8	8.4	9.0	8.9	8.6	33.3	–0.16	8.50
ZE-2	10.7	11.7	7.5	4.4	25.9	3.6	12.9	0.6	1.0	7.1	3.7	5.1	5.5	5.2	4.7	6.6	5.8	28.9	0.07	19.43
ZR-3	10.6	10.8	7.0	5.1	25.0	3.4	14.7	0.4	0.3	7.3	4.3	5.1	5.8	4.2	4.5	2.2	3.3	13.0	–0.08	26.83
ZR-2	9.6	10.7	8.0	3.9	26.0	3.3	14.6	0.4	0.2	6.7	4.9	5.0	6.5	3.6	4.3	3.0	3.4	14.5	0.17	24.92
ZR-1	10.0	10.5	7.7	4.4	23.9	3.4	16.0	0.4	0.5	7.6	4.3	5.1	6.0	3.8	5.0	6.7	3.7	16.9	0.00	25.68
Average	10.4	10.8	7.5	4.6	25.6	3.4	14.2	0.6	0.7	7.1	4.2	5.0	5.7	5.0	5.5	5.5	5.0	21.3	0.0	21.1
SD	0.7	0.6	0.4	0.5	1.2	0.1	1.4	0.3	0.5	0.4	0.5	0.2	0.6	2.0	2.0	2.8	2.3	9.2	0.1	7.6

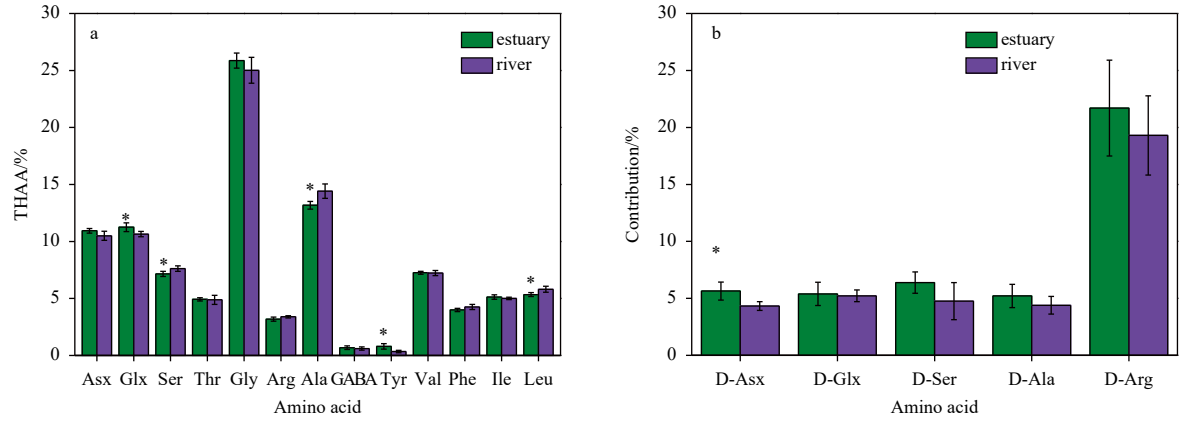

Fig. 3. The average concentration (mol percentage) of individual AA from SPM for the two regions with confidence intervals (p<0.05) (Asx, aspartic acid+aspargine; Glx, glutamic acid+glutamine; Ser, serine; Thr, threonine; Gly, glycine; Arg, arginine; Ala, alanine; GABA, Gamma (γ-)amino butyric acid; Tyr, tyrosine; Val, valine; Phe, phenylalanine; Ile, isoleucine; Leu, leucine) (a); and the percentage contribution of D-enantiomers of the individual AA in SPM of the Zuari River and estuary with confidence intervals (p<0.05) (b). * Significant differences (p<0.05).

marine and/or terrestrial OC (Meyers, 1997; Xu et al., 2018). The δ^{13}C values of OM in the riverine stations were more depleted as compared to the estuarine region and these values were within the range of C_3 plants (–22.0‰ to –35.0‰), soils, marine and river phytoplankton. These results suggest that allochthonous/terrestrial sources (C_3 plant detritus and soil) contribute substantially to OM in the riverine region and autochthonous/marine sources (*in-situ* production) to the estuarine region. The stations located within the salinity range of 5–25 exhibit mixed sources suggesting the role of the ETM in the redistribution and mixing of OM within this region (Figs 2a, b). These results are in agreement with the results obtained by previous studies conducted in the same region wherein only the monsoon season was sampled (Kessarkar et al., 2013). Likewise, the variation in δ^{15}N values can also be used to differentiate the sources of OM. Usually δ^{15}N values for soils range from 2.0‰ to 5.0‰, for plants from 3.0‰ to 7.0‰ and for plankton from –15‰ to 20.0‰ (Wu et al., 2007; Zhang et al., 2007; Maya et al., 2011). In our study, the samples

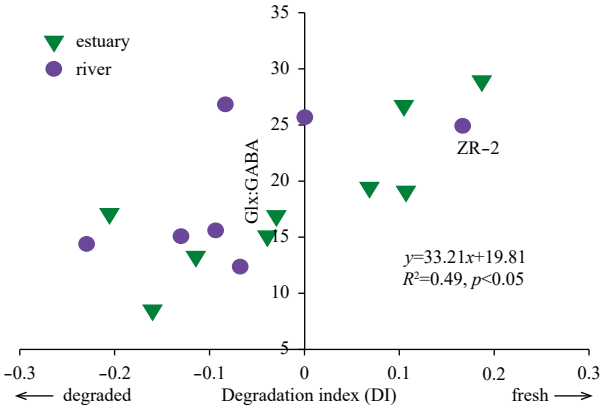

Fig. 4. The relationship between Glx:GABA and degradation index (DI).

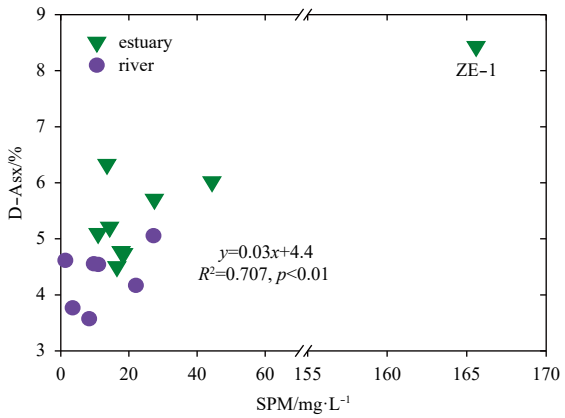

Fig. 5. Plot between D-Asx (%) and suspended particulate matter (SPM) (mg/L) of the Zuari River and estuary.

displayed higher values in the estuarine region and lower values in the riverine region (Table 1). Variations in δ^{15}N values of POM (7‰ to 9‰) collected from the estuarine can be attributed to the isotopic effects associated with nitrate uptake, nitrogen fixation and mixing of different OM sources. The isotopic values of the sampling stations located within the ETM exhibit narrow range suggesting the influence of the estuarine processes in redistributing the OM. A previous study conducted by Bardhan et al. (2015) concluded that the OM in the Zuari Estuary originated from two major pools, namely *in-situ* production and detritus (terrestrial and plankton). Station ZR-2 displays a much lower δ^{15}N isotopic signal during the monsoon season suggesting isotopic fractionation between the nitrogen assimilated by the phytoplankton and nutrients (Bardhan et al., 2015). In addition to the isotopic signatures, the POC:Chl *a* ratio are often used to distinguish the sources of OM from living resources mainly autotrophs and heterotrophs (Cifuentes at al., 1988; Krishna et al., 2018). Usually the POC:Chl *a* ratio of fresh OM produced by marine phytoplankton varies from ~40 (Montagnes et al., 1994) to <200 (Cifuentes at al., 1988) and these variations are attributed to differences in regional temperature, species composition and growth rates. As most of the stations exhibited values <200, it suggests mixed contributions. Some stations exhibited values >200 indicating that POM is dominated by detritus in the estuarine region during the monsoon and pre-monsoon season (Table 1). The possible explanation for this phenomenon can be attributed to the physico-chemical processes occurring within the ETM.

Along with the allochthonous and autochthonous sources, the POM of estuaries and coastal regions originate from anthropogenic sources which is usually consumed by the grazers and/or degraded by heterotrophic organisms. Thus, along with the terrestrial and marine sources, the heterotrophic bacteria and their remnants also contribute to OM, as indicated by the AA data (L- and D-enantiomers). The higher values of glycine (>23 mol%; Table 3) were observed in the estuarine region (Fig. 3a) pointing towards diatoms as a possible source (Keil et al., 2000), in addition to the accumulation of detrital OM (Dauwe and Middelburg, 1998; Wu et al., 2007). The relatively higher mole percentage contributions of Asx and Ala (>10 mol%, Fig. 3a) points towards the contributions from bacteria and its remnants, as cell wall material originating from heterotrophic organisms have an Ala signal (Mayer et al., 1995). The substantial contributions of D-AA in all the SPM samples suggest that bacteria and their remnants contribute substantially to the OM reservoir (Fig. 3b). The D-AA are major the components of bacterial cell wall (peptidoglycan) and are not produced by algae or vascular plants (Jørgensen et al., 2003; Wu et al., 2007). The D-AA are less accessible to biodegradation than the bulk ON (L-enantiomer) (Tanoue et al., 1996; Nagata et al., 1998), thus they accumulate during diagenesis. Interestingly, strong positive correlation is observed between the D-AA monomers, THPAA, D/(D+L) ratio, GABA and SPM (Table S1), which further supports the above statement about contributions from heterotrophic bacterial sources. Although there was no significant difference between the D-AA of the estuarine and riverine stations, the higher values were observed in the estuarine region. An alternative explanation for the occurrence of D-AA in the samples investigated could be from the discharge of treated and untreated effluents from industrial and urbanized areas located within close proximity of the estuarine region. This practice has a negative influence on the water quality. Although, the autotrophic and heterotrophic bacteria were not analyzed, the presence of D-aspartic acid (D-Asx) and D-serine (D-Ser) points towards substantial contributions from heterotrophic sources (Kaiser and Benner, 2008). The values D-Asx reported in the present study are lower than those of the Russian rivers (Dittmar and Kattner, 2003) but were higher than Changjiang River (Yangtze River) (Wu et al., 2007), which is also an estuary that is impacted due to anthropogenic activities. Furthermore, this is in concurrence with a previous study conducted by Nagvenkar and Ramaiah (2009) wherein they reported the presence of bacteria within the estuarine region. Our results match a more recent study conducted by Bardhan et al. (2015) wherein they attribute the poor water quality within the estuarine region to anthropogenic activities such as discharge of untreated or partially treated sewage. Hence, heterotrophic organisms and their remnants contribute substantially to the OM entrained within the SPM of the Zuari River and its estuary along with an overlap of sources observed within the ETM.

4.2 *Quantification of OM in the Zuari River and estuary*

Assuming that different sources have relatively uniform composition and similar preservation (Fry and Sherr, 1989) and based on the δ^{13}C and C:N_{atomic} ratio (Fig. 7a), we applied the three end-member mixing model for quantification OM sources and calculated the percentage contribution. The three end-members were C_3 plants, soils, and river plankton for the river samples, and C_3 plants, river and marine plankton for the estuar-

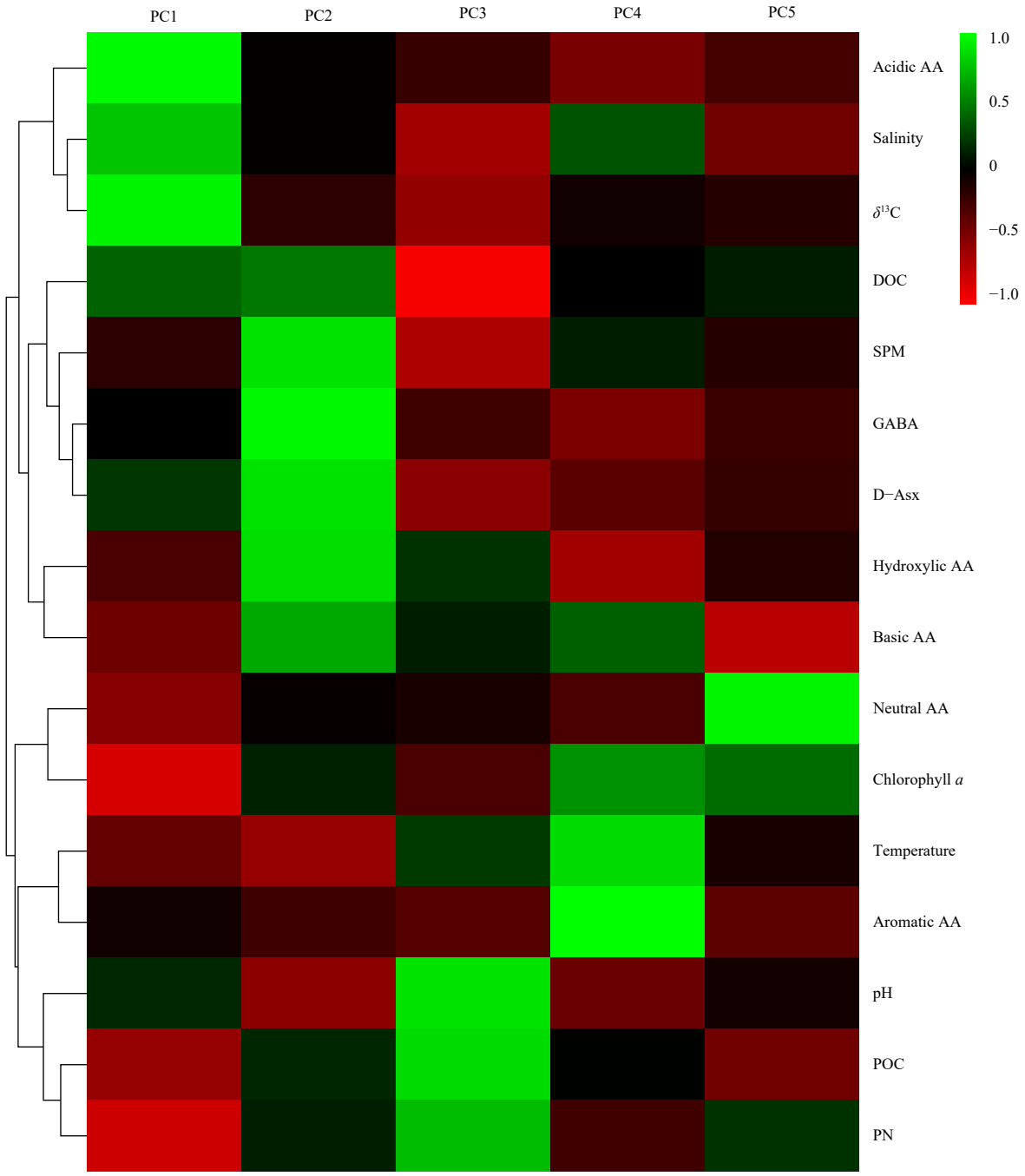

Fig. 6. Heat map of principal components (PC) extracted by R–mode factor analysis with Varimax rotation. The green color indicates positive loadings, black color indicates zero loading, and the red color indicates negative loadings.

ine region. The calculations were done using the Monte Carlo (MC) simulation strategy to track the source distribution in the particulate OC pool taking to consideration the spread of the end-member values (Andersson, 2011; Li et al., 2012). This quantification was based on the δ^{13}C and C:N_{atomic} ratio values of the end-member components adopted from literature and the present data set. We assume that the δ^{13}C and C:N_{atomic} ratio follow normal distribution. The following are the end-member values of δ^{13}C used in our study (C_3 plants (–28.1‰±1.0‰), soil (–21.3‰±1.1‰), marine plankton (–19.8‰±0.9‰) and river plankton (–35.0‰±1.0‰)). The end-member value of C:N_{atomic} ratio used were as follows (C_3 plants (30±10), soil (14.1±2.8), marine plankton (7±1) and river plankton (4±3); Meyers, 1994; Gordon and Goñi, 2003; Pradhan et al., 2014; Nasir et al., 2016). The program was run in Enthought Python Distribution 7.2. Basically, 400 000 out of 40 000 000 random samples from the normal distribution of each end-member were taken in order to simultaneously fulfill the following equations:

$$\text{for riverine samples}: f_{\text{river plankton}} + f_{C_3\text{ plant}} + f_{\text{soil}} = 1, \quad (4)$$

$$f_{\text{river plankton}} \times \delta^{13}C_{\text{river plankton}} + f_{C_3\text{ plant}} \times \delta^{13}C_{C_3\text{ plant}} + f_{\text{soil}} \times \delta^{13}C_{\text{soil}} = \delta^{13}C_{\text{sample}}, \quad (5)$$

$$f_{\text{river plankton}} \times \text{C/N}_{\text{river plankton}} + f_{\text{C}_3\text{ plant}} \times \text{C/N}_{\text{plant}} + f_{\text{soil}} \times \text{C/N}_{\text{soil}} = \text{C/N}_{\text{sample}}, \quad (6)$$

$$\text{for estuarine samples}: f_{\text{river plankton}} + f_{\text{marine plankton}} + f_{\text{C}_3\text{ plant}} = 1, \quad (7)$$

$$f_{\text{river plankton}} \times \delta^{13}\text{C}_{\text{river plankton}} + f_{\text{marine plankton}} \times \delta^{13}\text{C}_{\text{marine plankton}} + f_{\text{C}_3\text{ plant}} \times \delta^{13}\text{C}_{\text{C}_3\text{ plant}} = \delta^{13}\text{C}_{\text{sample}}, \quad (8)$$

$$f_{\text{river plankton}} \times \text{C/N}_{\text{river plankton}} + f_{\text{marine plankton}} \times \text{C/N}_{\text{marine plankton}} + f_{\text{C}_3\text{ plant}} \times \text{C/N}_{\text{plant}} = \text{C/N}_{\text{sample}}, \quad (9)$$

where f represents the fraction of river plankton, C_3 plant, marine plankton and soil OC contribution to the samples, respectively. The contribution of each end-member was calculated based on these 400 000 results (Li et al., 2012). The results of the percentage contributions are presented in Fig. 7b. The percentage contribution from soil to the riverine region varied from approximately 7% to 45% with relatively less contributions during the dry season in the estuarine region. The OM in the estuarine region of the Zuari River appeared to be mainly derived from in-situ marine plankton, terrestrial C_3 plants, and river plankton. Marine plankton contributed to the bulk of the OM in the estuarine region and varied from approximately 35% to 88%. During the post- and pre-monsoon season river phytoplankton was the main source of OM in the riverine region. Higher percentage contributions from autochthonous sources was observed during the dry season due to the dominance of tidal activity, resulting in strong lateral and vertical mixing which aids in the transport of marine OM into the estuary. During the dry season the estuary transforms into an extended part of the sea as there is minimal flow of freshwater (Subha Anand et al., 2014). The lower percentage contribution of allochthonous sources observed in the lower reaches can be explained as a result of reduced flow of freshwater during the dry season. Mixing and transport of OM within the estuary is controlled by water discharge and residence time of the water masses. The residence time of the water masses of the Zuari River and its estuary is known to be longer than its neighboring river (Mandovi River, 5–6 d during the SWM to about ~50 d during the non-monsoon season) (Qasim and Sen Gupta, 1981). The prevalence of the ETM within the estuarine region tends to increase the suspension time of the particles. Physical processes (tidal activity) coupled with longer hydraulic residence time provide ideal conditions for heterotrophic organisms to work and rework the OM suspended in the water column thereby controlling its biochemical status.

4.3 *Diagenesis of POM within the ETM*

In order to understand the diagenetic status of OM, the THAA yields (%OC), DI and Glx:GABA ratio of SPM (Fig. 4) were calculated and examined. The yields and ratios serve as the indicators of diagenesis. The degradation index (DI) developed by Dauwe and Middelburg (1998) provides insights into the diagenetic state of OM. The DI values decrease from positive values (1 to 1.5) for fresh phytoplankton to negative values (<–1) for diagenetically altered OM from deep sea sediments (Dauwe et al., 1999). As the DI values of the SPM in the river investigated varies from –0.21 to 0.19, it indicates a minor to moderate diagenetic alterations. Nonetheless, the DI values of riverine stations investigated were more negative during the three seasons indicating the presence of refractory OM. Except Sta. ZR-2 (pre-monsoon) which displays a positive value of DI suggesting the presence of labile OM coupled with low $C:N_{atomic}$ ratio revealing the occurrence of fresh production. A strong positive correlation observed between the diagenetic indicators (Glx:GABA vs. DI) suggests the reliability of these indicators in assessing the overall status of SPM transported by the Zuari River. Furthermore, the estuarine stations displayed mixed characteristics, with both positive and negative values occurring due to lateral and vertical mixing taking place within the ETM resulting from tides and river discharge. Furthermore, the high D-Asx (%) content as observed in the estuarine region was found to be associated with SPM (Figs 4b and 6). The selective preservation of structural compounds in contrast to preferential degradation of cell wall components is an indicator of the heterogeneous nature of OM (Dauwe and Middelburg, 1998). Low salinity conditions within the estuary facilitate flocculation and adsorption processes thereby allowing the particles to stay in suspension for longer periods during the dry season. Deposition-resuspension processes due to wind driven waves and circulation patterns coupled with the narrowing of the estuarine channel alters the quality of OM within the ETM. Complex processes take place within the ETM (mixing zone) such as particle solute interactions, flocculation, coagulation, re-suspension and sedimentation are responsible for altering the characteristics of OM before they are deposited into the sediments (Kessarkar et al., 2013). From these results we can ascertain the influence of the ETM in controlling the diagenesis of OM.

Another possible explanation for the presence of older material in the estuarine region can be attributed to the funnel shape structure of the estuary resulting in additional turbulence. Lighter particle are re-suspended and remain exposed to oxidative diagenesis as they remain in the water column for longer durations. Gravitational circulation (tides), together with rainfall and freshwater discharge during the monsoon season lead to salinity stratification of the water column at the mouth of the river. This leads to the formation of a salt wedge during the SWM and it extends to about 12 km upstream (Qasim and Sen Gupta, 1981). Salinity measured during the monsoon season from the head of the river to the upstream part of the estuary was almost negligible, which is an outcome of increased fresh water discharge. The quantity of fresh water discharged from the river during the dry season is trifling (about 0.03 km^3/a) (Wagle et al., 1988). It is to be noted that salinity stratification of the water column occurs near the mouth of the river during the monsoon season and remains well-mixed during the non-monsoon season. The tidal surge and geomorphological constriction (funnel shape) enhances the drag and lift forces resulting in resuspension of materials from the surface sediments there by exposing the particles to multiple cycles of suspension and deposition before eventual settling down into the sediments of the coastal region. Thus the impact of tidal activity along with wind induced currents results in flocculation of suspended matter at the saltwater-fresh water interface at the river mouth during the monsoon season. Whereas during the post- and pre-monsoon seasons, the mixing zone moves inwards into the estuary as freshwater discharge decreases, and the well-developed ETM moves into the estuarine region. Thus, OM entrained within the SPM of the ETM displays a mixed character due to lateral and vertical mixing of material in the river before they are deposited into the sediments of the coastal seas.

Unlike the Changjiang River where the turbidity maxima is fed by resuspension and erosion of the river bed (Li and Zhang, 1998), the ETM of the Zuari River results from tidal activity and

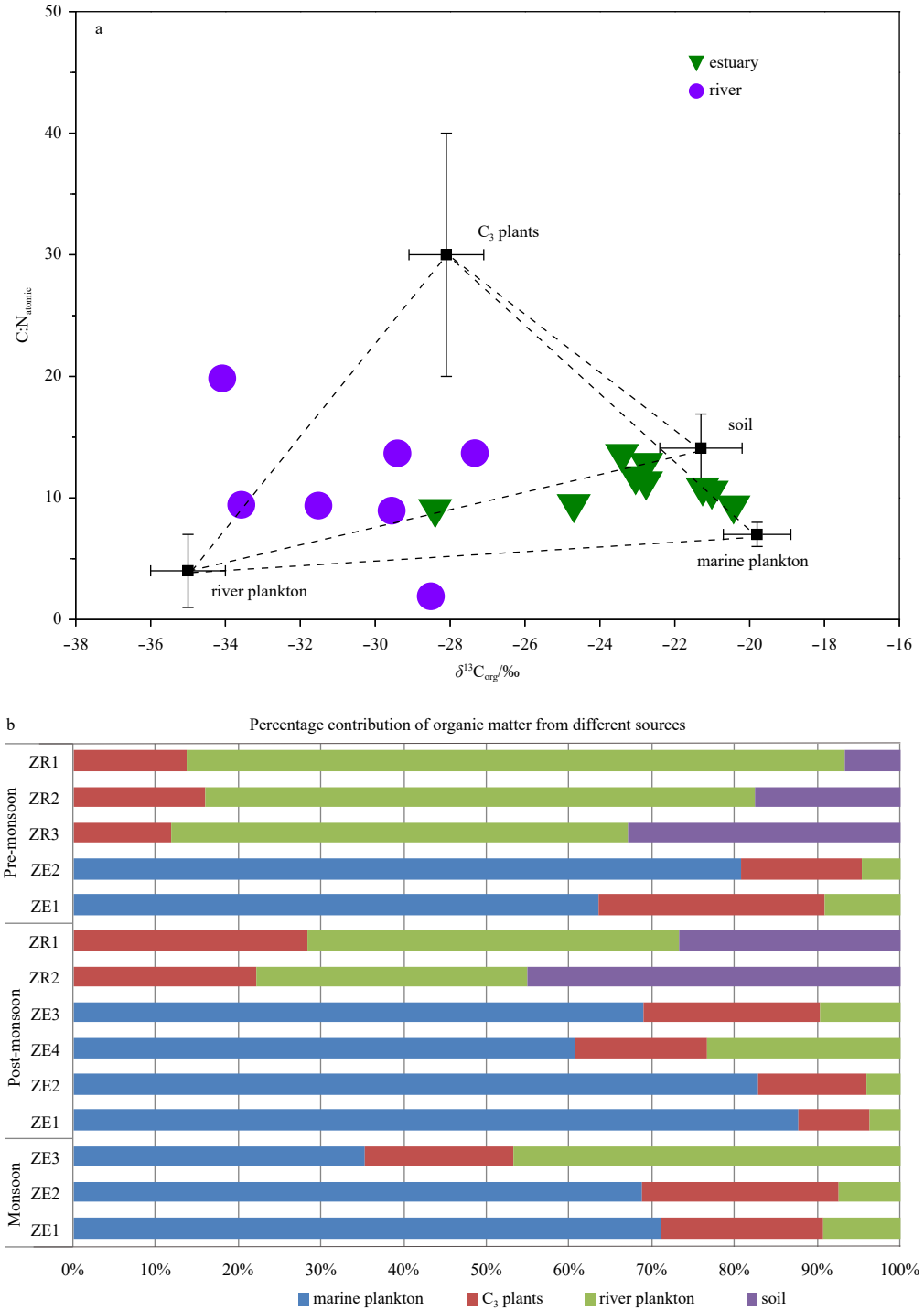

Fig. 7. Property-property plots of $C:N_{atomic}$ ratio vs. $\delta^{13}C_{org}$ values of particulate matter from the Zuari River and estuary along with the potential OM sources (C_3 plants, soils, marine and river plankton) (a); and calculated proportion OM contributed from different sources to the particulates based on the results of end-member mixing model (b).

structural shape of the estuary (funnel shape), thereby causing enhanced turbulence within the estuarine region. During the monsoon season erosion of top soils from the catchment area is a dominant process. Whereas, during the non-monsoon season, the fresh water flow into the river is reduced. This results in the movement of the ETM into the river and alters the composition and diagenetic status of OM. Thus, combination of tidal resuspension and reduced freshwater influx into the estuary results in hydrodynamic sorting of particles along the estuary whereby some marine OM is transported into the estuary during non-monsoon seasons (Fig. 7b).

The sources of OM ascertained qualitatively indicated non-conservative mixing behavior within the estuarine region. Similar observations were noticed with the AA investigated. They also displayed non-conservative mixing behavior within the ETM as no clear trend was observed. Similarly, other labile constituents,

i.e., chromophoric dissolved organic matter (CDOM) show non-conservative behavior within the estuaries as a result of different biogeochemical processes such as adsorption-desorption processes, mixing of terrestrial and marine OM, resuspension, microbial and photochemical degradation which takes place within the ETM (Yang et al., 2013). The non-conservative mixing behavior has been observed with the net fluxes of suspended matter, POC, and total nitrogen (TN) of the Winyah Bay, South Carolina, USA (Goñi et al., 2003).

Furthermore, based on the estuarine mixing diagrams of the nutrients with respect to salinity, the meso-tidal rivers showed greater flushing capacity and act as corridors for the passage and transport of nutrients between the river, estuary and open ocean (Fernandes et al., 2018). The dilution, size and developmental status of the river basin influence the quantity and quality of OM that is transported. Therefore, to increase our knowledge about the complex ecological systems such as ETM, future studies are needed. Additionally, the role of minor rivers and estuaries in modifying the OM trapped within the ETM during transport from river to coastal waters merits special attention as they are influenced and impacted by multiple natural (seasonal changes, tidal cycles) and anthropogenic stressors.

5 Conclusions

In this study, the sources, composition, and factors influencing diagenesis of POM within the Zuari River and estuary were investigated. By analyzing the bulk and ancillary parameters along with the biomarker (AA) of the SPM for the three different seasons we conclude that there was no significant temporal variability. Nonetheless, when the stations were grouped spatially (according to the region) they displayed spatial variability. Temperature, pH, salinity, POC, PN, δ^{13}C, δ^{15}N and AA-C% were significantly different spatially. From the values of POC, δ^{13}C, PN, δ^{15}N, C:N_{atomic} and POC:Chl *a* ratios, and AA (L- and D-enantiomers), the data indicated that the OM mostly originated from terrigenous sources (C_3 plant detritus and soils), *in-situ* production (marine and river phytoplankton) and heterotrophic organisms and their detrital matter. The contribution from marine phytoplankton was the maximum in the estuarine region followed by C_3 plant detritus and soils during the dry season. The average contribution from river phytoplankton during the pre-monsoon season was more than 66%, while the average contribution from soil OM was approximately 19%. River runoff transported refractory and more degraded materials from the head region of the river to the estuarine region during the monsoon season. The diagenetic status of OM is influenced by the formation of the ETM. The funnel shaped structure (geomorphological constriction) of the estuarine region coupled with the meso-tidal cycles experienced by the region play a critical role in altering the OM. The presence of higher proportions of D-AA in the estuary indicates contributions from bacteria and their remnants along with accumulation of older OM. By employing D-AA as a biomarker, bacteria and their remnants act as source indicators pointing towards enhanced contaminations, highlighting the deteriorating water quality of the estuary. Thus, by studying the biomarker (AA), and the other bulk and ancillary parameters of SPM we were able to ascertain the prevailing conditions, thereby contributing to the understanding of the sources, processes and factors controlling the nature OM within the ETM of small tropical rivers.

Acknowledgements

The first author sincerely thanks the Ministry of Human Resources Development (India), Chinese Scholarship Council (China) and East China Normal University, Shanghai, China for providing her the visiting fellowship. We deeply appreciated the field assistance provided by staff at the National Institute of Oceanography (NIO), India and for the use of the laboratory facilities at the institute for sample pre-treatment. We are thankful to Zhuoyi Zhu from the State Key Laboratory of Estuarine and Coastal Research, East China Normal University, Shanghai, China, for the technical support and providing the instrumental facility for amino acid analyses. We are thankful to the two anonymous reviewers for their valuable suggestions that have helped improve this manuscript.

References

Abril G, Borges A V. 2005. Carbon dioxide and methane emissions from estuaries. In: Tremblay A, Varfalvy L, Roehm C, et al., eds. Greenhouse Gas Emissions—Fluxes and Processes. Environmental Science. Berlin, Heidelberg: Springer, 187–207

Abril G, Commarieu M V, Guérin F. 2007. Enhanced methane oxidation in an estuarine turbidity maximum. Limnology and Oceanography, 52(1): 470–475, doi: 10.4319/lo.2007.52.1.0470

Abril G, Riou S A, Etcheber H, et al. 2000. Transient, tidal time-scale, nitrogen transformations in an estuarine turbidity maximum—fluid mud system (The Gironde, South-west France). Estuarine, Coastal and Shelf Science, 50(5): 703–715, doi: 10.1006/ecss.1999.0598

Andersson A. 2011. A systematic examination of a random sampling strategy for source apportionment calculations. Science of the Total Environment, 412–413: 232–238, doi: 10.1016/j.scitotenv.2011.10.031

Bardhan P, Karapurkar S G, Shenoy D M, et al. 2015. Carbon and nitrogen isotopic composition of suspended particulate organic matter in Zuari Estuary, west coast of India. Journal of Marine Systems, 141: 90–97, doi: 10.1016/j.jmarsys.2014.07.009

Bhaskar P V, Bhosle N B. 2008. Bacterial production, glucosidase activity and particle-associated carbohydrates in Dona Paula bay, west coast of India. Estuarine, Coastal and Shelf Science, 80(3): 413–424, doi: 10.1016/j.ecss.2008.09.005

Bhosle N B. 2007. Distribution of tributyltin (TBT) in the Mandovi estuary. In: The Mandovi and Zuari Estuaries. Goa, India: National Institute of Oceanography, 105–114

Bianchi T S, Allison M A. 2009. Large-river delta-front estuaries as natural "recorders" of global environmental change. Proceedings of the National Academy of Sciences of the United States of America, 106(20): 8085–8092, doi: 10.1073/pnas.0812878106

Census Organization of India. 2011. Census 2011. https://www.census2011.co.in/states.php [2013-05-20/2018-12-10]

Cifuentes L A, Sharp J H, Fogel M L. 1988. Stable carbon and nitrogen isotope biogeochemistry in the Delaware estuary. Limnology and Oceanography, 33(5): 1102–1115, doi: 10.4319/lo.1988.33.5.1102

Cowie G L, Hedges J I. 1994. Biochemical indicators of diagenetic alteration in natural organic matter mixtures. Nature, 369(6478): 304–307, doi: 10.1038/369304a0

Dauwe B, Middelburg J J. 1998. Amino acids and hexosamines as indicators of organic matter degradation state in North Sea sediments. Limnology and Oceanography, 43(5): 782–798, doi: 10.4319/lo.1998.43.5.0782

Dauwe B, Middelburg J J, Herman P M J, et al. 1999. Linking diagenetic alteration of amino acids and bulk organic matter reactivity. Limnology and Oceanography, 44(7): 1809–1814, doi: 10.4319/lo.1999.44.7.1809

Dessai D V G, Nayak G N. 2009. Distribution and speciation of selected metals in surface sediments, from the tropical Zuari estuary, central west coast of India. Environmental Monitoring and Assessment, 158(1–4): 117–137, doi: 10.1007/s10661-008-0575-0

Dittmar T, Fitznar H P, Kattner G. 2001. Origin and biogeochemical cycling of organic nitrogen in the eastern Arctic Ocean as evident from D- and L-amino acids. Geochimica et Cosmochimica

Acta, 65(22): 4103–4114, doi: 10.1016/S0016-7037(01)00688-3
Dittmar T, Kattner G. 2003. The biogeochemistry of the river and shelf ecosystem of the Arctic Ocean: A review. Marine Chemistry, 83(3): 103–120
Eglinton T I, Eglinton G. 2008. Molecular proxies for paleoclimatology. Earth and Planetary Science Letters, 275(1–2): 1–16, doi: 10.1016/j.epsl.2008.07.012
Fernandes D, Wu Y, Shirodkar P V, et al. 2019. Spatial and temporal variations in source, diagenesis, and fate of organic matter in sediments of the Netravati River, India. Hydrological Processes, 33(20): 2642–2657, doi: 10.1002/hyp.13516
Fernandes L L, Kessarkar P M, Suja S, et al. 2018. Seasonal variations in the water quality of six tropical micro- and meso-tidal estuaries along the central west coast of India. Marine and Freshwater Research, 69(9): 1418–1431, doi: 10.1071/MF17181
Fitznar H P, Lobbes J M, Kattner G. 1999. Determination of enantiomeric amino acids with high-performance liquid chromatography and pre-column derivatisation with o-phthaldialdehyde and N-isobutyrylcysteine in seawater and fossil samples (mollusks). Journal of Chromatography A, 832(1–2): 123–132, doi: 10.1016/S0021-9673(98)01000-0
Fry B, Sherr E B. 1989. δ^{13}C measurements as indicators of carbon flow in marine and freshwater ecosystems. In: Rundel P W, Ehleringr J R, Nagy K A, eds. Stable Isotopes in Ecological Research. New York: Springer-Verlag, 196–229
Geyer W R. 1993. The importance of suppression of turbulence by stratification on the estuarine turbidity maximum. Estuaries, 16: 113–125, doi: 10.2307/1352769
Goldsmith S T, Moyer R P, Harmon R J. 2015. Hydrochemistry and biogeochemistry of tropical small mountain rivers. Applied Geochemistry, 63: 453–455, doi: 10.1016/j.apgeochem.2015.11.005
Goñi M A, Teixeira M J, Perkey D W. 2003. Sources and distribution of organic matter in a river-dominated estuary (Winyah Bay, SC, USA). Estuarine, Coastal and Shelf Science, 57(5–6): 1023–1048, doi: 10.1016/S0272-7714(03)00008-8
Gordon E S, Goñi M A. 2003. Sources and distribution of terrigenous organic matter delivered by the Atchafalaya River to sediments in the northern Gulf of Mexico. Geochimica et Cosmochimica Acta, 67(13): 2359–2375, doi: 10.1016/S0016-7037(02)01412-6
Gupta L, Subramanian V, Ittekkot V. 1997. Biogeochemistry of particulate organic matter transported by the Godavari River, India. Biogeochemistry, 38(2): 103–128, doi: 10.1023/A:1005732519216
Hedges J I, Keil R G, Benner R. 1997. What happens to terrestrial organic matter in the ocean?. Organic Geochemistry, 27(5–6): 195–212, doi: 10.1016/S0146-6380(97)00066-1
Hibbert C, Hudson-Edwards K A, Widdoson M. 2015. Controls on seasonal elemental variation in tropical rivers in Goa, India. In: Goldschmidt 2015. Prague
Hilton R G, Galy A, Hovius N, et al. 2008. Tropical-cyclone-driven erosion of the terrestrial biosphere from mountains. Nature Geoscience, 1(11): 759–762, doi: 10.1038/ngeo333
India Meteorological Department (IMD), Ministry of Earth Sciences, Government of India. 2013. Rainfall Statistics of India. http://www.hydro.imd.gov.in [2013-12/2018-09-20]
Jennerjahn T C, Soman K, Ittekkot V, et al. 2008. Effect of land use on the biogeochemistry of dissolved nutrients and suspended and sedimentary organic matter in the tropical Kallada River and Ashtamudi estuary, Kerala, India. Biogeochemistry, 90(1): 29–47, doi: 10.1007/s10533-008-9228-1
Jørgensen L, Stedmon C A, Granskog M A, et al. 2014. Tracing the long-term microbial production of recalcitrant fluorescent dissolved organic matter in seawater. Geophysical Research Letters, 41(7): 2481–2488, doi: 10.1002/2014GL059428
Jørgensen N O G, Stepanauskas R, Pedersen A G U, et al. 2003. Occurrence and degradation of peptidoglycan in aquatic environments. FEMS Microbiology Ecology, 46(3): 269–280, doi: 10.1016/S0168-6496(03)00194-6
Kaiser K, Benner R. 2008. Major bacterial contribution to the ocean reservoir of detrital organic carbon and nitrogen. Limnology and Oceanography, 53(1): 99–112, doi: 10.4319/lo.2008.53.1.0099
Kara D. 2009. Evaluation of trace metal concentrations in some herbs and herbal teas by principal component analysis. Food Chemistry, 114(1): 347–354, doi: 10.1016/j.foodchem.2008.09.054
Ke Zhixin, Tan Yehui, Huang Liangmin, et al. 2017. Spatial distributions of δ^{13}C, δ^{15}N and C/N ratios in suspended particulate organic matter of a bay under serious anthropogenic influences: Daya Bay, China. Marine Pollution Bulletin, 114(1): 183–191, doi: 10.1016/j.marpolbul.2016.08.078
Keil R G, Tsamaki E, Hedges J I. 2000. Early diagenesis of particulate amino acids in marine systems. In: Goodfriend G A, Collins M J, Fogel M L, et al., eds. Perspectives in Amino Acid and Protein Geochemistry. Oxford: Oxford University Press, 69–82
Kessarkar P M, Shynu R, Rao V P, et al. 2013. Geochemistry of the suspended sediment in the estuaries of the Mandovi and Zuari rivers, central west coast of India. Environmental Monitoring and Assessment, 185(5): 4461–4480, doi: 10.1007/s10661-012-2883-7
Krishna M S, Mukherjee J, Dalabehera H B, et al. 2018. Particulate organic carbon composition in temperature fronts of the northeastern Arabian Sea during winter. Journal of Geophysical Research: Biogeosciences, 123(2): 463–478, doi: 10.1002/2018JG004387
Li Jiufa, Zhang Chen. 1998. Sediment resuspension and implications for turbidity maximum in the Changjiang Estuary. Marine Geology, 148(3–4): 117–124, doi: 10.1016/S0025-3227(98)00003-6
Li Xinxin, Bianchi T S, Allison M A, et al. 2012. Composition, abundance and age of total organic carbon in surface sediments from the inner shelf of the East China Sea. Marine Chemistry, 145-147: 37–52, doi: 10.1016/j.marchem.2012.10.001
Lomstein B A, Niggemann J, Jørgensen B B, et al. 2009. Accumulation of prokaryotic remains during organic matter diagenesis in surface sediments off Peru. Limnology and Oceanography, 54(4): 1139–1151, doi: 10.4319/lo.2009.54.4.1139
Mai-Thi N N, St-Onge G, Tremblay L. 2017. Contrasting fates of organic matter in locations having different organic matter inputs and bottom water O_2 concentrations. Estuarine, Coastal and Shelf Science, 198: 63–72, doi: 10.1016/j.ecss.2017.08.044
Manoj N T, Unnikrishnan A S. 2009. Tidal circulation and salinity distribution in the Mandovi and Zuari estuaries: case study. Journal of Waterway, Port, Coastal, and Ocean Engineering, 135(6): 278–287, doi: 10.1061/(ASCE)0733-950X(2009)135:6(278)
Maya M V, Soares M A, Agnihotri R, et al. 2011. Variations in some environmental characteristics including C and N stable isotopic composition of suspended organic matter in the Mandovi Estuary. Environmental Monitoring and Assessment, 175(1–4): 501–517, doi: 10.1007/s10661-010-1547-8
Mayer L M, Schick L L, Sawyer T, et al. 1995. Bioavailable amino acids in sediments: a biomimetic, kinetics based approach. Limnology and Oceanography, 40(3): 511–520, doi: 10.4319/lo.1995.40.3.0511
Meyers P A. 1994. Preservation of elemental and isotopic source identification of sedimentary organic matter. Chemical Geology, 114(3-4): 289–302, doi: 10.1016/0009-2541(94)90059-0
Meyers P A. 1997. Organic geochemical proxies of paleoceanographic, paleolimnologic, and paleoclimatic processes. Organic Geochemistry, 27(5–6): 213–250, doi: 10.1016/S0146-6380(97)00049-1
Milliman J D, Lee T Y, Huang J C, et al. 2017. Impact of catastrophic events on small mountainous rivers: Temporal and spatial variations in suspended- and dissolved-solid fluxes along the Choshui River, central western Taiwan, during typhoon Mindulle, July 2–6, 2004. Geochimica et Cosmochimica Acta, 205: 272–294, doi: 10.1016/j.gca.2017.02.015
Mitchell S B, West J R, Arundale A M W, et al. 1999. Dynamics of the turbidity maxima in the Upper Humber Estuary System, UK. Marine Pollution Bulletin, 37(3–7): 190–205, doi: 10.1016/S0025-326X(98)00178-7
Montagnes D J S, Berges J A, Harrison P J, et al. 1994. Estimating carbon, nitrogen, protein, and chlorophyll a from volume in marine phytoplankton. Limnology and Oceanography, 39(5): 1044–1060, doi: 10.4319/lo.1994.39.5.1044
Nagata T, Fukuda R, Koike I, et al. 1998. Degradation by bacteria of

membrane and soluble protein in seawater. Aquatic Microbial Ecology, 14: 29–37, doi: 10.3354/ame014029

Nagvenkar G S, Ramaiah N. 2009. Abundance of sewage-pollution indicator and human pathogenic bacteria in a tropical estuarine complex. Environmental Monitoring and Assessment, 155(1–4): 245–256, doi: 10.1007/s10661-008-0432-1

Nasir A, Lukman M, Tuwo A, et al. 2016. The use of C/N ratio in assessing the influence of land-based material in coastal water of south Sulawesi and Spermonde Archipelago, Indonesia. Frontiers in Marine Science, 3: 266

Ni Zhaokui, Wang Shengrui, Zhang Mianmian. 2016. Sediment amino acids as indicators of anthropogenic activities and potential environmental risk in Erhai Lake, Southwest China. Science of the Total Environment, 551-552: 217–227, doi: 10.1016/j.scitotenv.2016.02.005

Nunn B L, Keil R G. 2005. Size distribution and amino acid chemistry of base-extractable proteins from Washington Coast sediments. Biogeochemistry, 75(2): 177–200, doi: 10.1007/s10533-004-6546-9

Pradhan U K, Wu Ying, Shirodkar P V, et al. 2014. Sources and distribution of organic matter in thirty five tropical estuaries along the west coast of India—a preliminary assessment. Estuarine, Coastal Shelf Sciences, 151: 21–33, doi: 10.1016/j.ecss.2014.09.010

Qasim S Z, Sen Gupta R. 1981. Environmental characteristics of the Mandovi-Zuari estuarine system in Goa. Estuarine, Coastal and Shelf Science, 13(5): 557–578, doi: 10.1016/S0302-3524(81)80058-8

Rao V P, Shynu R, Kessarkar P M, et al. 2011. Suspended sediment dynamics on a seasonal scale in the Mandovi and Zuari estuaries, central west coast of India. Estuarine, Coastal and Shelf Science, 91(1): 78–86, doi: 10.1016/j.ecss.2010.10.007

Rao V P, Shynu R, Singh S K, et al. 2015. Mineralogy and Sr-Nd isotopes of SPM and sediment from the Mandovi and Zuari estuaries: Influence of weathering and anthropogenic contribution. Estuarine, Coastal and Shelf Science, 156: 103–115, doi: 10.1016/j.ecss.2014.07.004

Shetye S R, Gouveia A D, Singbal S Y, et al. 1995. Propagation of tides in the Mandovi-Zuari estuarine network. Proceedings of the Indian Academy of Sciences—Earth and Planetary Sciences, 104(4): 667–682

Shetye S R, Kumar M D, Shankar D. 2007. The Mandovi and Zuari Estuaries. Goa: National Institute of Oceanography

Strickland J D H, Parsons T R. 1972. A Practical Handbook of Seawater Analysis. Bulletin: Fisheries Research Board Canada

Subha Anand S, Sardessai S, Muthukumar C, et al. 2014. Intra-and inter-seasonal variability of nutrients in a tropical monsoonal estuary (Zuari, India). Continental Shelf Research, 82: 9–30, doi: 10.1016/j.csr.2014.04.005

Sundar D, Shetye S R. 2005. Tides in the Mandovi and Zuari estuaries, Goa, west coast of India. Journal of Earth System Science, 114(5): 493–503, doi: 10.1007/BF02702025

Suprit K, Shankar D. 2008. Resolving orographic rainfall on the Indian west coast. International Journal of Climatology, 28(5): 643–657, doi: 10.1002/joc.1566

Suzuki K W, Gwak W S, Nakayama K, et al. 2010. Instability of the turbidity maximum in the macrotidal Geum River estuary, western Korea. Limnology, 11(3): 197–205, doi: 10.1007/s10201-009-0303-7

Syvitski J P M, Cohen S, Kettner A J, et al. 2014. How important and different are tropical rivers? — An overview. Geomorphology, 227: 5–17, doi: 10.1016/j.geomorph.2014.02.029

Tanoue E, Ishii M, Midorikawa T. 1996. Discrete dissolved and particulate proteins in oceanic waters. Limnology and Oceanography, 41(6): 1334–1343, doi: 10.4319/lo.1996.41.6.1334

Uncles R J, Stephens J A, Law D J. 2006. Turbidity maximum in the macrotidal, highly turbid Humber Estuary, UK: Flocs, fluid mud, stationary suspensions and tidal bores. Estuarine, Coastal and Shelf Science, 67(1–2): 30–52, doi: 10.1016/j.ecss.2005.10.013

Unger D, Herbeck L S, Li Min, et al. 2013. Sources, transformation and fate of particulate amino acids and hexosamines under varying hydrological regimes in the tropical Wenchang/Wenjiao Rivers and Estuary, Hainan, China. Continental Shelf Research, 57: 44–58, doi: 10.1016/j.csr.2012.02.014

Veuger B, van Oevelen D, Middelburg J J. 2012. Fate of microbial nitrogen, carbon, hydrolysable amino acids, monosaccharides, and fatty acids in sediment. Geochimica et Cosmochimica Acta, 83: 217–233, doi: 10.1016/j.gca.2011.12.016

Vijith V, Sundar D, Shetye S R. 2009. Time-dependence of salinity in monsoonal estuaries. Estuarine, Coastal and Shelf Science, 85(4): 601–608, doi: 10.1016/j.ecss.2009.10.003

Wagle B G, Gujar A R, Subramanyam V, et al. 1988. Seabed surveys of Marmugoa harbour central west coast of India. Indian Journal of Marine Sciences, 17: 59–68

Wu Ying, Bao Hongyan, Unger D, et al. 2013. Biogeochemical behavior of organic carbon in a small tropical river and estuary, Hainan, China. Continental Shelf Research, 57: 32–43, doi: 10.1016/j.csr.2012.07.017

Wu Ying, Dittmar T, Ludwichowski K U, et al. 2007. Tracing suspended organic nitrogen from the Yangtze River catchment into the East China Sea. Marine Chemistry, 107(3): 367–377, doi: 10.1016/j.marchem.2007.01.022

Xu Yunping, Zhou Shangzhe, Hu Limin, et al. 2018. Different controls on sedimentary organic carbon in the Bohai Sea: River mouth relocation, turbidity and eutrophication. Journal of Marine Systems, 180: 1–8, doi: 10.1016/j.jmarsys.2017.12.004

Yang Liyang, Guo Weidong, Hong Huasheng, et al. 2013. Non-conservative behaviors of chromophoric dissolved organic matter in a turbid estuary: Roles of multiple biogeochemical processes. Estuarine, Coastal and Shelf Science, 133: 285–292, doi: 10.1016/j.ecss.2013.09.007

Zhang Yulong, Kaiser K, Li Li, et al. 2014. Sources, distributions, and early diagenesis of sedimentary organic matter in the Pearl River region of the South China Sea. Marine Chemistry, 158: 39–48, doi: 10.1016/j.marchem.2013.11.003

Zhang Jing, Wu Ying, Jennerjahn T C, et al. 2007. Distribution of organic matter in the Changjiang (Yangtze River) Estuary and their stable carbon and nitrogen isotopic ratios: Implications for source discrimination and sedimentary dynamics. Marine Chemistry, 106(1–2): 111–126, doi: 10.1016/j.marchem.2007.02.003

Supplementary information:

Table S1. Factor loadings calculated using principal component analysis (PCA) of the physical and biogeochemical parameters of the Zuari River and estuary, west coast of India.

Table S2. Pearson's correlation among the physical and biogeochemical parameters of the Zuari River and estuary, west coast of India.

The supplementary information is available online at https://doi.org/10.1007/s13131-020-1544-x. The supplementary information is published as submitted, without typesetting or editing. The responsibility for scientific accuracy and content remains entirely with the authors.

Acta Oceanol. Sin., 2020, Vol. 39, No. 4, P. 33–41
https://doi.org/10.1007/s13131-020-1543-y
http://www.hyxb.org.cn
E-mail: hyxbe@263.net

Carbon isotopes and lignin phenols for tracing the floods during the past 70 years in the middle reach of the Changjiang River

Zhongqiao Li[1, 2], Ying Wu[1]*, Liyang Yang[1, 3], Jinzhou Du[1], Bing Deng[1], Jing Zhang[1]

[1] State Key Laboratory of Estuarine and Coastal Research, East China Normal University, Shanghai 210012, China

[2] Key Laboratory of Marine Ecosystem Dynamics, Second Institute of Oceanography, Ministry of Natural Resources, Hangzhou 310012, China

[3] College of Environment and Resources, Fuzhou University, Fuzhou 350108, China

Received 23 February 2019; accepted 10 June 2019

Abstract

The Lake Tian E Zhou (TEZ, an oxbow lake) was formed during the rerouting of the Changjiang River in 1972, with strong influences from the main river channel and flood events. Herein, a sediment core was collected from the Lake TEZ for the measurements of carbon isotopes and biomarkers, including stable carbon isotopes ($\delta^{13}C$), radiocarbon composition ($\Delta^{14}C$), and lignin phenols, as well as lead-210 to reconstruct recent heavy flood events over the past 70 years. At the 24–26 cm interval, the sediment contained the highest OC%, TN%, and lignin phenols content, as well as significantly depleted ^{13}C but enriched ^{14}C, corresponding to the extreme flood event in 1998. In addition, statistics from *t*-test showed that lignin phenols normalized to OC ($\Lambda 8$), the concentration of 3, 5-dihydroxy benzoic acid (3, 5-BD), and the ratio of p-hydroxy benzophenone to total hydroxyl phenols (PHB/HP) were all significantly different between the layers containing flood deposits and the layers deposited under normal non-flood conditions ($p<0.05$). These results indicate that the later three parameters are highly related to flood events and can be used as compelling proxies, along with sediment chronology, for hydrological changes and storm/flood events in the river basin and coastal marine environments.

Key words: flood record, carbon isotopes, lignin phenols, Changjiang River, Lake Tian E Zhou

Citation: Li Zhongqiao, Wu Ying, Yang Liyang, Du Jinzhou, Deng Bing, Zhang Jing. 2020. Carbon isotopes and lignin phenols for tracing the floods during the past 70 years in the middle reach of the Changjiang River. Acta Oceanologica Sinica, 39(4): 33–41, doi: 10.1007/s13131-020-1543-y

1 Introduction

Organic carbon (OC) preserved in sediments is a net sink for CO_2 and is important in controlling the level of atmospheric CO_2 and, as such, is a key component in the global carbon cycle (Falkowski et al., 2000; Hedges et al., 1997). Rivers transported approximately one third of OC buried in the sea, which is of terrigenous origin, rather than via other pathways such as aeolian transit (Dalzell et al., 2005). Thus, rivers play a critical role in the regional carbon cycling. During fluvial discharge, extreme climatic events such as floods have a significant influence on the flux and composition of OC. Floods strongly influence the transport of OC by river systems (Dalzell et al., 2005; Yu et al., 2011; Wu et al., 2007). For example, extraordinary flood in the Changjiang River during July and August in 1998 resulted in a three and half fold increase over normal levels in the fluxes of particulate organic carbon to the East China Sea (Yu et al., 2011; Wu et al., 2007). Due to the importance of floods in the transportation of OC, it is essential to reconstruct historical floods through the analysis of sediment cores from river drainage basins (Bianchi et al., 2013; Dhillon and Inamdar, 2013; Korponai et al., 2016; van Metre and Horowitz, 2013; Wang et al., 2014).

The Changjiang River is one of the world's largest rivers, with a drainage area of 1.8×10^6 km^2 and a water discharge of 960 km^3/a (Chen et al., 2008). During 2003 and 2004, it carried about 2.83×10^9 kg of particulate OC to the East China Sea, of which 76% was transported during the flood season (Lin et al., 2007), which may also result in non-steady state deposition in coastal environments. However, the relationship between flood events and sediment composition and/or depositional history is poorly understood in the Changjiang Basin and coastal environment in the East China Sea. Previous studies have used geochemical and bulk parameters from core sediments to reconstruct flood events in the Changjiang Basin. Wang et al. (2011) analyzed multiple elements in a core from the subaqueous delta of the Changjiang River Estuary, and reconstructed the 600-a flood history of the basin between 1350 and 1950. Zhan et al. (2010) analyzed grain size and bulk OC profiles in a core sampled from a central bar, and concluded that human activities in the previous 50 years had disturbed flood deposit layers. However, few studies have used lignin phenols as tools for flood reconstruction in the Changjiang drainage basin.

The Lake Tian E Zhou (TEZ) is in the middle of the Changjiang River, with a catchment area of 68.7 km^2 and with mean water coverage of 18.97 km^2. It was formed in 1972 when the Chang-

Foundation item: The National Natural Science Foundation of China under contract Nos 41021064, 41276081 and 41606211; the 111 Project under contract No. B08022; the Scientific Research Fund of Second Institute of Oceanography, MNR under contract No. JG1806.

*Corresponding author, E-mail: wuying@sklec.ecnu.edu.cn

jiang Channel was rerouted and straightened. Historically, its lower section was always connected to the river. However, the flow was disconnected after the extreme flood event in 1998. After the 1998 flood, the local government built a dam to control the water level of the lake (Fig. 1). Prior to 1998, during floods the river transported massive amounts of sediment and organic carbon (OC) to the oxbow lake. Hence, sediment and OC burial in the lake might preserve signals from flood events.

Fig. 1. Location of the TEZ core (29.78°N, 112.56°E) from the oxbow lake in Hubei Province, China (a) and the sedimentary phase of the core (b).

While some studies have been successful in reconstructing flood events from cores, using parameters such as bulk organic matter (OM) content and grain size composition (Wang et al., 2011; Zhan et al., 2010), few studies have used biomarkers in reconstructing these events (Bianchi et al., 2015). Lignin phenols are useful biomarkers for tracing terrigenous OC from river to ocean (Hedges et al., 1997). A series of proxies based on lignin phenols could provide detailed information on the content, source and degradations state of terrestrial OC. During floods, loading of lignin is usually much higher under normal hydrodynamic conditions, due to strong water scouring, and the lignin is fresher (Dhillon and Inamdar, 2013). While the distinction of lignin phenols between different hydrological conditions is valuable for tracing OM transportation by floods, its application is limited in coastal oceanic environments due to the unstable depositional environment and low sedimentation rate. The characteristics of lignin phenols have the potential to provide accurate flood records in core sediments from stable depositional environments within a river basin, which are not subjected to any bias from long distance transport and resuspension or reworking in the dynamic coastal zone.

In this study, a sediment core was collected from the lake in April 2007 (Fig. 1). Grain size, stable isotopic and radio organic carbon ($\delta^{13}C$ and $\Delta^{14}C$), OC%, TN% and lignin phenols at different depths in the core were analyzed along with excess lead-210. The main goal was to investigate the sedimentology and geochemical profiles, in order to determine if these parameters could be used as an approach to trace historic floods in the Changjiang Basin.

2 Materials and methods

2.1 *Sample collection*

The core (a total length of 70 cm) was collected from the lake in Hubei Province, during April 2007 (29.78°N, 112.56°E; Fig. 1). The sampling location was on the shore, 2 m from the water's edge, in an area that is submerged during the wet season. The core was collected using a plastic pipe (diameter 10 cm) and was kept in a cold ice chest during transport to the laboratory, where it was cut into sections (1 cm intervals) which were then dried in an oven at 50°C.

2.2 *Chronology*

Excess ^{210}Pb was measured using an HPGe gamma-ray detector (Canberra Be3830). Dried samples were sealed in plastic boxes (Φ35 mm×35 mm) for three weeks to establish a secular equilibrium between ^{226}Ra and its daughter products, ^{214}Pb and ^{214}Bi. The activity of total ^{210}Pb was directly determined at 46.3 keV (refs). The ^{226}Ra activity was determined at 295.2 keV, and ^{214}Pb at 351.9 keV, and ^{214}Bi at 609.3 keV (46.1%) and 1 120.3 keV (15%). Excess ^{210}Pb activity was estimated by subtracting the ^{226}Ra activity from the total ^{210}Pb activity. Detector efficiencies and sample geometry were calibrated using efficiency curves obtained from LabSOCS (Bronson, 2003).

2.3 *Grain size analysis*

Sediment grain size was determined with a laser particle size analyzer (Coulter-LS100Q, Berkman Coulter Corporation, USA) that was used to divide each sample into 93 size fractions

between 0.2 μm and 2×10^3 μm. The chemical pretreatment procedure followed Luo et al. (2012), and mean grain diameter, along with the relative proportions of clay, silt and sand are reported here. The clay, silt and sand particles are defined here as <4, 4–63 and >63 μm, respectively (Trefethen, 1950).

2.4 *Bulk chemical analysis (OC%, TN%, δ^{13}C and Δ^{14}C)*

The samples were acidified with 1 mol/L HCl to remove inorganic carbon prior to measurements of OC and δ^{13}C. TN was measured directly in samples that had not been treated with acid. OC and TN were measured with an elemental analyzer (CHNOS Vario EL III) and δ^{13}C values using isotope ratio mass spectrometry (IRMS; Delta Plus XP, Thermo Finnigan). The relative standard deviation (RSD) for OC and TN values was <3%. δ^{13}C values were calculated:

$$\delta^{13}\mathrm{C} = \left(\frac{R_{\mathrm{sample}}}{R_{\mathrm{standard}}} - 1\right) \times 1\,000, \tag{1}$$

where R is the molar ratio of ^{13}C and ^{12}C. Vienna Peedee Belemnite (V-PDB) was used as the standard. The precision was less than 0.1‰.

Radiocarbon (Δ^{14}C) analysis was performed at the National Ocean Sciences Accelerator Mass Spectrometry (AMS) facility at Woods Hole Oceanographic Institution. The sediment, after removal of inorganic carbon, was combusted to CO_2, which was converted to graphite via Fe/H_2 catalytic reduction. The graphite was analyzed to obtain the radiocarbon composition from AMS. Radiocarbon values were expressed as Δ^{14}C in ‰, which was calculated:

$$\delta^{14}\mathrm{C} = \left(\frac{R_{\mathrm{sample}}}{R_{\mathrm{standard}}} - 1\right) \times 1\,000, \tag{2}$$

where R is the molar ratio of ^{14}C and ^{12}C.

$$\Delta^{14}\mathrm{C} = \delta^{14}\mathrm{C} - 2(\delta^{13}\mathrm{C} + 25) \times \left(1 + \frac{\delta^{14}\mathrm{C}}{1\,000}\right). \tag{3}$$

The general paradigm is that a more depleted value of Δ^{14}C means the older the organic carbon.

2.5 *Lignin phenols analysis*

Lignin phenols were analyzed following the alkaline CuO oxidation method (Hedges and Mann, 1979a, b). Dried and ground sediment was placed into a PTFE mini-bomb and digested with CuO and $Fe(NH_4)_2(SO_4)_2$ in 2 mol/L NaOH in the absence of O_2 at 160°C for 3 h. After cooling to room temperature, ethyl vanillin was added as a recovery standard, followed by 37% HCl to adjust the pH to <2. The reaction products were extracted with ethyl acetate (EtOAc), dried and converted to trimethylsilyl derivatives using 99% Bis(trimethylsilyl)trifluoroacetamide (BSTFA)+1% Trimethylchlorosilane (TMCS). Lignin phenols were then analyzed using gas chromatography (GC; Agilent 6890 series) equipped with a DB-1 column (i.d. 30 m×0.25 mm; film thickness 0.25 μm) and a flame ionization detector. The oven temperature was set at 100°C, then increased to 270°C (held 12.5 min) at 4°C/min. Σ8 and Λ8 are reported as the sum of eight phenolic products normalized to 10 g dry weight (dw) sediment and 100 mg OC, respectively. The 3, 5-BD (3, 5-dihydroxybenzoic acid, an additional CuO oxidation product that can be used as an indicator of soil degradation, was determined and normalized to OC (Farella et al., 2001; Hedges and Mann, 1979a, b). The PON/P ratio was used to trace the contribution of vascular plants because p-hydroxy acetophenone (PON) is derived mainly from plants, while the remaining two p-hydroxy phenol phenols (PAL+PAD) are typically derived from proteins and saccharides. The ratios of cinnamyl and syringyl phenols to the vanillyl phenols (C/V and S/V) were used to trace the different sources of lignin phenols. The lignin phenol vegetation index (LPVI) was calculated as follows:

$$\mathrm{LPVI} = \left[\frac{S(S+1)}{V+1} + 1\right] \times \left[\frac{C(C+1)}{V+1} + 1\right], \tag{4}$$

where V, S and C were expressed in % of the Λ8. The data were used in further identifying the source of lignin phenols (Tareq et al., 2004). The acidic to aldehyde group of vanillyl phenols [(Ad/Al)v] was employed as an indicator of lignin degradation.

2.6 *Statistical analysis*

Pearson analysis was used to test the correlation between different parameters. An independent t-test was conducted to compare the mean values of parameters for flood layers and normal layers, and Levene's test was used to examine the homogeneity of variance. All the analyses were performed using SPSS 20.0 for Windows (SPSS IBM, USA).

3 Results

3.1 *Sedimentation rate*

The sedimentation rate for the core was determined using ^{210}Pb geochronology. As shown in Fig. 2, the excess ^{210}Pb declined with depth, the rate of decline varying between the 0–24 cm and 26–70 cm sections of the core. The variation between the two sections would usually be ascribed to hydrodynamic variations and/or human interference. We divided the core into two parts and calculated the sedimentation rate using the constant activity model (CA) in each part. The rate was 2.83 cm/a in the upper 0–24 cm section and 0.74 cm/a in the 26–76 cm section. Based on these rates, the core represents sediment deposit in the lake between 1942 and 2007. The variation in sediment rate between 0–24 cm and 26–76 cm might be caused by the dam building in the lower section. Before the dam building, in the wet season, the Changjiang River carried sediments to the sampling station, and these sediments represented the signals of the hydrologic regime of the river. However, the sediment core of 0–24 cm was deposit massively after the dam building, which recorded the regional environmental change.

3.2 *Core description and grain size*

The core consisted of yellow, yellow grey, and grey sediments (Fig. 1). The 0–40 cm and 55–68 cm sections were mainly yellow and yellow grey, but in the other sections the sediment was predominantly grey. The 24–26 cm section contained some plant tissues, which might indicate that strong hydrodynamic conditions prevailed during that time period. As shown in Fig. 3, the mean grain size varied with depth. Between the 0 and 24 cm, sediment grain size was mostly in the 4.3 to 5.0 μm and that increased to the 5.7–7.4 μm size range in the depth of 40 cm. Sediment grain size continued to increase with depth between 40 and 55 cm, and then steadily decreased until the depth of 68–70 cm, where sediment abruptly changed to sand-sized grains. The proportions of clay, silt and sand also varied sharply with depth along the core

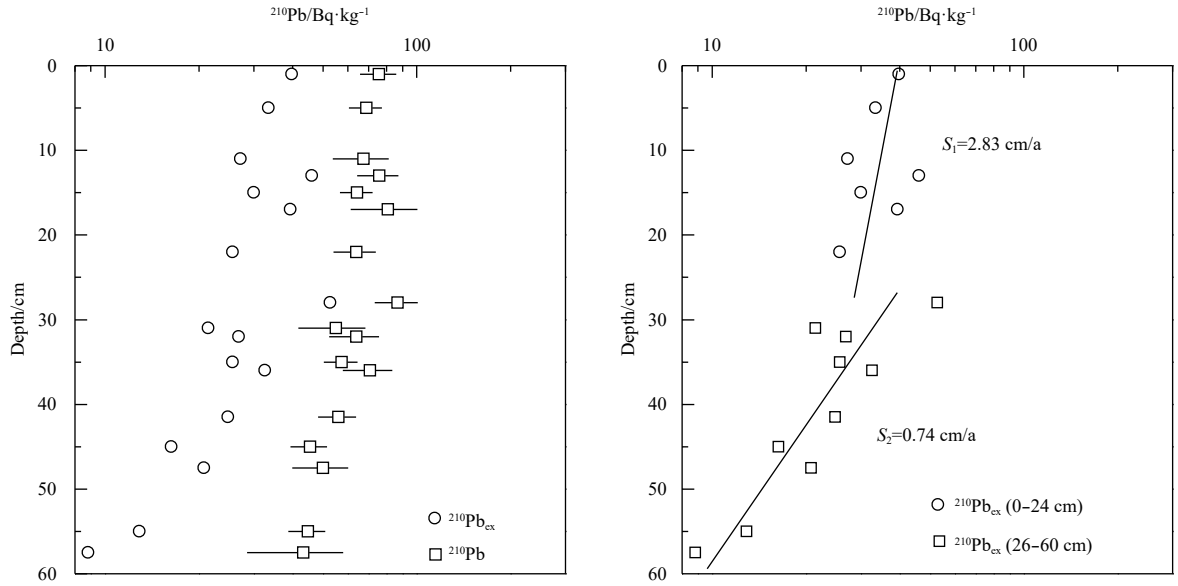

Fig. 2. ^{210}Pb profiles along the TEZ core.

(Fig. 3). The proportions in clay and silt were inversely correlated in all layers, except the 68–70 cm layer, where a negative correlation was observed between them (r^2=0.85, p<0.001). Sand was absent between the 0–26 cm, but was present at a nearly constant percentage in the 26–68 cm section; the maximum proportion of sand was at a depth of 68–70 cm. The absence of sand between 0 and 26 cm indicated that the construction of the dam had changed the hydrological conditions and sediment sources in the lake (Fig. 1).

3.3 *Bulk properties (OC, TN, δ^{13}C and Δ^{14}C)*

The OC% value varied from 0.22% to 3.13% with an average of 0.85% (Fig. 4). The 68–70 cm layer had the lowest value, while the highest was measured at 24–26 cm. The average value of TN% was 0.09%, with a range of 0.02%–0.33%. As with the OC profile, the lowest and highest TN% values were observed at 68–70 cm and 24–26 cm, respectively. The C/N ratio was calculated as the ratio of organic carbon to total nitrogen by mole. In the core, C/N varied from 9.6 to 17.2 (average 11.3). The variations in OC and TN along the core had a similar trend, and there was a positive correlation between them (r^2=0.95, p<0.001, Fig. 5). δ^{13}C ranged from –29.4‰ to –23.0‰, with the lowest value at the 24–26 cm, indicating different OC sources with depth. Three samples were selected (0–1 cm, 24–26 cm and 68–69 cm) for measuring Δ^{14}C and results are shown in Fig. 4. The youngest OC appeared at the 24–26 cm, with a Δ^{14}C value of –7.4‰. The surface layer (0–1 cm) and the bottom layer (68–69 cm) both had more depleted Δ^{14}C values than the middle layer between 24–26 cm (Fig. 4).

3.4 *Lignin phenols*

The lignin phenols (Σ8 and Λ8) varied analogously with OC% and TN% throughout the core (Fig. 6). As expected, the 24–26 cm layer contained the highest concentration of lignin phenols and the 68–70 cm layer the lowest. The 3, 5-BD is produced from plants by bacteria in soil and can be used as an indicator of soil OC input (Dittmar et al., 2001). In the core, the trend of 3, 5-BD was comparable to the trends of OC% and lignin content. The 24–26 cm layer had the highest concentration of 3, 5-BD, indicating a significant amount of soil-derived OC. PON/P was employed to distinguish the signals of OC from fresh plants (Dittmar et al., 2001). There were several extremely high values of PON/P (Fig. 6). The highest values of C/V, S/V and LPVI were observed in the 24–26 cm layer, and the lowest appeared between 68–70 cm; there were no significant changes in the remainder of the core. The variation in (Ad/Al)v with depth showed an opposite compared to those for Σ8 and Λ8. The highest (Ad/Al)v value was observed at the 68–70 cm depth, which also has the lowest lignin content. The lowest (Ad/Al)v value was at 24–26 cm, which has the highest concentration of lignin phenols.

4 Discussion

4.1 *Record of 1998 flood in the core*

All available parameters measured from the TEZ sediment core (Fig. 1) pointed to a typical flood deposit in the 24–26 cm layer, which corresponded to the 1998 flood. The organic geochemistry data also support this inference. During field sampling, a large amount of plant tissue was observed in the 24–26 cm layer and, despite removing the tissue prior to chemical analysis, OC%, TN%, δ^{13}C and lignin phenols were all significantly different in the 24–26 cm layer vs. other layers (Figs 4 and 6). OC and TN values in the 24–26 cm layer were three times higher than the average values for the rest of the core. High values of OC% and TN% in flood layers have also been reported for a core collected from a newly-emerged bar in the lower Changjiang River in 2010 (Zhan et al., 2010). The δ^{13}C value at 24–26 cm layer was as low as –29.4‰, which is significantly more depleted than the values measured for other layers (t-test, p<0.05). Most of the plants around the Changjiang River use the Calvin cycle (C3) to absorb CO_2 and have depleted δ^{13}C values (–26‰ to –32‰, Still et al., 2003; Wu et al., 2007). Although soil carbon is derived from fresh plants, its δ^{13}C value is more positive than that of plants due to biodegradation. In the Changjiang Basin, the δ^{13}C of soil organic carbon varies from –20‰ to –24‰ (Yu et al., 2011). The δ^{13}C value for the 24–26 cm layer is within the range for fresh plants, but lower than the range reported for soils. Thus, the depleted δ^{13}C values in the 24–26 cm layer indicates that fresh plant tissue contributes significantly to the OC in this layer. This is in accord

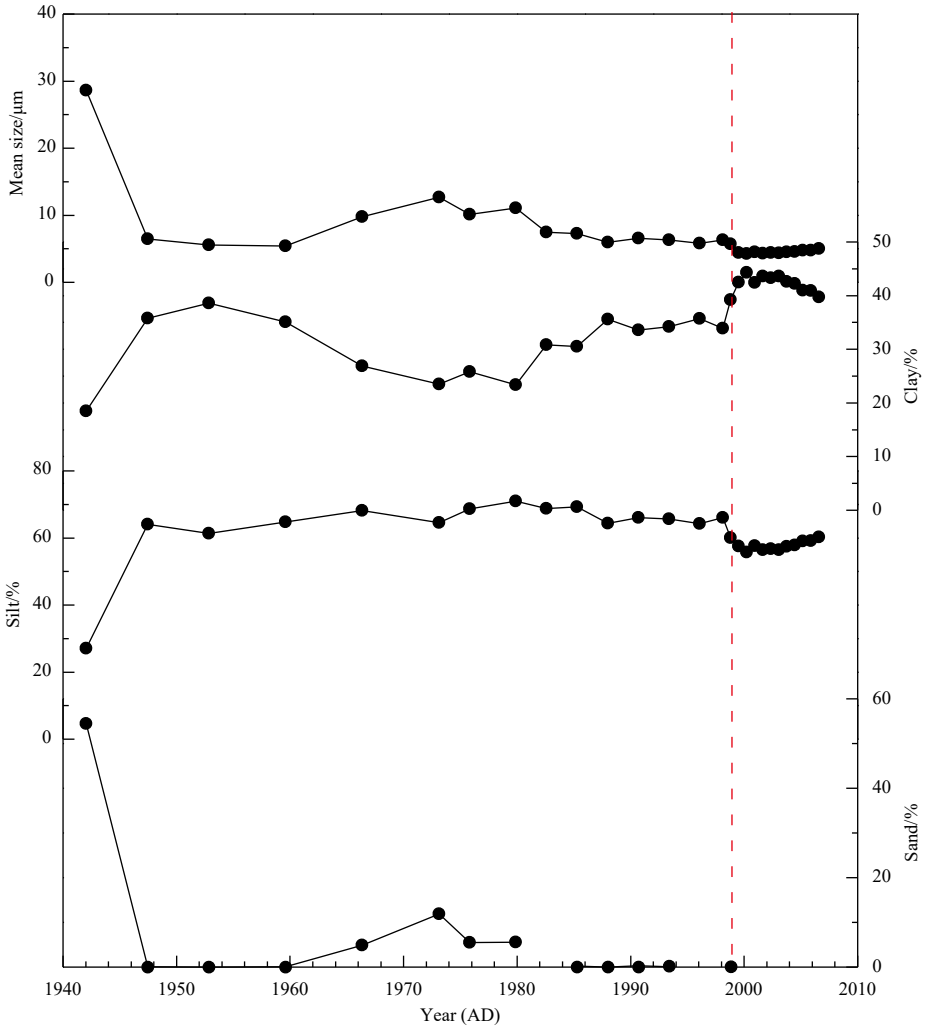

Fig. 3. Grain size distribution in the TEZ core. Red dashed line refers to the time of dam building in the lower estuary of the TEZ oxbow lake.

with observations that flood deposits typically contain OC from fresh plant tissue (Zhan et al., 2010). The $\Delta^{14}C$ value can be used as an indicator of the age of OC. A more depleted $\Delta^{14}C$ means the older the OC. Different source OCs contain different $\Delta^{14}C$, such that the $\Delta^{14}C$ of fresh plant tissues is greater than 0, but the value of fossil OC is less than –1 000 (Hedges et al., 1997). For the three sediment layers of the core, the $\Delta^{14}C$-OC in the 24–26 cm was most enriched (Fig. 4), and the converted OC age of this layer was about 5 a BP. The distinction in bulk properties between 24–26 cm and other layers implies that this layer contains much fresh, supported by higher $\Delta^{14}C$ and lower $\delta^{13}C$ values, and a high content of OC, which might be transported by the extreme heavy flood in 1998. The difference in bulk properties between the 24–26 cm layer and other layers implies that this layer contains a large amount of fresh OC that might have been transported by the extreme flood in 1998.

The content and composition of lignin phenols are also distinct in the 24–26 cm section. As shown in Fig. 6, the Σ8 and Λ8 are eight times and one time higher in this layer than in other layers, respectively; they are also higher than the values of surrounding soils in the Changjiang Basin (Yu et al., 2011). According to the *t*-test, both Σ8 and Λ8 in the 24–26 cm layer are significantly different from other layers (both $p<0.05$). C/V and S/V in the 24–26 cm layer are 1.51 and 0.28, respectively, significantly higher than the average values for other layers (*t*-test: both $p<0.05$; Fig. 6). The ranges of C/V and S/V values in the 24–26 cm layer indicate an elevated contribution from non-woody angiosperms. The results suggest that C/V and S/V were strongly influenced by biodegradation processes in soil. Degradation by fungi in soil would decrease the contents of C, S and V group phenols, with the degradation preference C>S>V. This difference in degradation rate results in a decrease in C/V and S/V. In the core, the distinct C/V and S/V values in the 24–26 cm layer also indicate that a relatively large amount of fresh plant tissue is present in this layer. Similar to C/V and S/V, the LPVI value in the 24–26 cm layer is much higher than that in other layers (Fig. 6). The acid to aldehyde ratio of the V group of phenols [(Ad/Al)v] is an index reflecting the degree of degradation of lignin. In the 24–26 cm layer, the (Ad/Al)v value is 0.20, which falls within the range of fresh plant tissue and is significantly lower than the mean value for the other layers (0.47±0.11, Yu et al., 2011). Low (Ad/Al)v value indicates that the flood carried a large quantity of fresh plant tissues to the location of the TEZ core. The 3, 5-BD is another CuO oxidation product that originates from soil OC. The concentration of the 3, 5-BD in the 24–26 cm layer is higher than that in the other layers, indicating that this layer contains abundant soil-derived

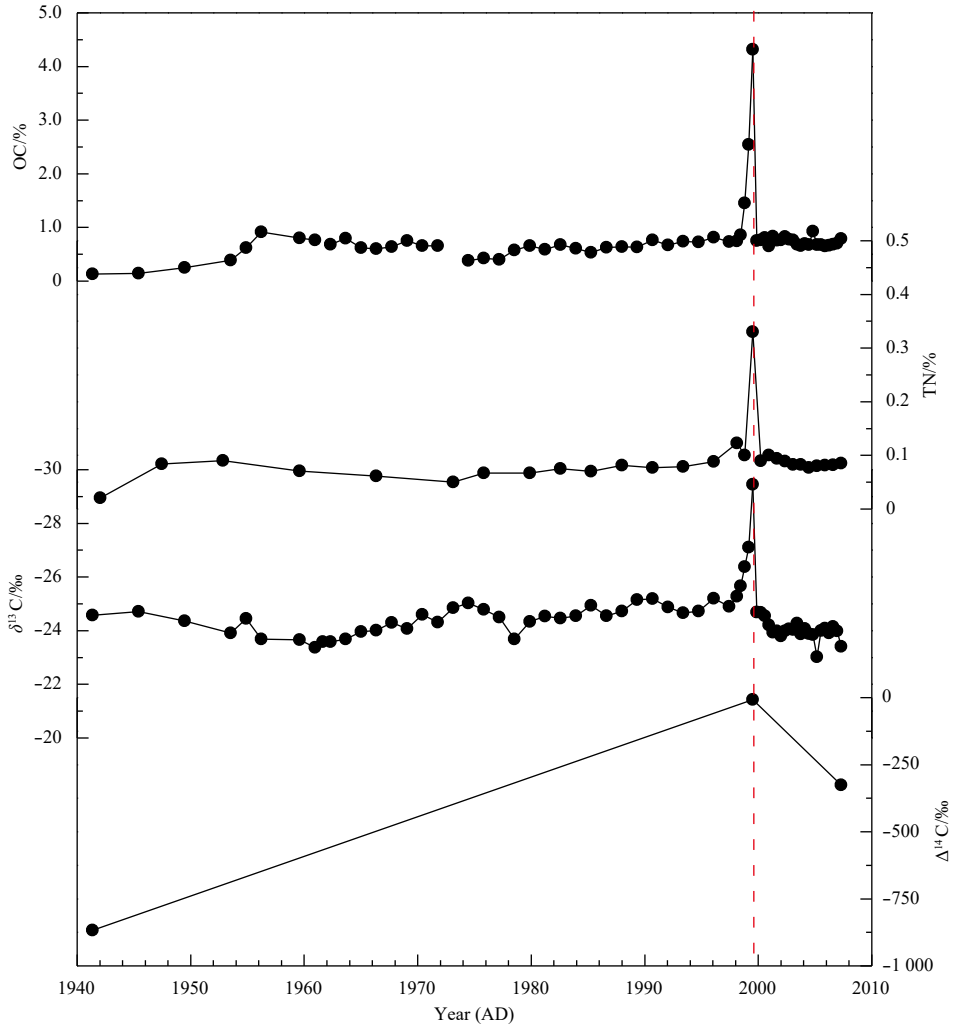

Fig. 4. Bulk properties along the TEZ core. Red dashed line refers to the flood deposit of 1998.

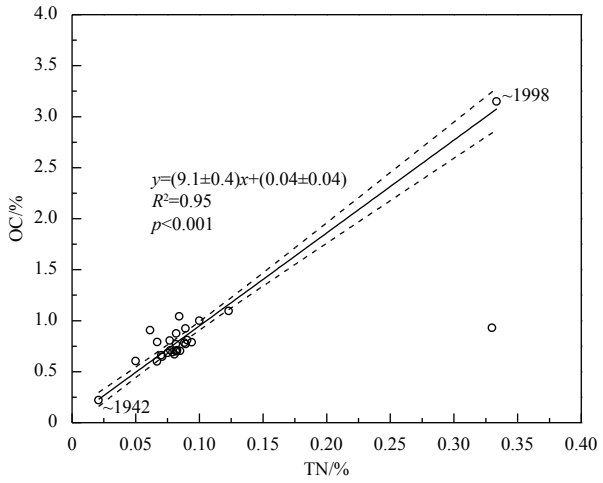

Fig. 5. Correlation between OC and TN. Unbroken and dashed lines refer to linear regression and 95% confidence band.

OC. PON is the ketone group of P phenols, which originate from the degradation of lignin. PAL and PAD are the other two phenols of the P group and are usually derived from protein. The PON/P ratio is defined as the percentage of PON relative to the total P phenols. A high PON/P value implies a high contribution of plant-derived OC (Dittmar et al., 2001). In the 24–26 cm layer, PON/P is higher than that in other layers, and several layers below the 24–26 cm also show high values (Fig. 6). The high value of PON/P in the 24–26 cm layer suggests that the 1998 flood transported a large amount of plant-derived OC to the TEZ oxbow lake. In the 24–26 cm layer, all the organic geochemistry indices are significantly different from those in other layers. This clearly indicates that this layer contained materials mostly from flood deposit. With reference to the sediment chronology and flood record in the Changjiang Basin (Shi et al., 2004), it can be inferred that this layer was deposited during the flood of 1998.

Due to the construction of a dam in the lower estuary of the oxbow lake (Fig. 1), the sediment profiles of TEZ did not prominently show flood events since 1998. The flood events in the Changjiang Basin, according the Shi et al. (2004), are listed in Table 1, while Fig. 6 (red dashed lines) shows the sections of the TEZ core in which the geochemical parameters are significantly different from adjacent layers. Based on sediment chronology derived from ^{210}Pb depth profiles, the layers shown in Fig. 6 are related to the flood events of 1949, 1954, 1969, 1980–1983, 1991 and 1998, respectively. The 2–3 year differences between some individual flood events and historical documents may be the results of analytical errors from the ^{210}Pb dating or unstable hydrological con-

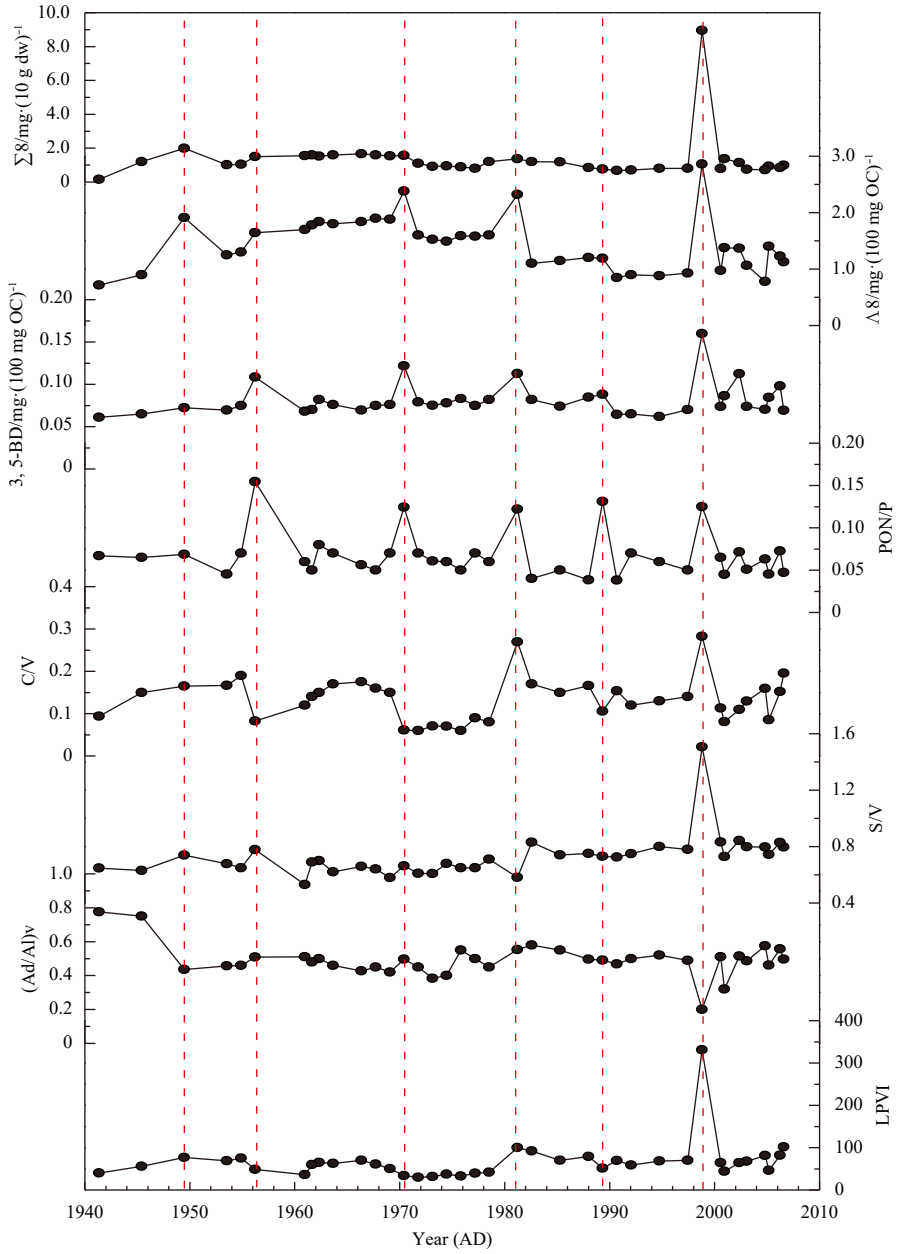

Fig. 6. Lignin-derived phenol profiles along TEZ core. Red dashed lines represent the six flood deposits in the past 70 years, which occur around 1949, 1954, 1969, 1980–1983, 1991, and 1998, respectively.

ditions (Zhan et al., 2010). Except for the 24–26 cm layer, the Λ8, 3, 5-BD and PON/P parameters are the most prominent indictors of flood events. The high values clearly indicate an increase in the contribution of plant and soil OC to these layers. During flood events, the high-water level and rapid water flow would erode surface soil, and transport large quantities of fresh plants and soil OC to the sampling sites. Hence, the Λ8, 3, 5-BD and PON/P values are higher in layers deposited during floods than in non-flood layers. This characteristic of flood deposits has also been observed in the Changjiang River Estuary. We also investigated the lignin profiles of a core (E4) sampled in the subaqueous delta of the estuary and found that annual sediment discharge was the main factor controlling lignin content in the core. In the E4 core, high precipitation indeed corresponded to high lignin content and, as a result, the E4 core provides a record of flood events in the Changjiang Basin. These results support the notion that lignin phenol concentrations and component ratios are a suitable proxy for flood deposits in sediments.

4.2 *Characteristics of flood deposits*

By comparing the 1998 flood deposit with other layers with or without flood events in the core, distinct differences among these layers can be identified. As shown in Fig. 7 and Table 2 based on statistics, the grain composition shows an abrupt change at the 24–26 cm layer (Fig. 3). Above this layer, sand is absent from the core and the proportion of clay is relatively high. This is consistent with the local hydrodynamic variations, whereby the construction of a dam has prevented sand from reaching the sampling location (Jia et al., 2015). The grain size profile shows no difference between flood and non-flood layers, in contrast to those

Table 1. Recognized flood events in Changjiang Basin during 1940–2007 (Shi et al., 2004)

Year	Area	Level	Layer in TEZ core
1998	the whole stream	heavy flood	24–26 cm
1991	middle and low stream	flood	33–34 cm
1980–1983	middle and low stream	flood	39–40 cm
1969	middle and low stream	flood	47–48 cm
1954	the whole stream	heavy flood	57–58 cm
1949	middle and low stream	flood	62–63 cm

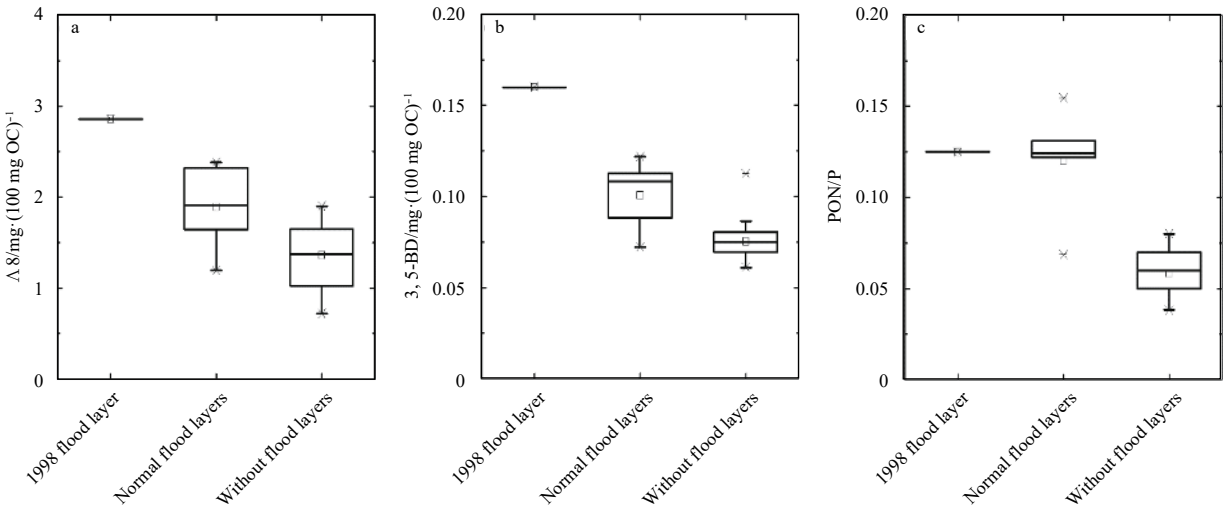

Fig. 7. Λ8 (a), 3, 5-BD (b) and PON/P (c) in different types of deposits in the TEZ core.

Table 2. The *t*-test results between three different type deposits (at 95% confidence interval)

	Flood at 1998 vs. no flood layers	Floods without 1998 vs. no flood layers	Flood at 1998 vs. floods without 1998
Grain size	$p>0.05$	$p>0.05$	$p>0.05$
OC%	$p<0.05$	$p>0.05$	$p>0.05$
TN%	$p<0.05$	$p>0.05$	$p>0.05$
δ^{13}C/‰	$p<0.05$	$p>0.05$	$p<0.05$
Σ8/mg·(10 g)$^{-1}$	$p<0.05$	$p>0.05$	$p<0.05$
Λ8/mg·(100 mg)$^{-1}$	$p<0.05$	$p<0.05$	$p>0.05$
3, 5-BD/mg·(100 mg)$^{-1}$	$p<0.05$	$p<0.05$	$p>0.05$
S/V	$p<0.05$	$p>0.05$	$p<0.05$
C/V	$p<0.05$	$p>0.05$	$p>0.05$
(Ad/Al)v	$p<0.05$	$p>0.05$	$p<0.05$
PON/P	$p<0.05$	$p<0.05$	$p>0.05$
LPVI	$p<0.05$	$p>0.05$	$p<0.05$

reported by Zhan et al. (2010), who observed a relationship between grain size and flood events. Secondly, the organic parameters observed in the other flood deposit layers are less distinct than in the 24–26 cm layer (Fig. 7, Table 2). Notably, Σ8, C/V, S/V, LPVI and (Ad/Al)v are considerably more pronounced in the 24–26 cm flood layer. However, the flood layers at depths below 26 cm all have comparable values of Σ8, C/V, S/V, LPVI and (Ad/Al)v. This might reflect two factors. First, the dam construction in the lower estuary of the oxbow lake in 1999 cut off the lake's seasonal connection to the main stream of the Changjiang River, thereby altering the hydrodynamic conditions of the lake. Prior to 1998, deposition and erosion were apparently in balance with each other, and each wet season flow to the lake would erode the low-density material from previous flood deposits. This low-density material contains the highest proportion of OC and fresh lignin (Ertel and Hedges, 1985). As a result of the removal of material, the flood deposits prior to 1998 did not contain as high level of OM as observed for the 1998 flood deposit. This mechanism resulted in the similar values of Σ8, C/V, S/V, LPVI and (Ad/Al)v in all of the flood layers observed at depths below 24–26 cm. Second, the degradation of OM over time may have contributed to the lower OM content in the older flood deposits, observed in the core below the 1998 deposit. The area surrounding the core was only covered seasonally with water, in which microorganisms would quickly degrade lignin. Feng and Simpson (2007) reported that the OM in subsoil was quickly and efficiently degraded in a vertical soil profile of Alberta grassland soil. This biodegradation may lead to the low lignin concentration in the flood deposits that formed prior to 1998.

5 Conclusions

From the investigation of depth profiles in the TEZ core, the following main conclusions can be made. First, grain size did not seem to be related to flood events in the core, even though floods would generally be expected to transport a larger quantity of coarse particles to the lake. Second, the extreme flood event of 1998 is clearly preserved by the organic indices, such as elevated concentrations of OC, TN and lignin phenols, in addition to lowest value of δ^{13}C. However, these parameters are less sensitive in identifying other floods events preserved in the core. Further, the PON/P, 3, 5-BD concentration and lignin phenols (normalized to OC), on the other hand, are clear markers of all flood events in the middle of the Changjiang River. Our results reported here have extended the application of lignin phenols as compelling markers to the reconstruction of extreme flood events in the river

basin and likely coastal marine environments.

Acknowledgements

We thank Tim I. Eglinton and his colleague for their help in the radiocarbon analysis.

References

Bianchi T S, Galy V, Rosenheim B E, et al. 2015. Paleoreconstruction of organic carbon inputs to an oxbow lake in the Mississippi River watershed: effects of dam construction and land use change on regional inputs. Geophysical Research Letters, 42(19): 7983–7991, doi: 10.1002/2015GL065595

Bianchi T S, Garcia-Tigreros F, Yvon-Lewis S A, et al. 2013. Enhanced transfer of terrestrially derived carbon to the atmosphere in a flooding event. Geophysical Research Letters, 40(1): 116–122, doi: 10.1029/2012GL054145

Bronson F. 2003. Validation of the accuracy of the LabSOCS software for mathematical efficiency calibration of Ge detectors for typical laboratory samples. Journal of Radioanalytical and Nuclear Chemistry, 255(1): 137–141, doi: 10.1023/A:1022248318741

Chen C T A, Zhai Weidong, Dai Minhan. 2008. Riverine input and air–sea CO_2 exchanges near the Changjiang (Yangtze River) Estuary: status quo and implication on possible future changes in metabolic status. Continental Shelf Research, 28(12): 1476–1482, doi: 10.1016/j.csr.2007.10.013

Dalzell B J, Filley T R, Harbor J M. 2005. Flood pulse influences on terrestrial organic matter export from an agricultural watershed. Journal of Geophysical Research, 110(G2): G02011, doi: 10.1029/2005JG000043

Dhillon G S, Inamdar S. 2013. Extreme storms and changes in particulate and dissolved organic carbon in runoff: entering uncharted waters?. Geophysical Research Letters, 40(7): 1322–1327, doi: 10.1002/grl.50306

Dittmar T, Lara R J, Kattner G. 2001. River or mangrove? Tracing major organic matter sources in tropical Brazilian coastal waters. Marine Chemistry, 73(3–4): 253–271

Ertel J R, Hedges J I. 1985. Sources of sedimentary humic substances: vascular plant debris. Geochimica et Cosmochimica Acta, 49(10): 2097–2107, doi: 10.1016/0016-7037(85)90067-5

Falkowski P, Scholes R J, Boyle E, et al. 2000. The global carbon cycle: a test of our knowledge of earth as a system. Science, 290(5490): 291–296, doi: 10.1126/science.290.5490.291

Farella N, Lucotte M, Louchouarn P, et al. 2001. Deforestation modifying terrestrial organic transport in the Rio Tapajós, Brazilian Amazon. Organic Geochemistry, 32(12): 1443–1458, doi: 10.1016/S0146-6380(01)00103-6

Feng Xiaojuan, Simpson M J. 2007. The distribution and degradation of biomarkers in Alberta grassland soil profiles. Organic Geochemistry, 38(9): 1558–1570, doi: 10.1016/j.orggeochem.2007.05.001

Hedges J I, Keil R G, Benner R. 1997. What happens to terrestrial organic matter in the ocean?. Organic Geochemistry, 27(5–6): 195–212

Hedges J I, Mann D C. 1979a. The characterization of plant tissues by their lignin oxidation products. Geochimica et Cosmochimica Acta, 43(11): 1803–1807, doi: 10.1016/0016-7037(79)90028-0

Hedges J I, Mann D C. 1979b. The lignin geochemistry of marine sediments from the southern Washington coast. Geochimica et Cosmochimica Acta, 43(11): 1809–1818, doi: 10.1016/0016-7037(79)90029-2

Jia Tiefei, Wang Feng, Yuan Shifei. 2015. Oxbow lake sedimentary characteristics and their environmental significance in Tianezhou and Zhongzhouzi lakes in the middle Yangtze River. Geographical Research (in Chinese), 34(5): 861–871

Korponai J, Gyulai I, Braun M, et al. 2016. Reconstruction of flood events in an oxbow lake (Marótzugi-Holt-Tisza, NE Hungary) by using subfossil cladoceran remains and sediments. Advances in Oceanography and Limnology, 7(2): 125–135

Lin Jing, Wu Ying, Zhang Jing, et al. 2007. Seasonal variation of organic carbon fluxes in the Yangtze River and influence of Three-Gorges engineering. China Environmental Science (in Chinese), 27(2): 246–249

Luo Xiangxing, Yang Shilun, Zhang Jing. 2012. The impact of the Three Gorges Dam on the downstream distribution and texture of sediments along the middle and lower Yangtze River (Changjiang) and its estuary, and subsequent sediment dispersal in the East China Sea. Geomorphology, 179: 126–140, doi: 10.1016/j.geomorph.2012.05.034

Shi Yafeng, Jiang Tong, Su Buda, et al. 2004. Preliminary analysis on the relation between the evolution of heavy floods in the yangtze river catchment and the climate changes since 1840. Journal of Lake Sciences (in Chinese), 16(4): 289–297, doi: 10.18307/2004.0401

Still C J, Berry J A, Collatz G J, et al. 2003. Global distribution of C_3 and C_4 vegetation: carbon cycle implications. Global Biogeochemical Cycles, 17(1): 1006, doi: 10.1029/2001GB001807

Tareq S M, Tanaka N, Ohta K. 2004. Biomarker signature in tropical wetland: lignin phenol vegetation index (LPVI) and its implications for reconstructing the paleoenvironment. Science of the Total Environment, 324(1–3): 91–103

Trefethen J M. 1950. Classification of sediments. American Journal of Science, 248: 55–62, doi: 10.2475/ajs.248.1.55

van Metre P C, Horowitz A J. 2013. An 80-year record of sediment quality in the lower Mississippi River. Hydrological Processes, 27(17): 2438–2448, doi: 10.1002/hyp.9336

Wang Jianjun, Chen Liqi, Li Li, et al. 2014. Preliminary identification of palaeofloods with the alkane ratio C_{31}/C_{17} and their potential link to global climate changes. Scientific Reports, 4: 6502

Wang Minjie, Zheng Hongbo, Xie Xin, et al. 2011. A 600-year flood history in the Yangtze River drainage: comparison between a subaqueous delta and historical records. Chinese Science Bulletin, 56(2): 188–195, doi: 10.1007/s11434-010-4212-2

Wu Y, Zhang J, Liu S M, et al. 2007. Sources and distribution of carbon within the Yangtze River system. Estuarine, Coastal and Shelf Science, 71(1–2): 13–25

Yu Hao, Wu Ying, Zhang Jing, et al. 2011. Impact of extreme drought and the Three Gorges Dam on transport of particulate terrestrial organic carbon in the Changjiang (Yangtze) River. Journal of Geophysical Research, 116(F4): F04029, doi: 10.1029/2011JF002012

Zhan Wang, Yang Shouye, Liu Xiaoli, et al. 2010. Reconstruction of flood events over the last 150 years in the lower reaches of the Changjiang River. Chinese Science Bulletin, 55(21): 2268–2274, doi: 10.1007/s11434-010-3263-8

Acta Oceanol. Sin., 2020, Vol. 39, No. 4, P. 42–56
https://doi.org/10.1007/s13131-020-1535-y
http://www.hyxb.org.cn
E-mail: hyxbe@263.net

Vertical variations in the bio-optical properties of seawater in the northern South China Sea during summer 2008

Guifen Wang[1]*, Wen Zhou[2], Zhantang Xu[2], Wenlong Xu[1], Yuezhong Yang[2], Wenxi Cao[2]

[1] College of Oceanography, Hohai University, Nanjing 210098, China

[2] State Key Laboratory of Tropical Oceanography, South China Sea Institute of Oceanology, Chinese Academy of Sciences, Guangzhou 510301, China

Received 28 January 2019; accepted 27 May 2019

Abstract

Vertical variability in the bio-optical properties of seawater in the northern South China Sea (NSCS) including inherent optical properties (IOPs) and chlorophyll *a* concentration (*Chl*) were studied on the basis of *in situ* data collected in summer 2008 using an absorption/attenuation spectrophotometer. An empirical model was developed to estimate *Chl* profiles based on the absorption line height at long wavelengths, with a relative root mean square error of 37.03%. Bio-optical properties exhibited large horizontal and vertical spatial variability. As influenced by coastal upwelling and the Zhujiang River (Pearl River) discharge, both IOPs and *Chl* exhibited high values in the surface waters of the inner shelf, which tended to decrease with distance offshore. Subsurface maximum layers of IOPs and *Chl* were observed in the middle and outer shelf regions, along with significantly higher values of attenuation coefficients beneath this layer that rapidly increased towards the bottom. In the open ocean, both IOPs and *Chl* exhibited consistent variability, with the subsurface maximum layer typically located at 34–84 m. Phytoplankton were found to be one of the major components in determining the vertical variability of bio-optical properties, with their vertical dynamics influenced by both physical forcing and light attenuation effects. The depth of the subsurface maximum layer was found to be closely related to the fluctuation of the oceanic thermocline and the depth of the euphotic zone, which also affected the total integrated biomass of the upper ocean. Typically high values of attenuation coefficients observed in the bottom waters of the continental shelf reflected the transport of particulate matter over the bottom boundary layer. Our results reveal large spatial differences in bio-optical profiles in response to complex marine ecodynamics in the NSCS. From the perspective of marine research, high-resolution optical measurements are clearly advantageous over conventional bottle sampling.

Key words: vertical distribution, phytoplankton, bio-optical properties, subsurface maximum layer, northern South China Sea

Citation: Wang Guifen, Zhou Wen, Xu Zhantang, Xu Wenlong, Yang Yuezhong, Cao Wenxi. 2020. Vertical variations in the bio-optical properties of seawater in the northern South China Sea during summer 2008. Acta Oceanologica Sinica, 39(4): 42–56, doi: 10.1007/s13131-020-1535-y

1 Introduction

Since the 1980s, ocean scientists have become increasingly aware of the importance of the biogeochemical state of the oceans in regulating the climate and its effects on the habitability of the planet (Buesseler, 2001). Physical forcing and coupling of physical and biological processes have been found to exert a great influence on biogeochemical cycles (Platt et al., 2005). Additionally, new technologies with high vertical- and spatial resolutions have generated better understandings of short-term shifts in ocean biogeochemistry and linkages between physical forcing, biological responses and chemical fluxes on different spatial scales (Dickey, 2001).

Bio-optical studies aim to characterize the biological and biogeochemical state of natural waters based on their optical properties, and to quantify the role of the ocean in the global carbon budget (Morel and Maritorena, 2001). Inherent optical properties (IOPs), including absorption, scattering, backscattering and attenuation coefficients could be used to obtain the information (such as the amount, type and composition) of suspended particles and colored dissolved organic matter (CDOM) (Mobley, 1994; Boss et al., 2007). With the development of new optical sensors and monitoring platforms, optical observations have played significant roles in studying the biogeochemical dynamics of the upper ocean (Morel, 1988; Morel and Maritorena, 2001; Boss et al., 2001; Behrenfeld and Boss, 2003; Platt et al., 2005; McGillicuddy, 2016). The introduction of new devices, such as the spectral absorption-attenuation meter (WETLabs ac9/acs) and the Spectral Backscattering Sensor (HOBILabs hs6), has permitted *in situ* measurements of IOPs, including spectral absorption/attenuation coefficients and backscattering coefficients, at high resolutions (Chang and Dickey, 2001; Oubelkheir and Sciandra, 2008; Boss et al., 2013; Brewin et al., 2016). Converting these

Foundation item: The National Natural Science Foundation of China under contract Nos 41776045 and 41576030; the Fundamental Research Funds for the Central Universities under contract No. 2017B06714; the Open Project Program of the State Key Laboratory of Tropical Oceanography under contract No. LTOZZ1602; the Science and Technology Program of Guangzhou, China under contract No. 201607020041.

*Corresponding author, E-mail: guifenwang@hhu.edu.cn

measured IOPs to meaningful biogeochemical quantities is therefore a promising approach for studying biogeochemical variability at the scale of these observations (Oubelkheir et al., 2005).

During the last two decades, many studies have focused on developing rapid, continuous, *in situ* techniques for retrieving information about biogeochemical constituents (e.g., phytoplankton, sediment and dissolved matter) based on their relationships with optical properties. For example, beam attenuation has been used as a proxy for particulate organic carbon (POC) in the open ocean (Bishop, 1999; Gardner et al., 1999), and chlorophyll fluorescence and absorption have been used as proxies for chlorophyll concentration (Boss et al., 2007; Cullen, 1982; Mignot et al., 2011; Roesler and Barnard, 2013; Lavigne et al., 2015). These optical data have improved our understanding of the vertical distributions of biogeochemical parameters (Boss et al., 2001; Chang and Dickey, 2001), the formation of subsurface phytoplankton biomass maxima (Fennel and Boss, 2003; Nencioli et al., 2010) and the diel and seasonal cycles of particulate organic matter (Oubelkheir and Sciandra, 2008; Gernez et al., 2011; Kheireddine and Antoine, 2014; Mignot et al., 2014). Optical properties are also thought to serve as a link between physical and biogeochemical processes, as changes in the underwater light field lead to changes in biological activity (Fujii et al., 2007; Xiu and Chai, 2014).

The South China Sea (SCS) is the largest tropical marginal sea in the world. It covers an area of 3.5×10^6 km^2, with a maximum depth of over 5 000 m. Strongly influenced by the Asian monsoon, the SCS is characterized by diverse spatial-, temporal-, physical- and biological dynamics which play an important role in regulating the biogeochemical state of the SCS on both the horizontal and vertical scales (Liu et al., 2002; Ning et al., 2004). Bio-optical properties including the chlorophyll *a* concentration (*Chl*), phytoplankton absorption and the light absorption of colored detrital materials in the surface ocean of the SCS have been widely used for studying the environmental effects of physical processes at large spatial and temporal scales (Ma et al., 2011; Shang et al., 2012; Liu et al., 2013; Pan et al., 2015). Phytoplankton has been found to be the major contributing component of variations in the bio-optical properties of SCS seawater (Lin et al., 2014; Wang et al., 2008). However, only a few studies have so far focused on determining the high resolution vertical-scale bio-optical properties of SCS seawater (e.g., Lin et al., 2014; Zhang et al., 2016; Cui et al., 2016; Xu et al., 2018). Recent discussion about the vertical distribution of phytoplankton is predominantly based on data obtained from samples collected at discrete depths in the SCS (Gong et al., 2015; Li et al., 2016; Wang et al., 2016, 2018). Previous studies have proposed that vertical mixing on the shelf is the primary mechanism for bringing nutrients from the subsurface of the adjoining northern SCS up to the mixed layer, thereby supporting primary production (Chen et al., 2006; Wong et al., 2015). In the northeastern SCS, an increasing role of turbulent diffusion from the coastal ocean zones to the offshore pelagic zones, but a decreasing role of curl-driven vertical transport of nutrients, has also been found to be an important factor controlling phytoplankton dynamics (Li et al., 2016). During the period of September 2014–August 2015, two Bio-Argo floats were successfully used to describe the vertical variability of *Chl* in the open SCS, demonstrating the invaluable advantages of this method for observing biogeochemical properties over long time periods (Zhang et al., 2016). High-resolution bio-optical profile data collected over the entire SCS region are needed to provide a better understanding of the vertical structure of biogeochemical properties in this region including the important driving mechanisms.

This paper presents high-resolution observations of vertical variations of IOPs and *Chl* across the shelf sea of the northern SCS (NSCS). These data enable us to examine variations of IOPs in NSCS seawater and to produce estimates of *Chl* based on collected absorption spectra and the ratio of *Chl* to $c_{pg}(650)$, which are used as an indices of phytoplankton abundance and particle composition, respectively. We also examine differences in the vertical distributions of bio-optical properties over the continental shelf and in the open ocean, and the response of these properties to various hydrographical characteristics. We likewise consider factors that influence the observed spatial differences in bio-optical profiles by considering physical drivers including complex hydrodynamic processes and variations in light attenuation.

2 Data and methods

2.1 *Study region*

Hydrographic, bio-optical, and biogeochemical data from the NSCS were simultaneously acquired during the Opening Research Cruise of the R/V *Shiyan 3*, operated by the South China Sea Institute of Oceanology, Chinese Academy of Sciences, from August 16 to September 6, 2008. Figure 1 shows a map of the investigated station locations. The NSCS shelf can be sub-divided into the inner shelf, the middle shelf and the outer shelf corresponding to water depths of <40 m, 40–90 m and 90–120 m, respectively (Wong et al., 2015). Open ocean generally refers to water depths greater than 120 m.

2.2 *Hydrographic data acquisition and process*

Vertical profiles of temperature and salinity were acquired using a ship-launched SeaBird CTD and sampling rosette. The ocean mixed layer is the top layer of the water column, where the temperature and salinity are vertically well mixed. The mixed layer depth (MLD) was defined using the threshold method with a finite difference criterion based on a near-surface reference value. The reference depth is set at 10 m to avoid much of the strong diurnal temperature cycle that occurs in the top few meters of the ocean. The chosen temperature criterion is 0.5°C absolute difference, as recommended by Kara et al. (2000).

2.3 *Measurements of in situ optical profiles*

In situ profiles of inherent optical properties (IOPs) were measured using a ship-deployed profiling package at 48 stations, as shown in Fig. 1. The WETLabs ac9, which consists of dual, 25 cm path length flow tubes for each path, was used to measure the spectral absorption and attenuation coefficients at nine wavelengths (412, 440, 488, 510, 532, 555, 650, 676 and 715 nm). The ac9 data were corrected for temperature- and salinity effects using the coefficients derived by Sullivan et al. (2006). The proportional method (Zaneveld et al., 1994) was the applied to correct for scattering errors in the absorption measurements. We did field calibration before and in the middle of the observation period to monitor the stability of the ac9. Here, $a_{pg}(\lambda)$ and $c_{pg}(\lambda)$ denote the non-water spectral absorption and attenuation coefficients, respectively. All notations are as shown in Table 1.

Apparent optical profile data were collected at about 16 stations during the daytime. A freefall spectroradiometer (Satlantic, Inc.) was used to measure the vertical profiles of downwelling spectral irradiance ($E_d(z, \lambda)$) and upwelling spectral radiance ($L_u(z, \lambda)$) at seven wavelengths (412, 443, 490, 520, 555, 620 and

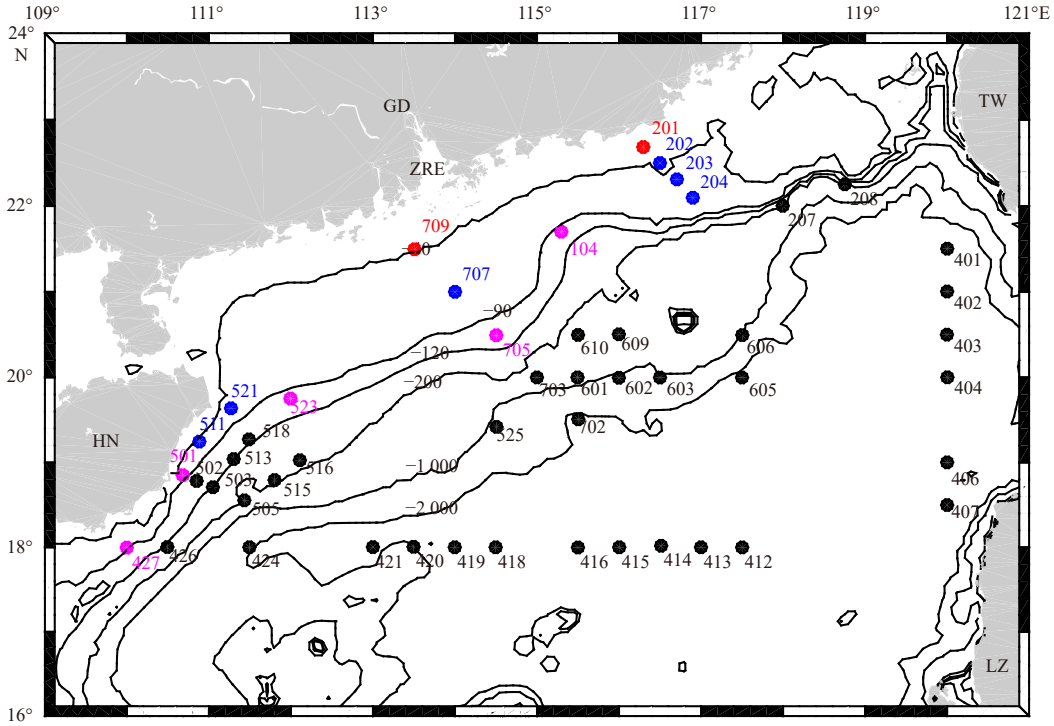

Fig. 1. Sampling stations in the northern South China Sea during the survey period of August 16–September 2, 2008. ● represents optical measurement station, ZRE Zhujiang River Estuary, GD Guangdong Province, TW Taiwan Island, LZ Luzon, and HN Hainan Island. Differently colored station labels refer to stations in different sub-regions: inner shelf (red), middle shelf (blue), outer shelf (magenta), and open ocean (black).

Table 1. Notations

Parameter	Value
λ	wavelength (nm)
$a_{pg}(\lambda)$	non-water absorption coefficient measured by the ac9 (m^{-1})
$a_p(\lambda)$	absorption coefficient of particle measured by spectrophotometer (m^{-1})
$a_{ph}(\lambda)$	absorption coefficient of phytoplankton measured by spectrophotometer (m^{-1})
$c_{pg}(\lambda)$	non-water attenuation coefficient measured by the ac9 (m^{-1})
$b_p(\lambda)$	scattering coefficient of particles measured by the ac9 (m^{-1})
$b_{bp}(\lambda)$	backscattering coefficient of particles measured by hs6 (m^{-1})
$a_{LH}(676)$	absorption line height at 676 nm (m^{-1})
Chl	chlorophyll *a* concentration (mg/m^3)
Chl_{surf}	surface chlorophyll *a* concentration (mg/m^3)
$<Chla>_{Zeu}$	integrated cholorophyll *a* biomass over the euphotic zone (mg/m^2)
POC	particulate organic carbon concentration (mg/m^3)
SCML	subsurface chlorophyll maximum layer
MLD	mixed layer depth (m)
Z_{eu}	euphotic zone depth (m)
Z_{SCM}	depth of the subsurface chlorophyll maximum layer (m^{-1})
Chl_{max}	magnitude of the subsurface chlorophyll maximum layer (mg/m^3)
T	temperature (°C)
S	salinity
θ	potential temperature (°C)
σ_θ	potential density (kg/m^3)
PAR	photosynthetic active radiation (quanta/(cm^2·s))

683 nm) away from the ship's shadow. Photosynthetic active radiation (PAR (quanta/(cm^2·s)) was calculated from $E_d(z, \lambda)$ spectra with the ProSoft software provided by Satlantic Inc. The depth of the euphotic zone, Z_{eu}, defined as the depth where irradiance was reduced to 1% of its surface value, was calculated based on the vertical profile of PAR.

2.4 *Collection and analysis of water samples*

Water samples were collected using Niskin bottles at selected depths (0 m, 10 m, 25 m, bottom in the coastal ocean, and 0 m, 25 m,

50 m, 100 m in the open ocean) to determine the *Chl*, the particulate absorption coefficient ($a_p(\lambda)$), and the particulate organic carbon (POC) concentration.

Water samples of roughly 0.5–1 L were collected at standard depths within the euphotic zone to be measured for *Chl*. Filters were flash-frozen and initially stored in liquid nitrogen and then stored at –80°C prior to analysis in the laboratory. Pigments were extracted with acetone at –20°C for about 24 h under dark conditions, and then analyzed with a Turner Designer 10 fluorometer (Parsons et al., 1984). Light absorption by suspended particles ($a_p(\lambda)$) was determined using the quantitative filter technique (QFT) (Mitchell et al., 2003; Lin et al., 2014). POC data were obtained using a method generally consistent with the Joint Global Ocean Flux Study (JGOFS) protocols (Knap et al., 1996; Wang et al., 2011).

2.5 *Remote sensing observations*

Daily sea level anomaly (SLA) data, based on a merged product from multiple satellite missions (T/P and ERS-1/2, followed by Jason-1/2 and Envisat) and distributed by Archiving, Validation and Interpretation of Satellite Oceanographic data (AVISO, http://www.aviso.oceanobs.com/) were used to describe the background physical properties of the seawater. These have been mapped to global Mercator grids with (1/4)°×(1/4)° spatial resolution. Maps of sea surface temperature (SST) with a 6 km×6 km spatial resolution were provided by the Group for High-Resolution Sea Surface Temperature (GHRSST) Project. Daily satellite chlorophyll data were collected from version 3.0 of the Ocean Colour Climate Change Initiative (OC-CCI) and a merged MERIS, MODIS-Aqua, SeaWiFS and VIIRS products available at http://www.oceancolour.org/).

2.6 *Bulk variability of IOPs and estimation of Chl profiles*

2.6.1 *Variations of non-water absorption and attenuation coefficients*

Our observed non-water absorption coefficients ($a_{pg}(\lambda)$) and non-water attenuation ($c_{pg}(\lambda)$) exhibited large variations among both coastal and offshore waters. A reference wavelength of 488 nm was selected to compare these data in the SCS with published results from other locations (Barnard et al., 1998; Boss et al., 2013). The $a_{pg}(488)$ ranged from 0.003 5–0.264 8 m^{-1}, with an average value of 0.029 5 m^{-1} (standard deviation (STD) = 0.016 3 m^{-1}); about 93% of the data points are less than 0.05 m^{-1}. On average, the value of $c_{pg}(488)$ is 6.68 times the value of $a_{pg}(488)$. About 98% of the calculated $c_{pg}(488)$ values lie between 0.059–0.50 m^{-1}, with an average value of 0.196 m^{-1} (STD=0.192 m^{-1}).

By matching data collected at discrete depth intervals, we performed a linear regression of the logarithms of total non-water absorption at 488 and 676 nm with *Chl* (Fig. 2a). $a_{pg}(488)$ and $a_{pg}(676)$ are closely related to *Chl*, and their relationships can be effectively described by power law functions, with an R^2 of 0.716 and 0.712, respectively. In the main absorption wavelengths (488 nm and 676 nm), the non-water absorption coefficients ($a_{pg}(\lambda)$) measured by the ac9 were linearly correlated with the total particulate absorption coefficients (a_p) measured for discrete samples and by QFT, with R^2 values of 0.744 and 0.577, respectively (Fig. 2b). The relationship between $c_{pg}(488)$ and *Chl* can be described by a linear function, with an R^2 value of 0.60 (Fig. 2c). The correlation between $c_{pg}(650)$ and bottle measurements of POC was examined using a least-square linear regression, with an R^2 value of approximately 0.544 and the Relative Root Mean Square Error (denoted as RMSE, %) of approximately 43.4% (Fig. 2d). This relationship showed some difference from that developed by Stramski et al. (2008) for the eastern South Pacific and eastern

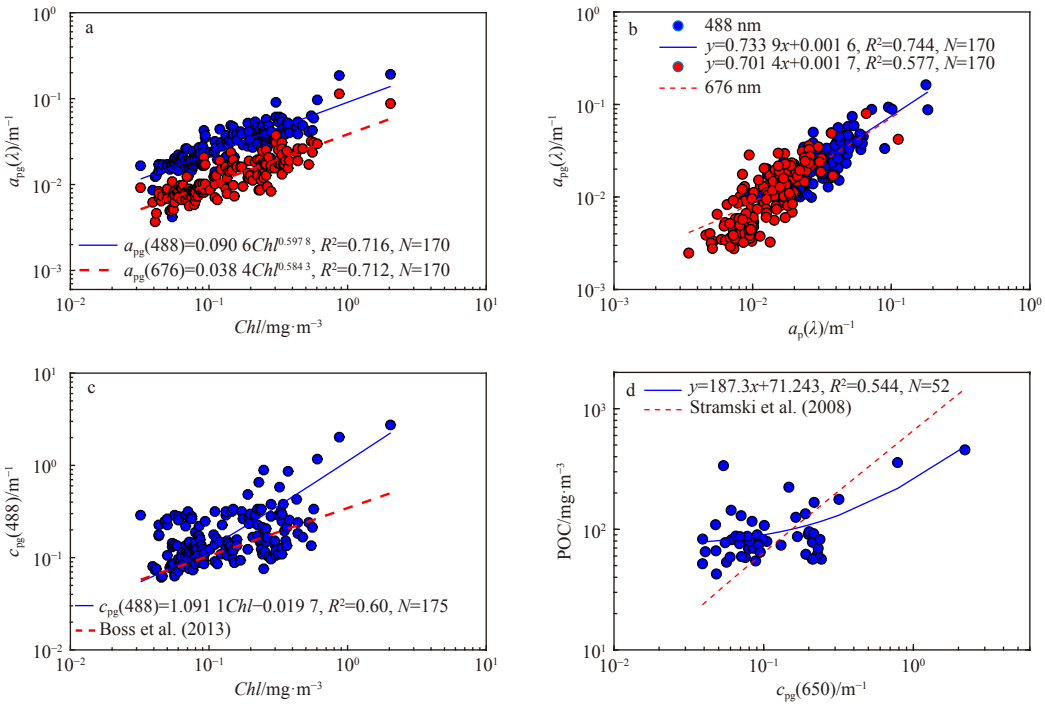

Fig. 2. Non-water absorption (a_{pg}) at 488 nm and 676 nm measured by ac9 vs. *Chl* (a), and their comparisons with total particulate absorption measured by the quantitative filter technique (b); non-water attenuation (c_{pg}) at 488 nm vs. *Chl* (c), and c_{pg} at 650 nm vs. particulate organic carbon (d).

Atlantic Ocean. Based on our data analysis, the POC in surface ocean was correlated with the *Chl*, with the R^2 being around 0.56 (N=50) for the power law relationship.

2.6.2 *Estimation of chlorophyll a concentration from absorption*

Different models have been developed to retrieve *Chl* from the absorption spectra. Since the pigment absorption peak in the red wavelength (676 nm) is primarily associated with chlorophyll *a*, we can obtain a proxy for *Chl* by regressing the power-law relationship between $a_{pg}(676)$ and *Chl*, as shown in Fig. 2a, with the RMSE of 42.56% and a log-transformed root mean square error (RMSE-log) of 0.170.

$$Chl = 33.377 a_{pg}(676)^{1.244}, \quad R^2 = 0.693, \ N = 168. \tag{1}$$

This empirical relationship is significantly different than that developed by Claustre et al. (2000), which might be due to a scattering offset in the absorption meter for longer wavelengths, as well as the absorption contribution of other pigments or colored detritus materials.

An alternative index is the difference between the absorption at 676 nm and that at 650 nm divided by the chlorophyll-specific absorption at 676 nm (0.014 m^2/mg) (Chang and Dickey, 2001; Fennel and Boss, 2003; Xiu et al., 2009), with the relationship being expressed mathematically by the following equation:

$$Chl = \frac{a_{pg}(676) - a_{pg}(650)}{0.014}. \tag{2}$$

This model (Eq. (2)) exhibited poor performance in our study area, with a RMSE of 85.46%, and a RMSE-log of 0.31. For certain samples, the $a_{pg}(650)$ was even higher than $a_{pg}(676)$, resulting in a negative value for *Chl*.

In recent years, some researchers have preferred to calculate the height of the peak absorption above a baseline drawn between the absorption at 650 nm and that at 715 nm (Boss et al., 2013; Roesler and Barnard, 2013) to approximate the phytoplankton absorption at 676 nm. The absorption line height ($a_{LH}(676)$) thus defined can be expressed as follows:

$$a_{LH}(676) = a_{pg}(676) - \left[\frac{39}{65}a_{pg}(650) + \frac{26}{65}a_{pg}(715)\right]. \tag{3}$$

The *Chl* can then be estimated from a linear correlation (Roesler and Barnard, 2013; Brewin et al., 2016) or a power-law relationship with $a_{LH}(676)$ (Boss et al., 2013). In this study, however, there was poor correlation between $a_{LH}(676)$ (estimated from Eq. (3)) and *Chl*, which might be related with the large variability of $a_{pg}(715)$ (–0.037 to 0.263 m^{-1}). We preferred to compute the absorption line height at 676 nm as $a_{pg}(676)$–0.6×$a_{pg}(650)$, and developed a power-law function for describing its relationship with *Chl*, as shown in Fig. 3a and Eq. (4), which exhibited a much high value of R^2 (0.77), with the RMSE and RMSE-log of 37.03% and 0.147, respectively.

$$Chl = 45.179\left[a_{pg}(676) - 0.6 \times a_{pg}(650)\right]^{1.139\,1}, \quad N = 168. \tag{4}$$

Unlike using the *in situ* fluorometric method to estimate chlorophyll, the absorption line height is not sensitive to the incident irradiance, in particular, the non-photochemical quenching that could promote initial chlorophyll fluorescence and result in an underestimation of *Chl* (Roesler and Barnard, 2013). A power-law function was recommended for describing the pigment packaging effect, which exhibited a robust relationship over the simple linear regression (Boss et al., 2013). By comparing the regional optimized model as shown by Eqs (1), (2) and (4), we can see that, by subtracting the absorption contribution by other components, the relationship between $a_{LH}(676)$ and *Chl* tends to converge. Therefore, this empirical algorithm (Eq. (4)) was used to estimate the vertical distribution of chlorophyll *a* based on the absorption profiles. According to frequency distribution of the 3 457 data points collected over 48 profiles (1 m interval) in the NSCS (Fig. 3b), our estimated *Chl* generally varies from 0.02 to 0.63 mg/m^3, with an average value of 0.161 mg/m^3.

2.6.3 *Definition and description of the subsurface chlorophyll maximum layer (SCML)*

Based on our estimated high-resolution chlorophyll profiles, we were able to calculate variations in the SCML, including thickness, depth (Z_{SCM}), and intensity (Chl_{max}). The thickness of the SCML can be estimated as the depth interval over which the *Chl* was 50% of the maximum *Chl* (Pérez et al., 2006; Gong et al., 2014). The deployed depth of the ac9 in some stations did not cover the whole profile of chlorophyll *a* (8 incomplete profiles out of 38). Therefore, the thickness of the SCML in our study was defined as 2×Δ*d*, where Δ*d* is the difference in depth between the location of Chl_{max} and *Chl*=50%Chl_{max} within the upper layer. The intensity of SCML (Chl_{max}) refers to the chlorophyll value at Z_{SCM}.

2.6.4 *Calculation of the integrated cholorophyll a biomass over the euphotic zone*

The integrated chlorophyll *a* biomass over the euphotic zone

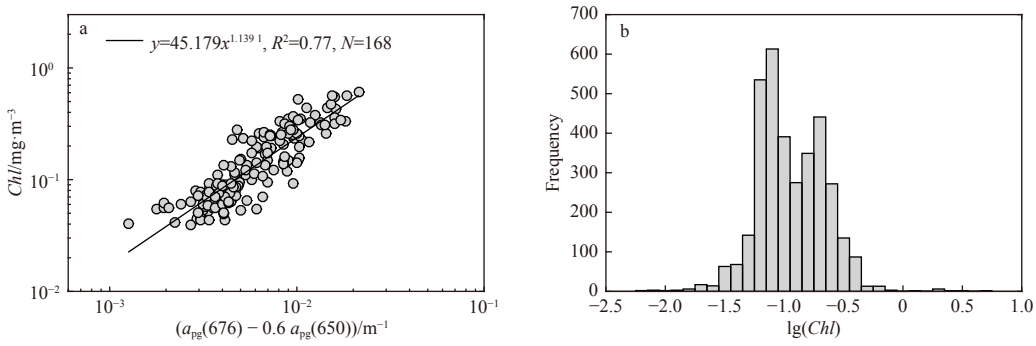

Fig. 3. Absorption difference ($a_{pg}(676)$–0.6×$a_{pg}(650)$) versus *Chl* (solid line represents the power-law function) (a), and frequency distribution of absorption-estimated *Chl* (b).

(<Chla>$_{Zeu}$) can be calculated from these *Chl* profiles. During the cruise, the depth of the bottom of the euphotic zone (Z_{eu}), which was measured at several stations, shows a clear relationship with the surface chlorophyll *a* concentration (Chl_{surf}) (Z_{eu}=26.767$Chl_{surf}^{-0.353}$, R^2=0.88, N=16). Thus, by using this modified bio-optical model, Z_{eu} can also be inferred from the surface value of *Chl*. Only the profiles where the bottom of the euphotic zone was reached are considered for such statistical analyses.

3 Results

3.1 *Hydrographic characteristics of the NSCS*

Following the classification of Wong et al. (2015), average hydrographic and IOPs in these hydrographic sub-divisions (inner shelf, middle shelf, outer shelf and the open ocean) in summer 2008 are summarized in Table 2. The relationship between potential temperature (θ, °C), and salinity (S) at observed stations across the shelf sea are shown in Fig. 4. The θ-S relationship in inner shelf waters is obviously different from that of the open ocean. Two stations collected in the inner shelf waters were located in a center of upwelling (with lower temperature and high salinity in the surface waters) and in the plume waters of the Zhujiang River Estuary (with high temperature and low salinity in the surface waters). In contrast, the water over the outer shelf was warm and saline, with a mean temperature of 28.7°C and a salinity of 33.56 in the mixed layer. The density of outer shelf water (mean σ_θ=21.10 kg/m^3) is even higher than that of the open ocean (σ_θ=20.82 kg/m^3). The middle shelf water was generally found to be a mixture of the inner- and outer shelf waters, with σ_θ=20.54 kg/m^3 and S=32.96. The extensions of θ-S relationships in the inner shelf converged with those further offshore at a salinity of roughly 34.2, a temperature of 22.03°C and a density of 23.74 kg/m^3. This point of convergence, which likely represents the source water of the inner shelf, was traced to a depth of about 40–50 m in the middle and outer shelf. Except for some specific points with low salinity in upper surface waters, the θ-S relationships in the outer shelf waters match well with those observed in the open ocean, which converged at a salinity of 34.5 and a temperature of 19.7°C.

Superimposed on these general hydrographic characteristics, coastal upwelling, river discharge in shelf waters, and meso-scale eddies in the open ocean are major additional sub-regional features in the study area. Intrusions of water from the Kuroshio Current, as well as the passage of typhoons, may also result in different vertical structures of hydrological properties. During the survey period (16 August–6 September 2008), the SST was generally high in most regions of the NSCS (>30°C), with the exception of two cold centers off the coast (Fig. 5a). One is located in the northeast part of the NSCS along the coast of Guangdong Province with the minimum value around 27.5°C, which is generally noted as the eastern Guangdong coastal upwelling (Wang et al., 2014). This upwelling event could also be detected in the SLA map, which displays significantly lower values in this region (Fig. 5b). The other cold center, which is relatively weaker (minimum SST = 29°C), appears to the northeast of Hainan Island, and is usually noted as the Hainan northeastern upwelling (Lin et al., 2016). Based on *in situ* data, obvious shoreward and upward tilting of the isotherms from the middle shelf to the inner shelf were observed in the eastern Guangdong coastal upwelling. The open ocean of the NSCS is mainly characterized by three anticyclonic eddies (ACE), detected by satellite sea level anomaly maps (SLA) (Fig. 5b). Two of them were located across the 18°N transect, with *in situ* sampling stations cutting through the centers of these ACEs. In the northeast part of SCS, there is another ACE across the Luzon Strait, with high SLA and high SST. Surface *Chl* exhibits obviously higher values along the coast of the NSCS (Fig. 5c), especially in the coastal upwelling regions and the Zhujiang River Estuary. In the offshore area, where water depth is greater than 120 m, *Chl* exhibits much lower values, with the spatial pattern largely matching that of SLA. Extremely low *Chl* values could be observed at the centers of identified ACEs. During the survey, the central part of the NSCS also exhibited high *Chl* as affected by the passage of typhoon Nuri (Ye et al., 2013).

3.2 *Vertical distributions of bio-optical properties in NSCS sub-regions*

3.2.1 *Inner shelf waters*

Two profiles were collected in the inner shelf region, at Stas 201 and 709 (Fig. 1). Station 201 lies near the center of coastal upwelling, with lower temperature and higher salinity present throughout the whole water column (Table 2, Fig. 6a). Station 201 also exhibited the highest values of IOPs and *Chl* (Fig. 7), in which the a_{pg}(488) and c_{pg}(650) were approximately 0.193 m^{-1} and 2.203 m^{-1}, respectively. Our absorption-estimated *Chl* for

Table 2. Average hydrographic properties and concentrations of chlorophyll *a* in the hydrographic sub-divisions in the northern South China Sea

Area	Inner shelf	Middle shelf	Outer shelf	Open ocean
Water depth/m	<40	40–90	90–120	>120
MLD/m		15–32	12–43	12–62
T/°C	24.43–29.58 (27)	27.83–29.82 (28.96)	28.06–29.47 (28.65)	27.64–29.75 (29.14)
S	31.53–33.41 (32.47)	32.08–33.68 (32.96)	33.41–33.70 (33.56)	33.05–33.66 (33.41)
σ_θ/kg·m^{-3}	19.27–22.31 (20.79)	20.22–20.82 (20.54)	20.86–21.29 (21.10)	20.56–21.48 (20.82)
a_{pg}(488)/m^{-1}	0.037–0.193 (0.115)	0.015–0.066 (0.029)	0.018–0.035 (0.025)	0.006–0.028 (0.017)
c_{pg}(650)/m^{-1}	0.111–2.203 (1.157)	0.072–0.507 (0.176)	0.067–0.237 (0.109)	0.04–0.224 (0.101)
Chl/mg·m^{-3}	0.207–2.109 (1.158)	0.066–0.382 (0.135)	0.086–0.143 (0.107)	0.022–0.113 (0.078)
Chl_{surf}[1)]/mg·m^{-3}	0.215–2.045 (1.13)	0.055–0.609 (0.182)	0.05–0.175 (0.090)	0.032–0.123 (0.067)
Z_{SCM}[2)]/m	9	25–56 (43)	34–50 (43.5)	34–84 (60.24)
Chl_{max}[2)]/mg·m^{-3}	5.139	0.243–0.811 (0.428)	0.437–0.490 (0.457)	0.184–0.481 (0.303)
<Chla>$_{Zeu}$[3)]/mg·m^{-2}	30.34	6.99–10.95 (9.34)	10.84–15.75 (13.11)	4.24–13.77 (8.17)
Thickness[2)]/m	3.8	4–44 (15.7)	12–26 (16.3)	7–54 (26.3)
Number of profiles	2	6	5	35

Note: [1)] *In situ* measured data at surface waters; [2)] only profiles with subsurface maximum layer of chlorophyll a are considered for statistics; [3)] only profiles where the euphotic depth are reached are considered for statistics.

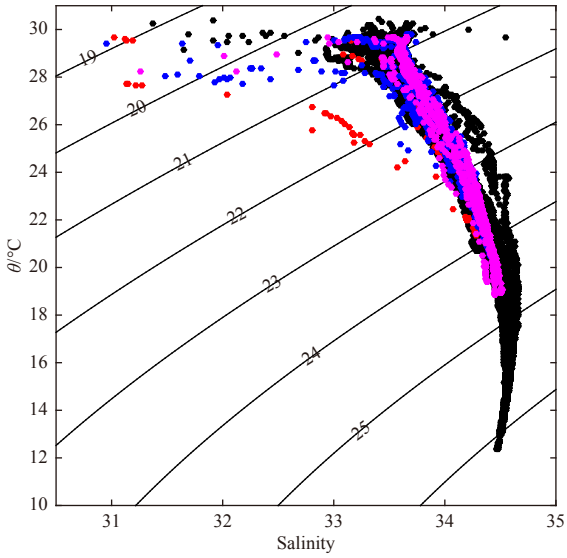

Fig. 4. The relationship between potential temperature (θ, °C) and salinity at each station observed in summer 2008 for stations from the inner shelf (red), middle shelf (blue), outer shelf (magenta), and open ocean (black). Lines of constant density (σ_θ, kg/m^3) are shown.

surface waters at Sta. 201 is 2.109 mg/m^3, which is similar to the results of *in situ* measured data (2.045 mg/m^3). An obvious SCML was observed at approximately 9 m with the thickness of about 3.8 m and Chl_{max} of up to 5.14 mg/m^3. Furthermore, the column-integrated biomass over the euphotic depth (<Chla>$_{Zeu}$) was up to 30.34 mg/m^2, indicating a strong contribution of coastal upwelling to phytoplankton growth. Both IOPs and *Chl*, as well as the ratio of *Chl* to $c_{pg}(650)$ ($Chl/c_{pg}(650)$), tend to decrease rapidly to a stable value below the SCM layer, which indicates the dominant role played by the scattering effect of particles in the bottom waters (Figs 7a and 8a).

The vertical distribution of bio-optical parameters at Sta. 709 is much different than that at Sta. 201. Station 709 lies in the mouth of Zhujiang River Estuary (Fig. 1). The upper surface water (about 4 m thick) was particularly fresh and the surface salinity dropped to as low as 31.53, which is about 2 lower than that of offshore waters (Fig. 6a). These characteristics were consistent with the influence of fresh water from the Zhujiang River. Both IOPs and our estimated *Chl* profiles exhibit high values in this upper layer compared with offshore stations (Fig. 7a). The vertical $a_{pg}(488)$ profile exhibits small peaks at approximately 16 m, and $c_{pg}(650)$ increases at depths below 21 m. There is no obvious peak in the vertical *Chl* profile and the average value over the water column is about 0.221 mg/m^3. The vertical profile of $Chl/c_{pg}(650)$ tends to at first increase and then decrease rapidly with the depth; the turning point for $Chl/c_{pg}(650)$ is at a depth of around 21 m (Fig. 8a).

3.2.2 *Middle shelf waters*

In the middle shelf, we collected six profiles: three in the eastern part of the Guangdong coastal area, two to the east of Hainan Island, and one at Sta. 707, offshore of the Zhujiang River Estuary (Fig. 1). Affected by coastal upwelling, surface water at Sta. 202 (as shown in Lin et al. (2014)) exhibits relatively lower temperature and higher IOPs and *Chl* than other stations (Fig. 6b). Elevated values of IOPs and *Chl* in the subsurface were observed at

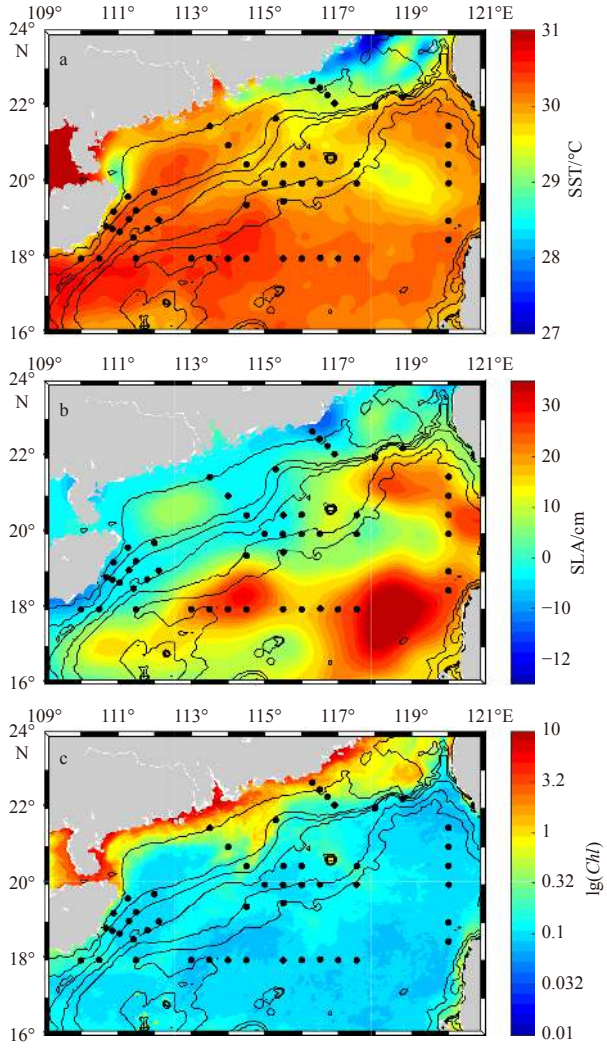

Fig. 5. The distribution of average sea surface temperature (SST, °C) (a), sea level anomaly (SLA, cm) (b), and surface chlorophyll *a* concentration (log-transformed) (c) in the NSCS during the summer 2008 survey period.

Sta. 511 along the coast of the Hainan Island, with a maximum *Chl* of 0.8 mg/m^3 (Fig. 7b). The location of Z_{SCM} varies from 25 m to 56 m, with the thickness of the SCML exhibiting a large variability from 4 m (202) to 44 m (521). Both IOPs and *Chl* are significantly lower than in inner shelf waters, but still higher than at outer shelf stations. <Chla>$_{Zeu}$ ranges from 6.99 mg/m^2 to 10.95 mg/m^2 exhibiting large spatial differences.

Another distinguishing characteristic of the vertical distribution of bio-optical properties in the middle shelf lies in the increasing trend of the attenuation coefficient towards the bottom below the Z_{SCM}. The particulate scattering coefficient provides a relatively large contribution to the light attenuation in the bottom waters. High concentrations of re-suspended particles are thought to be a major contributor to light attenuation, reflecting the transport of particulate matter across the shelf via the benthic nepheloid layer. Vertical plots of $Chl/c_{pg}(650)$ are generally characterized by constant values within the upper layer, gradually increasing to the depth of the SCML before rapidly decreasing toward the bottom (Fig. 8b).

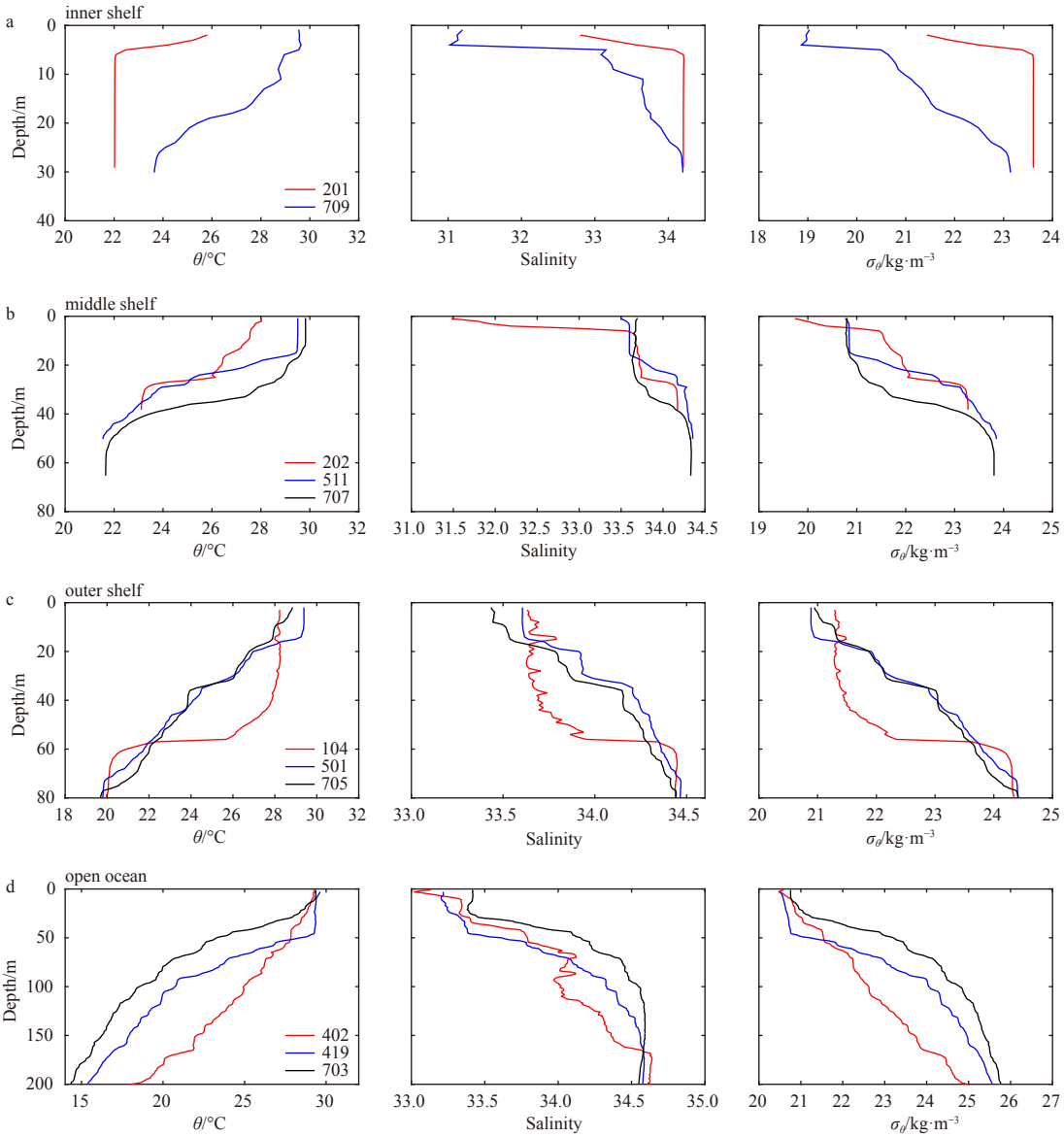

Fig. 6. Typical vertical distribution of potential temperature (θ, °C), salinity (S) and potential density (σ_θ, kg/m^3) at stations across the shelf of the NSCS: inner shelf (a), middle shelf (b), outer shelf (c), and open ocean (d).

3.2.3 *Outer shelf waters*

Outer shelf waters are obviously stratified, with the MLD ranging from 12 m to 43 m. For Stas 427 and 501, located around the Hainan Island, the thermoclines are relatively shallower than at other stations, with high values of $c_{pg}(650)$ observed in the bottom waters (Fig. 7c). Both the averaged hydrographical and bio-optical properties within the mixed layer are slightly higher than in middle shelf waters (Table 1, Figs 6c and 7c). The peaks of SCML are much more pronounced, with the Z_{SCM} varying from 34–50 m and an average thickness of roughly 16.3 m. The contribution of re-suspended particles in the bottom boundary layer to the light attenuation of re-suspended particles in the bottom boundary layer is relatively weak compared with waters in the middle shelf, and these also result in the gentle decrease of $Chl/c_{pg}(650)$ ratio below the depth of the SCML (Fig. 8c).

3.2.4 *Open ocean waters*

Open ocean waters over the ocean basin of the NSCS exhibit relatively high upper ocean temperatures and salinities (Fig. 6d). The average mixed layer depth (about 33.56 m) is deeper than that in the shelf waters (Table 1). Based on 35 vertical profiles measured *in situ*, bio-optical properties within the mixed layer are relatively lower than in the shelf waters. *Chl* within the mixed layer ranges from 0.022–0.113 mg/m^3, with an average value of 0.078 mg/m^3. Vertical profiles of IOPs and *Chl* are mainly characterized by a subsurface maximum, which occurs at similar depths and IOPs and *Chl* decrease in both the upward and downward directions away from the SCML. For most profiles in the open ocean, Z_{SCM} lies between 34–84 m and is deeper than the SCML observed in shelf waters. The average depth of Z_{SCM} is 60.24 m, though for some profiles, this depth is as much as 80 m. The magnitude of the SCML in open ocean water is significantly lower than that of shelf waters, with the values ranging from 0.184–0.481 mg/m^3 (average=0.303 mg/m^3). As estimated from the surface chlorophyll *a* concentration, the euphotic zone depth ranges from 60 m to 100 m, and the integrated $<Chla>_{Zeu}$ lies between

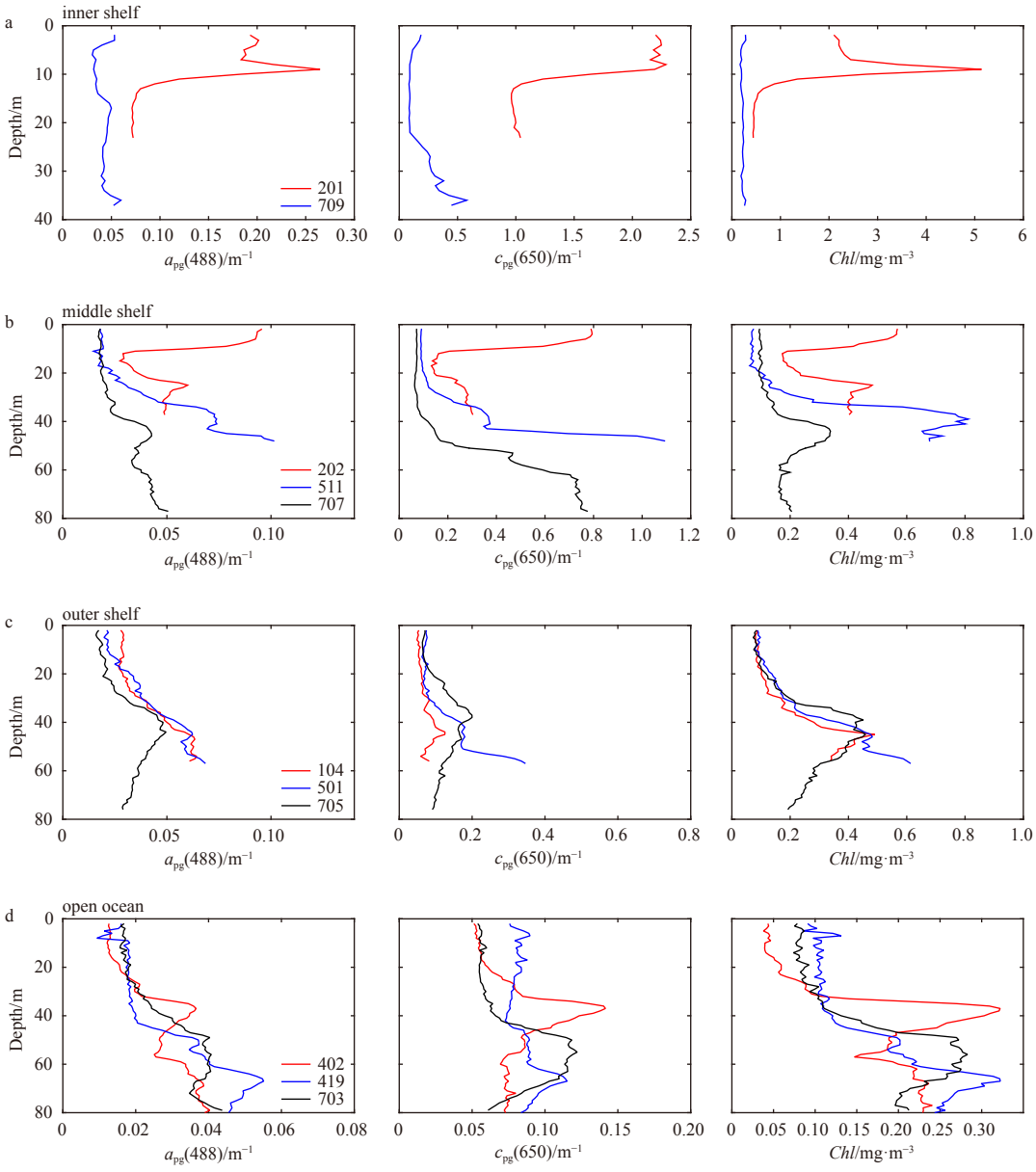

Fig. 7. Typical vertical distributions of non-water absorption coefficient at 488 nm ($a_{pg}(488)$, m^{-1}), non-water attenuation coefficient at 650 nm ($c_{pg}(650)$, m^{-1}) and absorption-estimated *Chl* (mg/m^3)) at stations across the shelf of the NSCS: Inner Shelf (a), Middle Shelf (b), Outer Shelf (c), and Open Ocean (d).

4.24 mg/m^2 and 13.77 mg/m^2, consistent with the very oligotrophic status of open ocean waters in the NSCS. Several typical profiles from the CTD casts were selected to describe regional differences in the vertical distributions of IOPs (Figs 6d and 7d). At Sta. 402, the depth of maximum IOPs is around 37 m, which is consistent with a shoaling of the mixed layer. In the vertical profile of IOPs at Sta. 703, which is representative of profiles in the open ocean, Z_{SCM} is around 56 m. Station 419 lies near the center of a warm eddy (Fig. 1). The water column at Sta. 419 is characterized by warmer and low salinity water in the upper ocean, with the mixed layer being around 50 m and the deep SCML being around 69 m. As demonstrated by the typical profiles, vertical plots of $Chl/c_{pg}(650)$ in open oceanic waters exhibit less variability within the mixed layer, and this variability tends to increase with depth to the bottom of the euphotic zone (Fig. 8d).

3.3 *Variations in the subsurface maximum layer of phytoplankton*

Subsurface maximum layers of phytoplankton were generally observed in most offshore regions of the South China Sea. Based on the estimated profiles of *Chl* from middle shelf waters to open ocean, Z_{SCM} was found to vary from 25 m to 84 m, with the magnitude of SCM between 0.184 mg/m^3 and 0.811 mg/m^3. For most stations, variations in Z_{SCM} followed fluctuations of the isopycnal, σ_θ=23 kg/m^3, and the isotherm, θ=23.38°C (Figs 9a, b). However, there are two abnormal stations that exhibit large deviations between Z_{SCM} and the isopycnal, σ_θ=23 kg/m^3. One is Sta. 402 (21°N, 120°E), located to the southwest of Taiwan Island, near the Luzon Strait (Fig. 1), where Z_{SCM} and the depth of the isopycnal (σ_θ=23 kg/m^3) are at 37 m and 119 m, respectively. As illustrated in the θ-S relationship, this area could be influenced by an intrusion of water from the Kuroshio Current through the Luzon Strait, as suggested by higher subsurface salinity and temperat-

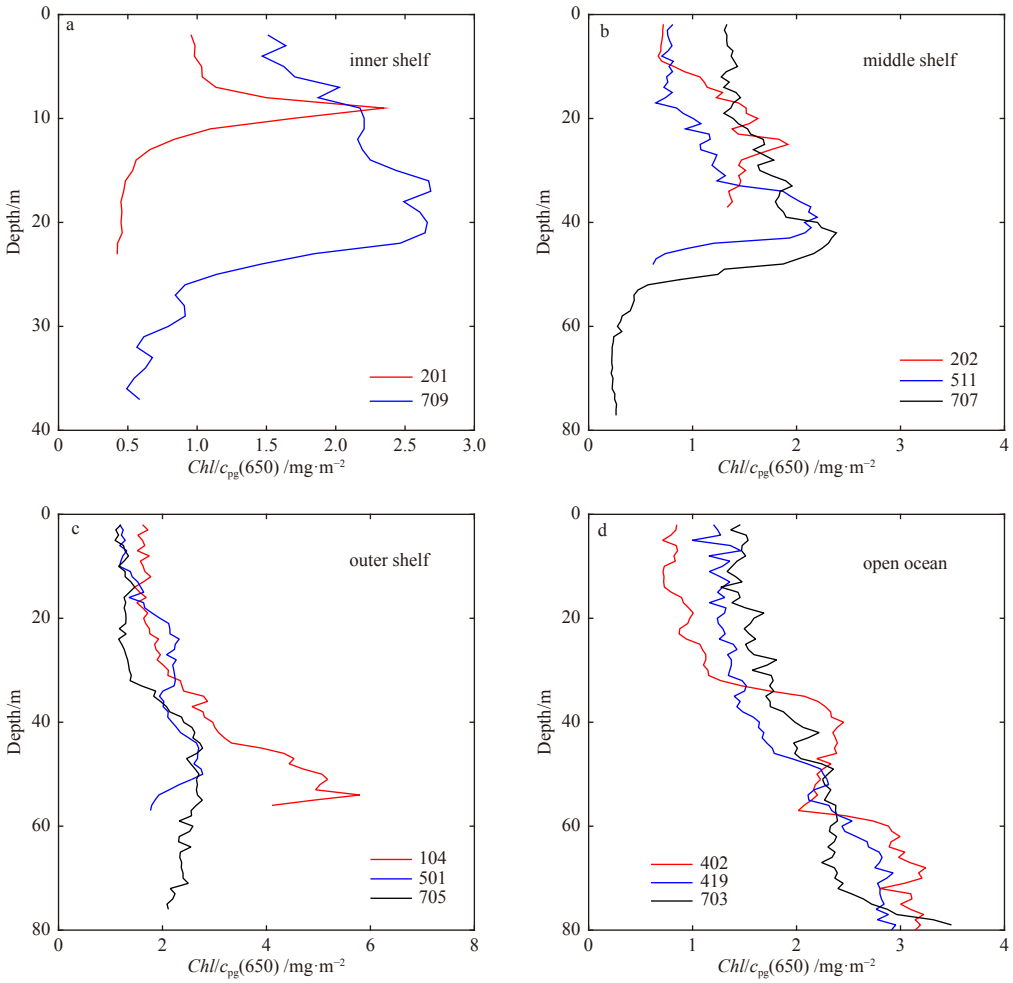

Fig. 8. Typical vertical distributions of the $Chl/c_{pg}(650)$ (mg/m^2) at stations across the shelf of the NSCS: inner shelf (a), middle shelf (b), outer shelf (c), and open ocean (d).

ure in the upper water column. Another abnormal station is 609, located in the central part of NSCS, with Z_{SCM} and depth of the isopycnal (σ_θ=23 kg/m^3) at 43 m and 83 m, respectively. This station was observed after the passage of typhoon Nuri (Ye et al., 2013). In both abnormal stations, the vertical hydrological properties showed unique structures with shallow density surface rising toward the surface, and the deep density surface dipping downward. These vertical structures are similar with the mode-eddy reported by McGillicuddy et al. (1999) and McGillicuddy (2016), which is composed of a lens-shaped disturbance that raises the seasonal pycnocline and lowers the main pycnocline.

Excluding these two anomalous stations, Z_{SCM} varies consistently with the depth of isopycnal (σ_θ=23 kg/m^3) and the isotherm (θ=23.38°C), as shown in Figs 9a and b, with the determination coefficients (R^2) for linear regression being 0.76 and 0.74, respectively. The magnitude of SCM (Chl_{max}) in the open ocean was much lower than that in the shelf waters. With the deepening of the SCML, Chl_{max} exhibits a decreasing trend (Fig. 9c). The thickness of the SCML ranges between 3.8 m and 54 m and exhibits a weak correlation with Z_{SCM} (R^2=0.36, N=38). Z_{SCM} lies primarily between the mixed layer depth and Z_{eu}, and a linear relationship was observed between Z_{SCM} and Z_{eu}, with R^2=0.76 (N=11).

Based on high-resolution *in situ* measurements, the column-integrated biomass over Z_{eu} (<Chla>$_{Zeu}$) could be quantitatively analyzed. The range of <Chla>$_{Zeu}$ is wide, from 4.24 mg/m^2 in the very oligotrophic waters to 30.34 mg/m^2 at the coastal upwelling station to the east of Guangdong Province. Large scatters were observed for the relationship <Chla>$_{Zeu}$ and Chl_{surf}, especially for open oceanic waters (Fig. 10a). With a deepening of the SCML, the <Chla>$_{Zeu}$ tended to decease, exhibiting a much closer power law relationship with depth, and R^2 reached a maximum of 0.73 (Fig. 10b). A close relationship between <Chla>$_{Zeu}$ and the ratio of Z_{SCM} and Z_{eu} (Z_{SCM}/Z_{eu}) was also observed, with an R^2 of 0.72 (Fig. 10c).

4 Discussion

4.1 *Physical processes influencing the profiles of bio-optical properties*

Bulk variabilities of absorption and attenuation coefficients with *Chl* and POC are consistent with previous studies in the SCS, which indicate the importance of phytoplankton and its accompanying materials (Wang et al., 2008; Cui et al., 2016). Physical processes play an important role in determining the spatial variations observed in our profiles of bio-optical properties in the NSCS. Coastal upwelling and river discharge are two important features of the inner and middle shelf waters of the NSCS, which supply nutrients that support phytoplankton growth by Ekman pumping and freshwater discharge, respectively. These results are consistent with previous studies in NSCS (Lu et al., 2010; Lin

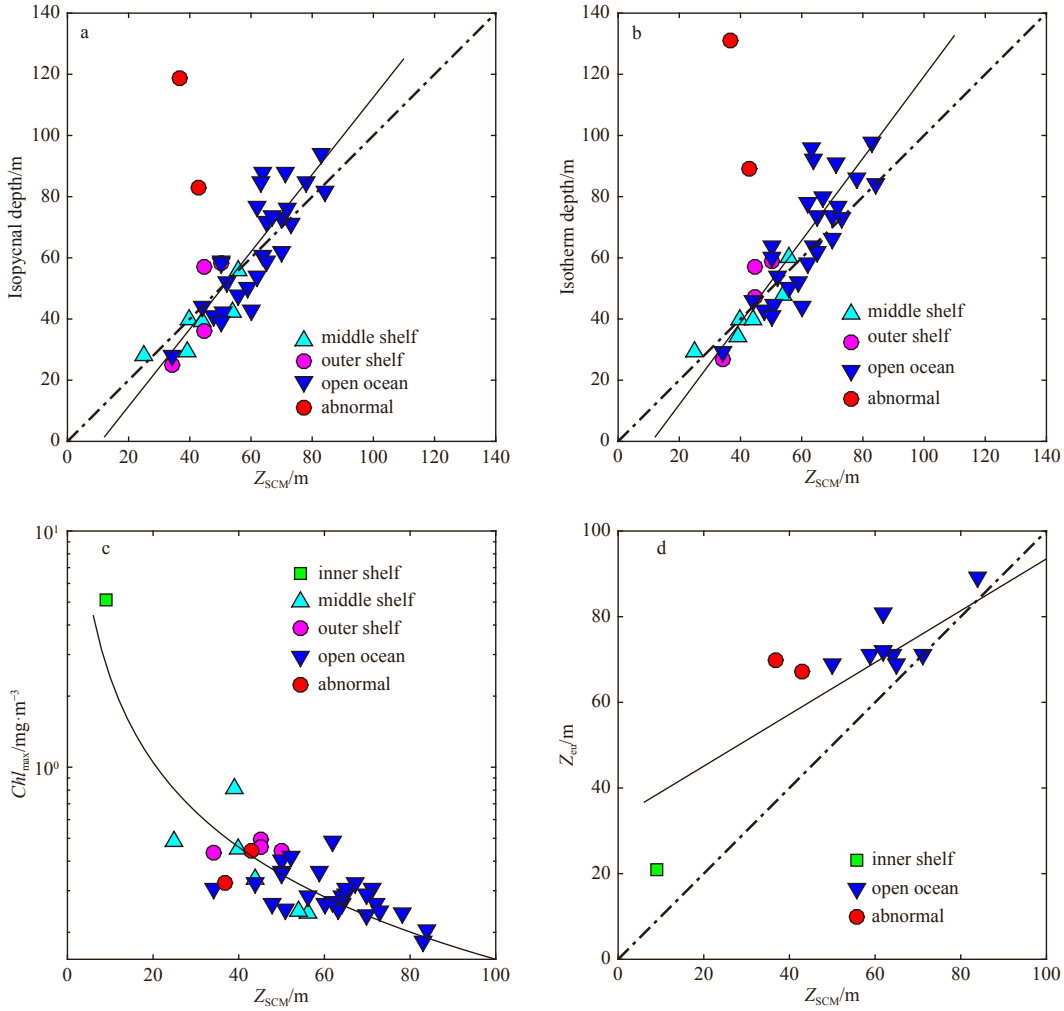

Fig. 9. Scatterplots of the depth of the SCML (Z_{SCM}) as function of the isopycnal depth at σ_θ=23 kg/m^3 (a), the isotherm depth at θ=23.38°C (b), the magnitude of SCM (Chl_{max}) (c), and depth to the bottom of the euphotic zone (Z_{eu}) (d). Colors/markers refer to the different sub-regions. The line corresponds to the linear (a, b, d) or power-law (c) fit function.

et al., 2014; Xu et al., 2018). Terrestrial material could also been exported from the Zhujiang River plume or the upwelling process which resulted higher attenuation coefficient (c_{pg}(650)) in the upper layer of inner shelf water (Cui et al., 2016). Conspicuous shoaling of the isotherms from the middle shelf to the inner shelf in coastal upwelling areas could induce resuspension of particles and the transport of detrital matter within the bottom boundary layer. This process would be consistent with the high attenuation coefficients observed below the SCML that increased rapidly towards the bottom, as well as the decreasing trend of Chl/c_{pg}(650) in the middle and outer shelf waters. Similar characteristics of attenuation coefficient profiles have been investigated in the bottom boundary layer of a continental shelf in the Mid-Atlantic Bight (Boss et al., 2001). These patterns observed in bio-optical properties are consistent with the summertime hydrography and nutrient dynamics of the NSCS as discussed by Wong et al. (2015). Vertical mixing within the NSCS shelf-sea area is the primary mechanism for bringing nutrients from the sub-surface of the adjoining ocean basin up to the mixed layer of the shelf, supporting primary production. Based on our survey data, coastal upwelling was found to be the primary mechanism contributing to vertical mixing in northeast and northwest part of the NSCS (Lin et al., 2014).

In the open ocean area, phytoplankton was the dominant factor influencing the vertical distribution of bio-optical properties (Figs 2 and 7d). The subsurface maximum of the a_{pg}(488) and c_{pg}(650) were corresponding to the subsurface maximum of *Chl*. Cui et al. (2016) has ever reported similar variability in the shelf and basin waters in the NSCS during summer. However, this is different from the vertical separation of the maxima of biomass (as reflected by c_p) and chlorophyll during stratified conditions observed in some oligotrophic system (e.g., Sta. ALOHA in the subtropical North Pacific Ocean), caused by algal photo-adaptation (Fennel and Boss, 2003 and references therein). The SCML is a nearly ubiquitous feature in stably stratified waters, and the depth of the SCML is found to be consistent with the top of the nitracline where phytoplankton growth is enhanced by the optimal combination of nutrient flux and irradiance (Cullen, 2015). In our study area, a combination of mesoscale eddies, intrusions of Kuroshio water, and occasional typhoons are responsible for the variability of the SCML in the open ocean observed during the survey period. A clear relationship was observed between the depth of the SCML (Z_{SCM}) and the fluctuation of thermocline depth as denoted by the isopycnal (σ_θ=23 kg/m^3) and the iso-

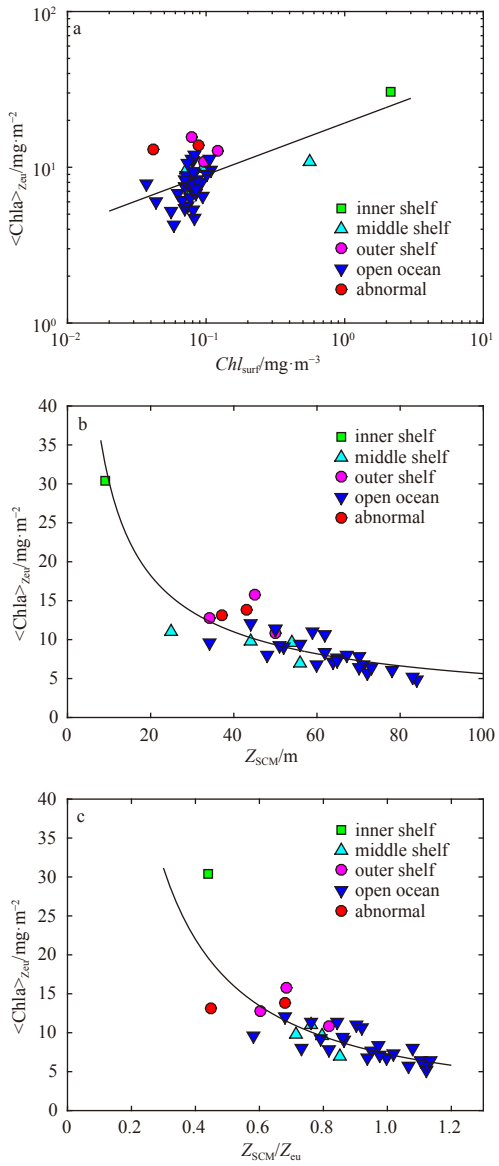

Fig. 10. Scatterplots of the column-integrated biomass over Z_{eu} (<Chla>$_{Zeu}$) as a function of Chl_{surf} (a), Z_{SCM} (b), and Z_{SCM}/Z_{eu} (c). Solid lines indicate the power-law fit function. Colors/markers refer to different sub-regions.

therm at 23.38°C. This observation confirms the importance of physical forcing on regulating the SCML within the euphotic zone (Wong et al., 2015). These results were also consistent with those reported in previous studies of the NSCS, which indicated that the vertical distribution of nutrients generally follows isopycnal (and largely isothermal) surfaces in the upper water column (Chen et al., 2006; Li et al., 2016; Zhang et al., 2016). These effects could be easily explained based on the doming of the isopycnals and the nutricline, where nutrient pumping may have been caused by a cold eddy, or by the passage of typhoon Nuri (McGillicuddy et al., 1999; McGillicuddy, 2016; Ye et al., 2013; Xu et al., 2018). However, the relationship may not hold true for specific profiles with complex hydrological structure, for example, at Stas 402 and 609. A clear uplift of the SCM was observed at both stations, however, the isopycnal depth (σ_θ=23 kg/m^3) relatively deeper than nearby stations. These phenomena might be related with the unique hydrological profiles caused by intrusion of Kuroshio waters or by the passage of typhoon Nuri, respectively. Shoaling density surfaces may lift nutrients into the euphotic zone, which are rapidly utilized by the biota, and the subsurface maximum layer of chlorophyll (SCML) could be lifted up (McGillicuddy et al., 1999; McGillicuddy, 2016). However, deepening density surface serve to push nutrient-depleted water out of the well-illuminated surface layers, which may result in the departures from general relationship between Z_{SCM} and the ispycnal at 23 kg/m^3 (as well as the isotherm at 23.38°C). Driving mechanisms may be even more complicated in the case of anticyclonic eddies (ACEs) (Wang et al., 2018). Based on our observations, for those profiles located in the two ACEs across the 18°N transact, the SCML lies mainly between 64–84 m, with Z_{SCM} generally following the depth patterns of the isopycnals (Figs 9a, b). Since the optical instrument (ac9) was mainly deployed to depths <90 m, there were also some profiles where the SCML was too deep to be detected. Full-depth observations and additional studies are expected in future work.

Based on *in situ* measured data with high vertical resolution, a more accurate assessment of *Chl* integrated over the whole water column of the euphotic zone could be achieved to investigate ecological responses to different physical processes. Although a general trend could be detected from surface *Chl* concentrations, which showed that the total biomass within the euphotic zone decreases from the coastal ocean to open oceanic waters, it is difficult to estimate the total chlorophyll *a* inventory of the surface phytoplankton biomass for those oligotrophic waters in the open ocean of the SCS (Fig. 10a). This may introduce a large uncertainty in the estimation of primary production from ocean color, since only the pigment content within the upper penetration depth is accessible to remote sensing techniques. The relationship between <Chla>$_{Zeu}$ and surface *Chl* is different from that developed for stratified waters in open ocean (Morel et al., 2001; Uitz et al., 2006). With deepening of the SCML, <Chla>$_{Zeu}$ tends to decease, exhibiting a much closer power law relationship. This variability is consistent with that observed by Mignot et al. (2011), confirming that the upward flux of nutrients driven by physical processes contributes to phytoplankton growth within the euphotic zone. The magnitude (that is the intensity) of the SCM (Chl_{max}) is sensitive to changes in the depth of the SCML and tends to decrease with deepening of the SCML. Similar results have been reported in previous studies, where they were attributed to nitrate transport from nitrate-rich waters to the euphotic zone (Chen et al., 2006; Mignot et al., 2011; Gong et al., 2015).

4.2 *The effect of light attenuation on the chlorophyll profile*

Light attenuation could be another factor determining the vertical variability of phytoplankton. Previous studies have proposed that both the intensity and the location of the SCML is the result of a balance between the upward flux of nutrients and the downward attenuation of light (Fennel and Boss, 2003; Cullen, 2015). Considering the seasonal variability of the SCML, light attenuation could be a critical factor in regulating the depth of the SCML, as discussed by Gong et al. (2015) based on physical-biogeochemical modelling and by Mignot et al. (2011) based on *in situ* observed profiles. During our survey period, the euphotic zone depth (Z_{eu}) was generally deeper than the mixed layer depth. Light was therefore readily available and likely not a limiting factor of phytoplankton growth in the mixed layer. Z_{SCM} lies primarily between the mixed layer depth and Z_{eu}, and a close relationship between Z_{SCM} and Z_{eu} was observed with R^2=0.76 (N=11). Due to the limit of *in situ* observations of underwater

light field, the relationship between Z_{SCM} and Z_{eu} (Fig. 9d) could be improved in future. For waters with low *Chl* in the upper layer, the SCML deepens and becomes closer to the nitracline, which may reduce the phytoplankton biomass at the SCML. Light attenuation in the upper water column is the primary factor affecting vertical variations in phytoplankton growth rates (Mignot et al., 2011, 2014; Gong et al., 2014, 2015). The relative positions of the SCML and the euphotic zone depth may result in variability of total integrated phytoplankton biomass within Z_{eu} (Fig. 10c). Since the distribution of the SCML depth was primarily regulated by fluctuations in the thermocline, this relationship reflects the combined effect of physical forcing and light attenuation to phytoplankton growth in our study area.

Vertical profiles of $Chl/c_{pg}(650)$ in the open ocean of the NSCS show similar patterns with vertical distributions of the *Chl*:C ratio observed in California Current pelagic ecosystem (Li et al., 2010). These patterns reveal the great advantage of optical measurements in quantifying phytoplankton dynamics in the ocean. Cui et al. (2016) also found similar correlations between $c_p(660)$ and POC for data collected in the NSCS, with the exception of nearshore stations with high sediment resuspension. The $Chl/c_{pg}(650)$ ratio is low at the sea surface as a result of the strong light intensity compared with deeper layers, and tends to increase with depth as a result of photoadaptation (Behrenfeld et al., 2005; Xing et al., 2014), exhibiting relatively constant values near the bottom of the euphotic zone. This is a common feature of open ocean waters characterized by strong stratification (e.g., Kitchen and Zaneveld, 1990; Fennel and Boss, 2003) and has been attributed to complex interactions between light, nutrients, temperature, and phytoplankton community structures (Li et al., 2010; Nencioli et al., 2010).

5 Conclusions

We studied the vertical distribution of bio-optical properties based on high-resolution profiles of absorption and attenuation in the NSCS during summer 2008. *Chl* profiles were estimated from the differences in absorption in the red wavelengths, which gave us detailed information about the vertical variability of phytoplankton in the NSCS, as well as the column-integrated biomass over the euphotic depth.

Vertical distributions of both IOPs and the estimated *Chl* in the NSCS exhibit significant differences across the continental shelf and between the shelf and open ocean. Physical processes including coastal upwelling and discharge from the Zhujiang River were found to be the main drivers controlling bio-optical properties in inner shelf waters, by supplying nutrients to the upper water column that support phytoplankton growth, and by transporting detritus along the bottom boundary layer. Profiles of IOPs and *Chl* in inner shelf stations were characterized by relatively high values at the surface and at the bottom, with or without a SCML. In the middle shelf and some of the outer-shelf stations, the attenuation coefficients below the SCML are high and tend to increase rapidly towards the bottom. This is a distinguishing characteristic that is consistent with the transport of colder and relatively nutrient-rich water from the open ocean to the shelf-sea along the bottom of the ocean, with the additional influence of resuspended particulate matter over the bottom boundary layer. For open ocean waters, vertical profiles of IOPs and *Chl* are much more similar, with the depth of their maximum values ranging from 34 m to 84 m with some stations even deeper. A combination of physical processes including mesoscale eddies, Kuroshio intrusions, and typhoons caused variability in the depth and thickness of the SCML in the open ocean during the survey period. The depth of Z_{SCM} varies consistently with fluctuations in the isopycnal (σ_θ=23 kg/m^3) and the isotherm (θ=23.38°C), which are primarily caused by meso-scale eddies. However, for waters affected by Kuroshio intrusions and typhoons, Z_{SCM} exhibits a significant displacement relative to the isolines of temperature and density due to unique hydrological structures with shallow density surface rising toward the surface, and the deep density surface dipping downward. Light attenuation was another important factor influencing the vertical structure of phytoplankton by regulating the depth of the SCML and the $Chl/c_{pg}(650)$ distribution. The column-integrated biomass over Z_{eu} ($<Chla>_{Zeu}$) exhibited a large scatter in offshore oligotrophic waters with low surface chlorophyll. Fluctuations in the depth of the SCML, especially the position of the SCML relative to that of Z_{eu}, played an important role in determining the variability of $<Chla>_{Zeu}$, confirming the combined effects of physical forcing and light attenuation on phytoplankton growth in NSCS.

Our observations of the vertical variations of phytoplankton provide much more detailed information about the marine ecological dynamics of the NSCS, with great improvements over data based on conventional bottle-sampling methods. With the advancement of bio-optical monitoring instruments, further intensive research can be conducted to study the vertical variability of phytoplankton biomass and associated carbon fluxes, as well as important driving factors over different spatial and temporal scales.

Acknowledgements

We thank all contributors to the dataset in the South China Sea Open Cruise by the R/V *Shiyan 3*, South China Sea Institute of Oceanology, CAS and Qian Li for his constructive suggestions on the initial version of the manuscript. We also thank Guy Evans from Liwen Bianji, Edanz Editing China (www.liwenbianji.cn/ac), for editing the English text of a draft of this manuscript.

References

Barnard A H, Pegau W S, Zaneveld J R V. 1998. Global relationships of the inherent optical properties of the oceans. Journal of Geophysical Research, 103(C11): 24955–24968, doi: 10.1029/98JC01851

Behrenfeld M J, Boss E. 2003. The beam attenuation to chlorophyll ratio: an optical index of phytoplankton physiology in the surface ocean?. Deep Sea Research Part I: Oceanographic Research Papers, 50(12): 1537–1549, doi: 10.1016/j.dsr.2003.09.002

Behrenfeld M J, Boss E, Siegel D A, et al. 2005. Carbon-based ocean productivity and phytoplankton physiology from space. Global Biogeochemical Cycles, 19(1): GB1006

Bishop J K B. 1999. Transmissometer measurement of POC. Deep Sea Research Part I: Oceanographic Research Papers, 46(2): 353–369, doi: 10.1016/S0967-0637(98)00069-7

Boss E S, Collier R, Larson G, et al. 2007. Measurements of spectral optical properties and their relation to biogeochemical variables and processes in Crater Lake, Crater Lake National Park, OR. Hydrobiologia, 574(1): 149–159, doi: 10.1007/s10750-006-2609-3

Boss E, Pegau W S, Gardner W D, et al. 2001. Spectral particulate attenuation and particle size distribution in the bottom boundary layer of a continental shelf. Journal of Geophysical Research: Oceans, 106(C5): 9509–9516, doi: 10.1029/2000JC900077

Boss E, Picheral M, Leeuw T, et al. 2013. The characteristics of particulate absorption, scattering and attenuation coefficients in the surface ocean; Contribution of the Tara Oceans expedition. Methods in Oceanography, 7: 52–62, doi: 10.1016/j.mio.2013.11.002

Brewin R J W, Dall'Olmo G, Pardo S, et al. 2016. Underway spectrophotometry along the Atlantic Meridional Transect reveals high

performance in satellite chlorophyll retrievals. Remote Sensing of Environment, 183: 82–97, doi: 10.1016/j.rse.2016.05.005
Buesseler K O. 2001. Ocean biogeochemistry and the global carbon cycle: an introduction to the U.S. joint global ocean flux study. Oceanography, 14(4): 5, doi: 10.5670/oceanog.2001.01
Chang G C, Dickey T D. 2001. Optical and physical variability on timescales from minutes to the seasonal cycle on the New England shelf: July 1996 to June 1997. Journal of Geophysical Research: Oceans, 106(C5): 9435–9453, doi: 10.1029/2000JC900069
Chen C C, Shiah F K, Chung S W, et al. 2006. Winter phytoplankton blooms in the shallow mixed layer of the South China Sea enhanced by upwelling. Journal of Marine Systems, 59(1–2): 97–110, doi: 10.1016/j.jmarsys.2005.09.002
Claustre H, Fell F, Oubelkheir K, et al. 2000. Continuous monitoring of surface optical properties across a geostrophic front: Biogeochemical inferences. Limnology and Oceanography, 45(2): 309–321
Cui Wansong, Wang Difeng, Gong Fang, et al. 2016. The vertical distribution of the beam attenuation coefficient and its correlation to the particulate organic carbon in the north South China Sea. In: Remote Sensing of the Ocean, Sea Ice, Coastal Waters, and Large Water Regions. Edinburgh, United Kingdom: SPIE, 2016
Cullen J J. 1982. The deep chlorophyll maximum: Comparing vertical profiles of chlorophyll *a*. Canadian Journal of Fisheries and Aquatic Sciences, 39(5): 791–803, doi: 10.1139/f82-108
Cullen J J. 2015. Subsurface chlorophyll maximum layers: Enduring enigma or mystery solved?. Annual Review of Marine Science, 7: 207–239, doi: 10.1146/annurev-marine-010213-135111
Dickey T D. 2001. The role of new technology in advancing ocean biogeochemical research. Oceanography, 14(4): 108–120, doi: 10.5670/oceanog.2001.11
Fennel K, Boss E. 2003. Subsurface maxima of phytoplankton and chlorophyll: Steady-state solutions from a simple model. Limnology and Oceanography, 48(4): 1521–1534, doi: 10.4319/lo.2003.48.4.1521
Fujii M, Boss E, Chai F. 2007. The value of adding optics to ecosystem models: a case study. Biogeosciences, 4(5): 817–835, doi: 10.5194/bg-4-817-2007
Gardner W D, Gundersen J S, Richardson M J, et al. 1999. The role of seasonal and diel changes in mixed-layer depth on carbon and chlorophyll distributions in the Arabian Sea. Deep Sea Research Part II: Topical Studies in Oceanography, 46(8–9): 1833–1858, doi: 10.1016/S0967-0645(99)00046-6
Gernez P, Antoine D, Huot Y. 2011. Diel cycles of the particulate beam attenuation coefficient under varying trophic conditions in the northwestern Mediterranean Sea: Observations and modeling. Limnology and Oceanography, 56(1): 17–36, doi: 10.4319/lo.2011.56.1.0017
Gong Xiang, Shi Jie, Gao Huiwang, et al. 2014. Modeling seasonal variations of subsurface chlorophyll maximum in South China Sea. Journal of Ocean University of China, 13(4): 561–571, doi: 10.1007/s11802-014-2060-4
Gong Xiang, Shi Jinhui, Gao Huiwang, et al. 2015. Steady-state solutions for subsurface chlorophyll maximum in stratified water columns with a bell-shaped vertical profile of chlorophyll. Biogeosciences, 12(4): 905–919, doi: 10.5194/bg-12-905-2015
Kara A B, Rochford P A, Hurlburt H E. 2000. An optimal definition for ocean mixed layer depth. Journal of Geophysical Research, 105(C7): 16803–16821, doi: 10.1029/2000JC900072
Kheireddine M, Antoine D. 2014. Diel variability of the beam attenuation and backscattering coefficients in the northwestern Mediterranean Sea (BOUSSOLE site). Journal of Geophysical Research: Oceans, 119(8): 5465–5482, doi: 10.1002/2014JC010007
Kitchen J C, Zaneveld J R V. 1990. On the noncorrelation of the vertical structure of light scattering and chlorophyll α in case I waters. Journal of Geophysical Research: Oceans, 95(C11): 20237–20246, doi: 10.1029/JC095iC11p20237
Knap A, Michaels A, Close A, et al. 1996. Protocols for the Joint Global Ocean Flux Study (JGOFS) core measurements. Reprint of the IOC Manuals and Guides No. 29, UNESCO, Paris
Lavigne H, D'Ortenzio F, D'Alcalà M R, et al. 2015. On the vertical distribution of the chlorophyll *a* concentration in the Mediterranean Sea: a basin-scale and seasonal approach. Biogeosciences, 12(16): 5021–5039, doi: 10.5194/bg-12-5021-2015
Li Q P, Dong Y, Wang Y. 2016. Phytoplankton dynamics driven by vertical nutrient fluxes during the spring inter-monsoon period in the northeastern South China Sea. Biogeosciences, 13: 455–466, doi: 10.5194/bg-13-455-2016
Li Q P, Franks P J S, Landry M R, et al. 2010. Modeling phytoplankton growth rates and chlorophyll to carbon ratios in California coastal and pelagic ecosystems. Journal of Geophysical Research, 115(G4): G04003
Lin Junfang, Cao Wenxin, Wang Guifen, et al. 2014. Inversion of bio-optical properties in the coastal upwelling waters of the northern South China Sea. Continental Shelf Research, 85: 73–84, doi: 10.1016/j.csr.2014.06.001
Lin Peigen, Cheng Peng, Gan Jianping, et al. 2016. Dynamics of wind-driven upwelling off the northeastern coast of Hainan Island. Journal of Geophysical Research: Oceans, 121(2): 1160–1173, doi: 10.1002/2015JC011000
Liu K K, Chao S Y, Shaw P T, et al. 2002. Monsoon-forced chlorophyll distribution and primary production in the South China Sea: observations and a numerical study. Deep Sea Research Part I: Oceanographic Research Papers, 49(8): 1387–1412, doi: 10.1016/S0967-0637(02)00035-3
Liu Fenfen, Tang Shilin, Chen Chuqun. 2013. Impact of nonlinear mesoscale eddy on phytoplankton distribution in the northern South China Sea. Journal of Marine Systems, 123–124: 33–40, doi: 10.1016/j.jmarsys.2013.04.005
Lu Zhongming, Gan Jianping, Dai Minhan, et al. 2010. The influence of coastal upwelling and a river plume on the subsurface chlorophyll maximum over the shelf of the northeastern South China Sea. Journal of Marine Systems, 82(1–2): 35–46, doi: 10.1016/j.jmarsys.2010.03.002
Ma Jinfeng, Zhan Haigang, Du Yan. 2011. Seasonal and interannual variability of surface CDOM in the South China Sea associated with El Niño. Journal of Marine Systems, 85(3–4): 86–95, doi: 10.1016/j.jmarsys.2010.12.006
McGillicuddy D J Jr. 2016. Mechanisms of physical-biological-biogeochemical interaction at the oceanic mesoscale. Annual Review of Marine Science, 8(1): 125–159, doi: 10.1146/annurev-marine-010814-015606
McGillicuddy D J Jr, Johnson R, Siegel D A, et al. 1999. Mesoscale variations of biogeochemical properties in the Sargasso Sea. Journal of Geophysical Research: Oceans, 104(C6): 13381–13394, doi: 10.1029/1999JC900021
Mignot A, Claustre H, D'Ortenzio F, et al. 2011. From the shape of the vertical profile of in vivo fluorescence to Chlorophyll-*a* concentration. Biogeosciences, 8(8): 2391–2406, doi: 10.5194/bg-8-2391-2011
Mignot A, Claustre H, Uitz J, et al. 2014. Understanding the seasonal dynamics of phytoplankton biomass and the deep chlorophyll maximum in oligotrophic environments: A Bio-Argo float investigation. Global Biogeochemical Cycles, 28(8): 856–876, doi: 10.1002/2013GB004781
Mitchell B G, Kahru M, Wieland J, et al. 2003. Determination of spectral absorption coefficients of particles, dissolved material and phytoplankton for discrete water samples. In: Mueller J L, Fargoin G S, McClain C R, eds. Ocean Optics Protocols for Satellite Ocean Color Sensor Validation, revision 4, Vol. IV (Chapter 4), NASA/TM-2003-211621/Rev4-vol. 4. Greenbelt, MD: NASA Goddard Space Flight Center, 39–64
Mobley C D. 1994. Light and Water: Radiative Transfer in Natural Waters. San Diego, CA, USA: Academic Press
Morel A. 1988. Optical modeling of the upper ocean in relation to its biogenous matter content (case I waters). Journal of Geophysical Research: Oceans, 93(C9): 10749–10768, doi: 10.1029/JC093iC09p10749
Morel A, Maritorena S. 2001. Bio-optical properties of oceanic waters: A reappraisal. Journal of Geophysical Research: Oceans,

106(C4): 7163–7180, doi: 10.1029/2000JC000319
Nencioli F, Chang G, Twardowski M, et al. 2010. Optical characterization of an eddy-induced diatom bloom west of the island of Hawaii. Biogeosciences, 7(1): 151–162, doi: 10.5194/bg-7-151-2010
Ning Xiuren, Chai Fei, Xue Huijie, et al. 2004. Physical-biological oceanographic couplinginfluencing phytoplankton and primary production in the South China Sea. Journal of Geophysical Research: Oceans, 109: C10005, doi: 10.1029/2004JC002365
Oubelkheir K, Claustre H, Sciandra A, et al. 2005. Bio-optical and biogeochemical properties of different trophic regimes in oceanic waters. Limnology and Oceanography, 50(6): 1795–1809, doi: 10.4319/lo.2005.50.6.1795
Oubelkheir K, Sciandra A. 2008. Diel variations in particle stocks in the oligotrophic waters of the Ionian Sea (Mediterranean). Journal of Marine Systems, 74(1–2): 364–371, doi: 10.1016/j.jmarsys.2008.02.008
Pan Xiaoju, Wong G T F, Tai J H, et al. 2015. Climatology of physical hydrographic and biological characteristics of the Northern South China Sea Shelf-sea (NoSoCS) and adjacent waters: Observations from satellite remote sensing. Deep Sea Research Part II: Topical Studies in Oceanography, 117: 10–22, doi: 10.1016/j.dsr2.2015.02.022
Parsons T, Takahashi M, Hargrave B. 1984. Biological Oceanographic Processes. 3rd ed. England: Pergamon Press, 330
Pérez V, Fernández E, Marañón E, et al. 2006. Vertical distribution of phytoplankton biomass, production and growth in the Atlantic subtropical gyres. Deep Sea Research Part I: Oceanographic Research Papers, 53(10): 1616–1634, doi: 10.1016/j.dsr.2006.07.008
Platt T, Bouman H, Devred E, et al. 2005. Physical forcing and phytoplankton distributions. Scientia Marina, 69(S1): 55–73, doi: 10.3989/scimar.2005.69s155
Roesler C S, Barnard A H. 2013. Optical proxy for phytoplankton biomass in the absence of photophysiology: Rethinking the absorption line height. Methods in Oceanography, 7: 79–94, doi: 10.1016/j.mio.2013.12.003
Shang Shaoling, Li Li, Li Jun, et al. 2012. Phytoplankton bloom during the northeast monsoon in the Luzon Strait bordering the Kuroshio. Remote Sensing of Environment, 124: 38–48, doi: 10.1016/j.rse.2012.04.022
Stramski D, Reynolds R A, Babin M, et al. 2008. Relationships between the surface concentration of particulate organic carbon and optical properties in the eastern South Pacific and eastern Atlantic Oceans. Biogeosciences, 5(1): 171–201, doi: 10.5194/bg-5-171-2008
Sullivan J M, Twardowski M S, Zaneveld J R V, et al. 2006. Hyperspectral temperature and salt dependencies of absorption by water and heavy water in the 400–750 nm spectral range. Applied Optics, 45(21): 5294–5309, doi: 10.1364/AO.45.005294
Uitz J, Claustre H, Morel A, et al. 2006. Vertical distribution of phytoplankton communities in open ocean: An assessment based on surface chlorophyll. Journal of Geophysical Research: Oceans, 111(C8): C08005
Wang Guifen, Cao Wenxi, Yang Dingtian, et al. 2008. Variation in downwelling diffuse attenuation coefficient in the northern South China Sea. Chinese Journal of Oceanology and Limnology, 26(3): 323–333, doi: 10.1007/s00343-008-0323-x
Wang Lei, Huang Bangqin, Chiang K P, et al. 2016. Physical-biological coupling in the western South China Sea: The response of phytoplankton community to a mesoscale cyclonic eddy. PLoS One, 11(4): e0153735, doi: 10.1371/journal.pone.0153735
Wang Lei, Huang Bangqin, Laws E A, et al. 2018. Anticyclonic eddy edge effects on phytoplankton communities and particle export in the northern South China Sea. Journal of Geophysical Research: Oceans, 123(11): 7632–7650, doi: 10.1029/2017JC013623
Wang Dongxiao, Shu Yeqiang, Xue Huijie, et al. 2014. Relative contributions of local wind and topography to the coastal upwelling intensity in the northern South China Sea. Journal of Geophysical Research: Oceans, 119(4): 2550–2567, doi: 10.1002/2013JC009172
Wang Guifen, Zhou Wen, Cao Wenxi, et al. 2011. Variation of particulate organic carbon and its relationship with bio-optical properties during a phytoplankton bloom in the Pearl River estuary. Marine Pollution Bulletin, 62(9): 1939–1947, doi: 10.1016/j.marpolbul.2011.07.003
Wong G T F, Pan Xiaoju, Li Kuoyuan, et al. 2015. Hydrography and nutrient dynamics in the Northern South China Sea Shelf-sea (NoSoCS). Deep Sea Research Part II: Topical Studies in Oceanography, 117: 23–40, doi: 10.1016/j.dsr2.2015.02.023
Xing Xiaogang, Claustre H, Uitz J, et al. 2014. Seasonal variations of bio-optical properties and their interrelationships observed by Bio-Argo floats in the subpolar North Atlantic. Journal of Geophysical Research: Oceans, 119(10): 7372–7388, doi: 10.1002/2014JC010189
Xiu Peng, Chai Fei. 2014. Connections between physical, optical and biogeochemical processes in the Pacific Ocean. Progress in Oceanography, 122: 30–53, doi: 10.1016/j.pocean.2013.11.008
Xiu Peng, Liu Yuguang, Li Gang, et al. 2009. Deriving depths of deep chlorophyll maximum and water inherent optical properties: A regional model. Continental Shelf Research, 29(19): 2270–2279, doi: 10.1016/j.csr.2009.09.003
Xu Wenlong, Wang Guifen, Zhou Wen, et al. 2018. Vertical variability of chlorophyll a concentration and its responses to hydrodynamic processes in the northeastern South China Sea in summer. Journal of Tropical Oceanography (in Chinese), 37(5): 62–73
Ye H J, Sui Y, Tang D L, et al. 2013. A subsurface chlorophyll a bloom induced by typhoon in the South China Sea. Journal of Marine Systems, 128: 138–145, doi: 10.1016/j.jmarsys.2013.04.010
Zaneveld J R V, Kitchen J C, Moore C C. 1994. Scattering error correction of reflecting-tube absorption meters. In: Ocean Optics XII. Bergen, Norway: SPIE
Zhang Wenzhou, Wang Haili, Chai Fei, et al. 2016. Physical drivers of chlorophyll variability in the open South China Sea. Journal of Geophysical Research: Oceans, 121(9): 7123–7140, doi: 10.1002/2016JC011983

Acta Oceanol. Sin., 2020, Vol. 39, No. 4, P. 57–64
https://doi.org/10.1007/s13131-020-1582-4
http://www.hyxb.org.cn
E-mail: hyxbe@263.net

Effects of acute salinity stress on the survival and prophenoloxidase system of *Exopalaemon carinicauda*

Qianqian Ge[1, 2†], Zhengdao Li[1, 2†], Jitao Li[1, 2*], Jiajia Wang[1, 2], Jian Li[1, 2*]

[1] Key Laboratory of Sustainable Development of Marine Fisheries, Ministry of Agriculture/Yellow Sea Fisheries Research Institute, Chinese Academy of Fishery Sciences, Qingdao 266071, China

[2] Laboratory for Marine Fisheries Science and Food Production Processes, Pilot National Laboratory for Marine Science and Technology (Qingdao), Qingdao 266237, China

Received 8 January 2018; accepted 20 August 2018

Abstract

The ridgetail white prawn *Exopalaemon carinicauda* is a euryhaline shrimp species in the estuarine and coastal areas of China. In this study, survival rates, transcription levels of two prophenoloxidase system-related genes (*EcLGBP* and *EcproPO*) and PO activity were determined quantitatively in juvenile and adult *E. carinicauda* under different salinity levels. The results showed that *E. carinicauda* juveniles could survive in a wider range of salinity conditions than adults. For juvenile *E. carinicauda*, the expression levels of *EcLGBP* and *EcProPO* were up-regulated in low salinities and showed no significant difference at 20–40, while PO activities in low salinities were higher compared to those in high salinities. For adult *E. carinicauda*, the expression profiles of *EcLGBP* and *EcproPO* had a different trend of up-regulation in salinity stress treatments and no obvious difference was observed in the gene expression levels and PO activity between 30 and 40. The salinity tolerance range of immunity for juvenile and adult *E. carinicauda* is 20–40 and 30–40, respectively.

Key words: *Exopalaemon carinicauda*, prophenoloxidase system, salinity stress, immunity, tolerant range

Citation: Ge Qianqian, Li Zhengdao, Li Jitao, Wang Jiajia, Li Jian. 2020. Effects of acute salinity stress on the survival and prophenoloxidase system of *Exopalaemon carinicauda*. Acta Oceanologica Sinica, 39(4): 57–64, doi: 10.1007/s13131-020-1582-4

1 Introduction

In recent decades, mass mortalities and great economic losses of shrimp have been documented, with numerous studies demonstrating that environmental factors, including temperature, salinity, dissolved oxygen and pH, can affect the immune system of shrimp (Pascual et al., 2003; Cheng and Chen, 2000; Chen et al., 2007). In particular, salinity changes have been known to suppress the physiological and immune system of shrimp, leading to an increased susceptibility to pathogens (de la Vega et al., 2007; Kumlu et al., 2000; Pan et al., 2007; Joseph and Philip, 2007; Cheng and Chen, 2000). Therefore, the research on the mechanism of immune regulation in shrimp under salinity changes is an urgent issue in shrimp aquaculture.

The shrimp defense system is categorized as innate immunity that includes circulating haemocytes and various active substances released into haemolymph such as the prophenoloxidase (proPO) system, antibacterial peptides, and lectins (Söderhäll and Cerenius 1992). Activation of the proPO system occurs due to the specific recognition of microorganisms (PRPs), triggering a serine proteinase cascade, eventually leading to the cleavage of the inactive proPO to the active phenoloxidase (PO) that functions to produce the melanin and toxic reactive intermediates against invading pathogens (Ishwarya et al., 2016). As important PRRs, lipopolysaccharide and β-1, 3-glucan binding protein (LGBP) has been documented to activate the prophenoloxidase system of shrimp (Lee et al., 2000; Cheng et al., 2005; Liu et al., 2009). The proPO system can either be specifically activated by microbial cell wall components including β-1, 3-glucan, lipopolysaccharide (LPS) and peptidoglycan (Amparyup et al., 2013; Johansson and Soderhall, 1989; Cerenius and Söderhäll, 2004; Cerenius et al., 2008; Li and Xiang, 2013; Yang et al., 2014) and can also be regulated by environmental or experimental factors including calcium, pH and temperature (Ai et al., 2008). Immune responses to salinity fluctuations can be well reflected in the proPO system. Phenoloxidase activity has been proved as an immune parameter under salinity stress in shrimp (Joseph and Philip, 2007; Cheng and Chen, 2000; Wang and Chen, 2006). Hu (2008) reported the effect of salinity changes on the proPO system of haemolymph in *Litopenaeus vannamei*. Recently, with the development of high-throughput next-generation sequencing techniques, Zhao et al. (2015) indicated that low salinity changes induced the proPO system in *L. vannamei* haemolymph by investigating the digital gene expression (DGE).

In general, salinity tolerance and immunity in shrimp are correlated with the developmental stages. Cieluch et al. (2005) reported that the adult pattern of osmoregulation in *Crangon crangon* is accomplished after metamorphosis from a moderately hyperosmoconforming decapodid to an effectively hyper-/hypo-

Foundation item: The National Key R&D Program of China under contract No. 2019YFD0900400; the China Agriculture Research System under contract No. CARS-48; the National Natural Science Foundation of China under contract No. 31702319; the Program of Shandong Leading Talent under contract No. LNJY2015002; the Central Public-interest Scientific Institution Basal Research Fund, CAFS under contract No. 2019ZD0603.

*Corresponding author, E-mail: lijt@ysfri.ac.cn; lijian@ysfri.ac.cn

†These authors contributed equally to this work.

regulating juvenile stage and the salinity tolerance and osmoregulatory capacity are closely correlated with the development of ion-transporting cells and the expression of iontransporting enzymes. Jiravanichpaisal et al. (2007) found no functional proPO system was present during larval stages in *Penaeus monodon* and suggested that the proPO system was not transferred from the mother to the offspring. The shrimp develop the complete and effective hyper-/hyporegulating immune system gradually after the post-larval stage, and there was little comparison in osmoregulatory capacity and immunity between the juvenile and adult.

Due to good reproductive performance, fast growth and adaptability to a range of environmental conditions, farming of the ridgetail white prawn, *Exopalaemon carinicauda*, has been booming along the coasts of the Yellow Sea and Bohai Sea, China (Xu et al., 2010; Li et al., 2012, 2015; Zhang et al., 2014). Some studies have reported that *E. carinicauda* can tolerate a low salinity level of 4 to a high salinity level of 35, and its optimal range of salinity for growth and first sexual maturity is 10–15 (Wang et al., 2005, 2010). However, shrimp in different life stages are usually tolerant to different salinity ranges. To examine the salinity ranges that juvenile and adult *E. carinicauda* are tolerant to, survival of *E. carinicauda* under different salinity stress was recorded in this study. In addition, the majority of previous studies focused on the salinity stress of shrimp were usually conducted at moderate salinity levels, whereas extreme salinity conditions are more typical for transporting and culturing shrimp (Dong, 1989). Currently, little information is available on the influence of salinity changes on the immune regulation of *E. carinicauda*. To study the immune responses of extreme and moderate salinity stressed *E. carinicauda*, the transcript profiles of *EcLGBP* and *EcproPO* in the proPO system associated with PO activity were determined in this study. The study aimed to obtain the salinity tolerant ranges of *E. carinicauda* of different sizes and gain insight into the proPO system in *E. carinicauda* under salinity stress. This will provide not only a theoretical basis for understanding the proPO system regulation mechanism in the shrimp under salinity stress, but also a technical reference for evaluating immune responses in shrimp aquaculture.

2 Materials and methods

2.1 *Experimental design of salinity stress levels*

A preliminary experiment was designed to confirm the tolerance limit of salinity by setting three low salinity groups (0, 1 and 3) and three high salinity groups (47, 49 and 50). Salinity was adjusted by adding fresh water or marine salts. Ultimately, the cumulative mortality rates under the lowest salinity 0 and the highest salinity 51 were almost 100% at 96 h. Then, ten salinity groups were designed for the survival experiment of juveniles and adults as follows: 1, 3, 6, 10, 20, 30 (control group), 40, 44, 47 and 49. For each group, there were three tanks used for three replicates, and each tank contained ten shrimp. The cumulative survival rates of the two shrimp sizes (juveniles and adults) were evaluated at different salinity levels. The cumulative survival rate was calculated at 24, 48, 72 and 96 h by the following formula: $R = [S_1+S_2+...+S_t]/N_t \times 100\%$, where R (%) indicates the survival rate, S indicates the number of surviving shrimp, t indicates the sampling time, and N_t indicates the total number of shrimp in every tank.

Six salinity groups were designed for the sampling experiments of juveniles and adults as follows: 1, 10, 20, 30 (control group), 40 and 49. For each group, there were three tanks used for three replicates, and each tank contained 50 shrimp. Because juveniles were too small to collect haemolymph, the whole individual was sampled. Six juvenile individuals and haemolymph from six adults were randomly sampled at 0, 24, 48, 72 and 96 h for each salinity group. For adults of each salinity group, 500 μL haemolymph was collected from the shrimp hearts with sterile syringes containing 500 μL anticoagulant solution (1.588 g sodium citrate, 3.92 g sodium chloride, 4.56 g glucose, 0.66 g EDTA-2Na, 200 mL ddH_2O) (Söderhäll and Smith, 1983). Haemolymph was centrifuged at 3 000 r/min at 4°C for 10 min. The supernatant fluid was stored at –20°C for the measurement of PO activity, while the hemocytes were dissolved with Trizol Reagent (Invitrogen, USA) and stored at –80°C for RNA extraction. For juveniles, individuals were ground into powder in liquid nitrogen. The powder was divided into two parts: 0.05 g was dissolved in 450 μL PBS for the measurement of PO activity, and 0.05 g was dissolved in 500 μL Trizol Reagent for RNA extraction.

2.2 *PO activity of juvenile and adult E. carinicauda under different salinity levels*

Phenoloxidase activity was measured spectrophotometrically by recording the formation of dopachrome produced from L-dihydroxyphenylalanine (L-DOPA) based on the modified method by Ashida (1971) and Lei et al. (2001). The optical density of the shrimp's PO activity at 490 nm was measured using an IMARK (model U-2000, Tokyo, Japan). Phenoloxidase activity was expressed as 200 μL 0.1 mol/L buffer solution of potassium phosphate (pH=6.4), followed by 10 μL 0.01 mol/L L-DOPA dopachrome formation per 10 μL of supernatant fluid. All samples for PO activity measure were replicated in triplicate. The activity was expressed as increase in absorbance per minute per 100 μL haemolymph.

2.3 *Expression of candidate genes under different salinity levels*

Quantitative real-time PCR was performed on an ABI PRISM 7500 Sequence Detection System (Applied Biosystems, USA) to investigate the expression patterns of candidate genes in juvenile and adult *E. carinicauda* at different salinity stress levels. The primers of the target genes are shown in Table 1. The 18S rRNA (GenBank accession number: GQ369794) of *E. carinicauda* was used as an internal control to verify the quantitative real-time PCR reaction for its stable expression in different tissues and times (Table 1). The qPCR amplifications were carried out in triplicate in a total volume of 20 μL containing 10 μL SYBR® Premix Ex Taq™ II (2×) (TaKaRa), 2 μL of the cDNA template, 0.8 μL each of F and R primer (10 mmol/L), 0.4 μL ROX Reference Dye II (50×) and 6.0 μL DEPC-treated water. The PCR program was 95°C for 30 s, then 40 cycles of 95°C for 5 s and 60°C for 34 s, followed by 1 cycle of 95°C for 15 s, 60°C for 1 min and 95°C for 15 s. The target expression levels at different salinity stress levels were calculated with $2^{-\triangle\triangle CT}$ methods (Livak and Schmittgen, 2001; Duan et al., 2013). All of the data were presented as mean±SE and subjected to one-way analysis of variance followed by Duncan's mul-

Table 1. Primer sequences used in this study

Primer	Sequence (5′–3′)
18S-F	TATACGCTAGTGGAGCTGGAA
18S-R	GGGGAGGTAGTGACGAAAAAT
EcLGBP-F	GGTCCAACACTTCACCCACT
EcLGBP-R	CGGCTTTCTCGCTGATACTG
EcProPO-F	AAACGATTCGACTACCATCTCCA
EcProPO-R	GTTCATTCGGTTTCCCCTCTC

tiple range tests. Differences were considered significant when $P<0.05$.

3 Results

3.1 *Cumulative survival rates of juvenile and adult E. carinicauda under different salinity stress levels*

Cumulative survival rates (%) are shown in Table 2 for juvenile *E. carinicauda* under different salinity stress levels. Almost all shrimp survived under 3–44 salinity stress levels. Eight or nine of ten shrimp reared at salinity 47 survived in the challenge experiment after 24 h. Only two or three of ten shrimp reared at salinity 49 survived after 48 h; the cumulative survival rates in the salinity 1 treatment group were significantly higher than the salinity 49 treatment group throughout the experimental period ($P<0.05$).

Cumulative survival rates (%) of adult *E. carinicauda* exposed to different salinity conditions are shown in Table 3. The shrimp in the salinity range of 6–44 showed almost 100% survival rates. Seven or eight of ten shrimp reared at salinity 3 or 47 survived in the challenged experiment after 48 h and no significant difference was observed between the two treatment groups ($P>0.05$). The cumulative survival rate of adult shrimp reared at salinity 49 at 24 h was significantly higher than that at salinity 1 ($P<0.05$). Only three or four of ten shrimp reared at salinity 1 or 49 survived in the challenge experiment after 72 h, and no significant difference was observed between the two treatment groups after 48 h ($P>0.05$). In addition, for both juvenile and adult *E. carinicauda*, 100% survival rates of shrimp reared at salinity 10–40 were observed throughout the experimental period.

3.2 *Expression of EcLGBP gene in juvenile and adult E. carinicauda under low and high salinity stress*

The expression profiles of the *EcLGBP* gene in juvenile *E. carinicauda* under low and high salinity stress are shown in Fig. 1. The transcriptional levels of *EcLGBP* in the salinity 1 group were down-regulated at first, and then the levels increased. The *EcLGBP* mRNA expression was up-regulated during the entire experimental period and reached a peak at 48 h in the salinity 10 group. No large change was observed at 24–96 h in the salinity 20 group (Fig. 1a). Under high salinity stress, the expression of *EcLGBP* was down-regulated in the salinity 49 group throughout the experimental period and reached the lowest level at 48 h. No significant changes in the expression of *EcLGBP* were observed in salinity 40 ($P<0.05$) (Fig. 1b).

The expression profiles of the *EcLGBP* gene in adult *E. carinicauda* under low and high salinity stress are shown in Fig. 2. Under low salinity stress levels, the expression levels of *EcLGBP* were up-regulated during the whole experimental period except 48 h in the salinity 1 group and reached a peak at 24 h and 72 h in both the salinity 10 and 20 groups (Fig. 2a). Under high salinity stress, the expression level of *EcLGBP* was up-regulated at 24 h and recovered to the control level after 48 h in the salinity 40 treatment group. In the salinity 49 group, the expression levels of *EcLGBP* fluctuated throughout the experimental period; the expression levels were up-regulated at 24 h, down-regulated at 48–72 h and then gradually up-regulated (Fig. 2b).

3.3 *Expression of the EcproPO gene in juvenile and adult E. carinicauda under low and high salinity stress*

The expression profiles of the *EcproPO* gene in juvenile *E. car-*

Table 2. Cumulative survival rates of juvenile *E. carinicauda* after exposure to different salinity stress levels

Salinity	Time/h			
	24	48	72	96
1	86.67±5.77^{b}	76.67±5.77^{b}	73.33±5.77^{b}	73.33±5.77^{b}
3	100±0.00^{c}	100±0.00^{c}	100±0.00^{d}	100±0.00^{d}
6	100±0.00^{c}	100±0.00^{c}	100±0.00^{d}	100±0.00^{d}
10	100±0.00^{c}	100±0.00^{c}	100±0.00^{d}	100±0.00^{d}
20	100±0.00^{c}	100±0.00^{c}	100±0.00^{d}	100±0.00^{d}
30	100±0.00^{c}	100±0.00^{c}	100±0.00^{d}	100±0.00^{d}
40	100±0.00^{c}	100±0.00^{c}	100±0.00^{d}	100±0.00^{d}
44	96.67±5.77^{c}	96.67±5.77^{c}	96.67±5.77^{d}	96.67±5.77^{d}
47	83.33±5.77^{b}	83.33±5.77^{b}	83.33±5.77^{c}	83.33±5.77^{c}
49	46.67±5.77^{a}	33.33±5.77^{a}	23.33±5.77^{a}	23.33±5.77^{a}

Note: Data without shared letters were significantly different ($P<0.05$) among treatments at the same exposure time.

Table 3. Cumulative survival rates of adult *E. carinicauda* after exposure to different salinity stress levels

Salinity	Time/h			
	24	48	72	96
1	53.33±5.77^{a}	40±10.00^{a}	33.33±5.77^{a}	33.33±5.77^{a}
3	86.67±5.77^{c}	76.67±5.77^{b}	73.33±5.77^{b}	73.33±5.77^{b}
6	96.67±5.77^{d}	96.67±5.77^{c}	96.67±5.77^{c}	96.67±5.77^{c}
10	100±0.00^{d}	100±0.00^{c}	100±0.00^{c}	100±0.00^{c}
20	100±0.00^{d}	100±0.00^{c}	100±0.00^{c}	100±0.00^{c}
30	100±0.00^{d}	100±0.00^{c}	100±0.00^{c}	100±0.00^{c}
40	100±0.00^{d}	100±0.00^{c}	100±0.00^{c}	100±0.00^{c}
44	96.67±5.77^{d}	96.67±5.77^{c}	96.67±5.77^{c}	96.67±5.77^{c}
47	83.33±5.77^{c}	80.00±10.00^{b}	76.67±5.77^{b}	76.67±5.77^{b}
49	63.33±5.77^{b}	46.67±5.77^{a}	40±0.00^{a}	40±0.00^{a}

Note: Data without shared letters were significantly different ($P<0.05$) among treatments at the same exposure time.

inicauda under low and high salinity stress are shown in Fig. 3. Under low salinity stress, the expression of *EcproPO* was up-regulated compared with the control group in the salinity 1 group throughout the experimental period except at 1 h, and the highest level was detected at 96 h. In the salinity 10 group, *EcproPO* mRNA expression was first up-regulated and then was down-regulated. In the salinity 20 group, the expression of *EcproPO* had no great change (Fig. 3a). Under high salinity stress, the expression levels of *EcproPO* were down-regulated at 24–48 h and then increased. In the salinity 49 treatment group, down-reg-

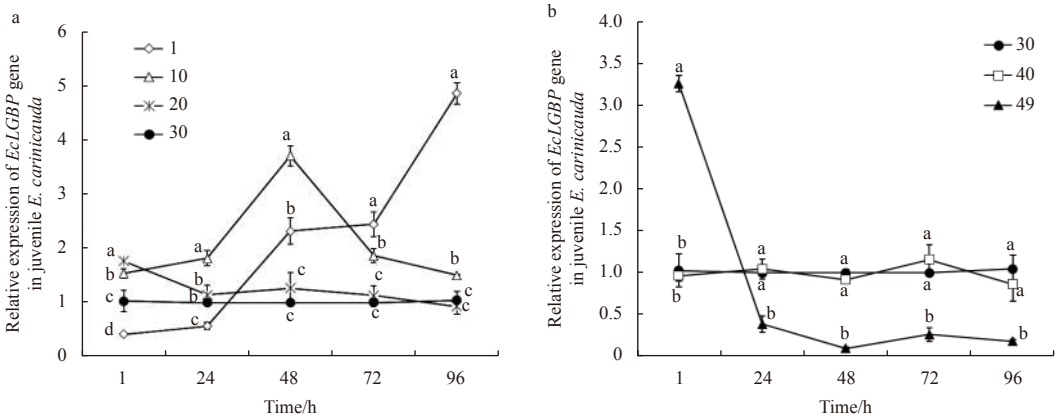

Fig. 1. The expression profiles of the *EcLGBP* gene in juvenile *E. carinicauda* after low salinity (a) and high salinity (b) stress. Vertical bars represent the mean±SE (n=3). Data without shared letters were significantly different (P<0.05) among treatments at the same exposure time.

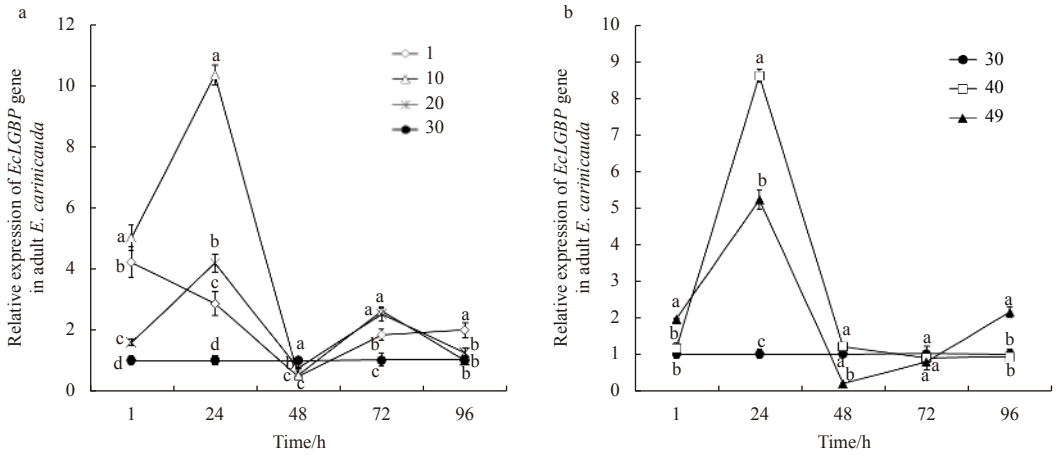

Fig. 2. The expression profiles of the *EcLGBP* gene in adult *E. carinicauda* after low salinity (a) and high salinity (b) stress. Data without shared letters were significantly different (P<0.05) among treatments at the same exposure time.

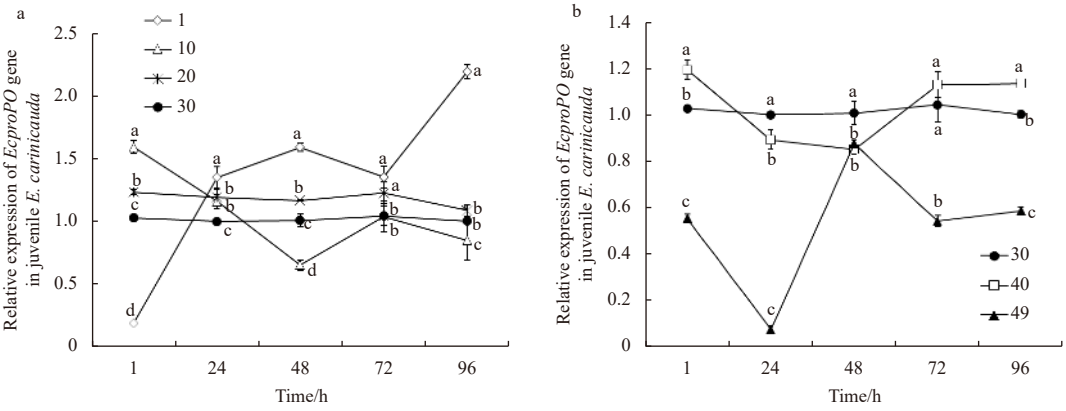

Fig. 3. The expression profiles of the *EcproPO* gene in juvenile *E. carinicauda* after exposure to low salinity (a) and high salinity (b) stress. Data without shared letters were significantly different (P<0.05) among treatments at the same exposure time.

ulated expression of *EcproPO* was detected throughout the experimental period compared with the salinity 30 group (Fig. 3b).

The expression profiles of the *EcproPO* gene in adult *E. carinicauda* under low and high salinity stress are shown in Fig. 4. Under low salinity stress, the expression profiles of *EcproPO* showed up-regulated and down-regulated changes with two-peaks at 24 h and 48 h, respectively (Fig. 4a). Under high salinity stress, mRNA expression was up-regulated at 24 h and then recovered to the normal level. In the salinity 49 treatment group, the transcriptional levels of *EcproPO* mRNA were up-regulated at 24, 72 and 96 h and down-regulated at 48 h (Fig. 4b).

3.4 *PO activity of juvenile and adult E. carinicauda under low and high salinity stress*

Changes of PO activity of juvenile *E. carinicauda* under low and high salinity stress are shown in Fig. 5. Compared with the control group (salinity 30), under low salinity stress, the PO activity showed significant decreases after transfer to the extremely low salinity condition (salinity 1). In the salinity 10 treatment group, the maximal reduction of PO activity appeared at 24 h, and then the PO activity increased gradually and recovered at 96 h. No differential PO activity was observed between the salinity 20 and 30 groups after 24 h (Fig. 5a). Under high salinity stress, PO activities in the salinity 40 treatment group in the first 24 h were higher than that in the salinity 30 group and then recovered to the normal level. Shrimp PO activities under extremely high salinity stress (salinity 49) were always lower than those in the salinity 30 group throughout the experiment (Fig. 5b). Phenoloxidase activities in low salinities were higher than high salinities.

For *E. carinicauda* adults, changes of PO activity under low and high salinity stress are shown in Fig. 6. Under sudden low salinity stress, the PO activity had a waving trend (Fig. 6a). Under high salinity stress, PO activity in the salinity 40 treatment group showed no obvious difference compared to the salinity 30 group. The PO activities in the salinity 49 treatment group were higher at 1, 24, 72 and 96 h than those in the salinity 30 group (Fig. 6b).

4 Discussion

Acute changes of salinity can significantly effect the survival and immunity of crustaceans, even though they have a greater ability to survive extreme salinity conditions (Le Moullac et al., 1998; Jiravanichpaisal et al., 2004; Li and Chen, 2008; Wang and Chen, 2006; Pan et al., 2010). Previous studies have demonstrated that the optimum salinity range for farming *E. carinicauda* is between 20–28 (Wang et al., 2005). In this study, *E. carinicauda* juveniles could survive at a low salinity of 3 and a high salinity of 40 with survival rates more than 95%, indicating a strong tolerance to salinity changes. In addition, the survival rates of *E. carinicauda* juveniles under low salinity stress were higher than those of high salinity stress, indicating that the *E. carinicauda* juveniles might have stronger tolerance to low salinity conditions than high salinity conditions. For *E. carinicauda*

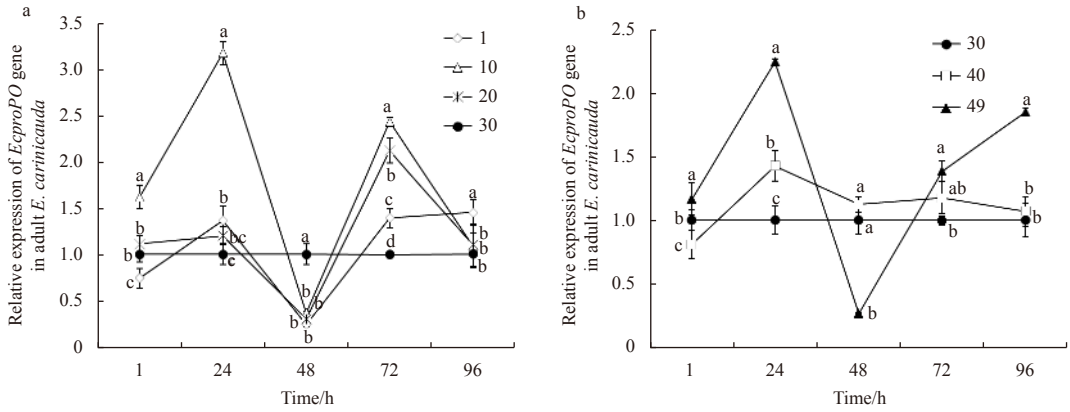

Fig. 4. The expression profiles of the *EcproPO* gene in adult *E. carinicauda* after low salinity (a) and high salinity (b) stress. Data without shared letters were significantly different (P<0.05) among treatments at the same exposure time.

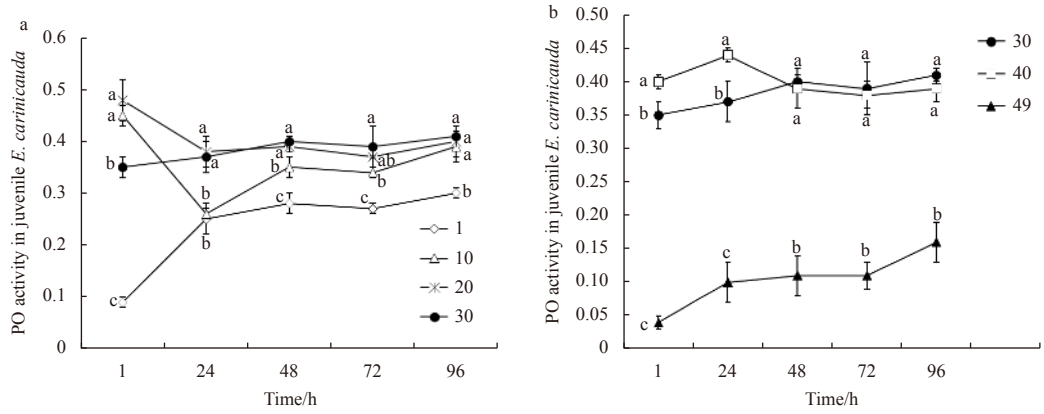

Fig. 5. Phenoloxidase (PO) activity of juvenile *E. carinicauda* after exposure to low salinity (a) and high salinity (b) stress treatments. Data without shared letters were significantly different (P<0.05) among treatments at the same exposure time.

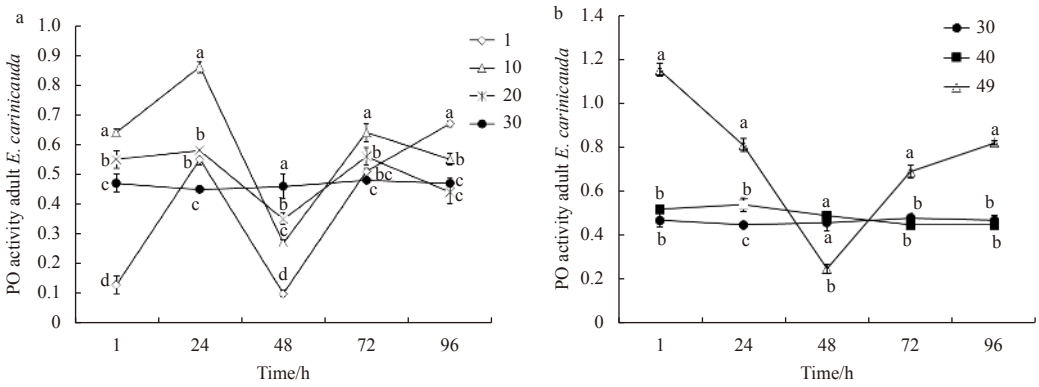

Fig. 6. Phenoloxidase (PO) activity of adult *E. carinicauda* after exposure low salinity (a) and high salinity (b) stress treatments. Data without shared letters were significantly different (P<0.05) among treatments at the same exposure time.

adults, survival rates at salinity 1 were significantly less than that at salinity 3. Gu et al. (2004) reported that the survival rate of *E. carinicauda* was drastically reduced when salinity decreased below 1.08, which was similar to our results. Our preliminary study showed that the salinity tolerance range of adult *E. carinicauda* was 6–44, which was narrower than that of juveniles.

As a key immune gene, the expression of *LGBP* has been used to evaluate the effect of salinity stress in crustaceans (Lin et al., 2012). For juvenile *E. carinicauda*, the initially down-regulated expression levels of *LGBP* under 1 salinity stress indicated that the immune system might be weakened by extremely low salinity at the onset of salinity stress. Then, the expression levels of *LGBP* were up-regulated, demonstrating that *EcLGBP* could be related to the induction of the innate immune system for resisting short term detrimental consequences from low salinity. It is well known that crustaceans are easily vulnerable to diseases under high stresses (Vargas-Albores et al., 1998; Cheng and Chen, 2000). Hence, the down-regulation of *EcLGBP* mRNA at high salinity conditions implied that immune molecules in the defense system of juveniles were inhibited under high salinity stress. For the adult *E. carinicauda*, *EcLGBP* expression was initially up-regulated under all salinity stress treatments, which showed that the induction of this gene could respond to variation of the salinity timely. Further, the fluctuation of the *EcLGBP* expression levels at 48–96 h might be related to the melanization process and the loss of reproductive capacity (De Gregorio et al., 2002; Pascual et al., 2003).

The proPO system is considered a constituent of the humoral immune system and can be activated by different chemical and several microbial elicitors in crustaceans (Hernández-López et al., 1996). For juvenile *E. carinicauda*, the expression levels of *EcproPO* were negatively affected by hyper-salinity, which could lead to a reduction of the immunity of shrimp. The up-regulated expressions of *EcproPO* under extremely low salinity stress suggested that this gene played an important role in low salinity conditions. The expression tendency of *proPO* in juveniles in this study was partially in agreement with the preceding observation in gills of *E. carinicauda* after low salinity stress (4–25) (Li et al., 2015). Previous studies have reported that prophenoloxidase-activating enzyme 1a was up-regulated in *L. vannamei* in response to low salinity, suggesting that *L. vannamei* induced its phenoloxidation cascade and cleaved *proPO* to release PO after low salinity stress (Nikapitiya et al., 2014). For adult *E. carinicauda*, the significantly up-regulated expression levels of *EcproPO* under both high and low salinity stress indicated that salinity changes in the environment could induce the immune responses in crustaceans. Therefore, *EcproPO* could be considered a responsive gene and potential candidate for developing gene markers to evaluate shrimp immunity variations in the environment.

Phenoloxidase is the terminal enzyme in the proPO system that has been proposed as a potential health indicator in shrimp haemolymph (Joseph and Philip, 2007). In the present study, for juvenile *E. carinicauda*, the PO activity decreased in extreme hypo/hyper-salinity treatments, while initially increased in moderate hypo/hyper-salinity, which indicated that the appropriate hypo/hyper-salinity could increase the immune system, but short-term extremely low/high salinity could weaken immune protection potentially resulting in death. Further, the PO activity values were higher in salinity 20–40 than the values in other salinity treatments, suggesting that juvenile *E. carinicauda* reared in salinity 20–40 should be the optimal salinity range to maintain the immune system. Moreover, the PO activity values in hypo-salinity conditions were relatively higher than that in hyper-salinity, which indicated that juveniles might have higher tolerance to resistant pathogens in low salinity. An increasing trend in PO activity of *Panulirus homarus* from salinity 20 to 45 could be due to significant reduction in plasma inhibitors regulating the proPO system (Verghese et al., 2007), which was in agreement with the tendency of PO activity in this study. For adult *E. carinicauda*, PO activity increased directly under salinity stress in the first 24 h, which might be correlated with the higher resistance of shrimp against pathogen infection by increasing its immunity. White shrimp, *L. vannamei*, transferred from a salinity of 35 to 25, 20, and 15 exhibited significant decreases in immunity as evidenced by reductions in immune parameters including PO activity after 1–6 h (Li et al., 2010). Hence, adult shrimp farming should be maintained at a constantly high salinity level to prevent exacerbated decreases in innate immunity of shrimp when infected by pathogens, as low-salinity stress led to mortality.

In conclusion, *E. carinicauda* juveniles could survive in a wider range of salinity conditions than adults. For juvenile *E. carinicauda*, the expression levels of *EcLGBP* and *EcProPO* were up-regulated against low salinities, and PO activities in low salinities were higher compared to those in high salinities. For adult *E. carinicauda*, the expression profiles of *EcLGBP* and *EcproPO* had a different trend of up-regulation under hypo/hyper-salinity stress treatments. The salinity tolerance range of immunity for juvenile and adult *E. carinicauda* is 20–40 and 30–40, respectively.

References

Ai Huashui, Huang Yongchun, Li Sedong, et al. 2008. Characterization of a prophenoloxidase from hemocytes of the shrimp *Litopenaeus vannamei* that is down-regulated by white spot syndrome virus. Fish & Shellfish Immunology, 25(1–2): 28–39

Amparyup P, Charoensapsri W, Tassanakajon A. 2013. Prophenoloxidase system and its role in shrimp immune responses against major pathogens. Fish & Shellfish Immunology, 34(4): 990–1001

Ashida M. 1971. Purification and characterization of pre-phenoloxidase from hemolymph of the silkworm *Bombyx mori*. Archives of Biochemistry and Biophysics, 144(2): 749–762, doi: 10.1016/0003-9861(71)90383-3

Cerenius L, Lee B L, Söderhäll K. 2008. The proPO-system: pros and cons for its role in invertebrate immunity. Trends in Immunology, 29(6): 263–271, doi: 10.1016/j.it.2008.02.009

Cerenius L, Söderhäll K. 2004. The prophenoloxidase-activating system in invertebrates. Immunological Reviews, 198(1): 116–126, doi: 10.1111/j.0105-2896.2004.00116.x

Chen Jinghua, Mai Kangsen, Ma Hongming, et al. 2007. Effects of dissolved oxygen on survival and immune responses of scallop (*Chlamys farreri* jones et preston). Fish & Shellfish Immunology, 22(3): 272–281

Cheng W, Chen J C. 2000. Effects of pH, temperature and salinity on immune parameters of the freshwater prawn *Macrobrachium rosenbergii*. Fish & Shellfish Immunology, 10(4): 387–391

Cheng W, Liu C H, Tsai C H, et al. 2005. Molecular cloning and characterisation of a pattern recognition molecule, lipopolysaccharide- and β-1, 3-glucan binding protein (LGBP) from the white shrimp *Litopenaeus vannamei*. Fish & Shellfish Immunology, 18(4): 297–310

Cieluch U, Charmantier G, Grousset E, et al. 2005. Osmoregulation, immunolocalization of Na^+/K^+-ATPase, and ultrastructure of branchial epithelia in the developing brown shrimp, *Crangon crangon* (Decapoda, Caridea). Physiological and Biochemical Zoology, 78(6): 1017–1025, doi: 10.1086/432856

De Gregorio E, Han S J, Lee W J, et al. 2002. An immune-responsive Serpin regulates the melanization cascade in *Drosophila*. Developmental Cell, 3(4): 581–592, doi: 10.1016/S1534-5807(02)00267-8

de la Vega E, Degnan B M, Hall M R, et al. 2007. Differential expression of immune-related genes and transposable elements in black tiger shrimp (*Penaeus monodon*) exposed to a range of environmental stressors. Fish & Shellfish Immunology, 23(5): 1072–1088

Dong Cunyou. 1989. The biological properties of *Exopalaemon carinicauda* in Zhujiang river estuary. Sichuan Journal of Zoology (in Chinese), 8(4): 36–38

Duan Yafei, Liu Ping, Li Jitao, et al. 2013. cDNA cloning, characterization and expression analysis of peroxiredoxin 5 gene in the ridgetail white prawn *Exopalaemon carinicauda*. Molecular Biology Reports, 40(12): 6569–6577, doi: 10.1007/s11033-013-2702-4

Gu Jun, Li Guofeng, Zhang Zhenhua, et al. 2004. The response of *Exopalaemon carinicauda* to acute salinity stress. Journal of Aquaculture (in Chinese), 25(2): 39–40

Hernández-López J, Gollas-Galván T, Vargas-Albores F. 1996. Activation of the prophenoloxidase system of the brown shrimp (*Penaeus californiensis* Holmes). Comparative Biochemistry and Physiology Part C: Pharmacology, Toxicology and Endocrinology, 113(1): 61–66, doi: 10.1016/0742-8413(95)02033-0

Hu Fawen. 2008. Effect of dopamine injection, salinity changes on the prophenoloxidase system and defence parameters of the White Shrimp *Litopenaeus vannamei* (in Chinese) [dissertation]. Qingdao: Ocean University of China

Ishwarya R, Jayanthi S, Muthulakshmi P, et al. 2016. Immune indices and identical functions of two prophenoloxidases from the haemolymph of green tiger shrimp *Penaeus semisulcatus* and its antibiofilm activity. Fish & Shellfish Immunology, 51: 220–228

Jiravanichpaisal P, Puanglarp N, Petkon S, et al. 2007. Expression of immune-related genes in larval stages of the giant tiger shrimp, *Penaeus monodon*. Fish Shellfish Immunol, 23(4): 815–824, doi: 10.1016/j.fsi.2007.03.003

Jiravanichpaisal P, Söderhäll K, Söderhäll I. 2004. Effect of water temperature on the immune response and infectivity pattern of white spot syndrome virus (WSSV) in freshwater crayfish. Fish & Shellfish Immunology, 17(3): 265–275

Johansson M W, Soderhall K. 1989. Cellular immunity in crustaceans and the proPO system. Parasitology Today, 5(6): 171–176, doi: 10.1016/0169-4758(89)90139-7

Joseph A, Philip R. 2007. Acute salinity stress alters the haemolymph metabolic profile of *Penaeus monodon* and reduces immunocompetence to white spot syndrome virus infection. Aquaculture, 272(1–4): 87–97, doi: 10.1016/j.aquaculture.2007.08.047

Kumlu M, Eroldogan O T, Aktas M. 2000. Effects of temperature and salinity on larval growth, survival and development of *Penaeus semisulcatus*. Aquaculture, 188(1–2): 167–173, doi: 10.1016/S0044-8486(00)00330-6

Le Moullac G, Soyez C, Saulnier D, et al. 1998. Effect of hypoxic stress on the immune response and the resistance to vibriosis of the shrimp *Penaeus stylirostris*. Fish & Shellfish Immunology, 8(8): 621–629

Lee S Y, Wang Ruigong, Söderhäll K. 2000. A lipopolysaccharide- and β-1, 3-glucan-binding protein from hemocytes of the freshwater crayfish *Pacifastacus leniusculus* Purification, characterization, and cDNA cloning. Journal of Biological Chemistry, 275(2): 1337–1343, doi: 10.1074/jbc.275.2.1337

Lei Zhiwen, Huang Jie, Yang Bing, et al. 2001. Immune factors in haemolymph supernatant of *Penaeus chinensis* infected by WSSV. Journal of Fishery Sciences of China (in Chinese), 8(4): 46–51

Li Changche, Chen J C. 2008. The immune response of white shrimp *Litopenaeus vannamei* and its susceptibility to *Vibrio alginolyticus* under low and high pH stress. Fish & Shellfish Immunology, 25(6): 701–709

Li Jitao, Han Junying, Chen Ping, et al. 2012. Cloning of a heat shock protein 90(HSP90) gene and expression analysis in the ridgetail white prawn *Exopalaemon carinicauda*. Fish & Shellfish Immunology, 32(6): 1191–1197

Li Jitao, Ma Peng, Liu Ping, et al. 2015. The roles of Na^+/K^+-ATPase α-subunit gene from the ridgetail white prawn *Exopalaemon carinicauda* in response to salinity stresses. Fish & Shellfish Immunology, 42(2): 264–271

Li Fuhua, Xiang Jianhai. 2013. Recent advances in researches on the innate immunity of shrimp in China. Developmental & Comparative Immunology, 39(1–2): 11–26

Li Changche, Yeh S T, Chen J C. 2010. Innate immunity of the white shrimp *Litopenaeus vannamei* weakened by the combination of a *Vibrio alginolyticus* injection and low-salinity stress. Fish & Shellfish Immunology, 28(1): 121–127

Lin Yong-Chin, Chen Jiann-Chu, Li Changche, et al. 2012. Modulation of the innate immune system in white shrimp *Litopenaeus vannamei* following long-term low salinity exposure. Fish & Shellfish Immunology, 33(2): 324–331

Liu Fengsong, Li Fuhua, Dong Bo, et al. 2009. Molecular cloning and characterisation of a pattern recognition protein, lipopolysaccharide and β-1, 3-glucan binding protein (LGBP) from Chinese shrimp *Fenneropenaeus chinensis*. Molecular Biology Reports, 36(3): 471–477, doi: 10.1007/s11033-007-9203-2

Livak K J, Schmittgen T D. 2001. Analysis of relative gene expression data using real-time quantitative PCR and the $2^{-\Delta\Delta C_T}$ method. Methods, 25(4): 402–408, doi: 10.1006/meth.2001.1262

Nikapitiya C, Kim W S, Park K, et al. 2014. Identification of potential markers and sensitive tissues for low or high salinity stress in an intertidal mud crab (*Macrophthalmus japonicus*). Fish & Shellfish Immunology, 41(2): 407–416

Pan Luqing, Xie Peng, Hu Fawen. 2010. Responses of prophenoloxidase system and related defence parameters of *Litopenaeus vannamei* to low salinity. Journal of Ocean University of China, 9(3): 273–278, doi: 10.1007/s11802-010-1711-3

Pan Luqing, Zhang Linjuan, Liu Hongyu. 2007. Effects of salinity and pH on ion-transport enzyme activities, survival and growth of *Litopenaeus vannamei* postlarvae. Aquaculture, 273(4): 711–720, doi: 10.1016/j.aquaculture.2007.07.218

Pascual C, Sánchez A, Sánchez A, et al. 2003. Haemolymph metabolic variables and immune response in *Litopenaeus setiferus* adult males: the effect of an extreme temperature. Aquaculture, 218(1–4): 637–650, doi: 10.1016/S0044-8486(02)00300-9

Söderhäll K, Cerenius L. 1992. Crustacean immunity. Annual Review of Fish Diseases, 2: 3–23, doi: 10.1016/0959-8030(92)90053-Z

Söderhäll K, Smith V J. 1983. Separation of the haemocyte populations of *Carcinus maenas* and other marine decapods. Developmental & Comparative Immunology, 7(2): 229–239

Vargas-Albores F, Hinojosa-Baltazar P, Portillo-Clark G, et al. 1998. Influence of temperature and salinity on the yellowleg shrimp, *Penaeus californieinsis* Holmes, prophenoloxidase system. Aquaculture Research, 29(8): 549–553, doi: 10.1046/j.1365-2109.1998.00235.x

Verghese B, Radhakrishnan E V, Padhi A. 2007. Effect of environmental parameters on immune response of the Indian spiny lobster, *Panulirus homarus* (Linnaeus, 1758). Fish & Shellfish Immunology, 23(5): 928–936

Wang F I, Chen J C. 2006. Effect of salinity on the immune response of tiger shrimp *Penaeus monodon* and its susceptibility to *Photobacterium damselae* subsp. *Damselae*. Fish & Shellfish Immunology, 20(5): 671–681

Wang Xingqiang, Sudha K, Mei Cao, et al. 2010. Effects of low salinity and low temperature on survival, growth, and energy budget of juvenile *Exopalaemon carinicauda*. Journal of Shellfish Research, 29(4): 1035–1041, doi: 10.2983/035.029.0405

Wang Xingqiang, Yan Binlun, Ma Shen, et al. 2005. Study on the biology and cultural ecology of *Exopalaemon carinicauda*. Shandong Fisheries, 22(8): 21–23

Xu Wenjun, Xie Jianjun, Shi Hui, et al. 2010. Hematodinium infections in cultured ridgetail white prawns, *Exopalaemon carinicauda*, in eastern China. Aquaculture, 300(1–4): 25–31, doi: 10.1016/j.aquaculture.2009.12.024

Yang Ya'nan, Bao Chenchang, Liu An, et al. 2014. Immune responses of prophenoloxidase in the mud crab *Scylla paramamosain* against *Vibrio alginolyticus* infection: *in vivo* and *in vitro* gene silencing evidence. Fish & Shellfish Immunology, 39(2): 237–244

Zhang Chengsong, Li Fuhua, Xiang Jianhai. 2014. Effect of salinity on growth and first sexual maturity of *Exopalaemon carinicauda* (Holthuis, 1950). Chinese Journal of Oceanology and Limnology, 32(1): 65–70, doi: 10.1007/s00343-014-3040-7

Zhao Qun, Pan Luqing, Ren Qin, et al. 2015. Digital gene expression analysis in hemocytes of the white shrimp *Litopenaeus vannamei* in response to low salinity stress. Fish & Shellfish Immunology, 42(2): 400–407

Acta Oceanol. Sin., 2020, Vol. 39, No. 4, P. 65–72
https://doi.org/10.1007/s13131-020-1583-3
http://www.hyxb.org.cn
E-mail: hyxbe@263.net

Dietary separation between co-occurring copepods in a food-limited tropical coral reef of the Sanya Bay

Simin Hu[1, 2], Tao Li[1, 3]*, Sheng Liu[1, 2]*, Hui Huang[1, 3]

[1] Key Laboratory of Tropical Marine Bio-Resources and Ecology, South China Sea Institute of Oceanology, Chinese Academy of Sciences, Guangzhou 510301, China

[2] Guangdong Provincial Key Laboratory of Applied Marine Biology, South China Sea Institute of Oceanology, Chinese Academy of Sciences, Guangzhou 510301, China

[3] Tropical Marine Biological Research Station in Hainan, Chinese Academy of Sciences, Sanya 572000, China

Received 19 February 2019; accepted 22 April 2019

Abstract

Food differentiation among coexistent species in the field is important strategy for copepods to acquire materials and maintain population stabilization. *In situ* diet analysis of co-occurring six copepod species in coral waters of the Sanya Bay was conducted using a PCR protocol based on 18S ribosomal gene. Various prey organisms were uncovered, including dinoflagellate, diatom, green algae and plant, protozoa and metazoan. All these spatially co-existing six species showed different dietary diversity, with the food niche breadth (B) ranging from 1.00 (*Temora turbinate* in morning) to 10.68 (*Calanopia elliptica* in night). While food overlap between all these copepods were low, with the average value of the diet niche overlap index being approximately 0.09. Even temporally co-existing species sampled from the same time point fed on different groups of prey items with the food overlap index of 0.04 to 0.07 in midday and night but 0 in morning. As the most important dominant copepod in the Sanya Bay, *Subeucalanus subcrassus* seems to be capable to regulate its feeding, by exhibiting a rhythm of herbivorous feeding in midday and carnivorous feeding in morning and night, to better coordinate with other competitors for utilization of food resources. For most copepods, none of the prey items belonged to the dominant phytoplankton in the ambient water, indicating that copepod can better their survival by widening the choice of potential food resources in food limited environment. The dietary separation observed here might be important strategy for copepod to maintain population stabilization and thriving in the Sanya coastal waters.

Key words: copepod, food partitioning, Sanya Bay, coral reef ecosystem

Citation: Hu Simin, Li Tao, Liu Sheng, Huang Hui. 2020. Dietary separation between co-occurring copepods in a food-limited tropical coral reef of the Sanya Bay. Acta Oceanologica Sinica, 39(4): 65–72, doi: 10.1007/s13131-020-1583-3

1 Introduction

The question of resource partitioning often arises when considering the ecology of plankton in marine ecosystem, which was first discussed as a paradoxical situation of plankton by Hutchinson (1961). Namely, it is very important question how it is possible for plankton to coexist in the same environment competing for the same materials. For maintaining coexistence, these species might exhibit different strategies of resource utilization and thus occupy different niche. Differences in the niche of different species could be important functional traits to express the ecosystem functioning (Aranguren-Riaño et al., 2018). Among all these functional traits, feeding is the most vital process which determines energy supply and thus sustains the stabilization of the cooccurrence of different species (Lee et al., 2012). While it was difficult to perform field observation of food use for different species, especially for small-sized zooplankton.

Copepods are the most abundant zooplankton in marine ecosystem and play an important role in energy transfer to higher trophic levels and many copepod species are often found in the same area with very high abundance (Kleppel, 1993). As most of copepod species showed a similar way using food resources, various feeding strategies had been reported for copepod to deal with the food competition. Laakmann et al. (2009) found that co-occurring large-sized copepod species exhibited different ecological niche by vertical partitioning and different food preferences among water layers in pelagic deep-sea ecosystems (Laakmann et al., 2009; Sato et al., 2011). Unlike the almost homogeneous environment in deep sea, coastal waters were characterized by variable hydrodynamic factors and uneven food environment, and thus copepod in coastal waters was potentially vulnerable to food limitations and they might be especially dependent on sufficient food supply within close range (David et al., 2006). Previous studies using amino acid composition or marker pigment as indicator to distinguish distinct food sources had found that co-occurring copepod showed asymmetric reaction in incubation experiment even there is no apparent resources competition among them in the field (Arroyo et al., 2007).

Although previous studies had shown that dominant zo-

Foundation item: The Strategic Priority Research Program of Chinese Academy of Sciences under contract No. XDA13020102; the National Key Research and Development Program of China under contract No. 2016YFC0502800; the National Natural Science Foundation of China under contract No. 41806188; the Science and Technology Planning Project of Guangdong Province, China under contract No. 2017B030314052.

*Corresponding author, E-mail: litao@scsio.ac.cn; shliu@scsio.ac.cn

oplankton taxa exhibited different trophic level and feeding selectivity in variable coastal environment (Carrasco and Perissinotto, 2011), copepod was found to apply an "opportunistic feeding" strategy in food-limited conditions and had to utilize insufficient food resources according to their availability, which would exacerbate feeding competition among different species (Lee et al., 2012; Lombard et al., 2013; Hu et al., 2014). In this circumstance, it is vital for these co-existence copepods to allocate limited resources properly and efficiently in order to maintain their population stabilization. As it was difficult to perform field observation of food use of copepod, rare data had obtained about exact diets composition of different species in the same community though previous studies using amino acids or pigments analysis had revealed trophic niche of different populations (Guisande et al., 2002). The benefit from development of molecular methods for feeding studies makes it possible now to obtain exact diets information of copepods in natural sea (Nejstgaard et al., 2003; Hu et al., 2014, 2015).

The Sanya Bay located in the southernmost coast of Hainan Island in the South China Sea. With an area of about 120 km^2 and mean depth of 16 m, the bay features several coastal coral reefs situated at Luhuitou, Dongmao Island and Ximao Island (Huang et al., 2003). While in the coastal coral waters, the primary production was low (with an average chlorophyl *a* concentration of about 0.95 mg/m^3) but high biomass of copepod was always observed, with *Subeucalanus*, *Temora*, *Calanopia*, *Paracalanus* and *Acartia* being the most abundant groups (Ke et al., 2011). In our previous study of copepod *in situ* diets conducted in summer 2010, three dominant copepod species, *Temora turbinata*, *S. subcrassus* and *Canthocalanus pauper*, consumed large amount of terrigenous detritus as supplementary food resources in phytoplankton-limited condition (Hu et al., 2015). Considering high concentration of terrigenous materials brought by the Sanya River or coastal land plants, copepod seemed to apply an "opportunistic feeding" strategy in such food-limited environment. As a tropic open bay, seasonal succession of dominant species was not obvious in the Sanya Bay, thus the mechanism supporting coexistence of these copepod groups is of great importance for understanding the production of zooplankton but remains unclear. The aim of this study was to determine *in situ* diet compositions of co-occurring dominant copepod populations by a PCR protocol, which was proved to be effective in detecting copepod preys in field (Hu et al., 2014), in order to demonstrate the food use strategy of copepod in the Sanya coastal waters.

2 Materials and methods

2.1 *Sample collection*

Copepods and ambient water samples were collected at Sta. SY-C (18°13.199′N, 109°28.799′E) near Luhuitou coral waters in the Sanya Bay on May 21, 2011 at three time points (6:00, 12:00, 18:00) (Fig. 1). Copepods were collected using a plankton net (505 μm) and were fixed immediately in neutral Lugol's solution at 2% final concentration. Ambient water samples were also collected using a Niskin bottle and 500 mL was fixed immediately. The samples were covered with black bags and taken to the laboratory for next analysis.

2.2 *Microscopic analysis of water sample*

Water samples were gently mixed by inversion and 50 mL subsample was taken into a 50 mL centrifuge tube. Then the tube was kept for >24 h and concentrated to 1 mL according to the Utermöhl Settling method. From the concentrated samples plankton were identified and enumerated in a Sedgwick-Rafter counting chamber under an Olympus BX51 microscope.

2.3 *In situ diet analysis of copepod samples*

Dominant copepod species from different time were identified under stereomicroscope and sorted. The sorted copepod samples were serially rinsed thoroughly with autoclaved 0.45 μm filtered seawater for >3 times and then with sterilized water for several times, examined under stereomicroscope to ensure no at-

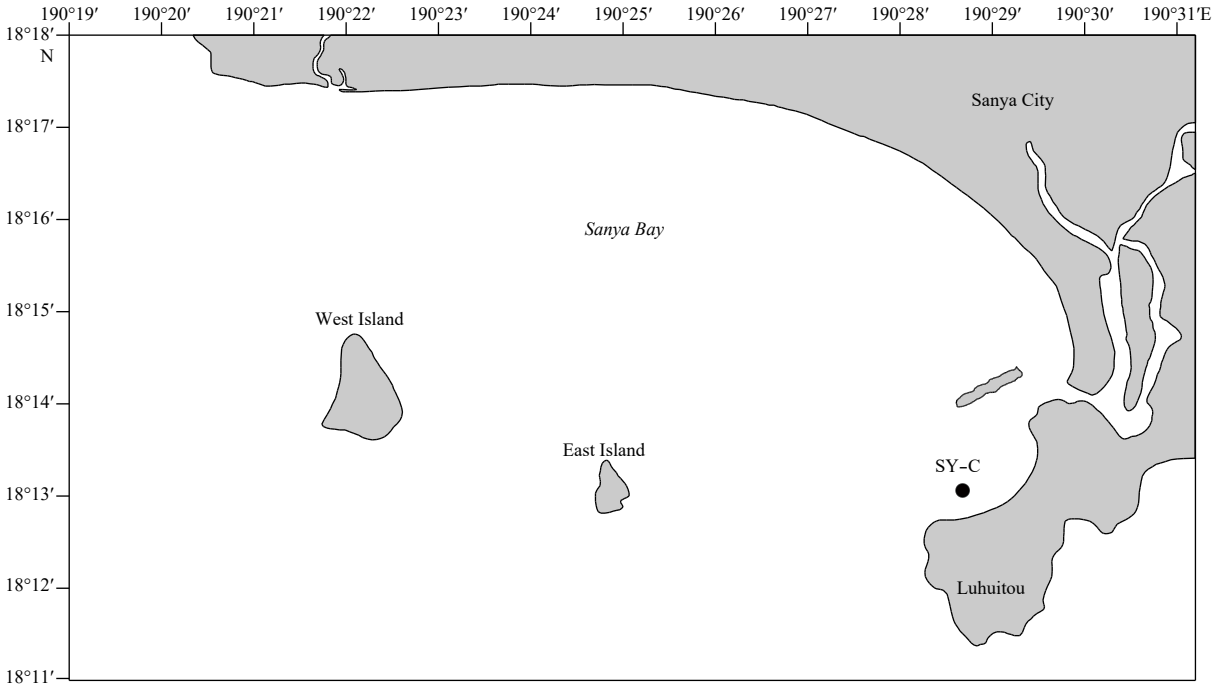

Fig. 1. Sampling location (SY-C) in coral waters near Luhuitou of the Sanya Bay.

tachment of other visible organisms on the surface body, and homogenized in a microfuge tube using a disposable micro-pestle. The homogenates were re-suspended in 500 μL DNA buffer (1% SDS, 100 mmol/L EDTA, and 200 μg/mL proteinase K) and incubated for 3 d at 55°C for thorough cell lysis and DNA from all samples were extracted. 18S rDNA of copepod samples were PCR amplified using the copepod-excluding eukaryote-inclusive primer set (CEEC) and the PCR products were purified, cloned and 30–50 clones for each sample were picked randomly and sequenced (Hu et al., 2014).

2.4 *Phylogenetic analyses*

Sequences obtained were searched against the GenBank database using the Basic Local Alignment Search Tool. The best hits were aligned with new sequences obtained in this study using CLUSTAL W (1.8) after the primer sequences were trimmed. Then the alignment results were exported to MEGA 4.0 and a Neighbor Joining (NJ) tree was inferred from the aligned dataset.

2.5 *Food niche overlap analysis*

A percentage of each sequence from the whole clone library of each copepod sample was used to estimate the relative diet proportion. The percentage was then recorded to calculate diet diversity, which was described by food niche breadth (B), a reciprocal of Simpson's diversity index, following Levins (1968):

$$B = \frac{1}{\sum_{i=1}^{n} P_i^2}, \tag{1}$$

where P_i is the relative abundance of prey i and n is the total taxa of all the preys in the diet of copepod.

Diet niche overlap (O) was also calculated by the percentage of overlapped diet species between different copepod species (Pianka, 1973):

$$O_{xy} = 1 - \frac{1}{2} \times \sum \left| P_{ix} - P_{iy} \right|, \tag{2}$$

where x and y denote different species of copepod.

Bipartite network was also used based on percentage of each diet on species-level, to intuitively reflect main dietary specialization and overlaps of different copepods, and visualization was performed with the R package "bipartite".

3 Results

3.1 *Phytoplankton and copepod community*

Microscopic analysis of ambient water identified 35 phytoplankton species totally, including diatom, dinoflagellates, chrysophyta and cyanobacteria (Table 1). Diatom dominated the community both in species numbers and cell density with 68.4% and 74.2%, 85% and 95.9%, 85% and 52.6% in morning, midday and night, respectively. And the cell density presented an increase trend in time series morning (9.7×10^3 cells/L), midday (25.4×10^3 cells/L) and night (73.3×10^3 cells/L). *Skeletonema* sp. was dominant group both in morning and midday, while *Trichodesmium erythraeum* occupied almost half of the total abundance (46.5%) in night. *Rhizosolenia* sp. was also abundant group in midday and night.

Different composition patterns were also observed for copepod community in different time, 13, 10 and 19 species were identified in morning, midday and night, respectively. The highest density of copepods (38.1 ind./m^3) presented in night, being much higher than that in morning (8.26 ind./m^3) and midday (7.93 ind./m^3), respectively. As for the species community, small copepods (<2 mm), such as *Paracalanus*, *Acrocalanus*, *Temora*, *Centropages* and *Acartia*, showed similar but lower densities in morning, midday and night, but occupied almost 95% of total community in midday. Large copepods in genus of *Labidocera*, *Pontella*, *Calanopia* and *Undinula* appeared only in night and dominated the copepod community. *Subeucalanus subcrassus* was the dominant species in all three times, and other species with different sizes, such as *Neocalanus tenuicornis*, *Acrocalanus gibber*, *Temora turbinate*, *Acrocalanus gibber*, *Acartia negligens* and *Calanopia elliptica*, which were sorted out for diets analysis, were also abundant in different community.

Table 1. Phytoplankton community of ambient water from different times

	Species number	Percentage /%	Density/10^3 cells·L^{-1}	Percentage /%
Morning				
Diatom	13	68.4	7.2	74.2
Dinoflagellate	5	26.3	2.2	22.6
Others	1	5.3	0.3	3.2
Sum	19	100	9.7	100
Midday				
Diatom	17	85	24.3	95.9
Dinoflagellate	3	15	1.0	4.1
Others				
Sum	20	100	25.4	100
Night				
Diatom	17	85	38.6	52.6
Dinoflagellate	2	10	0.6	0.9
Others	1	5	34.1	46.5
Sum	20	100	73.3	100

Note: Others include Cyanobacteria (mostly) and Chrysophyta.

3.2 *Food diversity*

The 18S rDNA clone libraries were constructed for diet analyses of all these six species of copepod from different time points. Different taxa (1–10) of preys were revealed by randomly sequenced clones for each library. Chao1 estimates indicated that the actual numbers of taxa were similar with sequenced taxa, showing adequate coverage of diversity (Table 2). Diverse diets were detected for all the copepods as shown by the wide phylogenetic range and taxonomic distribution of these prey species

Table 2. Diversity indices of prey organisms in the eight copepod samples analyzed

Sample ID	Taxa_S	Individuals	Simpson_1-D	Shannon_H	Chao-1
Subsu-m	2	15	0.124 4	0.244 9	2
Subsu-md	6	23	0.544 4	1.166	7.5
Subsu-n	3	12	0.291 7	0.566 1	4
Temtu-m	1	15	0	0	1
Neote-m	2	22	0.0867 8	0.184 9	2
Acrne-md	3	20	0.625	1.04	3
Acrgi-md	3	17	0.214 5	0.443 8	4
Calel-n	10	27	0.776 4	1.867	12.5

Note: Subsu represents *Subeucalanus subcrassus*, Temtu *Temora turbinate*, Neote *Neocalanus tenuicornis*, Acrne *Acartia negligens*, Acrgi *Acrocalanus gibber*, Calel *Calanopia elliptica*, m morning, md midday, and n night.

(Fig. 2), including phytoplankton (e.g., diatom, dinoflagellate, green algae), plant, protozoa and different groups of metazoan (e.g., cnidarian, tunicate, crustacean). Metazoan was among the most abundant and diverse groups of prey items, with a variety of crustacean preys, such as *Erythrops* (Mysis), *Processidae*, and *Galathea* (coral shrimp). Other metazoan included ctenophora, cnidaria (jellyfish), tunicate (appendicularia), and Echinodermata (brittle star). Diatoms were also among the most diverse groups of prey items, including *Coscinodiscus*, *Chaetoceros*, *Skeletonema*, *Proboscia* and *Nitzschia*, which were all microscopic

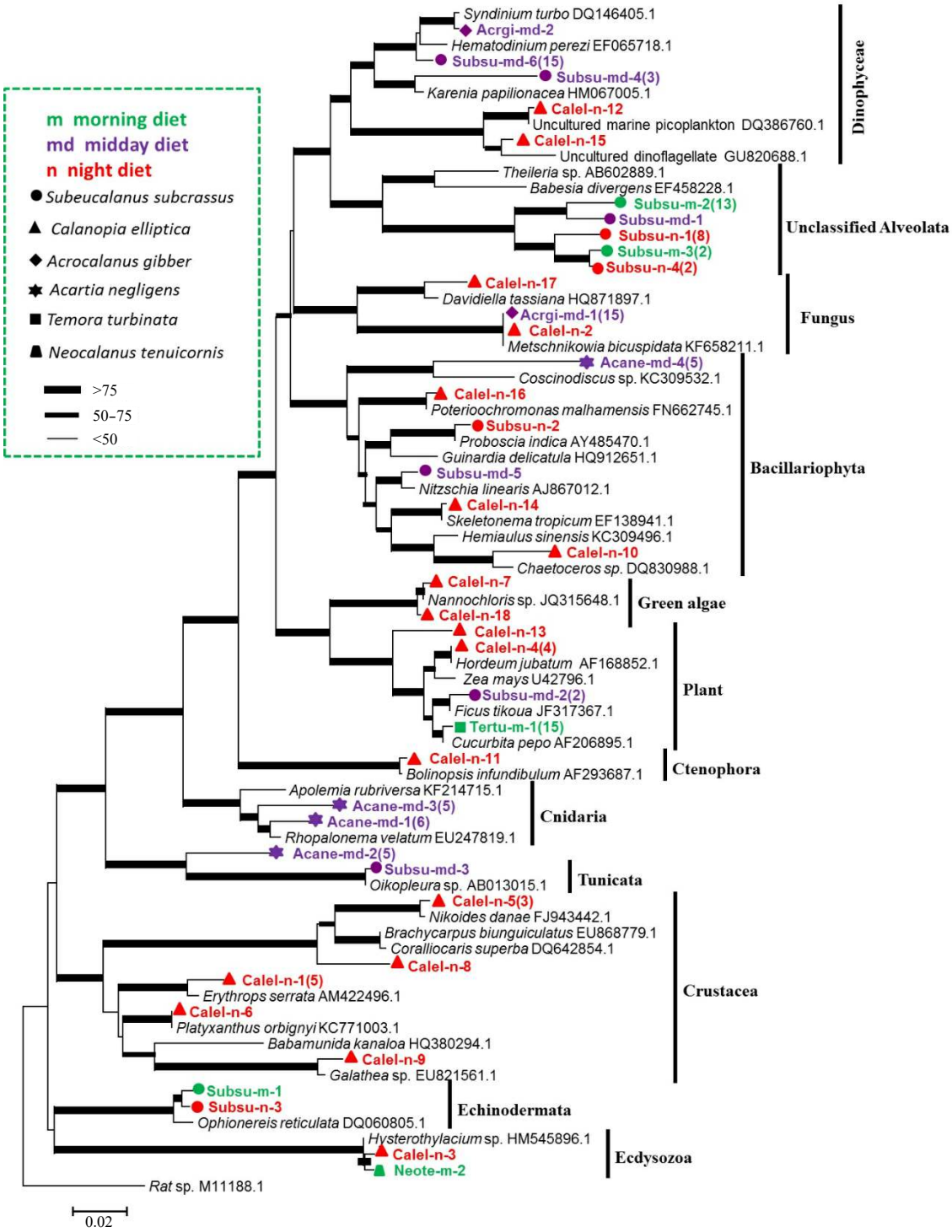

Fig. 2. 18S rDNA phylogram for different copepod species from different sampling time in the Sanya Bay. Neighbour-Joining (NJ) phylogenetic tree was shown here and only representative clones from each major lineage were included in the tree. Different colors denote different sampling time and different symbols denote different copepods. Canle-n represents *Calanopia elliptica* from night, Temtu-m *Temora turbinate* from morning, Neote-m *Neocalanus tenuicornis* from morning, Acane-md *Acartia negligens* from midday, Acrgi-md *Acrocalanus gibber* from midday, Subsu-m *Subeucalanus subcrassus* from morning, Subsu-md *S. subcrassus* from midday, and Subsu-n *S. subcrassus* from night.

identified in the ambient water. Relatively, dinoflagellates were less abundant prey items only for some copepod species (e.g., *S. subcrassus*), with *Karenia*, *Syndinium* and two unclassified species being detected. Land plant was also abundant prey items for some copepod species (e.g., *C. elliptica*, *T. turbinate*, *S. subcrassus*), with *Hordeum*, *Ficus* and *Cucurbita* being detected. A species of green algae (*Nannochloris* sp.) was also detected in *C. elliptica*. Some other organisms, such as Fungus and unclassified Alveolata, were also detected in some copepod species.

3.3 *Diet composition of different species*

The diets composition of spatially co-occurring six species were different from each other as shown by the wide taxonomic distribution of these prey species and diverse phylogenetic affiliations that received strong bootstrap supports (Fig. 2). Large copepod *S. subcrassus* fed mostly on protozoa and dinoflagellates, and *N. tenuicornis* diet consisted of a large fraction of metazoan and fungus. While another large copepod *C. elliptica*, which was the most abundant species in night, exhibited a much wider prey spectrum, including diatom, dinoflagellates, green algae and plant, ctenophore and a large amount of crustacean. Relatively, small copepods showed much lower diet diversity. *Acartia negligens* consumed a large fraction of metazoan (e.g. cnidarian, appendicularia) and a little diatom (*Coscinodiscus* sp.), while large amount of fungus and plant were detected in *A. gibber* and *T. turbinate*. Generally, metazoan, plant and phytoplankton were common prey items for these copepods, but with different preference in different populations. For instance, metazoan dominated the diet of *A. negligen* with two species of cnidarian, and *C. elliptica*'s with a large fraction of crustacean and a species of ctenophore, respectively. *Proboscia indica* and *Skeletonema tropicum,* which were abundant in ambient water, were detected in the diet of *S. subcrassus* and *C. elliptica*, respectively.

Food niche breadth (*B*) of six copepod species differed greatly from each other. *Calanopia elliptica* showed the highest *B* index of 10.48, followed by *A. negligens* with a value of 4. The *B* index for other species varied from 1.0 to 2.2.

On the other hand, although temporally co-exiting copepod populations sharing the same restricted food resources, diet differentiation was also observed. Thirty-eight feeding events were observed totally by the bipartite network analysis (Fig. 3). All these copepod species showed very limited food overlap as demonstrated by low (<0.2) diet niche overlap (*O*) index (Table 3). The three species from morning showed no overlap with each other in diet composition, with an *O* index of 0. Copepods from midday and night showed very limited diet overlap as the *O* index ranging from 0.04 to 0.07.

4 Discussion

Competition for food is generally thought to exert a strong evolutionary pressure, driving trophic niche separation, either by specialization and/or by widening the choice of potential food resources, and determining the final assemblage (Guisande et al., 2003). To keep population stabilization for coexistence copepods in a competitive food environment was important question to help understanding of the ecosystem function (Kimmel, 2011). Previous studies had revealed several potential mechanisms for this question in coastal waters, such as variations of vertical distribution among different populations, different feeding rhythm and selective feeding of different species (Ishii, 1990; Pierson et al., 2013). All these results were obtained indirectly by trophic biomarker analysis which can provide dietary signals over longer time periods of days to several weeks (Teuber et al., 2014). In our study, exact *in situ* food species of copepods was uncovered directly by the molecular detection. The real time diets of different species provided intuitive evidence of food niche separation among coexisting copepods, which could support food partitioning and thus decrease competition for food resources between species. This feeding strategy for copepod populations was of great importance for their survival and production in food limited coastal waters like the Sanya Bay.

4.1 *Widened food spectrum*

Diverse diet items were detected from the clone libraries of

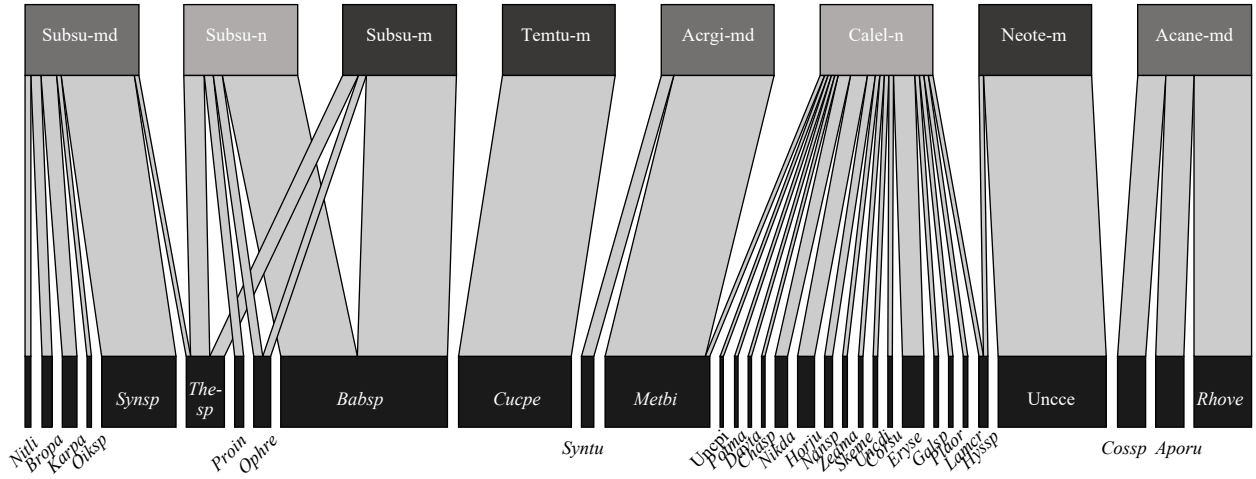

Fig. 3. Bipartite networks depicting the main dietary specialization and overlaps of different copepod samples. Bars on the top line represent different copepod sampled from different time (Canle-n represents *Calanopia elliptica* from night, Temtu-m *Temora turbinate* from morning, Neote-m *Neocalanus tenuicornis* from morning, Acane-md *Acartia negligens* from midday, Acrgi-md *Acrocalanus gibber* from midday, Subsu-m *Subeucalanus subcrassus* from morning, Subsu-md *S. subcrassus* from midday, and Subsu-n *S. subcrassus* from night). Bars on the bottom line represent different food items on species level (shortening the names with the first three letters of the genus name and first two letters of the species names), and the width of bars denote the relative percentage of each food items. A line connecting the bars between copepod and food species represents an intaking event.

Table 3. Diet niche overlap indexes of all the copepods samples

	Subsu-m	Temtu-m	Neote-m	Subsu-md	Acrgi-md	Acane-md	Subsu-n	Calel-n
Subsu-m	1	0[1)]	0[1)]	0.04	0	0	0.9	0
Temtu-m	0	1	0[1)]	0.09	0	0	0	0.19
Neote-m	0	0	1	0	0.06	0	0	0.04
Subsu-md	0.04	0.09	0	1	0.06[1)]	0.04[1)]	0.09	0.17
Acrgi-md	0	0	0.06	0.06	1	0[1)]	0	0.11
Acane-md	0	0	0	0.04	0	1	0.09	0.18
Subsu-n	0.9	0	0	0.09	0	0.09	1	0.07[1)]
Calel-n	0	0.19	0.04	0.17	0.11	0.18	0.07	1

Note: [1)] The diet niche overlap indexes of copepods from the same sampling time (morning, midday and night).

six copepods with 35 taxa totally, including not only common food reported by previous studies, such as diatoms, dinoflagellates, chlorophyta and protozoan, but also diet species uncovered recently by new methods, such as metazoan and land plants. Metazoan and land plants were the most common prey items among six copepod species analyzed here, followed by diatom, and this was consistent to some extent with previous study conducted in the same area in the Sanya Bay (Hu et al., 2015). Diatom was abundance group in prey items but with relatively low percentage of clone libraries. *Skeletonema tropicum*, *Chaetoceros* sp. and *Proboscia indica* were also identified in ambient water. However, among all the prey items detected, metazoan exhibited highest species diversity and relative abundance, with different phyla (e.g., Ctenophhora, Ophionereididae, Crustacea). It had been confirmed that copepod could feed on metazoan by both gut content analysis (Schnetzer and Steinberg, 2002) and molecular detection (Hu et al., 2014, 2015). Most of the crustacea detected here were from Malacostraca, such as *Erythrops*, *Nikoides*, *Coralliocaris*, *Galathea* and *Platyxanthus*, which might be the eggs or larva. In the Sanya Bay of spring (April to June), almost all the aquatic organisms were in spawning or breeding stage, and planktonic larvae could reach a percentage of 25% in zooplankton community with diverse species (e.g., Mysidacea larva, Luciferinae larva and Zoea larva) (Yin et al., 2004). Ophiuroids were also common benthic echinoderms in coral reef ecosystem (Lewis and Bray, 1983) and had only a spawning period during spring to summer (Yokoyama et al., 2008). Another group of metazoan worth noting was Hydrozoa (jellyfish), which was considered to be predators of copepod (Ishii and Tanaka, 2001), indicating complex trophic relationships among zooplankton in coastal waters. Land-plant detritus were another abundant food resource for copepods, and this was consisted with our previous results which found that copepods consumed large amounts of land plant detritus as a supplementary food source when faced with food limited situation (Hu et al., 2015). Widened food spectrum of these copepods could help to reduce food completion to some extent, and this might be important strategy for copepod populations to acquire food for their community development in complex natural environment (Leising et al., 2005; Kiørboe et al., 2010).

4.2 *Dietary separation of different copepod species*

Copepods differed in both diet diversity and food preference in our results. The highest diversity was observed in larger copepod populations in night, with 18 and 4 taxa in *C. elliptica* and *S. subcrassus* respectively. This was consistent with previous studies that copepods would increase feeding activity from dusk, which could decrease the danger of predation (Saito and Taguchi, 1996; Calliari and Antezana, 2001). While there were also some species which showed enhanced feeding in daytime, such as *S. subcrassus* in this study with 6 taxa detected in midday (Wong et al., 1991). *Subeucalanus subcrassus* fed mostly on protozoa and dinoflagellates, while *C. elliptica* and *A. negligens* consumed a large fraction of metazoan. Plant dominated the diet of *T. turbinata* and protozoa (Rhizaria) dominated the diet of *N. tenuicornis*.

The spatially co-exiting species in our study could be divided into different ecological groups according to their ecological habits and distribution characters. *Calanopia elliptica* and *A. negligens* were subtropical coastal epipelagic species, and *S. subcrassus* and *T. turbinata* were warm water nearshore groups, while *N. tenuicornis* was widely-distributed warm water pelagic group (Yin et al., 2004). It is obvious that coastal population groups, such as *C. elliptica*, *T. turbinata* and *A. negligens* consumed large amount of metazoan and plant, which might originate from organic detritus, indicating a detritivorous feeding of these omnivorous copepods. These copepods were considered to be omnivores and they might apply a filter feeding during the day time, as the time-averaged fluid signal and the consequent predation risk is much less for copepods >1 mm using this feeding pattern (Kiørboe et al., 2010). We also found that the population structure varied by copepod size-fractions. The abundance of small copepods (<2 mm), such as *Paracalanus*, *Acrocalanus*, *Temora* and *Acartia*, showed little variations from morning, midday and night, but they occupied a large fraction (>50%) of the total biomass in midday, while large copepods (>2 mm) were more abundant and diverse in night. Dagg (1977) measured starvation time of different copepods, and showed that small coastal species, such as *Acartia* spp., were more vulnerable to starvation than larger ones (such as *Pseudocalanus minutus* and *Calanus finmarchicus*), so they might reside within specific environment to reduce energy consumption.

As the sampling site was reported to have high suspended matter and terrigenous input accounted for 44.5% of total sediments, primary production was much lower and might be insufficient to support zooplankton biomass (Zhao et al., 2013). Lombard et al. (2013) found that copepod can detect chemical trails originating from sinking marine snow particles, indicating that organic detritus in the water column might be potential sources of food supplements for coastal copepods like the coastal groups detected in this study. While as the most important dominant copepod in the Sanya Bay, *S. subcrassus* exhibited a more flexible feeding pattern due to its high capacity of migration and ambush feeding, indicating that organic detritus might be important supplementary food sources for omnivorous coastal populations (Lee et al., 2012). As the only pelagic group, *N. tenuicornis* consumed mostly unknown rhizaria, which was not detected in other copepods, indicating they might occupy different ecological niche through food partitioning even if spatially collocated in the same environment.

Moreover, copepods sampled from the same time also showed different food preference. Sequences of metazoan and protozoa were abundant in diets of *S. subcrassus* and *N. tenuicornis* in the morning, while *T. turbinate* consumed large amount of plant. Dominant small copepod, *A. negligens*, in midday community also consumed a large amount of organic detritus from metazoan (e.g., tunicate, cnidaria), while the larger population of *S. subcrassus* mainly fed on dinoflagellate. Even though the night community was dominated by two large species with similar size (*S. subcrassus* and *C. elliptica*), they showed apparent differences in diets diversity. The food partitioning here might be important strategy for the stabilization and survival of copepod assemblage (Guisande et al., 2003). In the morning, all the three copepods showed lowest diet diversity and none of the dominant phytoplankton in ambient water were detected for prey. This was consistent with previous conclusions that copepod would decrease feeding activity since dawn, especially pigment prey which would make them more visible to predators (Ishii, 1990). While in night, the diversity of all dominant populations was high, as the copepod biomass was highest in night and the strengthened feeding competition make the copepod more selective to acquire nutritional needs.

4.3 *Potential significance of dietary separation for copepod in coastal ecosystem*

Variations of the phytoplankton community in our results suggested a changing food environment in the study area during the sampling time in the Sanya coastal waters. Copepod was reported to be capable of switching feeding pattern to better utilize the food resources in such conditions. *Subeucalanus subcrassus* copepods here could switch their feeding behavior to corporate with co-occurring copepods in food allocation, with a more herbivorous feeding at midday and relatively carnivorous feeding in morning and night. *Subeucalanus subcrassus* was dominant species during the sampling time and they had strong ability to migrate throughout the whole water column in the Sanya Bay (Yin et al., 2004). When faced with harsh competition and relatively lower predation risk in night, they consumed mainly protozoa by ambush feeding, while in midday with high predation risk they fed on more diverse preys by filter feeding. Different feeding mode will generate different fluid signal and hence exposes the grazers differently to predators. For such large copepods as *S. subcrassus*, fluid signal and the consequent predation risk is much less by filter feeding than ambush feeding (Kiørboe et al., 2010). It was clear from the results that *S. subcrassus* consumed a large amount of dinoflagellates in midday, even though diatom dominated the phytoplankton. The discrepancy between preys detected and ambient phytoplankton community might indicate selective feeding of *S. subcrassus*, consisting with that Carrasco and Perissinotto (2011) demonstrated copepod was more selective in complex coastal ecosystem and hence support food partitioning between species (Pagano et al., 2003). These feeding switching and selectivity might be vital mechanism to ensure *S. subcrassus* being the most important ecological groups throughout the year in the Sanya Bay (Mackas et al., 1993, Yin et al., 2004).

The variations of dominant species like *S. subcrassus* in community will bring different extent of feeding competition for co-occurring populations, as copepods exhibit a wide array of foraging behaviors across many spatial scales, depending on copepod species and ambient food environment (Leising et al., 2005). The selective differences amongst copepods could well avoid inter-specific competition within assemblage temporally appeared in the same water column (Arroyo et al., 2007; Laakmann et al., 2009). Such varied food niche differentiation pattern in field might be an important adaptive mechanism for copepod to survival in complex environment like the Sanya coastal water here.

5 Conclusions

Coastal coral ecosystem in the Sanya Bay was characterized by low primary production (phytoplankton biomass). The Sanya Bay was also an open bay with diverse ecological groups of copepod collocated. As reported previously, diverse prey items detected here for different copepod species suggested they may potentially be able to feed opportunistically and opportunistic feeding may intensify feeding competition (Hu et al., 2015). In this study, we found that spatially co-exiting six copepod species exhibit an obvious dietary separation as almost none of them have food overlap. Furthermore, the dietary difference was not caused by ambient food environment as temporally co-exiting species also consumed different preys even they were caught in the same site. Dietary separation observed here indicates that different copepod populations could occupy non-overlapping trophic niche to meet their energy and material requirement in such complex food environment. This *in situ* evidence indicated that trophic-niche differentiation might play a key role in stabilization and survival of copepod assemblage in coastal ecosystems.

References

Aranguren-Riaño N J, Guisande C, Shurin J B, et al. 2018. Amino acid composition reveals functional diversity of zooplankton in tropical lakes related to geography, taxonomy and productivity. Oecologia, 187(3): 719–730, doi: 10.1007/s00442-018-4130-6

Arroyo N L, Aarnio K, Ólafsson E. 2007. Interactions between two closely related phytal harpacticoid copepods, asymmetric positive and negative effects. Journal of Experimental Marine Biology and Ecology, 341(2): 219–227, doi: 10.1016/j.jembe.2006.10.032

Calliari D, Antezana T. 2001. Diel feeding rhythm of copepod size-fractions from Coliumo Bay, Central Chile. Scientia Marina, 65(4): 269–274, doi: 10.3989/scimar.2001.65n4269

Carrasco N K, Perissinotto R. 2011. The comparative diet of the dominant zooplankton species in the St Lucia Estuary, South Africa. Journal of Plankton Research, 33(3): 479–490, doi: 10.1093/plankt/fbq126

Dagg M. 1977. Some effects of patchy food environments on copepods. Limnology and Oceanography, 22(1): 99–107, doi: 10.4319/lo.1977.22.1.0099

David V, Sautour B, Galois R, et al. 2006. The paradox high zooplankton biomass-low vegetal particulate organic matter in high turbidity zones: what way for energy transfer?. Journal of Experimental Marine Biology and Ecology, 333(2): 202–218, doi: 10.1016/j.jembe.2005.12.045

Guisande C, Bartumeus F, Ventura M, et al. 2003. Role of food partitioning in structuring the zooplankton community in mountain lakes. Oecologia, 136(4): 627–634, doi: 10.1007/s00442-003-1306-4

Guisande C, Maneiro I, Riveiro I, et al. 2002. Estimation of copepod trophic niche in the field using amino acids and marker pigments. Marine Ecology Progress Series, 239: 147–156, doi: 10.3354/meps239147

Hu Simin, Guo Zhiling, Li Tao, et al. 2014. Detecting *in situ* copepod diet diversity using molecular technique: development of a copepod/symbiotic ciliate-excluding eukaryote-inclusive PCR protocol. PLoS One, 9(7): e103528, doi: 10.1371/journal.pone.0103528

Hu Simin, Guo Zhiling, Li Tao, et al. 2015. Molecular analysis of *in situ* diets of coral reef copepods: evidence of terrestrial plant detritus as a food source in Sanya Bay, China. Journal of Plank-

ton Research, 37(2): 363–371, doi: 10.1093/plankt/fbv014
Huang Liangmin, Tan Yehui, Song Xingyu, et al. 2003. The status of the ecological environment and a proposed protection strategy in Sanya Bay, Hainan Island, China. Marine Pollution Bulletin, 47(1–6): 180–186, doi: 10.1016/S0025-326X(03)00070-5
Hutchinson G E. 1961. The paradox of the plankton. The American Naturalist, 95(882): 137–145, doi: 10.1086/282171
Ishii H. 1990. In situ feeding rhythms of herbivorous copepods, and the effect of starvation. Marine Biology, 105(1): 91–98, doi: 10.1007/BF01344274
Ishii H, Tanaka F. 2001. Food and feeding of *Aurelia aurita* in Tokyo Bay with an analysis of stomach contents and a measurement of digestion times. Hydrobiologia, 451(1–3): 311–320, doi: 10.1023/A:1011814525325
Ke Zhixin, Huang Liangmin, Tan Yehui, et al. 2011. Plankton community structure and diversity in coral reefs area of Sanya Bay, Hainan Province, China. Biodiversity Science (in Chinese), 19(6): 696–701
Kiørboe T, Jiang Houshuo, Colin S P. 2010. Danger of zooplankton feeding: the fluid signal generated by ambush-feeding copepods. Proceedings of the Royal Society B: Biological Sciences, 277(1698): 3229–3237, doi: 10.1098/rspb.2010.0629
Kimmel D G. 2011. Plankton consumer groups: copepods. In: Wolanski E, McLusky D S, eds. Treatise on Estuarine and Coastal Science. Amsterdam: Elsevier, 95–126
Kleppel G S. 1993. On the diets of calanoid copepods. Marine Ecology Progress Series, 99: 183–195, doi: 10.3354/meps099183
Laakmann S, Kochzius M, Auel H. 2009. Ecological niches of Arctic deep-sea copepods: Vertical partitioning, dietary preferences and different trophic levels minimize inter-specific competition. Deep Sea Research Part I: Oceanographic Research Papers, 56(5): 741–756, doi: 10.1016/j.dsr.2008.12.017
Lee D B, Song H Y, Park C, et al. 2012. Copepod feeding in a coastal area of active tidal mixing: diel and monthly variations of grazing impacts on phytoplankton biomass. Marine Ecology, 33(1): 88–105, doi: 10.1111/j.1439-0485.2011.00453.x
Leising A W, Pierson J J, Cary S, et al. 2005. Copepod foraging and predation risk within the surface layer during night-time feeding forays. Journal of Plankton Research, 27(10): 987–1001, doi: 10.1093/plankt/fbi084
Levins R. 1968. Evolution in Changing Environments: Some Theoretical Explorations. Princeton: Princeton University Press, 65–70
Lewis J B, Bray R D. 1983. Community structure of ophiuroids (Echinodermata) from three different habitats on a coral reef in Barbados, West Indies. Marine Biology, 73(2): 171–176, doi: 10.1007/BF00406885
Lombard F, Koski M, Kiørboe T. 2013. Copepods use chemical trails to find sinking marine snow aggregates. Limnology and Oceanography, 58(1): 185–192, doi: 10.4319/lo.2013.58.1.0185
Mackas D L, Sefton H, Miller C B, et al. 1993. Vertical habitat partitioning by large calanoid copepods in the oceanic subarctic Pacific during Spring. Progress in Oceanography, 32(1–4): 259–294, doi: 10.1016/0079-6611(93)90017-8
Nejstgaard J C, Frischer M E, Raule C L, et al. 2003. Molecular detection of algal prey in copepod guts and fecal pellets. Limnology and Oceanography: Methods, 1(1): 29–38, doi: 10.4319/lom.2003.1.29
Pagano M, Kouassi E, Saint-Jean L, et al. 2003. Feeding of *Acartia clausi* and *Pseudodiaptomus hessei* (Copepoda: Calanoida) on natural particles in a tropical lagoon (Ebrié, Côte d'Ivoire). Estuarine, Coastal and Shelf Science, 56(3–4): 433–445, doi: 10.1016/S0272-7714(02)00193-2
Pianka E R. 1973. The structure of lizard communities. Annual Review of Ecology and Systematics, 4: 53–74, doi: 10.1146/annurev.es.04.110173.000413
Pierson J J, Frost B W, Leising A W. 2013. Foray foraging behavior: seasonally variable, food-driven migratory behavior in two calanoid copepod species. Marine Ecology Progress Series, 475: 49–64, doi: 10.3354/meps10116
Saito H, Taguchi S. 1996. Diel feeding behavior of neritic copepods during spring and fall blooms in Akkeshi Bay, eastern coast of Hokkaido, Japan. Marine Biology, 125(1): 97–107, doi: 10.1007/BF00350764
Sato K I, Yamaguchi A, Ueno H, et al. 2011. Vertical segregation within four grazing copepods in the Oyashio region during early spring. Journal of Plankton Research, 33(8): 1230–1238, doi: 10.1093/plankt/fbr018
Schnetzer A, Steinberg D. 2002. Natural diets of vertically migrating zooplankton in the Sargasso Sea. Marine Biology, 141(2): 403, doi: 10.1007/s00227-002-0917-3
Teuber L, Schukat A, Hagen W, et al. 2014. Trophic interactions and life strategies of epi- to bathypelagic calanoid copepods in the tropical Atlantic Ocean. Journal of Plankton Research, 36(4): 1109–1123, doi: 10.1093/plankt/fbu030
Wong C K, Chen Qingchao, Huang Liangmin. 1991. Fluorescence analysis of the gut contents of calanoid copepods in the Zhujiang River Estuary. Marine Sciences, (3): 60–64
Yin Jianqiang, Zhang Guxian, Huang Liangmin, et al. 2004. Diel vertical migration of zooplankton in Sanya Bay, Hainan Province, China. Journal of Tropical Oceanography (in Chinese), 23(5): 25–33
Yokoyama L Q, Lembo Duarte L F, Zacagnini Amaral A C. 2008. Reproductive cycle of *Ophionereis reticulata* (Ophiuroidea, Echinodermata) on the southeast coast of Brazil. Invertebrate Reproduction & Development, 51(2): 111–118, doi: 10.1080/07924259.2008.9652261
Zhao Meixia, Yu Kefu, Shi Qi, et al. 2013. Source, distribution and influencing factors of sediments on Luhuitou fringing reef, Northern South China Sea. Chinese Science Bulletin (in Chinese), 58(17): 1583–1589

Acta Oceanol. Sin., 2020, Vol. 39, No. 4, P. 73–83
https://doi.org/10.1007/s13131-020-1584-2
http://www.hyxb.org.cn
E-mail: hyxbe@263.net

A new pelagic *Polyconchoecia* Xiang, Chen and Du, 2018 (Ostracoda: Myodocopa: Halocyprididae) from the South China Sea

Peng Xiang[1*†], Yu Wang[1†], Ruixiang Chen[1], Youyin Ye[1], Chunguang Wang[1], Xiaoyin Chen[1], Mao Lin[1, 2*]

[1] Laboratory of Marine Biology and Ecology, Third Institute of Oceanography, Ministry of Natural Resources, Xiamen 361005, China

[2] Collaborative Innovation Center of Deep Sea Biology, Hangzhou 310012, China

Received 20 November 2018; accepted 6 May 2019

Abstract

Halocyprid ostracods are appreciable part of ostracods floating through virtually everywhere in marine environment. In this study, we describe a new species of genus *Polyconchoecia* Xiang, Chen and Du, 2018, tribe Conchoeciini Chavtur and Angel, 2011, family Halocyprididae Dana, 1853 from the middle of the South China Sea. *Polyconchoecia chenii* sp. nov. is very close to *P. commixtus* Xiang, Chen and Du, 2018. But it differs from *P. commixtus* by the distinctions of locations of major glands of carapace and the characteristics of appendages: more posteriorly situated left asymmetric gland of carapace, no right asymmetric gland; segmented frontal organ; the endopod 2 of the first antenna with a very small seta; a- and c-setae of the first antenna with long end joint have long end joint, the b- and d-setae have no end joint, spinose e-seta without end joint; the e-seta of the second antenna is present; teeth side is distinctive; the setal counts of the mandible, maxilla, fifth limb, and sixth limb are individual. The locations of the major glands on carapace and the characteristics of the first antenna can be the key of the new species. This work is the second discovery of the genus *Polyconchoecia* from the world.

Key words: taxonomy, Ostracoda, Halocyprididae, Conchoeciini, *Polyconchoecia chenii* sp. nov., new species, South China Sea

Citation: Xiang Peng, Wang Yu, Chen Ruixiang, Ye Youyin, Wang Chunguang, Chen Xiaoyin, Lin Mao. 2020. A new pelagic *Polyconchoecia* Xiang, Chen and Du, 2018 (Ostracoda: Myodocopa: Halocyprididae) from the South China Sea. Acta Oceanologica Sinica, 39(4): 73–83, doi: 10.1007/s13131-020-1584-2

1 Introduction

Class Ostracoda Latreille, 1802, emend. Martin and Davis, 2001 are a big group of small bivalved crustaceans. They inhabit almost all aquatic environments with high taxonomic diversity (Karanovic, 2010). Ostracods are one of the momentous groups of marine organisms, and are functionally important in the process of bio-geo-chemical cycles in marine ecosystem, especially in the tropics and subtropical regions (Angel et al., 2007; George and Nair, 1980). They also play a significant participant of marine deposition, because their calcified valves are preserved as fossils (Di Celma et al., 2016). The studies of ostracods have been well improved in last two decades, and many new taxa have been erected (Harrison-Nelson and Kornicker, 2000; Chavtur, 2003; Lum et al., 2008; Karanovic, 2010; Chavtur and Angel, 2011; Pinto and Jocqué, 2013; Xiang et al., 2017a, b, 2018; Du et al., 2018). These faunae might no-monophyletic, phylogeny remains indistinct, and classification is based on typical characteristics (Fortey and Thomas, 1998; Yamaguchi and Endo, 2003).

Halocyprid ostracods constitute appreciable part of marine zooplankton. They are floating through virtually everywhere in marine environment including surface, hydrothermal vent, cold seep and abyss (van Harten, 1992; Oakley et al., 2013; Tanaka and Yasuhara, 2016; Yamaguchi et al., 2016). In 1853, the largest family Halocyprididae Dana, 1853 (Chavtur, 2003; Martin and Davis, 2001; Brandão et al., 2019) within order Halocyprida Dana, 1853 was erected. And then, the subfamily Conchoeciinae Müller, 1912 was erected under this family. In 2011, Chavtur and Angel (2011) designated the tribe Conchoeciini Chavtur and Angel, 2011 on the basis of the locational shifts of glands. Not long ago, Du et al. (2018) erected genus *Polyconchoecia* Xiang, Chen and Du, 2018 with the type species *P. commixtus* Xiang, Chen and Du, 2018 based on the definite characteristics of locations of major glands on carapace. Soon after that, genus *Conchoecia* Dana, 1849 was subdivided into five genera: *Conchoecia*; *Macrochoecilla* Chavtur, 2018; *Lophuroecia* Chavtur, 2018; *Parvidentoecia* Chavtur, 2018; and *Hyalocoecia* Chavtur, 2018; and genus *Parthenoecia* Chavtur, 2018 was erected, mainly based on characteristics of lateral gland, armature of seta-e on the first antenna in the male, and copulatory appendage (Chavtur and Bashmanov, 2018). Thus far, the tribe Conchoeciini has contained 27 genera (Brandão et al., 2019).

In this study, a new species of genus *Polyconchoecia* from the South China Sea was described.

Foundation item: The Global Climate Change and Ocean Atmosphere Interaction Research under contract No. GASI-01-02-04; the National Natural Science Foundation of China under contract Nos 41406216 and 41506217; the project sponsored by the Scientific Research Foundation of Third Institute of Oceanography, MNR under contract No. 2017009; the National Special Project on Gas Hydrate of China under contract No. DD20190218.

*Corresponding author, E-mail: xiangpeng@tio.org.cn; linmao@tio.org.cn

†These authors contributed equally to this work.

2 Methods

2.1 *Sampling and morphological methods*

Collections were obtained from two cruises of the South China Sea in 2014–2015. All zooplankton specimens were collected using a Multinet sampling system (Type Midi, Mesh-size aperture 200 μm, HydroBios Inc., Kiel, Germany) by vertical and stratified hauls from bottom to surface. Collections were preserved by immersion in 5% buffered formaldehyde.

Specimens were dissected under a Carl Zeiss Discovery V20 zoom-stereomicroscope. Dissected appendages were mounted in permanent slides with CMC-9AF medium (Masters Company Inc., Illinois, USA). Observations were done by a Carl Zeiss Axio Imager Z2 differential interference contrast microscope system with AxioVision Image-Pro software (Carl Zeiss Inc., Oberkochen, Germany). All drawings were made from micro-images of dissected appendages, followed the methodology in Chavtur and Angel (2011), and further processed with Adobe Photoshop CS6 (Adobe Inc., San Jose, CA, USA).

The type specimens/appendages were deposited in the Marine Biological Sample Museum of the Chinese Offshore Investigation and Assessment, Third Institute of Oceanography, MNR (Xiamen, China), under the collection numbers TIO-OHH-PP-201 to TIO-OHH-PP-204.

Fig. 1. *Polyconchoecia chenii* sp. nov. (♀). a. Left valve, external view; b. carapace, internal view; and c. postero-ventral corner of right valve, internal view.

2.2 *Nomenclatural acts*

The electronic edition of this article conforms to the requirements of the amended International Code of Zoological Nomenclature, and hence the new names contained herein are available under that code from the electronic edition of this article. This published work and the nomenclatural acts it contains have been registered in ZooBank, the online registration system for the ICZN. The ZooBank LSIDs (Life Science Identifiers) can be resolved and the associated information viewed through any standard web browser by appending the LSID to the prefix "http://zoobank.org/". The LSID for this publication is: urn:lsid:zoobank.org:pub:C8D3334A-AA1C-4355-AB53-140B299051B0. The electronic edition of this work was published in a journal with an ISSN, and has been archived and is available from the following digital repositories: SpringerLink, PubMed Central, LOCKSS.

3 Results

3.1 *Systematics*

Oder Halocyprida Dana, 1853

Family Halocyprididae Dana, 1853

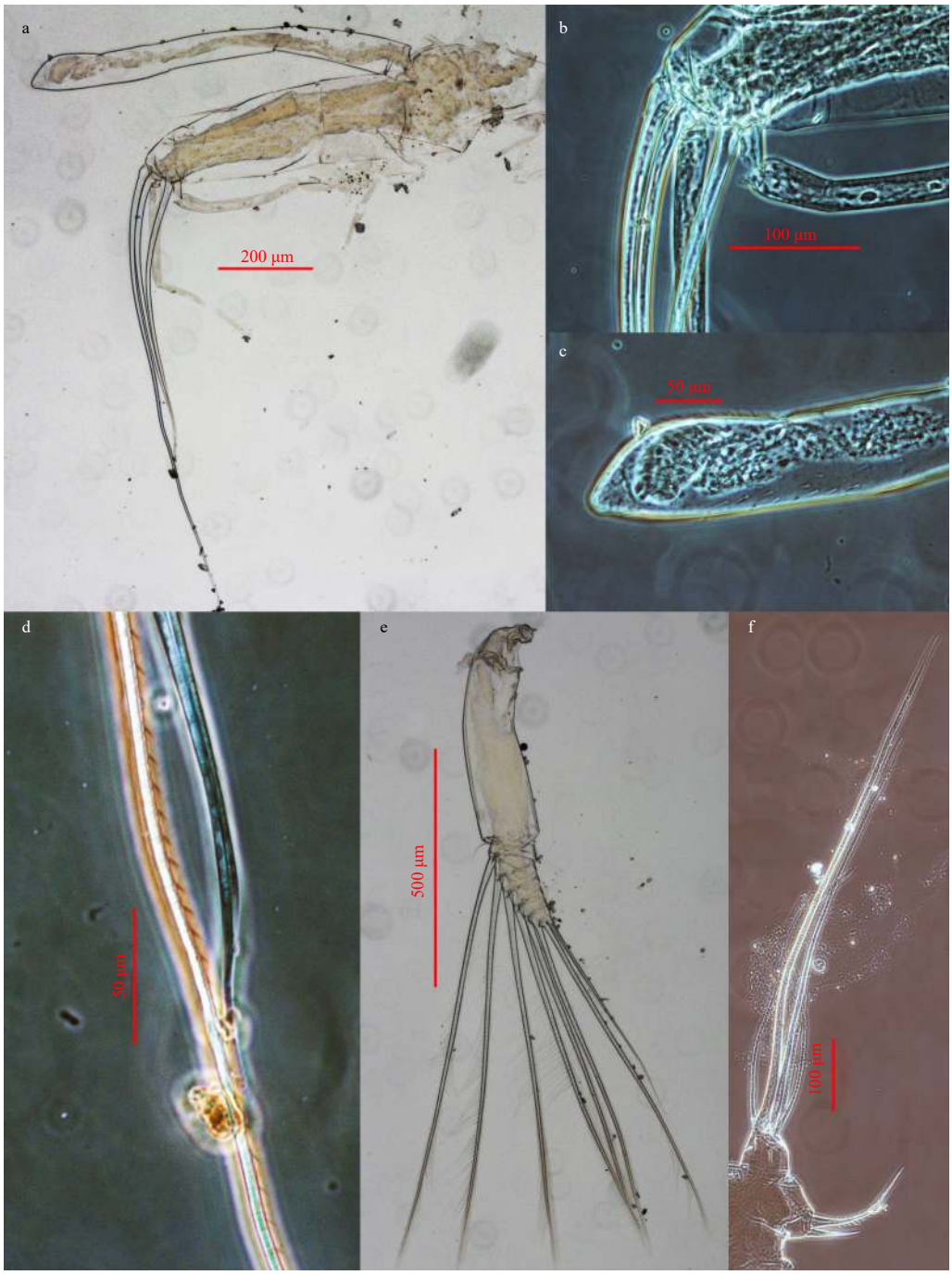

Fig. 2. *Polyconchoecia chenii* sp. nov. (♀). a. First antenna and frontal organ, external view; b. tip of first antenna, external view; c. tip of frontal organ, external view; d. detail of e-seta, external view; e. second antenna, external view; and f. exopod of second antenna, external view.

Subfamily Conchoeciinae Müller, 1912
Tribe Conchoeciini Chavtur and Angel, 2011
Genus *Polyconchoecia* Xiang, Chen and Du, 2018
Species *Polyconchoecia chenii* Xiang, Wang and Chen sp. nov.

3.2 *Species Polyconchoecia chenii sp. nov.*

Figs 1–8

LSID: urn:lsid:zoobank.org:act:9B60314F-EE85-46C7-8213-737601ED74D8

Etymology. Latinized name of Ruixiang Chen, our teacher, a scientist of the planktonic research group, Third Institute of Oceanography, MNR, in recognition of his important contributions of marine ostracods of China.

Holotype. No. TIO-OHH-PP-201, adult female, length 2.57 mm, height 1.47 mm from Sta. CS-068 (14°31′N, 114°54′E) in the top of the South China Sea, 200–500 m water layer, 12 January 2015. Specimen was dissected on slide and deposited in the Marine Biological Sample Museum, in the Third Institute of Oceanography, MNR, China (Xiamen, China).

Paratypes. No. TIO-OHH-PP-202, adult female, length 2.33 mm, height 1.35 mm, No. TIO-OHH-PP-203, adult female, length 2.45 mm, height 1.41 mm, from the same locality of the

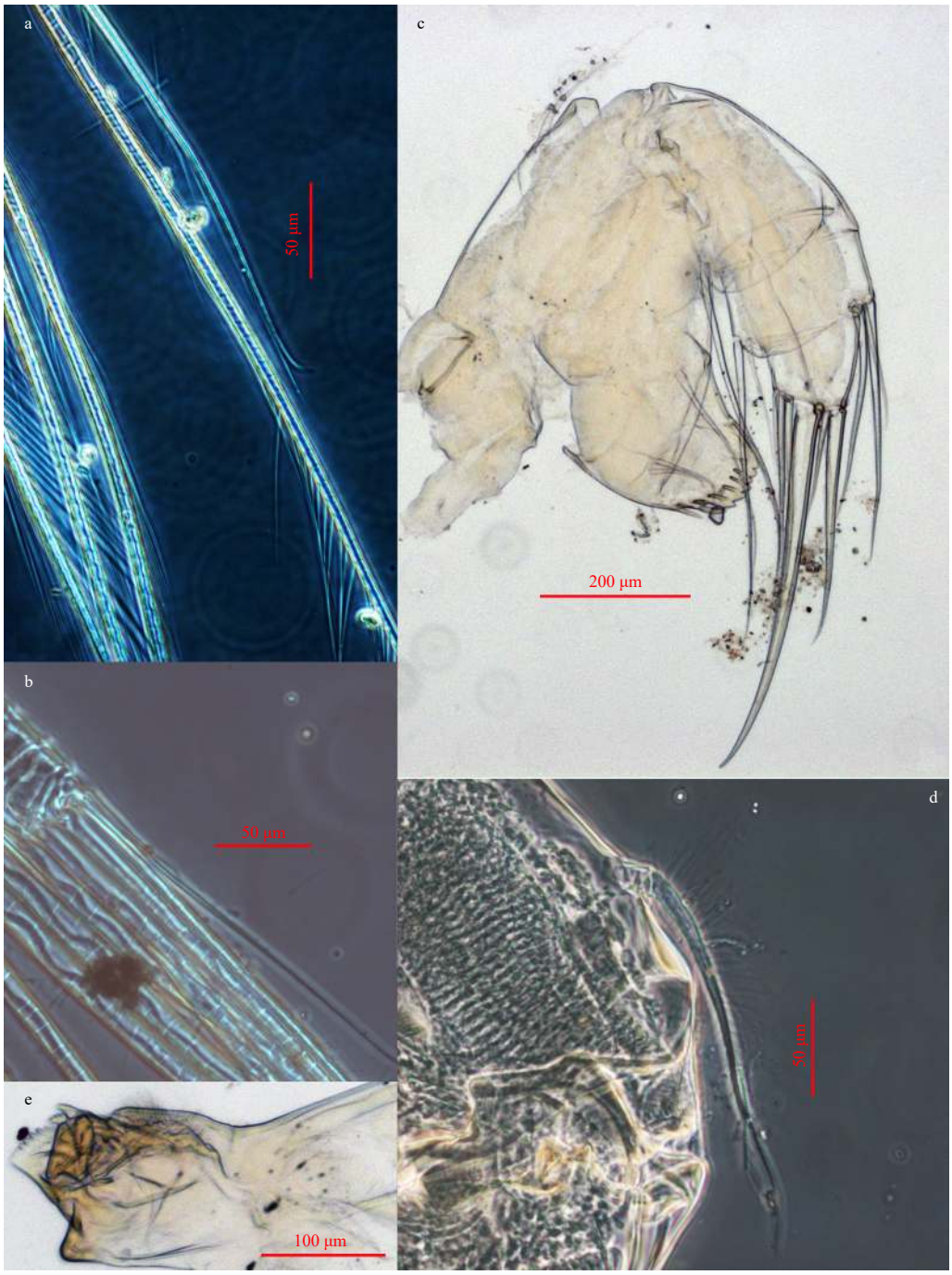

Fig. 3. *Polyconchoecia chenii* sp. nov. (♀). a. Details of swimming seta of second antenna, external view; b. terminal seta of second antenna, external view; c. mandible, internal view; d. exopod of mandible, internal view; and e. coxal endite of left mandible, internal view.

holotype, and dissected on slide. TIO-OHH-PP-204, adult female, length 2.35 mm, height 1.33 mm, collected from Sta. CS-012 (7°06.46′N, 113°53.6′E) in the South China Sea, 200–500 m water layer on 2 January 2014, deposited in 5% buffered formaldehyde. Paratypes were deposited with the holotype.

Distribution. The mesopelagic water in the South China Sea.

Diagnosis. Carapace without ornamentation or setae, height about 56.5%–57.9% of length, sub-rectangle in lateral view with rounded corners; rostrums wide, developed, equilong, anteriorly and curved to downward; shoulder vaults unconspicuous, higher in anterior part, ventral margin with slightly concave, left asymmetric gland opening on postero-dorsal corner, a lateral gland opening on right postero-ventral corner, dense edge glands placed along all ventral margin; left postero-ventral margin without gland. Frontal organ segmented. In first antenna, a- and c-setae analogic with long end joint, b- and d- setae analogic without end joint. E-seta of second antenna present. Maxilla with five disto-anterior setae, one disto-medial seta, two medial setae, and three disto-posterior setae on endopod 2. Proximal-ventral group of setae of fifth limb with seven setae, endopod 1 with two ventral setae. Vesting of exopod of sixth limb strong and spinose, basale with seven ventral plumose setae, endopod 1 bare, endo-

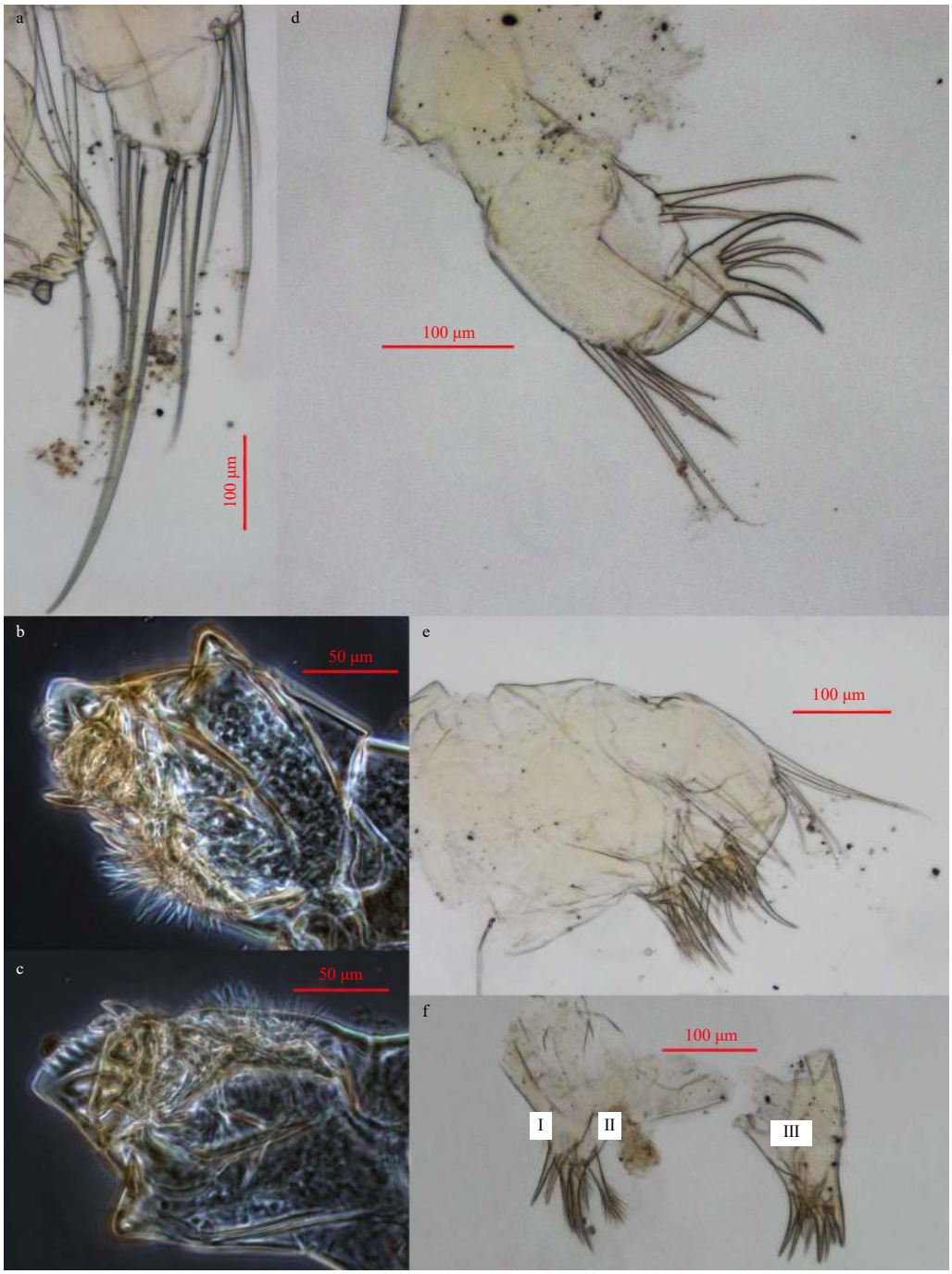

Fig. 4. *Polyconchoecia chenii* sp. nov. (♀). a. Tip of mandible, internal view; b. coxal endite of right mandible, internal view; c. coxal endite of left mandible, internal view; d. maxilla, internal view; e. maxilla with endites, internal view; and f. endites of maxilla, internal view.

pod 2 without ventral seta. Furca with unpaired seta.

3.3 *Description*

Carapace (Figs 1a–c and 7a, b). Carapace smooth without setae and ornamentation (pits or grooves), sub-rectangle in lateral view; shoulder vaults unconspicuous; rostrum subequal anteriorly with acutangular tip, curved downward, wide and developed; antero-ventral margin, postero-dorsal and postero-ventral corner rounded; anterior part slightly higher than posterior part; dorsal margin approximately flat; ventral margin with slightly concavity. Carapace with three groups of glands: one asymmetric gland opening on postero-dorsal corner of left valve, one lateral gland opening on right postero-ventral corner; dense edge glands placed along anterior to posterior ventral margin; postero-ventral corner of left valve without gland. Length 2.33–2.57 mm, height 1.33–1.47 mm, height about 56.5%–57.9% of length.

Frontal organ (Figs 2a, c and 7c, d). Stem and capitulum separated, straight and clavate with blunt tip, small disto-dorsal and ventral spines. Capitate base separated from first antenna.

First antenna (Figs 2a, b, d and 7c). First antenna uniramous. Basale and endopod 1 bare. Endopod 2 with one small dorsal spinose seta. Endopod 3–5 very short and small. Endopod 4 with two ventral sensory setae (a- and b-setae). Endopod 5 blunt con-

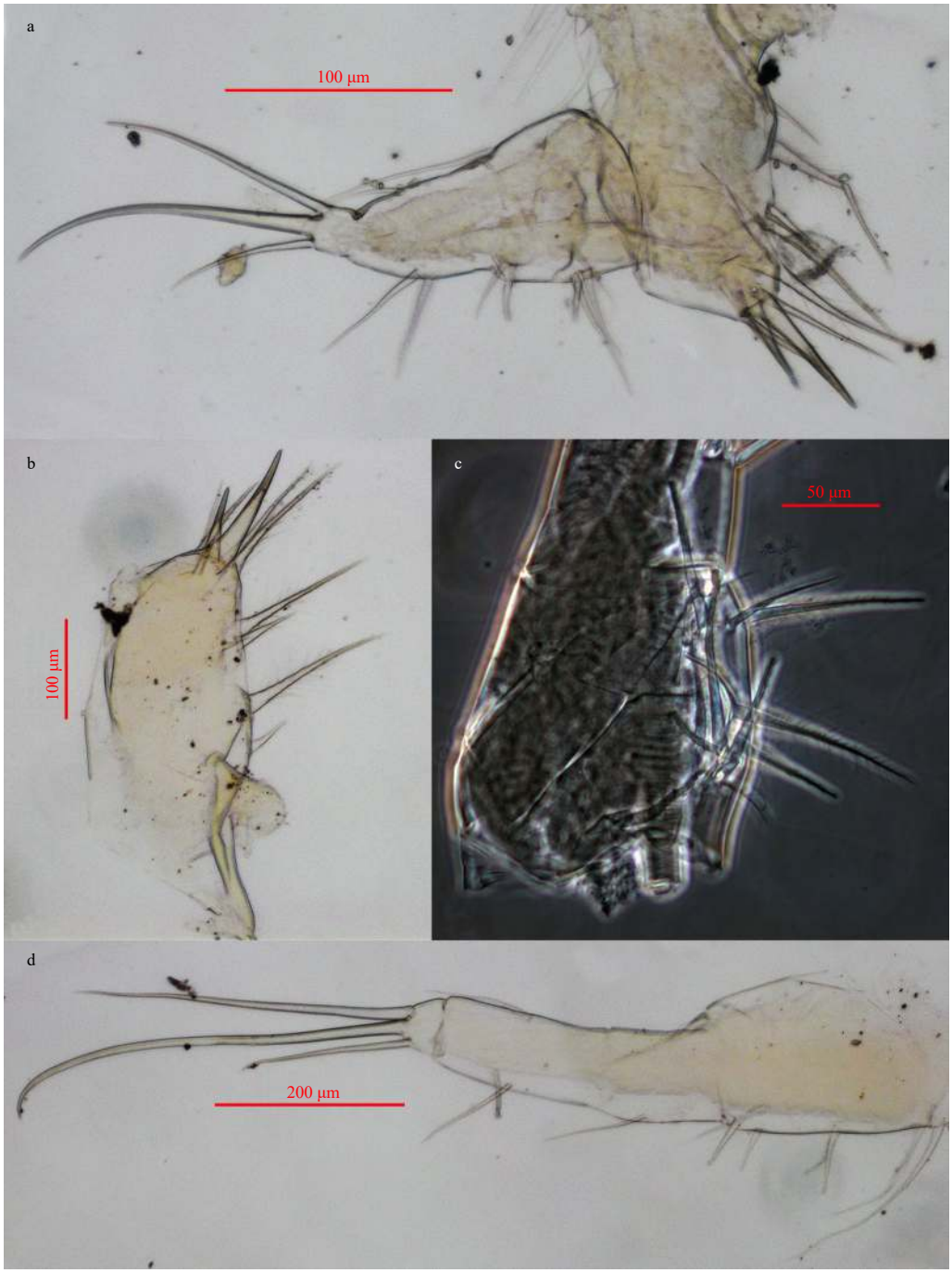

Fig. 5. *Polyconchoecia chenii* sp. nov. (♀). a. Fifth limb, external view; b. endites of fifth limb; c. basale of fifth limb, external view; and d. sixth limb, external view.

ical with three disto-ventral sensory setae (c-, d-, e-setae). A- and c-setae analogic long columnar, thin walled and bare with long end joint; b- and d- setae equilong and bare without end joint, slightly longer than a- and c-setae; e-seta extremely long (approximately one and half length of a-seta) and spinose ventral spines with numerous small ventral spines on distal half.

Second antenna (Figs 2e, f, 3a, b and 7e, f). Limb biramous with large protopodite with powerful muscles. Endopod without c- and d-setae. Endopod 1 large, folded forward, with bend a- and b-setae, a-seta bare and short, b-seta long and spinose, about twice length of a-seta; processus mamillaris normal. Endopod 2 and 3 integrated into a small peg shaped bulge on disto-dorsal margin of endopod 1, with bare 5 setae; g-seta longest and ringed; f-seta second longest; h-, i-, j- setae equilong. Exopod 1 more than seventeen times length of 2, with one bend acerose spine on disto-dorsal margin instead of plumose seta; exopod 2–7 very short with analogous long plumose swimming seta on disto-ventral margin respectively; exopod 8 and 9 fused with one long plumose seta, one shorter plumose seta and one very small seta on tip.

Mandible (Figs 3c–e, 4a–c and 7g–j). Basale large. Exopod tiny peg shaped, with one dorsal plumose seta with bare distal part. Endopod 1 more than two times length of 2, with one disto-ventral seta. Endopod 2 short, with two setae on disto-ventral margin:

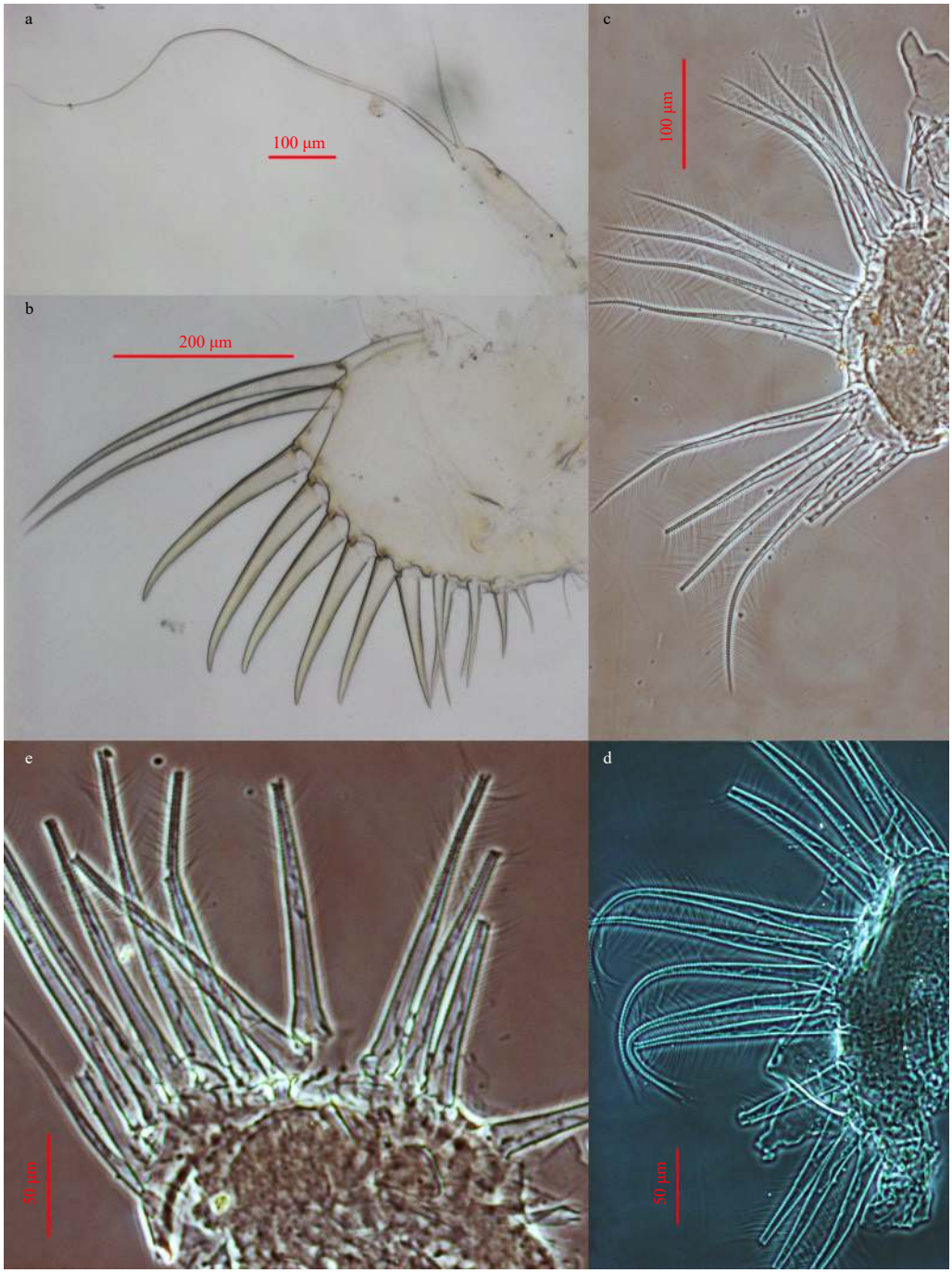

Fig. 6. *Polyconchoecia chenii* sp. nov. (♀). a. Seventh limb, external view; b. furcal lamellae, external view; c epipod of fifth limb, external view; d. epipod of sixth limb, external view; and e. epipod of seventh limb, external view.

outer one bare and short, inner one long with small spines on distal half length; three setae on disto-dorsal edge: mid one short and bare, others long with small ventral spines. Endopod 3 very short, with six setae on tip: seta 1 claw-shaped with distal ventral spines; seta 2 small with ventral spines; seta 3 claw-shaped and biggest with disto-ventral spines; setae 4 and 6 subequal in length; seta 5 about twice length of seta 4. Toothed edge of basale big and triangular with two bare long setae on medio-ventral side and two bare short setae on medio-distal side. Toothed edge of basale with eight distal teeth in one list. Coxal endite constituting by three parts: distal teeth list with one big and bend distal triangular papillae, one big papilla constituted four small teeth, five strip papillae, and one flat papilla; proximal teeth list with small teeth; medial part with some long and big papillae and numerous long cilia.

Maxilla (Figs 4d–f and 8a, b). Exopod with two spinose setae on tip. Endopod 1 big rectangular, with two long and three short bare setae on antero-distal edge, one spinose seta on disto-posterior edge, two long spinose setae on medial side, one long and two short spinose setae on posterior side. Terminal segment with

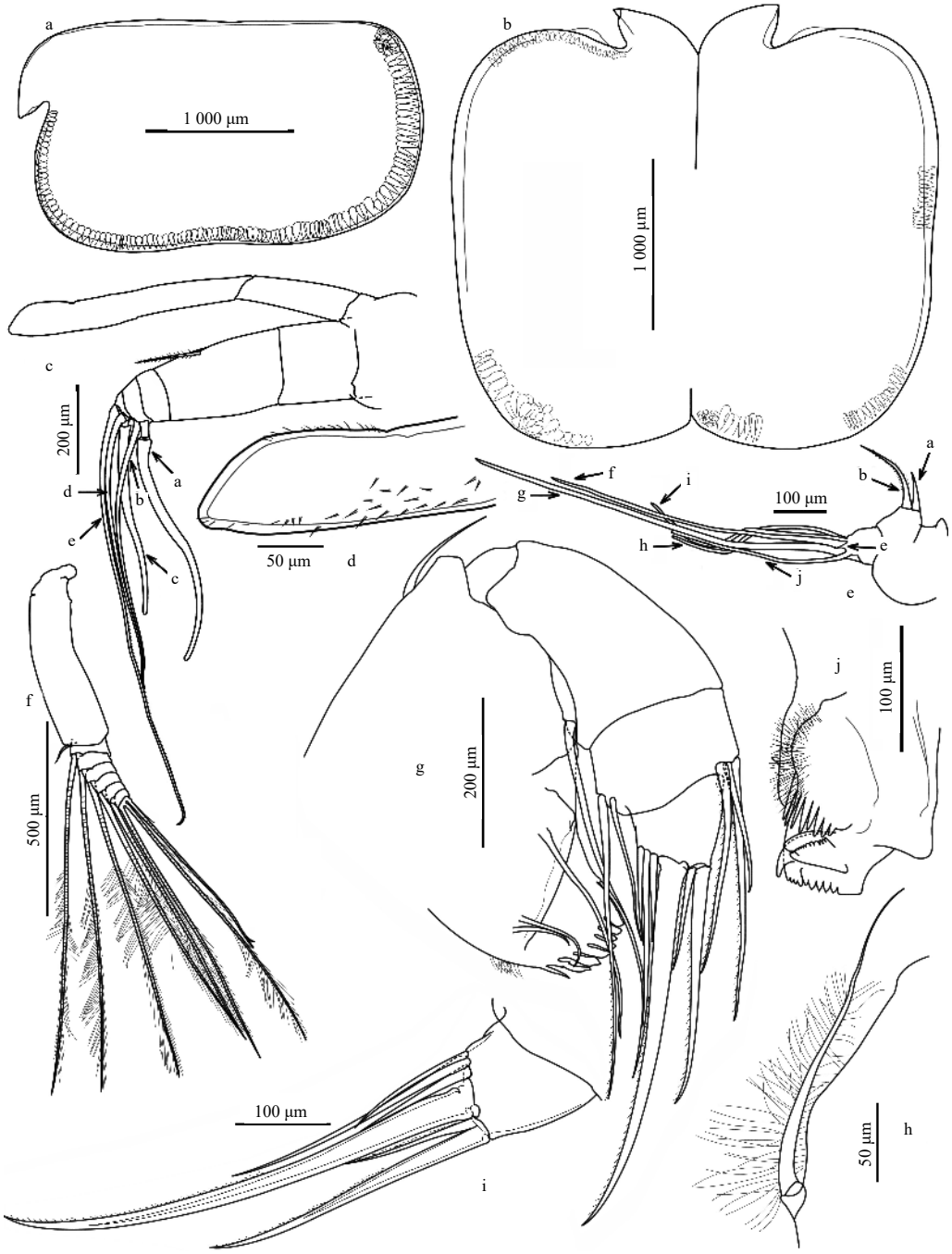

Fig. 7. Line drawings of *Polyconchoecia chenii* sp. nov. (♀). a. Carapace, external view; b. carapace, internal view; c. first antenna and frontal organ, external view; d. tip of frontal organ, external view; e. exopod of second antenna, external view; f. second antenna, external view; g. mandible, internal view; h. exopod of mandible, internal view; i. tip of mandible, internal view; and j. coxal endite of mandible, internal view.

five claws: two bilateral stout spinose claws, two inner puny bare claws and one mid spinose claw; spinose claws with disto-ventral spines. Maxilla with three hirsute endites: endite I with five plumose setae; endite II with one bare and three plumose setae; endite III with ten bare setae.

Fifth limb (Figs 5a–c, 6c and 8c). Limb biramous. Basale large and wide with eleven setae: dorsal seta (vestige of exopod) long and bare; proximal-ventral group of setae with five plumose setae and a pair of symmetric ventral spinose setae; disto-ventral group of setae with one central seta and a pair of symmetric ventral spinose setae. Endopod 1 long with two ventral setae and one dorsal seta; endopod 2 short with three long bare curved claws on tip, mid claw longest, mid and ventral claws with numerous small ventral spines. Coxale with three endites: endite I big rectangular with one short bare and one long plumose proximal setae, one small bare one small plumose and one long plumose distal setae; endite II very short with one long plumose seta; ventral group of setae of endite III with two strong bare and blunt setae, and four sharp plumose setae. Epipod with one small bare inner seta and about sixteen lathy lithe plumose setae.

Sixth limb (Figs 5d, 6d and 8d). Basale broad with one long plumose seta (vesting of exopod), two long proximo-ventral, two short ventral and three short disto-ventral plumose setae; basale without dorso-lateral seta. Exopod 1 short with one ventral seta. Exopod 2 long and thin, with one dorsal and one ventral seta. Terminal segment blunt and very short with three very long acer-

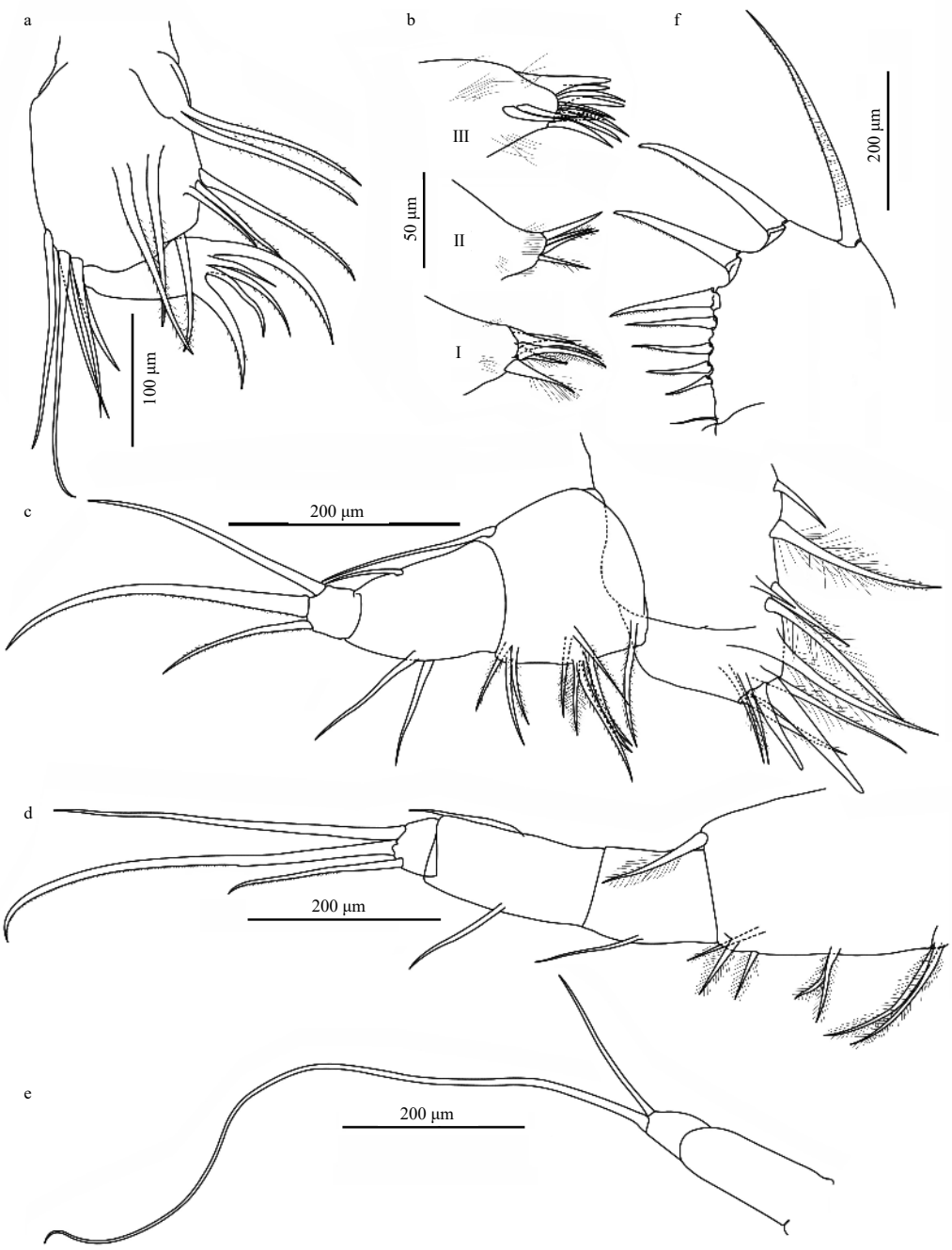

Fig. 8. Line drawings of *Polyconchoecia chenii* sp. nov. (♀). a. Maxilla, internal view; b. endites of maxilla, internal view; c. fifth limb, external view; d. sixth limb, external view; e. seventh limb, external view; and f. furcal lamella, external view.

ose claws on tip; mid claw longest with curved distal part; mid and ventral claws with numerous small disto-ventral spines. Epipod with one small bare inner seta and about seventeen lathy lithe plumose setae.

Seventh limb (Figs 6a, e and 8e). Segment 1 slender and bare. Segment 2 very short conical with one bare long seta and one bare lathy lithe seta (four times length of another) on tip. Epipod with one small bare inner seta and about fourteen lathy lithe plumose setae.

Furca (Figs 6b and 8f). Each furcal lamella with one large dorsal seta and seven claws, from long to short in turn arrangement. Seta and claws with numerous small disto-ventral spines. Furca with ventral unpaired seta.

4 Discussion

These specimens are considered to be one species of the subfamily Conchoeciinae Müller, 1912 of family Halocyprididae Dana, 1853, according to the Chen and Chavtur's diagnosis (Chen and Lin, 1995; Chavtur and Angel, 2011), and then we can put them into the tribe Conchoeciini, Chavtur and Angel, 2011 easily. They are very close to *Polyconchoecia commixtus*, the type species of genus *Polyconchoecia*, which genus has been reported recently and with only one species yet. They have shared characteristics as followed: (1) similar size of full adult; (2) the shapes of carapace are very close; (3) left valve has a left asymmetric gland near postero-dorsal corner; (4) right valve has a lateral gland on right postero-ventral corner; (5) dense edge glands are placed along anterior to posterior ventral margin of carapace in line; (6) exopod 1 of second antenna has one bend acerose spine on disto-dorsal margin instead of plumose seta; (7) the structures of main limbs are similar.

Although these specimens are very close to *P. commixtus*, *P. chenii* sp. nov. is discriminated by the morphological comparisons shown in Table 1. They have obvious and individual distinctions to separate from *P. commixtus*: (1) left asymmetric gland of carapace of the new species is moved posteriorly, the carapace have no right asymmetric gland or compound gland (Figs 1b, c and 7a, b); (2) the frontal organ of this species is separated to stem and capitulum, and has more ventral spines (Figs 2a and 7c, d); (3) in *P. chenii* sp. nov., the seta of endopod 2 of the first antenna is very small; (4) in *P. commixtus*, a- to d-setae of the sensory setae of the first antenna are analogic with long end joint, e-

Table 1. Comparisons between *Polyconchoecia chenii* sp. nov. and *P. commixtus* (♀)

Characteristics		*P. commixtus*	*P. chenii* sp. nov.
Carapace	left asymmetric gland	near postero-dorsal margin, moved anteriorly	on postero-dorsal corner
	right asymmetric gland	on right postero-ventral corner	none
	right lateral gland	constituting a compound gland with right asymmetric gland	only on right postero-ventral corner
Frontal organ	stem and capitulum	fused	separated
	spines	small disto-ventral and mid-ventral spines	small disto-dorsal and ventral spines
First antenna	endopod 2	with one long dorsal plumose seta	with one small dorsal plumose seta
	sensory setae	a- to d-setae analogic, long columnar, thin walled and bare, with long end joint; e-seta bare, with short end joint	a- and c-setae analogic, long columnar, thin walled and bare with long end joint; b- and d-setae analogic, equilong and bare without end joint, slightly longer than a- and c-setae; e- seta spinose, without short end joint
Second antenna	endopod	c-, d-, e-setae absent; b-seta bare; one small oval hump with central concave on mid-ventral margin, instead of processus mamillaris	e-setae present; b-seta spinose; processus mamillaris normal.
	exopod	exopod 1 and 2 fused, exopod 2-4 bare, exopod 8 and 9 separated; terminal plumose seta with single tip	exopod 1 and 2 separated, exopod 2-4 with plumose setae, exopod 8 and 9 fused
Mandible	coxale teeth side	with eight distal teeth	with six distal teeth
	tooth endites	with four tooth plates	with three tooth plates
	endopod	endopod 1 with one ventral seta, and one dorsal seta; endopod 2 with one disto-ventral seta; terminal segment with seven spinose setae	endopod 1 with one ventral seta, without dorsal seta; endopod 2 with two disto-ventral setae; terminal segment with six setae, ventral three bare
Maxilla	endopod	endopod 1 with six disto-anterior setae, one disto-medial seta, none medial seta, and two disto-posterior setae; mid seta of terminal segment bare	endopod 1 with five disto-anterior setae, one disto-medial seta, two medial setae, and three disto-posterior setae; mid seta of terminal segment spinose
	endites	endite I with eleven plumose setae, endite II with ten plumose setae, endite III with eight plumose setae	endite I with five plumose setae; endite II with one bare and three plumose setae; endite III with ten bare setae
Fifth limb	basale	proximal-ventral group of setae with four setae	proximal-ventral group of setae with seven setae
	endopod	endopod 1 with one ventral seta	endopod 1 with two ventral setae
	endites	endite I with one seta; endite II with two setae; endite III with one proximal seta, three sharp and two blunt distal setae	endite I with five setae; endite II with one seta; endite III with none proximal seta, four sharp and two blunt distal setae
Sixth limb	basale	disto-dorsal seta (vesting of exopod) small and bare; three small ventral setae.	disto-dorsal seta (vesting of exopod) strong and spinose; seven ventral plumose setae
	endopod	endopod 1 with one ventral seta; endopod 2 with one ventral seta	endopod 1 bare; endopod 2 without ventral seta
Furca	unpaired seta	no	yes

seta has short end joint; in these specimens, a- and c-setae are analogic with long end joint, b- and d-setae are analogic without end joint, e-seta has no end joint; (5) in *P. commixtus*, the endopod of the second antenna has not c-, d- and e-setae, and one small oval hump with central concave on mid-ventral margin, instead of processus mamillaris; in these specimens, e-seta is present and the processus mamillaris is normal (Figs 2f and 7e); (6) in *P. commixtus*, the exopod 2-4 of the second antenna have no swimming setae (Figs 2e, 3a and 7f); (7) they have unsimilar tooth edge of the coxal endite (Figs 3b, c, 7j and Table 1); (8) they have different setal counts of the mandible, maxilla, fifth limb, and sixth limb (detailed numbers are given in Table 1); (9) *P. chenii* sp. nov. has unpaired seta on the furcal lamella (Figs 6b and 8f).

The ostracod faunae of the South China Sea have been known mainly from plankton surveys in surface water or euphotic zone (0–200 m). The local ostracod diversity of deep environments may equal or exceed that of their epi-pelagic relatives (Gianni, 2004; Danovaro et al., 2008). In these years, there are more and more deep-water species have been discovered and reported (Yin et al., 2014; Tanaka and Yasuhara, 2016; Du et al., 2018; Xiang et al., 2018). This work is the second discovery of the genus *Polyconchoecia* from the world.

Acknowledgements

We thank Patrick Page-McCaw (Vanderbilt University, USA), Mingyu Li (Xiamen University, China), Guangcheng Chen for critical reading of the manuscript. We are thankful for our zooplankton research group of Third Institute of Oceanography, MNR, for their valuable suggestions for the manuscript preparation.

References

Angel M V, Blachowiak-Samolyk K, Drapun I, et al. 2007. Changes in the composition of planktonic ostracod populations across a range of latitudes in the North-east Atlantic. Progress in Oceanography, 73(1): 60–78, doi: 10.1016/j.pocean.2006.11.002

Brandão S N, Angel M V, Karanovic I, et al. 2019. World ostracoda database. http://www.marinespecies.org/Ostracoda [2019–04–17]

Chavtur V G. 2003. Morphology and distribution of some new pelagic Ostracods of genus *Metaconchoecia* (Halocyprida: Halocyprididae) from the North Pacific. Zootaxa, 229(1): 1–102, doi: 10.11646/zootaxa.229.1.1

Chavtur V G, Angel M V. 2011. Revision of *Metaconchoecia* (Ostracoda: Halocyprididae) and the designation of two new tribes Conchoeciini and Metaconchoeciini. Zootaxa, 2857(1): 1–87, doi: 10.11646/zootaxa.2857.1.1

Chavtur V G, Bashmanov A G. 2018. Pelagic ostracods of the new subtribe Conchoeciina (Ostracoda, Crustacea) from the North Pacific. Zootaxa, 4516(1): 1–127, doi: 10.11646/zootaxa.4516.1.1

Chen Ruixiang, Lin Jinghong. 1995. Pelagic Ostracod in China Sea. Beijing: China Ocean Press

Dana J D. 1853. Crustacea. In: Wilkes C, Drayton J, United States Exploring Expedition, eds. United States Exploring Expedition, During the Year 1838, 1839, 1840, 1841, 1842 Under the Command of Charles Wilkes, U. S. N. Vol. 14, Crustacea, Part II. Philadelphia: Sherman

Danovaro R, Gambi C, Dell'Anno A, et al. 2008. Exponential decline of deep-sea ecosystem functioning linked to benthic biodiversity loss. Current Biology, 18(1): 1–8, doi: 10.1016/j.cub.2007.11.056

Di Celma C, Ragaini L, Caffau M. 2016. Marine and nonmarine deposition in a long-term low-accommodation setting: an example from the middle Pleistocene Qm2 unit, eastern central Italy. Marine and Petroleum Geology, 72: 234–253, doi: 10.1016/j.marpetgeo.2016.02.010

Du Feiyan, Xiang Peng, Chen Ruixiang, et al. 2018. *Polyconchoecia commixtus* gen. et sp. nov. (Ostracoda: Myodocopa: Halocyprididae) from the South China Sea. Acta Oceanologica Sinica, 37(10): 70–78, doi: 10.1007/s13131-018-1302-5

Fortey R A, Thomas R H. 1998. Arthropod Relationships. Dordrecht: Springer

George J, Nair V R. 1980. Planktonic ostracods of the northern Indian Ocean. Quarterly Review of Biology, 13(1): 29–44

Gianni M. 2004. High Seas Bottom Trawl Fisheries and Their Impacts on the Biodiversity of Vulnerable Deep-Sea Ecosystems: Options for International Action. Gland: IUCN

Harrison-Nelson E, Kornicker L S. 2000. *Euphilomedes cooki*, a new species of myodocopid ostracode from Moreton Bay, SE Queensland, Australia. Proceedings of the Biological Society of Washington, 113(2): 465–749

Karanovic I. 2010. A new *Euphilomedes* Kornicker, 1967 (Myodocopida: Philomedidae) from Tasmania with a key to the species of the genus. Marine Biodiversity, 40(3): 219–236, doi: 10.1007/s12526-010-0047-y

Latreille P A. 1802. Histoire Naturelle, Générale et Particulière des Crustacés et Des Insectes. Histoires des Cypris et des Cytherées, 8(4): 232–254

Lum K E, Syme A E, Schwab A K, et al. 2008. *Euphilomedes chupacabra* (Ostracoda: Myodocopida: Philomedidae), a new demersal marine species from coastal Puerto Rico with male-biased vespertine swimming activity. Zootaxa, 1684: 35–57, doi: 10.11646/zootaxa.1684.1.2

Martin J W, Davis G E. 2001. An Updated Classification of the Recent Crustacea. Los Angeles: Natural History Museum of Los Angeles County

Müller G W. 1912. Ostracoda. In: Schule F E, ed. Das Tierreich. Berlin: Friedländer und Sohn

Oakley T H, Wolfe J M, Lindgren A R, et al. 2013. Phylotranscriptomics to bring the understudied into the fold: monophyletic ostracoda, fossil placement, and pancrustacean phylogeny. Molecular Biology and Evolution, 30(1): 215–233, doi: 10.1093/molbev/mss216

Pinto R L, Jocqué M. 2013. A new species of *Elpidium* (Crustacea, Ostracoda) from bromeliads in Cusuco National Park, Honduras. ZooKeys, 313: 45–59, doi: 10.3897/zookeys.313.4904

Tanaka H, Yasuhara M. 2016. A new deep-sea hydrothermal vent species of ostracoda (crustacea) from the western pacific: implications for adaptation, endemism, and dispersal of ostracodes in chemosynthetic systems. Zoological Science, 33(5): 555–565, doi: 10.2108/zs160079

van Harten D. 1992. Hydrothermal vent Ostracoda and faunal association in the deep sea. Deep Sea Research Part A. Oceanographic Research Papers, 39(6): 1067–1070

Xiang Peng, Chen Xiaoyin, Chen Ruixiang, et al. 2017a. Two new benthic *Euphilomedes* Kornicker, 1967 (Ostracoda, Myodocopida, Philomedidae) from the Taiwan Strait (East China Sea). PeerJ, 5(2): e3146

Xiang Peng, Wang Yu, Chen Ruixiang, et al. 2018. A bathypelagic ostracod *Conchoecissa nigromaculatus* sp. nov. (Myodocopa, Halocyprididae) from the South China Sea. PeerJ, 6(3): e5557

Xiang Peng, Ye Youyin, Chen Xiaoyin, et al. 2017b. *Euphilomedes biacutidens* (Ostracoda, Myodocopida, Philomedidae), a new species from China Sea. PeerJ, 5(3): e3488

Yamaguchi S, Endo K. 2003. Molecular phylogeny of Ostracoda (Crustacea) inferred from 18S ribosomal DNA sequences: implication for its origin and diversification. Marine Biology, 143(1): 23–38, doi: 10.1007/s00227-003-1062-3

Yamaguchi T, Goedert J L, Kiel S. 2016. Marine ostracodes from Paleogene hydrocarbon seep deposits in Washington State, USA and their ecological structure. Geobios, 49(5): 407–422, doi: 10.1016/j.geobios.2016.06.003

Yin Jianqiang, Chen Qingchao, Li Kaizhi. 2014. *Bathyconchoecia liui* n. sp., a new species of Ostracod (Myodocopa, Halocyprididae) from the South China Sea. Crustaceana, 87(8–9): 1027–1035, doi: 10.1163/15685403-00003340

Acta Oceanol. Sin., 2020, Vol. 39, No. 4, P. 84–88
https://doi.org/10.1007/s13131-020-1581-5
http://www.hyxb.org.cn
E-mail: hyxbe@263.net

Three new species of Anthomedusae (Hydrozoa: Hydroidomedusa) from the Guangdong coastal water, China

Caixue Zhang[1]*, Jiaqi Huang[2], Shengli Sun[1], Sheng Ke[1], Guohuan Yang[1], Zhiguang Song[1], Yaoqian Liu[1]

[1] College of Chemistry and Environmental Sciences, Guangdong Ocean University, Zhanjiang 524088, China

[2] College of Ocean and Earth Sciences, Xiamen University, Xiamen 361005, China

Received 28 September 2018; accepted 29 July 2019

Abstract

The samples of Anthomedusae were collected from the Guangdong coastal water, China. Three new species of Anthomedusae, i.e. *Zhangiella condensum* Huang, Zhang et Sun, sp. nov., *Hydractinia leizhouensis* Huang, Zhang et Yang, sp. nov., and *Cladosarsia simplex* Huang, Zhang et Ke, sp. nov. are described. All type specimens are deposited in College of Ocean and Earth Sciences, Xiamen University.

Key words: Anthomedusae, Australomedusidae, Hydractiniidae, Corynidae, new species, China

Citation: Zhang Caixue, Huang Jiaqi, Sun Shengli, Ke Sheng, Yang Guohuan, Song Zhiguang, Liu Yaoqian. 2020. Three new species of Anthomedusae (Hydrozoa: Hydroidomedusa) from the Guangdong coastal water, China. Acta Oceanologica Sinica, 39(4): 84–88, doi: 10.1007/s13131-020-1581-5

1 Introduction

The samples of Anthomedusae were collected at the Leizhou Bay of Zhanjiang and Shuidong Bay of Maoming, Guangdong Province in May and August 2013. The vertical trawl method is used for sampling zooplankton specimens by dropping a 505-μm mesh-size plankton nets (net gape diameter, 50 cm) to the bottom of water and vertically lifted to the surface of water. The samples were stored in a solution of 5% formalin and classified and enumerated in the laboratory. All type specimens were stored at College of Ocean and Earth Sciences in Xiamen University.

2 The categorization of three new species in the classification system of Bouillon et al. (2006)

Superclass Hydrozoa Owen, 1843
Class Hydroidomedusa Claus, 1877 emend. (Bouillon and Boero, 2000)
Subclass Anthomedusae Haeckel, 1879
Order Filifera Kühn, 1913
Suborder Margelina Haeckel, 1879
Family Australomedusidae Russell, 1971
Genus *Zhangiella* Bouillon, Gravili, Pagès, Gili & Boero, 2006
Zhangiella condensum Huang, Zhang et Sun, sp. nov.
Family Hydractiniidae L. Agassiz, 1862
Genus *Hydractinia* van Beneden, 1841
Hydractinia leizhouensis Huang, Zhang et Yang, sp. nov.
Order Capitata Kühn, 1913
Suborder Tubulariida Fleming, 1828
Family Corynidae Johnston, 1836
Genus *Cladosarsia* Bouillon, 1978
Cladosarsia simplex Huang, Zhang et Ke, sp. nov.

2.1 *Zhangiella condensum Huang, Zhang et Sun, sp. nov.*

Diagnosis: Medusae pear-shaped, jelly thick; manubrium flat, without gastric peduncle, mouth cruciform; gonads perradial, shuttle shaped; four radial canals, one ring canal; four kidney-shaped tentacular bulbs with 5–6 hollow tentacles, one red brown ocellus at the base of each tentacle; velum narrow.

Description: Umbrella pyriform, 2.5–3.5 mm high, 2.2–3.0 mm wide; jelly thick; flat stomach without peduncle; cruciform mouth with four simple oral lips; gonad perradial, shuttle shaped; four radial canals, narrow and unbranched, a ring canal; four kidney-shaped tentacular bulbs with 5–6 hollow tentacles, one red brown ocellus at the base of each tentacle; velum narrow (Figs 1 and 2).

Type specimen: Holotype (GHU001), paratype (GHU002), two samples of *Zhangiella condensum* collected by Caixue Zhang, Jibiao Zhang, Guohuan Yang, and Sheng Ke from Sta. 03 (20°58′50.00″N, 110°11′55.00″E) in the coastal waters of the Leizhou Bay, Zhanjiang, Guangdong Province, China in May 2013.

Etymology: The species name "*condensum*" means thick umbrella in Latin, based on the thick umbrella character of the new species.

Distribution: The coastal waters of Guangdong Province in China.

Discussion: *Zhangiella condensum* has a flat stomach without oral tentacles; gonads on the stomach; umbrella margin with four perradial marginal tentacular bulbs. Therefore, the new species belongs to Subclass Anthomedusae Haeckel, 1879, Order Filifera Kühn, 1913, Family Australomedusidae Russell 1971 and Genus

Foundation item: The China Marine Special Nonprofit Scientific Research under contract No. 201505027; the Marine Science Research Team Project of Guangdong Ocean University under contract No. 002026002004.
*Corresponding author, E-mail: gdzhangcx@126.com

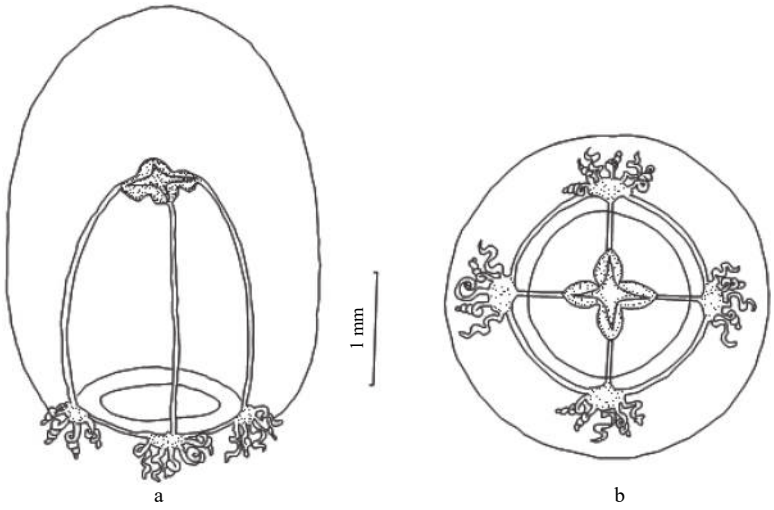

Fig. 1. The drawings of *Zhangiella condensum* Huang, Zhang et Sun, sp. nov. a. Lateral view and b. oral view.

Fig. 2. Photo images of *Zhangiella condensum* Huang, Zhang et Sun, sp. nov. a. Lateral view; b. oral view; and c. gonads, apical view.

Zhangiella Bouillon, Gravili, Pagès, Gili & Boero, 2006. Only three species are known, i.e., *Z. bitentaculata*, *Z. dongshanensis*, and *Z. nanhaiensis* (Zhang, 1982; Xu and Huang, 1994; Xu et al., 1991, 2014; Bouillon et al., 2006). *Zhangiella bitentaculata* umbrella thin, stomach with medusa buds, marginal tentacular bulbs with only two tentacles; *Z. dongshanensis* with interradial globular gonads on stomach; *Z. nanhaiensis* umbrella thin with a short peduncle, which differs from the new species, umbrella thick without peduncle, gonad perradial on the stomach and 4 marginal tentacular bulbs with 5 or 6 hollow tentacles.

Key to the new species of the genus *Zhangiella*

1. With short cone-shape peduncle; flat stomach; cross-shaped mouth; gonads on the stomach wall; 4 marginal tentacular bulbs with 5–6 hollow tentacles; with ocelli.....*Z. nanhaiensis* (Zhang, 1982)
   Without peduncle 2
2. Umbrella thin; with medusa buds; 4 marginal tentacular bulbs with two hollow tentacles; without ocelli.....*Z. bitentaculata* (Xu et al., 1991)
   Umbrella thick; without medusa buds; 4 marginal tentacular

bulbs with 5–6 tentacles; with ocelli.....3
3. With interradial globular shaped gonads .....
.....*Z. dongshanensis* (Xu and Huang, 1994)
With perradial shuttle-shaped gonads.....
..... *Z. condensum* Huang, Zhang et Sun, sp. nov.

2.2 *Hydractinia leizhouensis Huang, Zhang et Yang, sp. nov.*

Diagnosis: Umbrella almost hemispherical, flattened apex without apical projection; manubrium long, one-third of which extending beyond umbrellar margin, with a conical gastric peduncle; strip-shaped gonads interradial on manubrium; four well-developed oral arms, with terminal cnidocyst clusters; eight marginal tentacles in different size, the perradial tentacles longer than those interradial; marginal tentacular bulbs without ocelli, and each tentacle covered by numerous cnidocyst rings; four radial canals, one ring canal; velum narrow.

Description: Medusa 0.5 mm high and 0.7 mm wide, umbrella nearly hemispherical, flattened apex without apical projection; manubrium long, one-third of which extending beyond umbrellar margin, with a conical gastric peduncle; strip-shaped gonads interradial on manubrium, without medusa buds; four well-developed oral arms, with terminal cnidocyst clusters; eight marginal tentacle in different size, the perradial tentacles longer than those interradial; marginal tentacular bulbs without ocelli, and each tentacle covered by numerous cnidocyst rings; four radial canals, one ring canal; velum narrow (Figs 3 and 4).

Type specimen: Holotype (GHU003), the sample of *Hydractinia leizhouens* collected by Caixue Zhang, Jibiao Zhang, Guohuan Yang, and Sheng Ke from Sta. 06 (20°55′25.00″N, 110°17′60.00″E) of the coastal water of Leizhou Bay, Zhanjiang, Guangdong Province, China in May 2013.

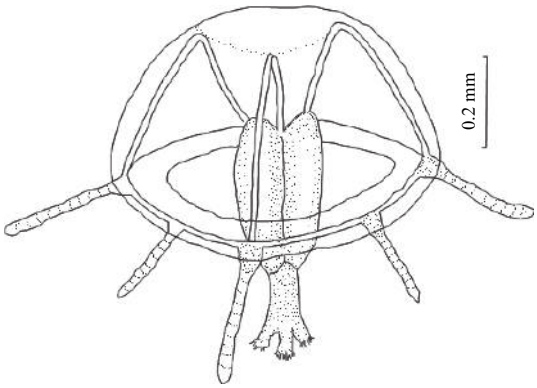

Fig. 3. The drawing of *Hydractinia leizhouensis* Huang, Zhang et Yang, sp. nov.

Fig. 4. Photo image of *H. leizhouensis* Huang, Zhang et Yang, sp. nov.

Etymology: This new species is named as *leizhouensis,* referring to the place of Leizhou Bay where the type specimen was collected.

Distribution: Coastal waters of Guangdong Province, China.

Discussion: *Hydractinia leizhouensis* has 8 marginal tentacles; gonads on the stomach; mouth with 4 oral lips perradial on stomach elongated to form oral arms; 4 radial canals, 1 ring canal. Those features place the medusa in the genus belongs to Subclass Anthomedusae Haeckel, 1879, Order Filifera Kühn, 1913, Family Hydractiniidae L. Agassiz, 1862 and Genus *Hydractinia* van Beneden, 1841. At the present time, there are 101 kinds of *Hydractinia* van Beneden, 1941, including hydroids and medusae, 32 kinds of medusae are known (Boero et al., 1998; Schuchert, 1996; Stampar et al., 2006; Bouillon and Boero, 2000; Kramp, 1961; Edwards, 1972; Lin et al., 2010; Li et al., 2010; Mayor, 1910; Mills, 1976; Wang et al., 2015; Xu and Huang, 2006). The new species has eight marginal tentacles, and the valid adult medusae species in the same genus with 8 tentacles are *H. tenuis*, *H. moniliformis*, *H. uniformis*, *H. carnea*, and *H. australis*. The first two species have oral lips without oral arms, whereas *H. carnea* do not have peduncles. The oral arms of *H. uniformis* are divided into several branches, with ocelli on the tentacle bulbs. *Hydractinia australis* has tentacles covered by numerous ring cnidocysts, and a short manubrium that does not stretch out of the umbrella cavity. These characteristics are different from those of the new species which has 4 well-developed and unbranched oral arms, with peduncle, gonads without medusa buds; manubrium stretching out of the umbrella cavity; tentacle bulbs without ocelli and tentacles covered by numerous ring cnidocysts.

Key to similar valid species of the genus *Hydractinia*

1. Without oral arms, only four oral lips with terminal clusters of cnidocyst.....2
With oral arms.....3
2. With peduncle; without ocelli.....
.....*H. tenuis* (Browne, 1902)
Without peduncle; with ocelli.....
.....*H. moniliformis* Huang, Zhong and Zhang Y J, 2010
3. Oral arms grow into two branches; 8–12 marginal tentacles, with ocelli .....
.....*H. uniformis* Stampar, Tronolone and Morandini, 2006
Simple oral arms without branches.....4
4. Without peduncle; 4–8 marginal tentacles.....
..... *H. carnea* (M. Sars, 1846)
With gastric peduncle.....5
5. Manubrium short, about one-half to two-thirds the length of the inner umbrella cavity; spared nematocysts on tentacles .....*H. australis* (Schuchert, 1996)
Manubrium long, one-third stretched out of umbrella cavity; ring-like nematocysts on tentacles .....
.....*H. leizhouensis* Huang, Zhang et Yang, sp. nov.

2.3 *Cladosarsia simplex Huang, Zhang et Ke, sp. nov.*

Diagnosis: Umbrella bell-shaped; with long manubrium reaching slightly beyond velum; with simple mouth, ring-shape; gonads completely surrounding the manubrium; four perradial marginal tentacular bulbs presenting adaxial pads of cnidocyst and abaxial red ocelli; marginal tentacle short, with one short pedunculated cnidocyst knob and with a terminal cnidocyst knob; four radial canals, one ring canal; velum moderately broad.

Description: Umbrella 2.5–3 mm in height, 1.6–2 mm in width, with bell-shaped umbrella, exumbrella smooth, apical mesoglea thick, lateral walls thin, without scattered nematocysts; with long and mallet-shaped manubrium reaching slightly beyond velum; with simple mouth, ring-shape; gonads completely surrounding the manubrium; four perradial marginal tentacles, with adaxial nematocyst pad at tentacular bulbs with abaxial red ocelli; short tentacles bend inward, about a quarter of the umbrella height, with one short pedunculated cnidocyst knob and with a terminal cnidocyst knob; four radial canals, one ring canal; the ends of each radial canal connected to the endoderm of the tentacular bulbs, velum medium width (Figs 5 and 6).

Type specimen: Holotype (GHU004), paratype (GHU005), two samples of *Cladosarsia simplex* collected by Caixue Zhang, Jibiao Zhang, Guohuan Yang and Sheng Ke from coastal water of Shuidong Bay (21°28′24.48″N, 111°05′0.14″E), Maoming, Guangdong Province, China in October 2013.

Etymology: This species is named after *simplex* in Latin, which means simple, and suggests that the tentacle structure is simple.

Distribution: Coastal waters of Guangdong Province, China.

Discussion: *Cladosarsia simplex* has adaxial pads of cnidocyst at the marginal tentacle bulbs with abaxial red ocelli; 4 equally long perradial marginal tentacles, one short pedunculated cnidocyst knob to form a branch with terminal cnidocyst knob; gonads completely surround the manubrium, so the species belongs to Anthomedusae Haeckel, 1879, Capitata Kühn, 1913, Corynidae Johnston, 1836, and *Cladosarsia* Bouillon, 1978. At the present time, there are 4 species of *Cladosarsia* Bouillon, 1978 (Bouillon, 1978; Xu and Huang, 2006; Huang et al., 2008), i.e., *C. minima* Bouillon, 1978, *C. capitata* Bouillon, 1978, *C. gulangensis* Xu et Huang, 2006 and *C. quanzhouensis* Huang, Xu, Li et Qiu, 2008. *Cladosarsia minima* has a short manubrium in a half height bell cavity and marginal tentacles with 3–4 short pedunculated cnidocyst knobs and with a terminal long branch. *Cladosarsia capitata* has a long manubrium more than twice the height of the umbrella; tentacles with 4–6 short pedunculated knobs. *Cladosarsia gulangensis* has a short manubrium less than the bell cavity and tentacles with long 5–10 pedunculated cnidocyst knobs. *Cladosarsia quanzhouensis* has a thin and long manubrium nearly sesqui height of the bell cavity and tentacles with 8–14 pedunculated knobs. These characteristics are different from those of the new species, which has a long manubrium and tentacles with one short pedunculated knob to form a branch with the terminal cnidocyst knob.

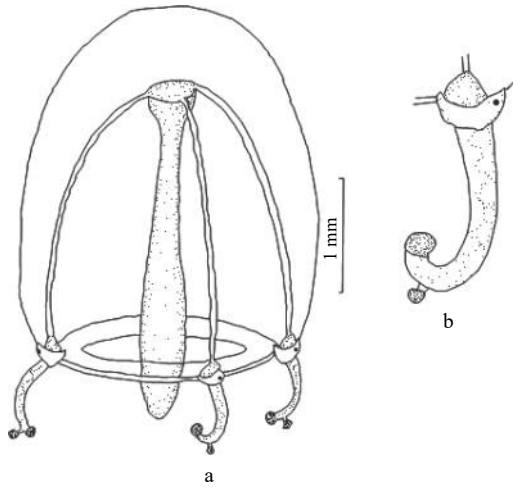

Fig. 5. The drawings of *Cladosarsia simplex* Huang, Zhang et Ke, sp. nov. a. Lateral view and b. enlarged tentacle.

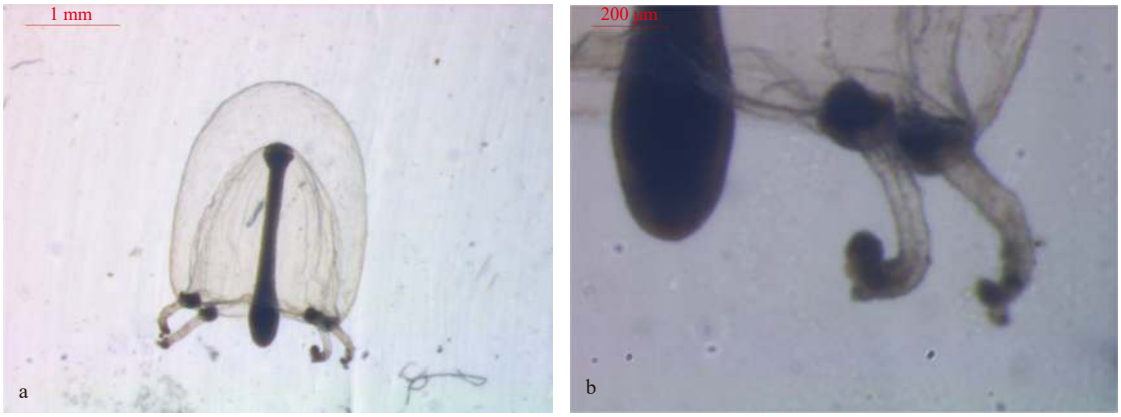

Fig. 6. Photo images of *Cladosarsia simplex* Huang, Zhang et Ke. sp. nov. a. Lateral view and b. enlarged marginal umbrella.

Key features to the new species of the genus *Cladosarsia*

1. Two branches at the end of tentacles; tentacles with 8–14 long pedunculated knobs.....*C. quanzhouensis* Huang, Xu, Li and Qiu, 2008
   Only one branch at end of tentacles 2
2. Short manubrium, not stretched out of cavity 3
   Long manubrium, stretched out of cavity 4
3. Tentacular bulbs with ocelli, short tentacles with 3–4 pedunculated knobs.....*C. minima* Bouillon, 1978
   Tentacular bulbs without ocelli, long tentacles curved at proximal, with 5–10 pedunculated cnidocyst knobs.....*C. gulangensis* Xu and Huang, 2006
4. Long manubrium, over two times the length of the umbrella, proximal thin and long, distal expanded; tentacles with 4–6 short pedunculated cnidocyst knobs.....*C. capitata* Bouillon, 1978
   Wooden-club-shape manubrium, long, stretched out cavity; tentacles with one short pedunculated cnidocyst knob forms a branch with terminal cnidocyst knob.....*C. simplex* Huang, Zhang et Ke, sp. nov.

Acknowledgements

We are grateful for sampling and embellishing assistance from our colleagues of Jibiao Zhang, Zike Zhao, and Zhongji Qian.

References

Boero F, Bouillon J, Piraino S. 1998. Heterochrony, generic distinction and phylogeny in the family Hydractiniidae (Hydrozoa: Cnidaria). Zoologische Verhandelingen, 323(4): 25–36

Bouillon J. 1978. Hydroméduses de l'archipel des Séchelles et du Mozambique. Revue de Zoologie Africaine (in French), 92: 118–172

Bouillon J, Boero F. 2000. Phylogeny and classification of Hydroidomedusae. Thalassia Salentina, 24: 1–296

Bouillon J, Gravili C, Pagès F, et al. 2006. An Introduction to Hydrozoa. Vol 194. Paris: Publications Scientifiques du Museum Paris Paris France, 1–591

Edwards C. 1972. The hydroids and the medusae *Podocoryne areolata*, *P. borealis* and *P. carnea*. Journal of the Marine Biological Association of the United Kingdom, 52(1): 97–144, doi: 10.1017/S0025315400018609

Huang Jiaqi, Xu Zhenzu, Lin Junzhuo, et al. 2008. Three new species of Anthomedusae (Hydrozoa, Hydroidomedusae) from the Fujian sea water. Journal of Xiamen University (Natural Science) (in Chinese), 47(3): 408–412

Kramp P L. 1961. Synopsis of the medusae of the world. Journal of the Marine Biological Association of the United Kingdom, 40: 7–382, doi: 10.1017/S0025315400007347

Li Shangping, Zhong Qiuping, Zhang Chenxiao, et al. 2010. Two new species of the genus *Hydractinia* in Guangxi coast, China (Cnidaria, Anthomedusae, Hydractiniidae). Acta Zootaxonomica Sinica (in Chinese), 35(4): 853–856

Lin Mao, Xu Zhenzu, Huang Jiaqi, et al. 2010. Two new species of genus *Hydractinia* from China (Filifera, Hydractiniidae). Journal of Fisheries of China (in Chinese), 34(1): 67–71, doi: 10.3724/SP.J.1231.2010.06477

Mayor A G. 1910. Medusae of the World. Carnegie: Carnegie Institution of Washington, 109: 1–735

Mills C E. 1976. Podocoryne selena, a new species of hydroid from the Gulf of Mexico, and a comparison with *Hydractinia echinata*. The Biological Bulletin, 151(1): 214–224, doi: 10.2307/1540715

Schuchert P. 1996. The marine fauna of New Zealand: athecate hydroids and their medusae (Cnidaria, Hydrozoa). New Zealand Oceanographic Institute Memoir, 106: 1–159

Stampar S N, Tronolone V B, Morandini A C. 2006. Description and life cycle of the hydrozoan *Hydractinia uniformis*, sp. nov. (Cnidaria: Hydrozoa: Hydractiniidae), from the coast of southeastern Brazil. Zootaxa, 1200: 43–60

Wang Chunguang, Huang Jiaqi, Xu Zhenzu, et al. 2015. Two new species of genus *Hydractinia* from the South China Sea (Cnidaria, Anthomedusae, Filifera, Hydractiniidae). Journal of Fisheries of China (in Chinese), 39(8): 1199–1202

Xu Zhenzu, Huang Jiaqi. 1994. A new genus and two new species of Hydroidomedusae from Taiwan Strait. Journal of Xiamen University (Natural Science) (in Chinese), 33(S1): 149–153

Xu Zhenzu, Huang Jiaqi. 2006. On new genus, species and record of Laingiomedusae and Anthomedusae in Fujian coast (Cnidaria, Hydroidomedusae). Journal of Xiamen University (Natural Science) (in Chinese), 45(S2): 233–249

Xu Zhenzu, Huang Jiaqi, Chen Xu. 1991. On new species and record of Hydromedusae in the upwelling region off the Minnan-Taiwan Bank fishing ground, China. In: Hong Huasheng, Qiu Shuyuan, Ruan Wuqi, et al., eds. Minnan-Taiwan Bank Fishing Ground Upwelling Ecosystem Study (in Chinese). Beijing: Science Press, 469–486

Xu Zhenzu, Huang Jiaqi, Lin Mao, et al. 2014. The Superclass Hydrozoa of the Phylum Cnidaria in China (in Chinese). Beijing: China Ocean Press, 1–945

Zhang Jinbiao. 1982. A new family, genus and species of Anthomedusae from the northern South China Sea. Haiyang Xuebao (in Chinese), 4(2): 209–214

Acta Oceanol. Sin., 2020, Vol. 39, No. 4, P. 89–99
https://doi.org/10.1007/s13131-020-1536-x
http://www.hyxb.org.cn
E-mail: hyxbe@263.net

Evaluating impacts of pulse fishing on the effectiveness of seasonal closure

Lei Xing[1, 2], Yong Chen[2, 3], Chongliang Zhang[1], Bai Li[2], Yunne-Jai Shin[4, 5], Yiping Ren[1, 3*]

[1] College of Fisheries, Ocean University of China, Qingdao 266003, China

[2] School of Marine Sciences, University of Maine, Orono, Maine 04469, USA

[3] Laboratory for Marine Fisheries and Aquaculture, Pilot National Laboratory for Marine Science and Technology (Qingdao), Qingdao 266237, China

[4] Institut de Recherche pour le Développement (IRD), Université de Montpellier, CNRS, Ifremer, MARBEC, CC093, 34095 Montpellier Cedex 5, France

[5] Marine Research (MA-RE) Institute and Department of Biological Sciences, University of Cape Town, Private Bag X3, Rondebosch 7701, South Africa

Received 25 March 2019; accepted 24 June 2019

Abstract

Seasonal fishing closures are often used in fisheries management to conserve overfished stocks. As one of the unintended consequences, fishermen often contend for maximizing catches immediately after reopening fisheries. The resultant large catch landings in a short time period (i.e., pulse fishing) may undermine the benefit of closure. We implemented an end-to-end model OSMOSE-JZB (Object-oriented Simulator of Marine ecOSystem Exploitation OSMOSE) modelling ecosystem in the Jiaozhou Bay located in China to evaluate the impact of pulse fishing on the effectiveness of seasonal closure at levels of fish community, population, and individual. Our study demonstrated that the three-month closure was successful in conserving fish stocks. There were small variations on ecological indicators (i.e., total biomass of the community, mean trophic level of the community, mean trophic level of the catch, and Shannon-Wiener biodiversity index) when pulse fishing occurred. Pulse fishing seemed not to result in a great shift in community structure. Compared to other species, the biomass of two large predatory fishes were more susceptible to pulse fishing. Pulse fishing could change the pressure of predators to fish stocks via food webs, especially for young individuals. Our simulations indicate that we can improve the effectiveness of seasonal closure by managing pulse fishing. Although the results derived in this study may be specific to the target ecosystem, the general approach is applicable to other ecosystems when evaluating fishing impacts.

Key words: OSMOSE, pulse fishing, seasonal closure, Jiaozhou Bay

Citation: Xing Lei, Chen Yong, Zhang Chongliang, Li Bai, Shin Yunne-Jai, Ren Yiping. 2020. Evaluating impacts of pulse fishing on the effectiveness of seasonal closure. Acta Oceanologica Sinica, 39(4): 89–99, doi: 10.1007/s13131-020-1536-x

1 Introduction

Overfishing is a great threat to sustainable utilization of fisheries resources (Coll et al., 2013). As one of the most advocated management tools, seasonal closures can bring a reduction of fishing effort conducive to recovering fish stocks, and aim to benefit both ecosystems and fisheries socio-economics (Clarke et al., 2015; Samy-Kamal et al., 2015). Unrestrictive fishing activities can undermine the benefits from the fishing closure (Murawski et al., 2005). The large catch landing in a short time period can cause irreversible harm to fish stocks (Purcell et al., 2013) and incidental bycatch has a serious impact on food webs and ecological structure (Fulton et al., 2011). In practice, fishermen may change their harvest strategies in order to compensate the loss of landings resulted from the fishing moratorium (Wang et al., 2015). As the recognized importance of fishermen's behaviors in determining the effectiveness of fisheries management (van Putten et al., 2012), it is necessary to evaluate the impacts of temporal variations in fishing effort after seasonal fishing closure.

There is increasing attention to small-scale fisheries because of their contribution to food supply and economic income (Weeratunge et al., 2014). The fishermen's decisions, such as timing for entering or exiting fishing ground, are closely related to fish stock state (Kiyama and Yamazaki, 2018). Pulse fishing is a fishing strategy that lands large catches in a short time period and lets the stock grow in other periods (Da-Rocha et al., 2014). The summer moratorium of fishing has been implemented over twenty years across the coastal waters in China. Fishermen seek to maximize commercial profits resulting in an especial pulse fishing that substantial fishing effort concentrates immediately after the end of the seasonal closure. This management strategy seems not to prevent the depletion of natural resources resulting from high fishing effort. There are increasing reports on overexploited fisheries and disappeared fishing grounds (Jiang et al., 2009; Zhu, 2009). Many studies attribute this failure to high fishing effort during fishery openings (Wang, 2008; Shen and Heino, 2014). The effectiveness of the seasonal closure is closely tied to the seasonality of fishing effort during the harvest season (Cohen et al., 2013; Ichinokawa et al., 2015). Therefore, we hypothesize

Foundation item: The Fundamental Research Funds for the Central Universities under contract Nos 201512002 and 201612002.
*Corresponding author, E-mail: renyip@ouc.edu.cn

that whether it is possible to improve the effectiveness of seasonal closures by managing pulse fishing.

There is a worldwide consensus that ecosystem modelling approaches are a necessary complement to single-species approach by supporting fisheries management with the incorporation of ecosystem consideration (Hilborn, 2011). Ecosystem models can provide insights into variations of ecosystem under different management strategies, which can help optimize decision-making and avoid potentially irreversible harm on fish stocks (Fogarty, 2014). This study focuses on the small-scale fishery in the Jiaozhou Bay, China where has implemented the seasonal closure to conserve fish resources. Using an end-to-end model "OSMOSE-JZB" (Object-oriented Simulator of Marine ecOSystem Exploitation OSMOSE) previously developed for the Jiaozhou Bay (Xing et al., 2017), we simulate ecosystem dynamics from low trophic level (LTL) to high trophic level (HTL) in an individual-based way that helps us understand the change of different ecological components after pulse fishing arising.

There are four typical pulse fishing scenarios considered here based on different patterns of pulse fishing occurring in other coastal waters of China. The impact of pulse fishing on the effectiveness of seasonal closure were systematically evaluated at the levels of fish community, population, and individual. Besides, a scenario without seasonal closure was simulated used for quantifying the effectiveness of seasonal closure. Given the varying nature of fishing effort in realism ecosystem, an uncertainty analysis was conducted to examine the impacts of uncertain fishing effort on the model prediction and the robustness of our results. Our findings can improve our understanding on how pulse fishing influences the effectiveness of seasonal closure in a semi-closed bay ecosystem. This study can facilitate the development of management strategies for sustainable fisheries and the application of ecosystem modelling approach in tactical management.

2 Materials and methods

2.1 *Study area and data*

The Jiaozhou Bay is a semi-enclosed bay located on the south of Shandong Peninsula in China (Fig. 1). Its trophic structure has shifted greatly over the last two decades because of long-term heavy fishing activities (Han et al., 2015). The seasonal closure has been implemented over twenty years to improve the fisheries status. As there are few regulations constraining pulse fishing, it is essential to investigate whether pulse fishing impacts the effectiveness of the seasonal closure in the Jiaozhou Bay. An operational model OSMOSE-JZB was developed to simulate the ecosystem dynamics in the Jiaozhou Bay based on data collected from stratified random bottom trawl surveys in February, May, August, and November of 2011.

2.2 *The operational model: OSMOSE-JZB*

The OSMOSE-JZB consists of two main sub-models that describe two main biotic components: LTL groups and HTL groups. The spatio-temporal dynamics of LTL groups were simulated by hydrological model (the Finite Volume Coastal Ocean Model FVCOM; Chen et al., 2003) coupled with biogeochemical model (the North Pacific Ecosystem Model Used for Regional Oceanography NEMURO; Aita et al., 2007). The dynamics of trophic interactions and full life cycle for the HTL groups were described by OSMOSE model developed by Shin and Cury (2001). The model builds the food web, including five LTL groups and fourteen HTL groups, based on a one-way coupling approach that the distribution of LTL groups is just provided as a prey field for HTL groups. The detailed inputs, parameterization and calibration of the model can be found in Xing et al. (2017). We provide here a brief description of model structure and fishing configuration for each scenario. The detailed information of fourteen HTL groups are listed in Table 1.

OSMOSE is a multi-species individual-based model assum-

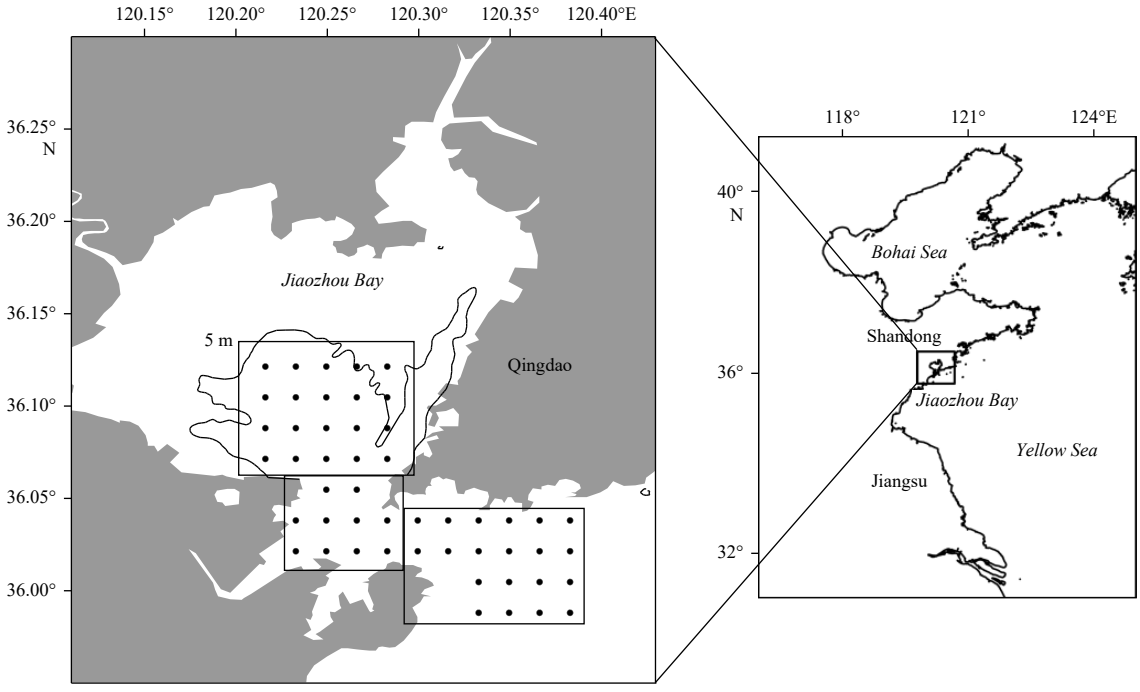

Fig. 1. Location and sampling design of survey in the Jiaozhou Bay, China. Stratified random bottom trawl surveys were conducted in February, May, August, and November of 2011.

Table 1. The fourteen high trophic level (HTL) groups modelled explicitly in the OSMOSE-JZB model

Type		HTL groups	Time steps for moving out of simulated domain	F_{annual}	
				(F0–F4)	(F5)
1	SP0:	*Oratosquilla oratoria* (Japanese mantis shrimp)	null	0.420	0.560
	SP1:	*Palaemon gravieri* (Chinese ditch prawn), *Parapenaeopsis tenella* (Smoothshell shrimp), *Alpheus japonicus* (Japanese snapping shrimp)	null	0.365	0.486
	SP5*:	*Octopus* sp. (Octopus)	null	0.350	0.467
	SP6:	*Sebastes schlegelii* (Korean rockfish)	null	0.482	0.643
	SP8:	*Amblychaeturichthys hexanema* (Pinkgray gody)	null	0.229	0.306
	SP11:	*Johnius belangerii* (Belanger's croaker)	null	0.411	0.548
	SP13:	*Cynoglossus joyneri* (Red tonguesole)	null	0.365	0.486
2	SP2*:	*Charybdis bimaculata* (Two-spot swimming crab)	0–5	0.314	0.470
	SP4*:	*Loligo* sp. (Squid)	0–5	0.419	0.628
	SP9*:	*Thryssa kammalensis* (Kammal thryssa)	0–5	0.467	0.700
3	SP3*:	*Charybdis japonica* (Japanese swimming crab)	0–11	0.246	0.369
	SP12*:	*Trachypenaeus curvirostris* (Southern rough shrimp)	0–11	0.426	0.638
4	SP7*:	*Pholis fangi* (Gunnel)	12–17	0.426	0.480
5	SP10*:	*Liparis tanakae* (Tanaka's snailfish)	0–5, 12–17	0.488	0.586

Note: The common name of each HTL group showed in the bracket. There were 24 time steps in a simulated year numbered from zero to 23. F_{annual} was annual fishing mortality summing up fishing mortality rate at each time step. The migratory species marked with *, and others were sedentary species that spent all life in the Jiaozhou Bay. In contrast to other migratory species, *Octopus* sp. migrated into or outside the study area at a given age, and could be available to fishing all year round similar to sedentary species.

ing that predation is opportunistic based on fish size and spatial co-occurrence. The fish school is a basic unit in the model, and the model assumes that the process of predation is opportunistic and size-based (Shin and Cury, 2004). There are six crucial processes in each time step (half a month), including: (1) the spatial distribution and random-walk movement mimicking the dispersal of fish (Halouani et al., 2016); (2) opportunistic predation based on spatial co-occurrence and size adequacy between prey and predators (Travers et al., 2009); (3) various mortalities (e.g., predation mortality, fishing mortality, starvation mortality, additional natural mortality) applied simultaneously based on the stochastic algorithm method making all mortalities stochastic and competitive that avoids the bias of mortality outcome (Grüss et al., 2016b); (4) growth calculated using von Bertalanffy growth model and weight-length relationship when individuals ingest enough food; (5) species-specific reproduction depending on sex ratio, spawning biomass, relative fecundity, and the percentage of eggs produced at each time step; and (6) migratory species migrating into or outside the simulated area (Xing et al., 2017).

The food web built by the OSMOSE-JZB covers most of components in the Jiaozhou Bay, and is proved that this model can capture ecosystem dynamics there (Xing et al., 2017). The summer moratorium of fishing from June 1 to September 1 is included in the model, and fishing effort is assumed to be evenly applied to the fisheries during the fishing season. In other words, fishing mortality rate of each HTL group set in the model is uniform in fishing season. Individuals are harvested when they reach the size of recruitment into fisheries, which is set at 5 cm for all HTL groups.

2.3 *Simulation scenario*

This study focuses on the evaluation of impacts of potential pulse fishing on the ecosystem of the Jiaozhou Bay where fishing is prohibited from June to August each year. The fishing mortality rate (i.e., $M_{fishing}$) was used to indicate impacts of fishing effort on fish individuals. We assumed the fishing effort was directly proportional to fishing mortality rate, and changed the $M_{fishing}$ at each time step to imitate different scenarios. According to relevant studies on potential pulse fishing situations in China (Chen, 2007; Zhu, 2009; Shen and Heino, 2014), there were six scenarios (i.e., F0–F5 below) considered here:

(1) F0: The configuration of fishing mortality rate is the same to the initial OSMOSE-JZB model built by Xing et al. (2017) (Fig. 2a).

(2) F1: Fishing mortality rate peaked at a maximum at the beginning of the fishing season. Afterwards it dropped abruptly, and then remained at a steady level until the end of the fishing season (Fig. 2b).

(3) F2: Fishing mortality rate reached a maximum, at a lower level than in F1, during the start of the fishing season, and then declined to reach a low stable level until the end of the fishing season (Fig. 2c).

(4) F3: Fishing mortality rate went up first with a peak in late autumn, and then dropped in subsequent time. Similarly to F1 and F2, fishing mortality rate remained at a low level from the start of the next year to the end of the fishing season (Fig. 2d).

(5) F4: Fishing mortality rate peaked twice, at the start and at the end of the fishing season (Fig. 2e).

(6) F5: The season closure was revoked. The additional fishing effort was imposed to HTL groups in June, July, and August. The fishing mortality rate followed a uniform distribution (Fig. 2f).

The first scenario (i.e., F0) was considered as the reference/base state representing the ecosystem of the Jiaozhou Bay without pulse fishing. The subsequent three scenarios (i.e., F1–F3) simulated pulse fishing starting early in the fishing season with three different trends. Scenario F4 simulated pulse fishing occurring before the beginning and after the end of seasonal closure. The last scenario (i.e., F5) simulated the situation that removed seasonal closure, and aimed to quantify the effectiveness of seasonal closure by comparing with the scenario F0.

Some species included in the model might migrate out of the study area at a given time in a year as part of the life history (Xing et al., 2017). Migratory species were assumed to be not harvested during the seasonal closure or periods outside simulated area. Subsequently, HTL groups were divided into five types on the basis of time they stayed in the simulated domain (Table 1). The detailed temporal distribution of fishing mortality rates and annual fishing mortality rate (i.e., F_{annual}) in each scenario were shown in Fig. 2 and Table 1, respectively. Our study only investig-

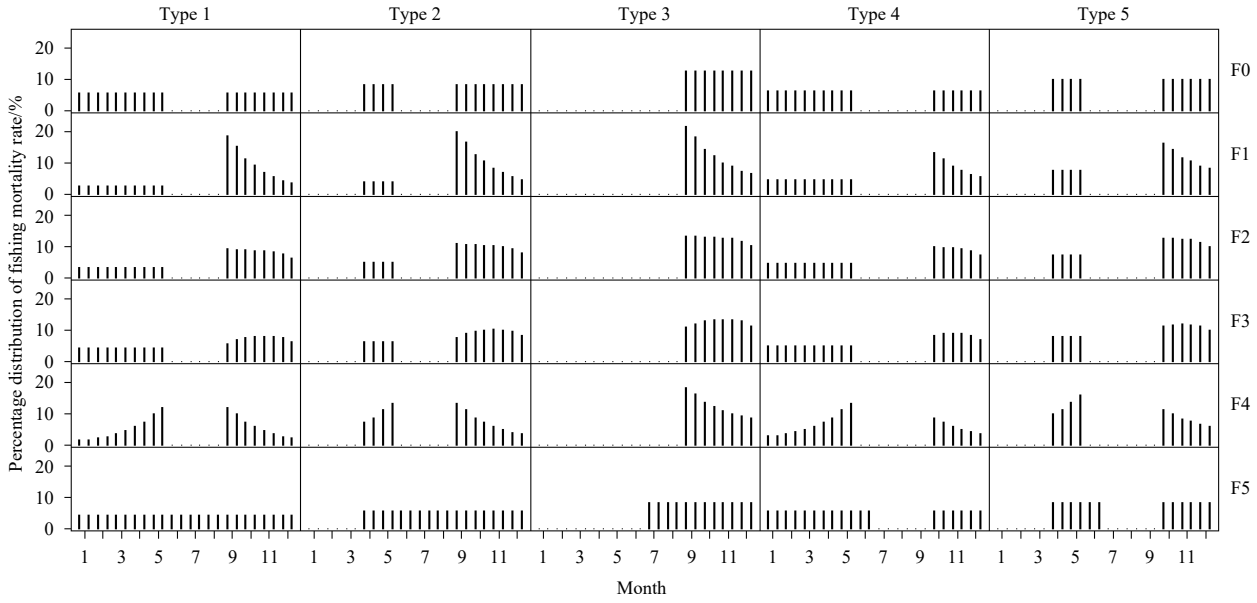

Fig. 2. Percentage distribution of fishing mortality rate for fourteen HTL groups that were divided into five types set explicitly in six scenarios. The sum of percentages for each HTL group at each time step was equal to 100% in a simulated year (24 time steps). The fishing mortality rate at each time step calculated dependent upon corresponding percentage ratio and annual fishing mortality rate. A seasonal closure implemented from June to August in scenarios F0–F4, and revoked in scenario F5.

ates the influence caused by pulse fishing rather than the magnitude of fishing effort. The annual fishing mortality rates of each HTL group in four pulse fishing scenarios (i.e., F1–F4) were kept the same to scenario F0. In scenario F5, fish populations were assumed to confront with an identical fishing pressure in June, July, and August as other period of fishing. The fishing mortality rate of HTL groups were evenly assigned to each time step when they stayed in the Jiaozhou Bay. Thus, annual fishing mortality rates in scenario F5 were higher than those in other scenarios.

Each scenario had a burn-in period of 80 years to ensure that the model was in a stable state with the same input configuration to the initial OSMOSE-JZB model, and then ran the model for another 40 years with configuration set in each scenario. Given the stochasticity incorporated in the model (Grüss et al., 2016a; Fu et al., 2017), each scenario was ran 100 times, and the outputs were averaged over the 100 simulation runs. The OSMOSE version used here is v3.2 coded in JAVA, and available online (http://www.osmose-model.org/).

2.4 *Uncertainty analysis*

As a result of observation and/or management implementation errors, we made an analysis on the consequences of uncertainty in fishing effort for the first five fishing scenarios (i.e., F0–F4). The new temporal distribution of fishing mortalities for all species was constructed for each scenario with a 10% level of uncertainty assigned to their values. The errors of fishing mortality rate in each time step were randomly generated by a Monte Carlo method and followed a uniform distribution with bounds related to their level of uncertainty (Han et al., 2017). Therefore, the sum of fishing mortality rate at each time step (i.e., annual fishing mortality rate) of each HTL group could vary between 0.9 and 1.1 times the initial value. There were 100 new constructed temporal distributions of fishing mortalities generated for all species in each scenario. Each of the above simulations was repeated for 12 times considering the stochasticity of the model, meaning that there were 1 200 simulations ran for each fishing scenario.

2.5 *Measurement of fisheries status*

The relative change of fisheries status were evaluated at levels of community, population, and individuals. The variations of fish community structure were described by four common ecological indictors relating to unexploited level (i.e., total biomass of the community), community trophic composition (i.e., mean trophic level of the community), capturing "fishing down marine food webs" (i.e., mean trophic level of the catch), and diversity (i.e., Shannon-Wiener biodiversity index) (Fulton et al., 2005; Shannon et al., 2009). Two population-based indicators (i.e., species biomass and mean body length) were used to measure the response of different fishes to different harvest strategies in terms of biomass and size structure of populations. At the level of individual, fishing mortality rate (i.e., M_{fishing}) stood for direct impact of fishing on individuals of two age groups, which were represented juveniles (below 1 year old) and adults (from 1 to 2 years old), respectively. The variations of predation mortality rate (i.e., $M_{\text{predation}}$) of individuals from two age groups showed how altered fishing activities changed interspecies interactions. The indicator M_{sum}, summing up relative predation and fishing mortality rates, was used to quantify the change of combined pressures from predators and fishing when pulse fishing arose (i.e., F1–F4) or seasonal closure was revoked (i.e., F5) (Table 2).

3 Results

3.1 *Relative changes at community level*

There were small differences of all ecological indicators between pulse fishing scenarios (i.e., F1–F4) and reference state (i.e., F0). Pulse fishing seemed not to result in a marked change of community structure (Fig. 3). The H' had an upward trend in scenario F1. In scenario F4, all ecological indicators increased when pulse fishing occurred. The H' was more susceptible to pulse fishing compared with other ecological indicators. In contrast to pulse fishing scenarios, all ecological indicators in scenario F5 declined after imposing additional fishing effort to fish

Table 2. Definitions of indicators that characterize fish community, population, and individual

Level	Indicators	Symbol	Definition	Sources
Community	total biomass of the community	Bio_{com}	$Bio_{com} = \sum_i Bio_i$, where Bio_i denotes the biomass of a given species i in the simulated area	
	mean trophic level of the community	mTL	$mTL = \sum_i TL_i \times \frac{Bio_i}{Bio_{com}}$, where Bio_i denotes the biomass of a given species i; Bio_{com} indicates the total biomass of the community; TL_i represents the mean trophic level of species i, and its computational method was the same as in Xing et al. (2017)	Travers et al. (2006), Xing et al. (2017)
	mean trophic level of the catch	mTL_{catch}	$mTL_{catch} = \sum_i TL_i \times \frac{Bio_{catch,\,i}}{Bio_{catch,\,com}}$, where $Bio_{catch,i}$ denotes the biomass of the given species i in catch; $Bio_{catch,\,com}$ indicates the total yield; TL_i represents the mean trophic level of a target species i, and its computational method was the same as in Xing et al. (2017)	Travers et al. (2006), Xing et al. (2017)
	Shannon-Wiener biodiversity index	H'	$H' = -\sum_i P_i \times \ln(P_i)$, where P_i denotes the proportion of the biomass of a given species i in the community	Travers et al. (2006)
Population	species biomass	Bio_i	The total biomass of a species i in the simulated area	
	mean body length	$\bar{L}$	$\bar{L} = \sum \frac{Lj}{N_i}$, where L_j is the body length (cm) of an individual fish j and N_i is the number of the species i in the simulated area	Shin et al. (2005)
Individual	predation mortality rate	$M_{predation}$	provided in outputs of the model	
	fishing mortality rate	$M_{fishing}$	provided in outputs of the model	
	relative change of two mortality rates	M_{sum}	the sum of relative fishing and predation mortality rates between pulse fishing scenarios and reference state	

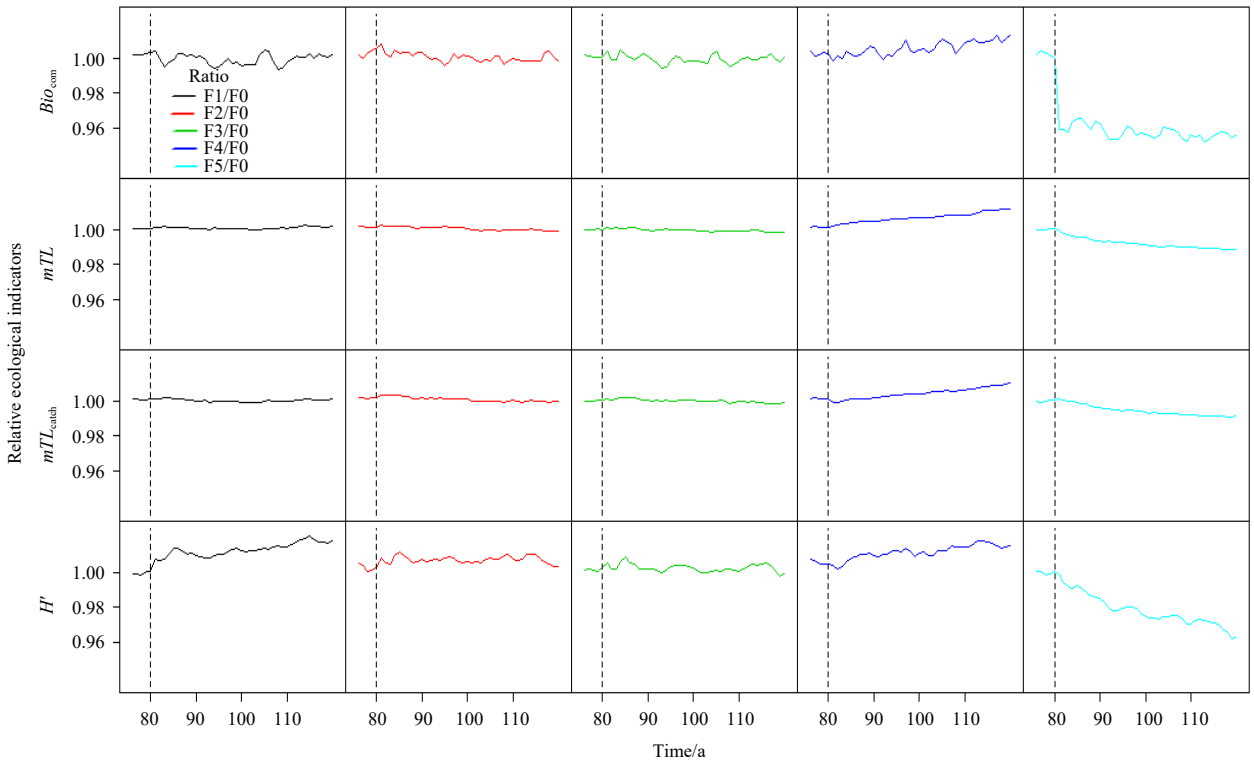

Fig. 3. Relative average annual changes in four ecological indicators, i.e., total biomass (Bio_{com}), mean trophic level of the community (mTL), mean trophic level of the catch (mTL_{catch}) and Shannon-Wiener biodiversity index (H'), of 14 HTL groups after the 75th year. The ratios of four indicators between last five fishing scenarios (i.e., F1–F5) and reference state (i.e., F0) were represented for relative changes. The predicted data are averages of 100 repeated simulations.

stocks in June, July, and August (Fig. 3). It implied that the three-month seasonal closure effectively protected fish community from further eroding by fishing activities.

3.2 *Relative changes at population level*

The two large predatory fishes, *S. schlegelii* (SP6) and *J. belangerii* (SP11), were more sensitive to pulse fishing, and other species fluctuated around the reference predictions. The biomass of *S. schlegelii* declined in front three pulse fishing scenarios, but increased significantly in scenario F4. The biomass of *J. belangerii* increased except in scenario F3 for which the biomass was close to that in F0. Similar to predictions in pulse fishing scenarios,

both of them showed a stronger response to additional fishing effort in June, July, and August, and declined to a lower level than other scenarios (Fig. 4).

The annual mean length of each HTL group varied less than species biomass, indicating that the modelled species size structure did not display a big shift. Mean body lengths of six species were sensitive to varying fishing effort: (1) For the first three pulse fishing scenarios (i.e., F1–F3), the mean body lengths of three species groups, i.e., small shrimp groups (SP1: *P. gravieri*, *P. tenella*, and *A. japonicus*), *J. belangerii*, and *C. joyneri* (SP13), were smaller than those for the reference state, however, the mean length of *S. schlegelii* was greater; (2) *O. oratoria* (SP0) showed a downward trend in scenarios F1 and F5; (3) in contrast to *S. schlegelii* and *J. belangerii*, the mean length of small shrimp groups, *Octopus* (SP5*), and *C. joyneri* increased in scenario F4; and (4) the proportion of small individuals for the small shrimp groups *A. hexanema* (SP8) in F5 increased contrary to *S. schlegelii* and *C. joyneri* (Fig. 5).

3.3 *Relative changes at individual level*

Pulse fishing could change the combined effects of the two mortalities and have greater impacts on the predation pressure exerted upon juveniles than upon adults. This suggests that fishing activities could have indirect impacts on juveniles via trophic interactions. There was a decline in the predation mortality of *S. schlegelii* (SP6) juveniles in July and August in F4 (Fig. 6), accompanied by an increased population biomass (Fig. 4). By contrast, the predation pressure on juveniles increased with subsequent decreased population biomass under other pulse fishing scenarios. This indicated that the survival of juveniles was crucial to fish repopulation and fishing activities were capable of influencing fish stock status during the closed fishing season as well. Although there were small variations on their fishing mortalities due to a low level of fishing pressure, the predation mortality of both age groups of *A. hexanema* (SP8) changed, implying pulse fishing indirectly influenced individuals through trophic interactions. *Johnius belangerii* (SP11) had a similar response to the fishing scenario F4. However, the biomass of *J. belangerii* increased in scenarios F1 and F2 (Fig. 4) with multilevel declines in predation mortality on juveniles.

In scenario F5, the pressure of predators to juveniles of three fishes decreased in most months after removing the three-month seasonal closure (Fig. 6), by contrast, there were small changes of predator pressures on adults (Fig. 7). The additional fishing effort in August had a bigger impacts on young *S. schlegelii* than other two fishes (Fig. 6). Adults of *S. schlegelii* and *J. belangerii* were underwent higher fishing pressures from June to August (Fig. 7).

3.4 *Uncertainty analysis*

In the uncertainty analysis, the biomass of *S. schlegelii* (SP6) and *J. belangerii* (SP11) had the same variation trends to simulated outcomes for the five scenarios (Fig. 8): (1) both fish species reached a stable biomass in scenario F0; (2) the biomass of *S. schlegelii* declined in the subsequent three scenarios (F1, F2 and F3), and increased in the last scenario (F4); and (3) the biomass of *J. belangerii* increased in scenarios F1 and F4, and had small variations in scenarios F2 and F3.

4 Discussion

Some closures are not effective on biological conservation due to cursory design and evaluation (Ichinokawa et al., 2015).

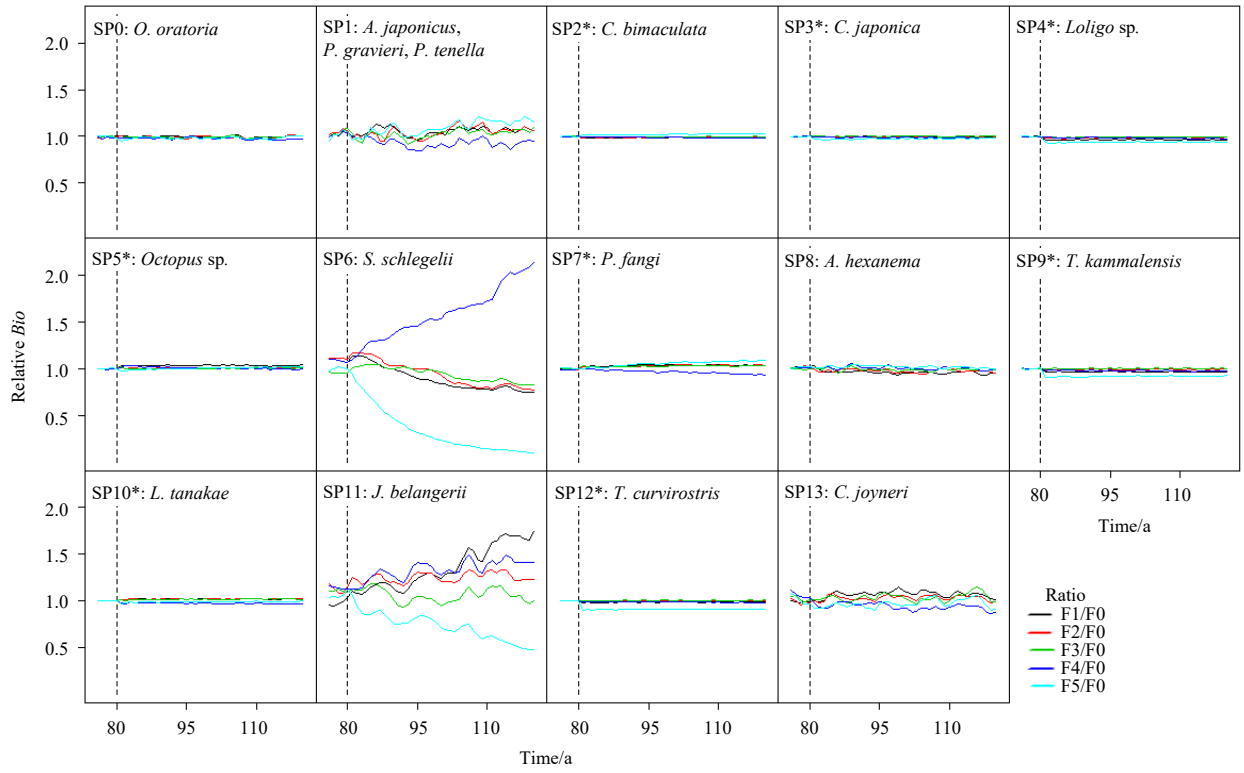

Fig. 4. Relative average annual changes in biomass of 14 HTL groups after the 75th year. The relative changes were represented by the ratios of species biomass between last five fishing scenarios (i.e., F1–F5) and reference state (i.e., F0). The predicted data are averages of 100 repeated simulations. * Migration species.

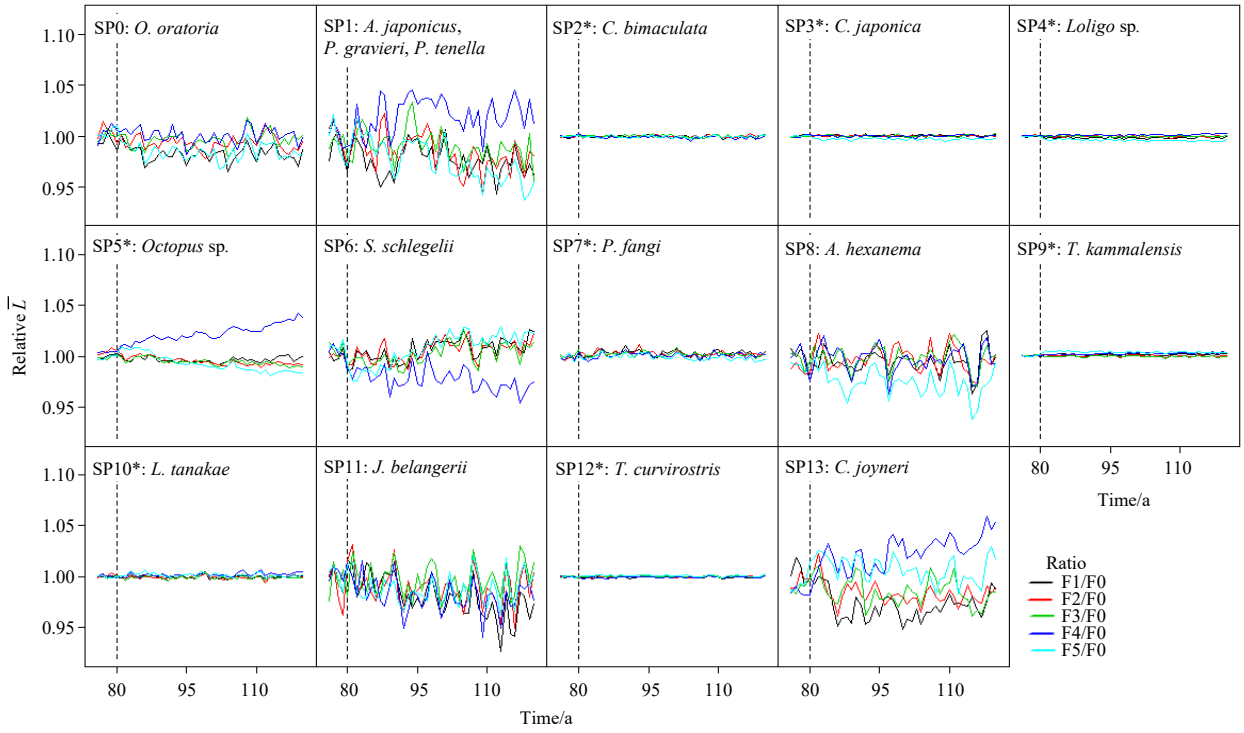

Fig. 5. Relative average annual changes in mean body length ($\bar{L}$) of 14 HTL groups after the 75th year. The relative changes were represented by the ratios of species-based mean body length between last five fishing scenarios (i.e., F1–F5) and reference state (i.e., F0). The predicted data are averages of 100 repeated simulations. * Migration species.

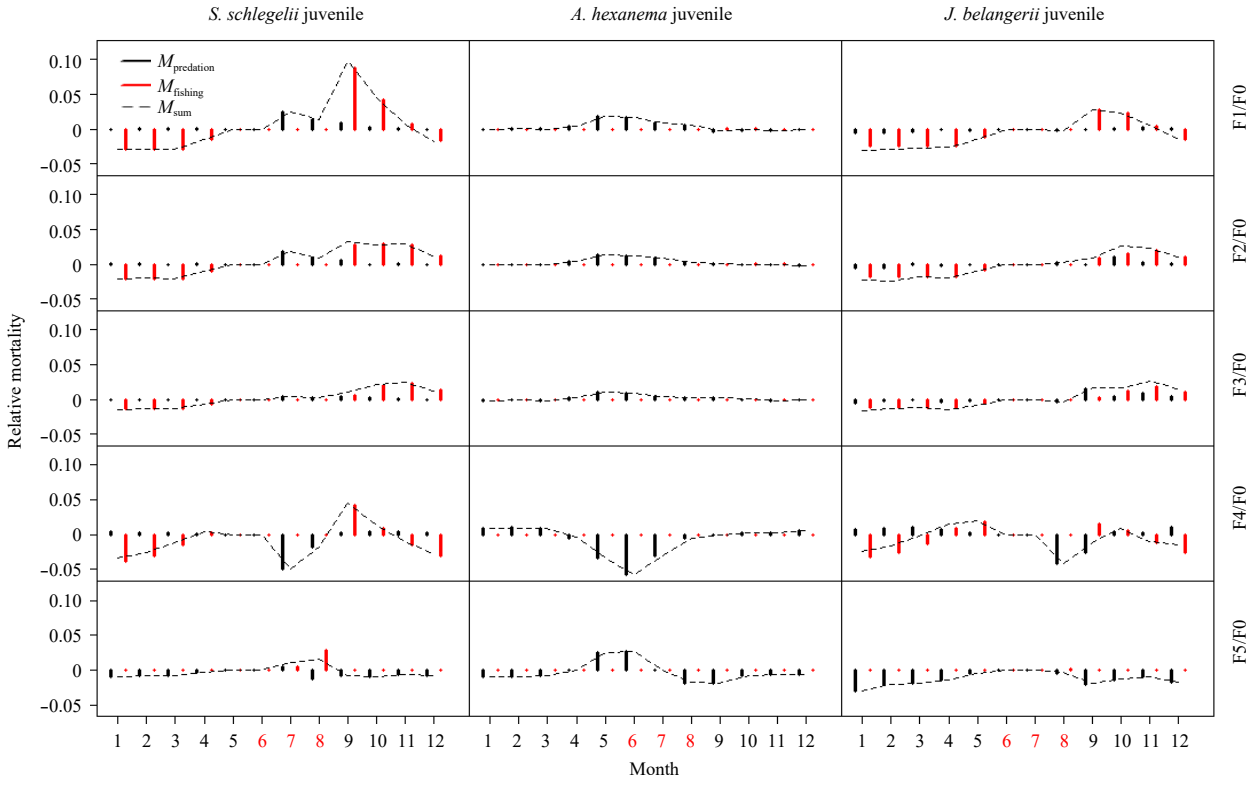

Fig. 6. Relative monthly mean changes of predation ($M_{predation}$, black bars) and fishing mortality ($M_{fishing}$, red bars) rates of young *S. schlegelii* (SP6), *A. hexanema* (SP8), and *J. belangerii* (SP11). The relative changes were the difference between predicted mortality rates in first five scenarios (i.e., F1–F5) and reference state (i.e., F0). The indicator M_{sum} (black broken line) was the sum of relative changes of $M_{predation}$ and $M_{fishing}$. The predicted data were averaged over 100 repeated simulations and over the last 40 years of the simulations. A seasonal closure implemented from June to August marked in red in scenario F0–F4, and revoked in scenario F5.

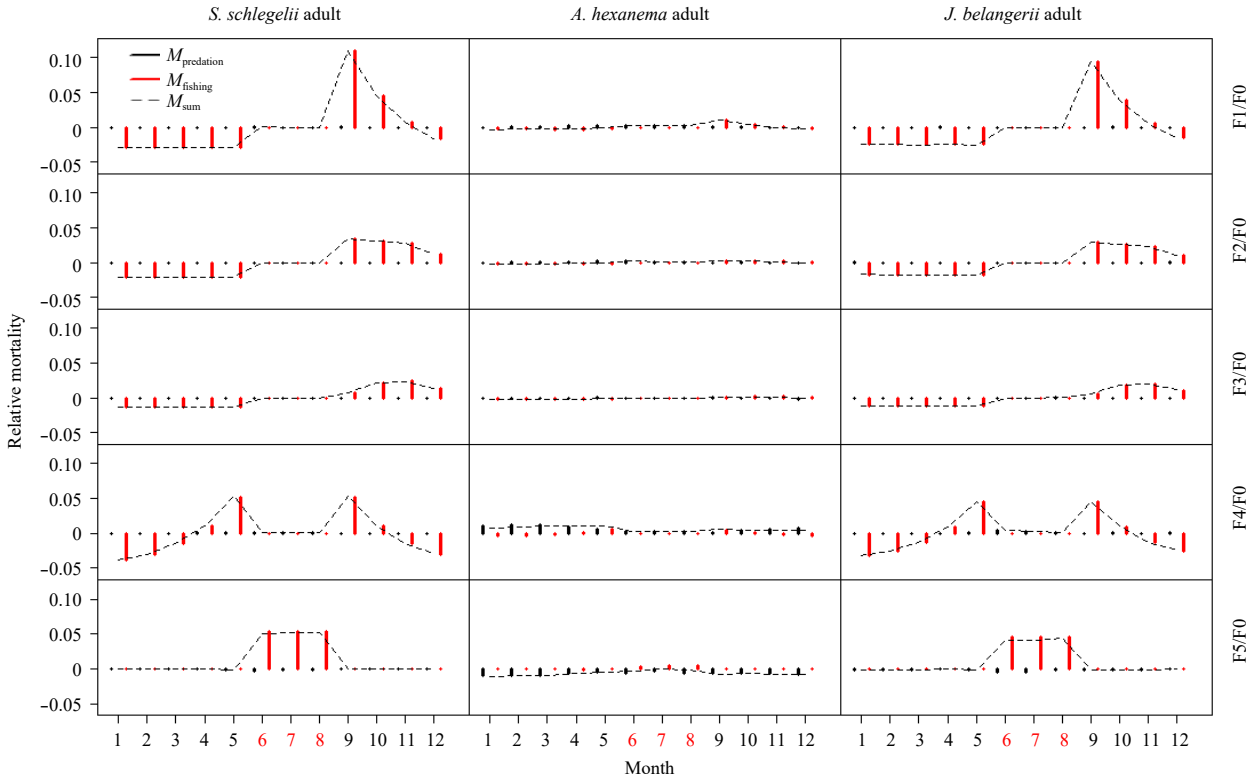

Fig. 7. Relative monthly mean changes of predation ($M_{predation}$, black bars) and fishing mortality ($M_{fishing}$, red bars) rates of adults of *S. schlegelii* (SP6), *A. hexanema* (SP8), and *J. belangerii* (SP11). The relative changes were the difference between predicted mortality rates in first five scenarios (i.e., F1–F5) and reference state (i.e., F0). The indicator M_{sum} (black broken line) was the sum of relative changes of $M_{predation}$ and $M_{fishing}$. The predicted data were averaged over 100 repeated simulations and over the last 40 years of the simulations. A seasonal closure implemented from June to August marked in red in scenario F0–F4, and revoked in scenario F5.

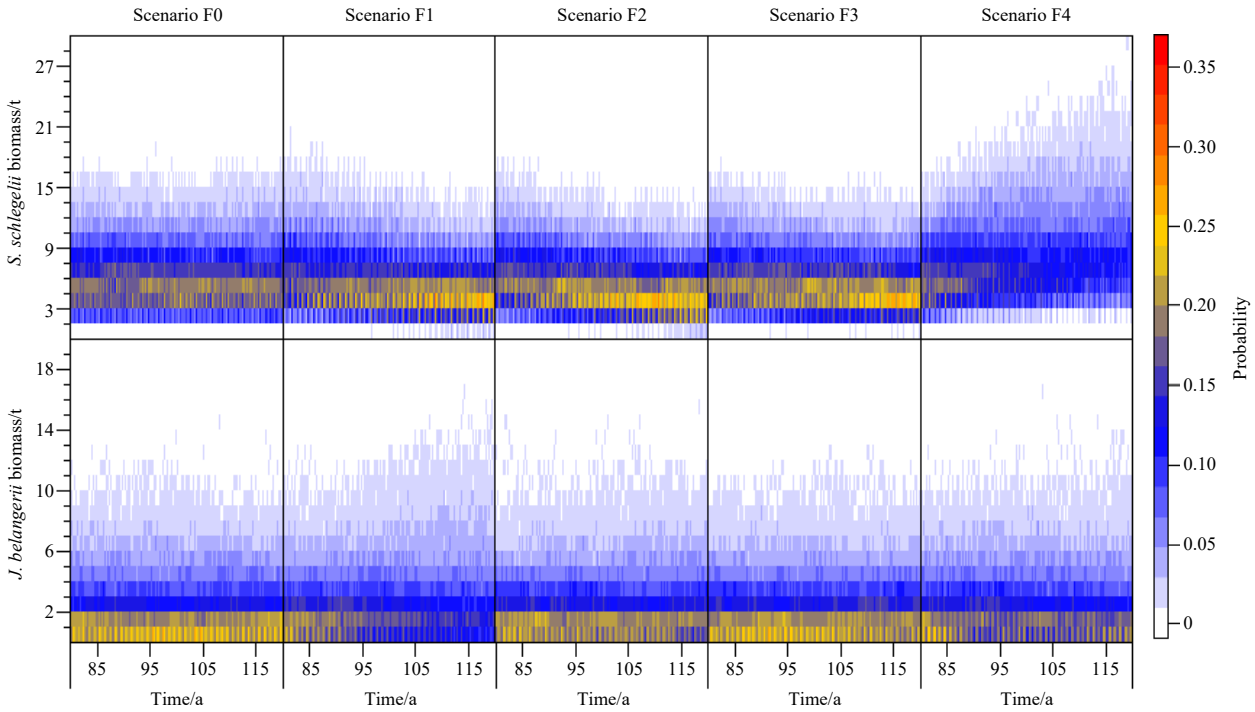

Fig. 8. Annual probability frequency distribution of *S. schlegelii* (SP6) and *J. belangerii* (SP11) population biomass under five fishing scenarios after the 80th year, with 1 200 Monte Carlo simulation runs and 10% level of uncertainty specified for fishing effort of all HTL groups at each time step.

The large predatory fish are often exposed to a high fishing pressure, and the slow growth makes them need a long time to recover from the heavy fishing pressure (Foale and Manele, 2004; Myers and Worm, 2005). They are often at a disadvantage against small pelagic forage fish when the closed fishing season is short (Williams et al., 2006; Cohen and Foale, 2013). Our results showed that two large predatory fishes with small populations (*S. schlegelii* and *J. belangerii*) got more benefit from the temporal buffer for compensatory growth of adults provided by the summer moratorium of fishing in the Jiaozhou Bay compared to others (Fig. 4). The stocks of *S. schlegelii* and *J. belangerii* declined markedly after revoking the fishing closure (Fig. 4), even though the pressure of predators to their juveniles mitigated (Fig. 6). It implied that benefits from reduced predators did not compensate the loss of adults from fishing. Similar to other study (Clark et al., 2015), our findings suggest that the protection of matured individuals is important to improving productivities of fish resources.

Comparing to other species, large catches in a short time (i.e., pulse fishing) can markedly influence the effectiveness of seasonal closure in recovering two large predatory fishes (*S. schlegelii* and *J. belangeri*). But the responses of *S. schlegelii* and *J. belangeri* to pulse fishing were different due to the species-specific growth traits. For the first three pulse fishing scenarios (i.e., F1–F3), pulse fishing occurring at the beginning of fishing season aggravated the decline in the *S. schlegelii* population. Conversely, the large loss of *J. belangerii* in September and October seemed to be compensated by the growth of stock in other periods. This was mainly attributed to the intense fishing pressure at the beginning of fishing season had a bigger negative impact on the stock recruitment of *S. schlegelii* compared to *J. belangerii* (Fig. 6). As what was reported by Xing et al. (2017), the proportion of young *S. schlegelii* which were longer than the size at first catch was higher than that of *J. belangerii* in September and October due to their specific growth traits. *S. schlegelii* juveniles were more likely to harvest when pulse fishing occurred after the seasonal closure. This likewise resulted in a decrease in matured individuals that weakened the "top-down control" feedback (Vergnon et al., 2008).

For scenario F4, more juveniles of *S. schlegelii* and *J. belangerii* survived by means of an intense fishing pressure in May lowering the pressure of predators (Fig. 6). The subsequent fishing closure provided a respite that favored their further growth. The high fishing effort imposed to spawning stock seemed not to result in the decline of fish population. Our simulations demonstrated that the performance of seasonal closure could be improved by managing pulse fishing. The small fish *A. hexanema* seemed to have the resistibility to pulse fishing. This was mainly attributed to a low fishing pressure. There were small variations on the predation and fishing mortality of adults in the four pulse fishing scenarios (F1–F4) (Fig. 7). It suggests that the species, which are imposed to a high fishing intensity, have a priority to monitor when pulse fishing occurs.

Various indicators have been developed to characterize exploited ecosystems (Shin et al., 2010, 2012; Moffitt et al., 2016), but their responsiveness and performance should be well understood before advising fisheries management (Blanchard et al., 2010). This study provided some insights on the utilization of indicators in assessing the fisheries status. When the annual fishing pressures imposed to fish stocks were unchanged, the four ecological indicators (Total biomass, mean trophic level of community, mean trophic level of catch, and Shannon-Wiener index) were not sensitive to changes caused by pulse fishing. This was mainly attributed that pulse fishing had a small impact on dominant species populations. In addition to this, sensitive fishes, such as *S. schlegelii* and *J. belangerii*, might have contrary responses to pulse fishing. This resulted in an offset that influenced the performance of ecological indicators on investigating fishing impacts. None of size-based indicators can singly reflect the response of ecosystem to fishing activities (Shin et al., 2005). Compared to species biomass, the mean body length of fish population was difficult in capturing the change after pulse fishing occurring. This suggested that species biomass had a high priority to be included in the monitoring programs. Since it is indeed impossible to survey every fish stock as money and time are limited, this ecosystem modelling approach can help us define the priority of species in monitoring programs.

Most of ecosystem models are applied in strategic management (Zhang et al., 2015; Collie et al., 2016), and decision makings provided by these models are more easily influenced by varying degrees of uncertainty as a result of complex and hierarchical model structure (Link et al., 2012; Lassalle et al., 2014). As the limitation of biological information and survey data, the parameterization of OSMOSE-JZB model is simplified and fishing mortality rates are not calibrated with catch data (Xing et al., 2017). In order to further solidify our findings, we conducted an uncertainty analysis on fishing mortality rates in four pulse fishing scenarios. Although each scenario was assigned a 10% level of uncertainty on fishing mortality rate of each species, the biomass of *S. schlegelii* and *J. belangerii* had the same variation tendency to outcomes in scenarios without adding errors. The insufficient verification may result in imprecise parameter values and influence model accuracy. It is necessary to make a sensitivity analysis of the model in the future study. The food web was simplified in our model, especially by the removal of rare species and by the aggregation of various species into functional groups. Both aspects need to be considered when interpreting the model results (Ward et al., 2012; Xing et al., 2017). Fish could change their life history strategy in response to fishing activities (Jørgensen et al., 2007; Anderson et al., 2008). We assumed that these responses had no effect on the fixed relationships in the model, such as the ranges of predator-prey size ratio, the selectivity of fishing nets, and the potential variability in species life history traits. This will certainly increase uncertainty in modelling process.

Ecosystem-based fishery management (EBFM) is advocated to avoid irreversible ecological degradation and rebuild fishery resources (Patrick and Link, 2015; Eddy et al., 2017). Admittedly, the implementation of EBFM is still impeded in many developing countries due to inadequate data for running ecosystem models (Hamel and Bryant, 2017). Our simulations indicated that the efficiency of seasonal closure could be improved by managing seasonality of fishing effort. Some of our results may not be fully applicable to other fisheries ecosystems due to the specificity of the Jiaozhou Bay ecosystem and limited data used in modelling. Our ecosystem modelling approach can be used as a heuristic tool to investigate and quantify impacts of pulse fishing on the ecosystem.

Acknowledgements

The computer simulation, data analysis, and paper writing was primarily done in the Chen Lab at the University of Maine, and supported by the China Scholarship Council, Ocean University of China, and University of Maine.

References

Aita M N, Yamanaka Y, Kishi M J. 2007. Interdecadal variation of the

lower trophic ecosystem in the northern Pacific between 1948 and 2002, in a 3-D implementation of the NEMURO model. Ecological Modelling, 202(1–2): 81–94

Anderson C N K, Hsieh C H, Sandin S A, et al. 2008. Why fishing magnifies fluctuations in fish abundance. Nature, 452(7189): 835–839, doi: 10.1038/nature06851

Blanchard J L, Coll M, Trenkel V M, et al. 2010. Trend analysis of indicators: a comparison of recent changes in the status of marine ecosystems around the world. ICES Journal of Marine Science, 67(4): 732–744, doi: 10.1093/icesjms/fsp282

Chen Bo. 2007. Discussion on improving the management of closed fishing season of summer and protecting the fisheries resources. Journal of Zhejiang Ocean University (Natural Science) (in Chinese), 26(2): 205–209

Chen Changsheng, Liu Hedong, Beardsley R C. 2003. An unstructured grid, finite-volume, three-dimensional, primitive equations ocean model: application to coastal ocean and estuaries. Journal of Atmospheric and Oceanic Technology, 20(1): 159–186, doi: 10.1175/1520-0426(2003)020<0159:AUGFVT>2.0.CO;2

Clarke J, Bailey D M, Wright P J. 2015. Evaluating the effectiveness of a seasonal spawning area closure. ICES Journal of Marine Science, 72(9): 2627–2637, doi: 10.1093/icesjms/fsv144

Cohen P J, Cinner J E, Foale S. 2013. Fishing dynamics associated with periodically harvested marine closures. Global Environmental Change, 23(6): 1702–1713, doi: 10.1016/j.gloenvcha.2013.08.010

Cohen P J, Foale S J. 2013. Sustaining small-scale fisheries with periodically harvested marine reserves. Marine Policy, 37: 278–287, doi: 10.1016/j.marpol.2012.05.010

Coll M, Navarro J, Palomera I. 2013. Ecological role, fishing impact, and management options for the recovery of a Mediterranean endemic skate by means of food web models. Biological Conservation, 157: 108–120, doi: 10.1016/j.biocon.2012.06.029

Collie J S, Botsford L W, Hastings A, et al. 2016. Ecosystem models for fisheries management: finding the sweet spot. Fish and Fisheries, 17(1): 101–125, doi: 10.1111/faf.12093

Da-Rocha J M, Nøstbakken L, Pérez M. 2014. Pulse fishing and stock uncertainty. Environmental and Resource Economics, 59(2): 257–274, doi: 10.1007/s10640-013-9727-y

Eddy T D, Lotze H K, Fulton E A, et al. 2017. Ecosystem effects of invertebrate fisheries. Fish and Fisheries, 18(1): 40–53, doi: 10.1111/faf.12165

Foale S, Manele B. 2004. Social and political barriers to the use of Marine Protected Areas for conservation and fishery management in Melanesia. Asia Pacific Viewpoint, 45(3): 373–386, doi: 10.1111/j.1467-8373.2004.00247.x

Fogarty M J. 2014. The art of ecosystem-based fishery management. Canadian Journal of Fisheries and Aquatic Sciences, 71(3): 479–490, doi: 10.1139/cjfas-2013-0203

Fu Caihong, Olsen N, Taylor N, et al. 2017. Spatial and temporal dynamics of predator-prey species interactions off western Canada. ICES Journal of Marine Science, 74(8): 2107–2119, doi: 10.1093/icesjms/fsx056

Fulton E A, Smith A D M, Punt A E. 2005. Which ecological indicators can robustly detect effects of fishing?. ICES Journal of Marine Science, 62(3): 540–551, doi: 10.1016/j.icesjms.2004.12.012

Fulton E A, Smith A D M, Smith D C, et al. 2011. Human behaviour: the key source of uncertainty in fisheries management. Fish and Fisheries, 12(1): 2–17, doi: 10.1111/j.1467-2979.2010.00371.x

Grüss A, Harford W J, Schirripa M J, et al. 2016a. Management strategy evaluation using the individual-based, multispecies modeling approach OSMOSE. Ecological Modelling, 340: 86–105, doi: 10.1016/j.ecolmodel.2016.09.011

Grüss A, Schirripa M J, Chagaris D, et al. 2016b. Estimating natural mortality rates and simulating fishing scenarios for Gulf of Mexico red grouper (*Epinephelus morio*) using the ecosystem model OSMOSE-WFS. Journal of Marine Systems, 154: 264–279, doi: 10.1016/j.jmarsys.2015.10.014

Halouani G, Lasram F B R, Shin Y J, et al. 2016. Modelling food web structure using an end-to-end approach in the coastal ecosystem of the Gulf of Gabes (Tunisia). Ecological Modelling, 339: 45–57, doi: 10.1016/j.ecolmodel.2016.08.008

Hamel P, Bryant B P. 2017. Uncertainty assessment in ecosystem services analyses: seven challenges and practical responses. Ecosystem Services, 24: 1–15, doi: 10.1016/j.ecoser.2016.12.008

Han Dongyan, Chen Yong, Zhang Chongliang, et al. 2017. Evaluating impacts of intensive shellfish aquaculture on a semi-closed marine ecosystem. Ecological Modelling, 359: 193–200, doi: 10.1016/j.ecolmodel.2017.05.024

Han Dongyan, Xue Ying, Ren Yiping, et al. 2015. Spatial and seasonal variations in the trophic spectrum of demersal fish assemblages in Jiaozhou Bay, China. Chinese Journal of Oceanology and Limnology, 33(4): 934–944, doi: 10.1007/s00343-015-4242-3

Hilborn R. 2011. Future directions in ecosystem based fisheries management: a personal perspective. Fisheries Research, 108(2–3): 235–239

Ichinokawa M, Okamura H, Watanabe C, et al. 2015. Effective time closures: quantifying the conservation benefits of input control for the Pacific chub mackerel fishery. Ecological Applications, 25(6): 1566–1584, doi: 10.1890/14-1216.1

Jiang Yazhou, Cheng Jiahua, Li Shengfa. 2009. Temporal changes in the fish community resulting from a summer fishing moratorium in the northern East China Sea. Marine Ecology Progress Series, 387: 265–273, doi: 10.3354/meps08078

Jørgensen C, Enberg K, Dunlop E S, et al. 2007. Ecology: managing evolving fish stocks. Science, 318(5854): 1247–1248, doi: 10.1126/science.1148089

Kiyama S, Yamazaki S. 2018. The impact of stock collapse on small-scale fishers' behavior: evidence from Japan. Canadian Journal of Fisheries and Aquatic Sciences, 75(12): 2241–2254, doi: 10.1139/cjfas-2017-0091

Lassalle G, Bourdaud P, Saint-Béat B, et al. 2014. A toolbox to evaluate data reliability for whole-ecosystem models: application on the Bay of Biscay continental shelf food-web model. Ecological Modelling, 285: 13–21, doi: 10.1016/j.ecolmodel.2014.04.002

Link J S, Ihde T F, Harvey C J, et al. 2012. Dealing with uncertainty in ecosystem models: the paradox of use for living marine resource management. Progress in Oceanography, 102: 102–114, doi: 10.1016/j.pocean.2012.03.008

Moffitt E A, Punt A E, Holsman K, et al. 2016. Moving towards ecosystem-based fisheries management: options for parameterizing multi-species biological reference points. Deep Sea Research Part II: Topical Studies in Oceanography, 134: 350–359, doi: 10.1016/j.dsr2.2015.08.002

Murawski S A, Wigley S E, Fogarty M J, et al. 2005. Effort distribution and catch patterns adjacent to temperate MPAs. ICES Journal of Marine Science, 62(6): 1150–1167, doi: 10.1016/j.icesjms.2005.04.005

Myers R A, Worm B. 2005. Extinction, survival or recovery of large predatory fishes. Philosophical Transactions of the Royal Society of London B: Biological Sciences, 360(1453): 13–20, doi: 10.1098/rstb.2004.1573

Patrick W S, Link J S. 2015. Myths that continue to impede progress in ecosystem-based fisheries management. Fisheries, 40(4): 155–160, doi: 10.1080/03632415.2015.1024308

Purcell S W, Mercier A, Conand C, et al. 2013. Sea cucumber fisheries: global analysis of stocks, management measures and drivers of overfishing. Fish and Fisheries, 14(1): 34–59, doi: 10.1111/j.1467-2979.2011.00443.x

Samy-Kamal M, Forcada A, Lizaso J L S. 2015. Effects of seasonal closures in a multi-specific fishery. Fisheries Research, 172: 303–317, doi: 10.1016/j.fishres.2015.07.027

Shannon L J, Coll M, Neira S. 2009. Exploring the dynamics of ecological indicators using food web models fitted to time series of abundance and catch data. Ecological Indicators, 9(6): 1078–1095, doi: 10.1016/j.ecolind.2008.12.007

Shen Gongming, Heino M. 2014. An overview of marine fisheries management in China. Marine Policy, 44: 265–272, doi: 10.1016/j.marpol.2013.09.012

Shin Y J, Bundy A, Shannon L J, et al. 2012. Global in scope and regionally rich: an IndiSeas workshop helps shape the future of marine ecosystem indicators. Reviews in Fish Biology and Fisheries, 22(3): 835–845, doi: 10.1007/s11160-012-9252-z

Shin Y J, Cury P. 2001. Exploring fish community dynamics through size-dependent trophic interactions using a spatialized individual-based model. Aquatic Living Resources, 14(2): 65–80, doi: 10.1016/S0990-7440(01)01106-8

Shin Y J, Cury P. 2004. Using an individual-based model of fish assemblages to study the response of size spectra to changes in fishing. Canadian Journal of Fisheries and Aquatic Sciences, 61(3): 414–431, doi: 10.1139/f03-154

Shin Y J, Rochet M J, Jennings S, et al. 2005. Using size-based indicators to evaluate the ecosystem effects of fishing. ICES Journal of Marine Science, 62(3): 384–396, doi: 10.1016/j.icesjms.2005.01.004

Shin Y J, Shannon L J, Bundy A, et al. 2010. Using indicators for evaluating, comparing, and communicating the ecological status of exploited marine ecosystems. 2. Setting the scene. ICES Journal of Marine Science, 67(4): 692–716, doi: 10.1093/icesjms/fsp294

Travers M, Shin Y J, Jennings S, et al. 2009. Two-way coupling versus one-way forcing of plankton and fish models to predict ecosystem changes in the Benguela. Ecological Modelling, 220(21): 3089–3099, doi: 10.1016/j.ecolmodel.2009.08.016

Travers M, Shin Y J, Shannon L, et al. 2006. Simulating and testing the sensitivity of ecosystem-based indicators to fishing in the southern Benguela ecosystem. Canadian Journal of Fisheries and Aquatic Sciences, 63(4): 943–956, doi: 10.1139/f06-003

van Putten I E, Kulmala S, Thébaud O, et al. 2012. Theories and behavioural drivers underlying fleet dynamics models. Fish and Fisheries, 13(2): 216–235, doi: 10.1111/j.1467-2979.2011.00430.x

Vergnon R, Shin Y J, Cury P. 2008. Cultivation, Allee effect and resilience of large demersal fish populations. Aquatic Living Resources, 21(3): 287–295, doi: 10.1051/alr:2008042

Wang Zhongyuan. 2008. The primary researching about Effectiveness of fishing ban in summer in our country (in Chinese) [dissertation]. Qingdao: Ocean University of China

Wang Ying, Duan Lijie, Li Shiyu, et al. 2015. Modeling the effect of the seasonal fishing moratorium on the Pearl River Estuary using ecosystem simulation. Ecological Modelling, 312: 406–416, doi: 10.1016/j.ecolmodel.2015.06.011

Ward B A, Dutkiewicz S, Jahn O, et al. 2012. A size-structured food-web model for the global ocean. Limnology and Oceanography, 57(6): 1877–1891, doi: 10.4319/lo.2012.57.6.1877

Weeratunge N, Béné C, Siriwardane R, et al. 2014. Small-scale fisheries through the wellbeing lens. Fish and Fisheries, 15(2): 255–279, doi: 10.1111/faf.12016

Williams I D, Walsh W J, Miyasaka A, et al. 2006. Effects of rotational closure on coral reef fishes in Waikiki-Diamond Head Fishery Management Area, Oahu, Hawaii. Marine Ecology Progress Series, 310: 139–149, doi: 10.3354/meps310139

Xing Lei, Zhang Chongliang, Chen Yong, et al. 2017. An individual-based model for simulating the ecosystem dynamics of Jiaozhou Bay, China. Ecological Modelling, 360: 120–131, doi: 10.1016/j.ecolmodel.2017.06.010

Zhang Chongliang, Chen Yong, Ren Yiping. 2015. Assessing uncertainty of a multispecies size-spectrum model resulting from process and observation errors. ICES Journal of Marine Science, 72(8): 2223–2233, doi: 10.1093/icesjms/fsv086

Zhu Yugui. 2009. Research on the effects of China's summer fishing moratorium—a perspective of institutional analysis (in Chinese) [dissertation]. Qingdao: Ocean University of China

Acta Oceanol. Sin., 2020, Vol. 39, No. 4, P. 100–109
https://doi.org/10.1007/s13131-019-1468-y
http://www.hyxb.org.cn
E-mail: hyxbe@263.net

Ecological footprint and vulnerability of marine capture fisheries in China

Qi Ding[1, 2], Xiujuan Shan[1, 2], Xianshi Jin[1, 2*]

[1] Key Laboratory of Sustainable Development of Marine Fisheries, Ministry of Agriculture and Rural Affairs/Shandong Provincial Key Laboratory of Fishery Resources and Ecological Environment, Yellow Sea Fisheries Research Institute, Chinese Academy of Fishery Sciences, Qingdao 266071, China

[2] Function Laboratory for Marine Fisheries Science and Food Production Processes, Pilot National Laboratory for Marine Science and Technology (Qingdao), Qingdao 266237, China

Received 12 January 2019; accepted 27 May 2019

Abstract

China (herein referred as China's mainland, and excluding Hong Kong, Macau and Taiwan) ranks as the world's leading fishing nation, with approximately 11.1 million tons of domestic marine catch acquired in 2017. Marine fisheries resources in China are mainly exploited by its 11 coastal provinces and municipalities, and the development of fishing industry varies among them. However, few studies have examined the exploitation history of the 11 coastal provinces and municipalities. In this paper, we systematically quantified the exploitation history of marine fishery resources in China and then measured the vulnerability of the 11 coastal provinces and municipalities of China to a reduction in marine catches. Our analysis suggested that Chinese marine fisheries experienced rapid growth from the mid-1980s to the end of the 20th century, and this rapid increase in marine catches were mainly promoted by increased fishing effort. The total primary production required level amounted to approximately 80% of the average primary productivity in 2017, and Zhejiang, Fujian, Shandong, Hainan and Guangdong provinces were the main fishing provinces in China. By assessing three dimensions of vulnerability (exposure, sensitivity and adaptive capacity) to the impacts of a reduction in marine catches in the 11 coastal provinces and municipalities, we found that Hainan, Guangxi, Zhejiang and Fujian provinces had high or very high vulnerability, while the municipalities of Shanghai and Tianjin had low vulnerability. Identifying suitable adaptation policies and management plans based on the differences in vulnerability among coastal provinces is important in sustainable fisheries management.

Key words: marine capture fisheries, coastal provinces and municipalities, exploitation history, vulnerability

Citation: Ding Qi, Shan Xiujuan, Jin Xianshi. 2020. Ecological footprint and vulnerability of marine capture fisheries in China. Acta Oceanologica Sinica, 39(4): 100–109, doi: 10.1007/s13131-019-1468-y

1 Introduction

Fishing is likely to have the greatest anthropogenic impact on marine ecosystems (Worm et al., 2009; Watson et al., 2013, 2014). Marine capture fisheries in China (herein referred as China's mainland, and excluding Hong Kong, Macau and Taiwan) have undergone considerable development in the past few decades, the domestic marine catch totaled only 0.6 million tons in 1950 but increased dramatically to 11.1 million tons in 2017. China is now the world's largest country in terms of marine catches, accounting for approximately one-fifth of the global catch (FAO, 2016). Not surprisingly, the rapid development of China's marine fisheries has placed tremendous pressure on the country's marine ecosystems (Liu, 2013; Shen and Heino, 2014). Studying and understanding the impacts of fishery-induced changes in marine ecosystems is important for developing effective policies and management strategies (Bell et al., 2017). Marine fishery resources in China are mainly exploited by the country's 11 coastal provinces and municipalities, and the developmental history of the fishing industry varies among them. Growing efforts have been made to document the sustainability of China's marine fisheries and discuss the need for new directions in fisheries management (Yu and Yu, 2008; Pauly et al., 2014; Cao et al., 2017). However, there is a lack of quantitative information regarding the exploitation histories of these 11 coastal provinces and municipalities.

Fishing impacts on marine ecosystems, which include species across the food chain, from herbivores to top predators, cannot be fully assessed with the study of single-species catches (Swartz et al., 2010; Watson et al., 2014). The primary production required (PPR) to sustain marine catches is a measure of the primary production (PP) needed to replace the biomass of fisheries landings removed from marine ecosystems (Pauly and Christensen, 1995). The PPR can be expressed per unit of PP of the marine ecosystem, measured as the relative PPR (PPR/PP, %PPR) (Pauly and Christensen, 1995). As a commonly used metric of the ecological footprint of fishing, the %PPR allows the comparison of catches with very different species compositions from different ecosystems, and it has been increasingly used in

Foundation item: The National Key R&D Program of China under contract No. 2017YFE0104400; the National Basic Research Program of China under contract No. 2015CB453303; the Special Funds for Taishan Scholars Project of Shandong Province; the AoShan Talents Cultivation Program supported by Qingdao National Laboratory for Marine Science and Technology under contract No. 2017ASTCP-ES07; the Central Public-interest Scientific Institution Basal Research Fund, CAFS under contract No. 2018GH20.
*Corresponding author, E-mail: jin@ysfri.ac.cn

the quantification of fishing pressure on marine ecosystems and the examination of historical fishing behavior of global fishing fleets (Pauly and Christensen, 1995; Swartz et al., 2010; Coll et al., 2013; Ding et al., 2017a). However, how much PP has been captured by Chinese fishing fleets over time and how the various fleets from each fishing province contribute to these changes remain unknown.

China's marine capture fisheries are currently underperforming, largely due to overfishing. The proportion of stocks assessed as overfished increased from 0% in 1950 to 52.4% in 2014 (Pauly and Zeller, 2015). To reduce the fishing pressure applied to fish stocks and achieve sustainable fishery development, the Ministry of Agriculture and Rural Affairs of the People's Republic of China (MARA) announced plans in 2017 to reduce the total marine catch to 10 million tons by 2020 (from 13 million tons in 2015). This change would require at least a 23.6% reduction in marine catches for each coastal province and municipality by the year 2020 compared to the year 2015. Marine fisheries are important as a source of food and employment in China, and understanding where a decline in marine catches may have the greatest socioeconomic impacts is therefore a necessary and important first step in informing management strategies and increasing the resilience of the coastal provinces (Cao et al., 2017).

Vulnerability is generally considered to be the degree to which a system is susceptible to and unable to cope with the adverse effects of a chronic or stochastic disturbance (Cutter, 1996; Adger, 2006), and vulnerability assessments are increasingly being used in various sectors and fields of society to develop appropriate adaptation policies and management plans for different economic sectors (Johnson and Welch, 2009; Huang et al., 2012; Ding et al., 2017b). Since Allison et al. (2009) first evaluated fisheries vulnerability to climate change, many authors have examined fisheries vulnerability in the face of various drivers (Cinner et al., 2012; 2013; Pelletier et al., 2014). The components of vulnerability—exposure, sensitivity and adaptive capacity—are expected to vary among different coastal provinces, and assessing the relative vulnerability of coastal provinces to a reduction in marine catches is an important step toward enhancing the understanding of this vulnerability and informing decision making to reduce it.

Marine capture fisheries in China have undergone rapid development over the past several decades, but how fishing fleets from various coastal provinces contribute to these changes remains an under-considered issue. The present paper examines the changes that have occurred since detailed catch statistics begin to be published annually in the mid-1980s. In this paper, we systematically evaluate the exploitation history of marine capture fisheries in China, focusing on the historical exploitation behavior of fishing fleets from the 11 coastal provinces and municipalities. Using the framework of vulnerability, we then present the most detailed comparative study to date on the vulnerability of these coastal provinces to the impacts of a reduction in marine catches. This study can assist policy makers and fisheries scientists to understand the exploitation dynamics of fishing fleets in the coastal provinces of China and provide guidance for the formulation of effective policies to reduce specific aspects of vulnerability.

2 Materials and methods

2.1 *Overview of China's fishing industry*

This study focused on domestic marine capture fisheries (excluding aquaculture, inland fisheries, and distant-water fisheries), and these fisheries data were all from China's mainland (Hong Kong, Macau and Taiwan were excluded). We used a time-series analysis of annual catch, fishing effort, and %PPR to quantify the general exploitation history of marine capture fisheries in China. Detailed catch statistics for the coastal provinces began to be published annually in the mid-1980s; thus, the time-series data for the %PPR and fishing effort started from the year 1985. The %PPR was used to quantify the fishing pressure on marine ecosystems, with a higher %PPR related to a higher level of exploitation and fishing pressure (Pauly and Christensen, 1995; Swartz et al., 2010; Watson et al., 2014). Following Pauly and Christensen (1995), the PPR can be calculated as follows:

$$\mathrm{PPR} = \sum_i \left[\frac{Y_i}{CR} \times \left(\frac{1}{TE} \right)^{TL_i - 1} \right],$$

where Y_i is the catch of species i, CR is the conversion rate of wet weight of catches to carbon, TE is the trophic transfer efficiency, and TL_i is the trophic level of species i.

Data on annual marine catch and fishing effort were obtained from the China Fisheries Statistical Yearbook (Fisheries Bureau of the Ministry of Agriculture, 1950–2018), and catch data were all corrected based on the Food and Agriculture Organization of the United Nation's (FAO) global fisheries landings statistics (www.fao.org/fishery/statistics/en). Species-specific trophic levels were obtained from FishBase (www.fishbase.org). Primary production data in the exclusive economic zone (EEZ) of China were acquired from the Sea Around Us project database (www.seaaroundus.org). Based on the United Nations Convention on the Law of the Sea, Law of the People's Republic of China on the Exclusive Economic Zone and the Continental Shelf, the total sea area under the jurisdiction of China is approximately 3 million square kilometers. Here, we applied a 9:1 ratio for CR and 10% for TE (Pauly and Christensen, 1995; Watson et al., 2014).

2.2 *Vulnerability assessment*

The MARA developed a Five-Year Plan for marine fisheries in 2017, which included at least a 23.6% reduction in marine catches for each coastal province by 2020. Using the methods of Allison et al. (2009), which were originally developed to evaluate fisheries vulnerability to climate change, we classified the vulnerability of coastal provinces to a decrease in marine catches. We used data from various sources to quantify vulnerability as a function of the following three components: a coastal province's exposure to a decrease in marine catches, its sensitivity to this change, and its adaptive capacity or potential to respond to this change (Adger, 2006) (Table 1). This paper aimed to evaluate provincial vulnerability to a reduction in marine catches to understand the causes of such vulnerability.

2.2.1 *Exposure*

The proportion of marine fisheries in total fishery production (including aquaculture, inland fisheries, and distant-water fisheries) varies significantly among the coastal provinces (Table 2); thus, different provinces may suffer from varying degrees of social-economic disturbances in the face of the same reduction in marine catches. In this paper, exposure was estimated using marine catches as a percentage of the total fishery production. All fishery production databases were obtained from the China Fishery Statistical Yearbook. For each indicator, average values for the period 2015–2017 or the most recent data available (indicator of flexibility) were used to counter interannual variability. This study assumed that a higher contribution of marine fisheries to total fishery production implied greater exposure to the reduction in marine catches.

Table 1. Summary of the variables and data sources used to calculate the exposure, sensitivity and adaptive capacity of coastal provinces to fishery vulnerability associated with a reduction in marine catches

Component	Interpretation	Variable	Data sources
Exposure	reliance on marine capture fisheries (2015–2017)	marine catches as a percentage of total fishery production	China Fishery Statistical Yearbook 2016–2018
Sensitivity	food security dependency (2015–2017)	$\frac{\text{fish protein intake/total animal protein intake}}{\text{total animal protein intake/required animal protein intake}}$	China Statistical Yearbook 2016–2018
	employment dependency (2015–2017)	marine capture fisheries employment as a percentage of the total employment	China Fishery Statistical Yearbook 2016–2018 and Statistical Yearbook of Related Provinces 2016–2018
	economic dependency (2015–2017)	economic value of marine capture fisheries as a percentage of the GDP	China Fishery Statistical Yearbook 2016–2018 and China Statistical Yearbook 2016–2018
Adaptive capacity	assets (2015–2017)	GDP per capita	China Statistical Yearbook 2016–2018
	flexibility (2010)	life expectancy at birth	China Population and Employment Statistics Yearbook 2017
	learning (2015–2017)	average years of education	China Statistical Yearbook 2016–2018
	social organization (2015–2017)	input intensity of R&D	China Statistical Yearbook on Science and Technology 2016–2018

Table 2. The percentage of fishery production of different fishery sectors in total fishery production for the 11 coastal provinces and municipalities of China, averaged over 2015–2017

Fishing provinces and municipalities	Marine capture fishery/%	Distant water fishery/%	Freshwater capture fishery /%	Aquaculture/%
Tianjin	10.5	4.1	2.2	83.2
Hebei	20.0	2.8	5.7	71.5
Liaoning	14.6	5.7	1.0	78.7
Shanghai	5.7	47.3	0.7	46.3
Jiangsu	10.6	0.5	6.1	82.8
Zhejiang	55.0	8.2	1.6	35.2
Fujian	25.7	4.7	1.0	68.6
Shandong	22.0	5.3	1.0	71.7
Guangdong	17.6	0.6	1.4	80.4
Guangxi	19.6	0.2	3.5	76.7
Hainan	65.1	0	0.9	34.0

Note: Data source: China Fishery Statistical Yearbook.

2.2.2 *Sensitivity*

Sensitivity was defined as the degree to which a coastal province was dependent on marine fisheries for its economy and food security, and it was calculated using three indices: employment dependency, economic dependency, and food security dependency (Barange et al., 2014). Employment dependency was represented using marine capture fisheries employment as a percentage of total employment. Economic dependency was estimated using the economic value of marine capture fisheries as a percentage of GDP. Food security dependency was calculated by adopting a previously developed methodology (Table 1). Data on fish protein intake, total animal protein intake, and GDP were sourced from the China Statistical Yearbook. Marine capture fisheries employment and its fishery economic value were derived from the China Fishery Statistical Yearbook. Total employment data for each province were obtained from the statistical yearbook of corresponding provinces. In accordance with earlier studies, we used a minimum requirement of 36 g animal protein per capita day for an average adult (Akpan et al., 2013). Sensitivity was determined by taking the average of the three indices, and we assumed that higher dependency on marine capture fisheries reflected greater sensitivity.

2.2.3 *Adaptive capacity*

Adaptive capacity was defined as the ability of coastal provinces to handle changes in marine catches. Based on an earlier work in which adaptive capacity was disaggregated into four categories—assets, flexibility, learning, and social organization (Cinner et al., 2009), this study calculated adaptive capacity using four key indicators in the above categories: GDP per capita, life expectancy at birth, average years of education, and input intensity of research and development (R&D). Data on GDP per capita and average years of education were obtained from the China Statistical Yearbook, while the data on the life expectancy at birth and input intensity of R&D were provided by the China Population and Employment Statistics Yearbook and China Statistical Yearbook on Science and Technology, respectively. Adaptive capacity was calculated as an average of the above four indicators, with higher values reflecting greater adaptive capacity.

2.3 *Analysis*

Vulnerability, as a broad concept, has the characteristics of uncertainty and relativity. Therefore, the criteria used to evaluate vulnerability are also uncertain and can be selected according to the actual situation (Monnereau et al., 2015). In this paper, the method of set pair analysis (SPA) was used to estimate the vul-

nerability of coastal provinces to a reduction in marine catches (Zhao, 2000).

The core concept behind SPA is to analyze the certainty and uncertainty factors in a set pair. Set E and set U have certain connections between each other, and these two sets are regarded as set pair H. We obtain N features by analyzing set pair H in the context of specific condition Q. Of the N features, the number of common features in sets E and U is represented by S and the number of different features in sets E and U is represented by P. The number of remaining uncertainty features is represented by F (F=N–S–P). Thus, the connection degree (u) of the two sets is

$$u = \frac{S}{N} + \frac{F}{N}i + \frac{P}{N}j = a + bi + cj,$$

where a, b and c are the identical degree, difference degree, and opposite degree, respectively. i is the tag of difference degree, and j is the coefficient of opposite degree. The value of i is between –1 and 1, and j is set at –1. a, b and c describe the connections between the above two sets from different aspects. We analyzed the connection degree of set pairs based on the size relationship of a, b and c.

We assessed the exposure, sensitivity, and adaptive capacity of coastal provinces to a reduction in marine catches based on SPA. Variables were standardized to a 0–1 scale using the following conversion: $(X–X_{\min})/(X_{\max}–X_{\min})$. The indicators were regarded as set E, and the corresponding evaluation criteria were treated as set U. The exposure, sensitivity and adaptive capacity indices were calculated as averages of the standardized variables. We identified the exposure, sensitivity, and adaptive capacity as

$$Q = \{E, G, W, D\},$$

where E is the set of evaluation objects (E=$\{e_1, e_2, \ldots, e_m\}$, and m is the number of coastal provinces assessed); G is the set of indicators (G=$\{g_1, g_2, \ldots, g_n\}$, and n is the number of indicators); and W is the set of indicator weights (W=$\{w_1, w_2, \ldots, w_n\}$). Evaluation matrix D for question Q is as follows, where d_{kp} is the indicator value for an assessed coastal province (k=1, 2, …, m; p=1, 2, …, n):

$$D = \begin{bmatrix} d_{11} & d_{12} & \cdots & d_{1n} \\ d_{21} & d_{22} & \cdots & d_{2n} \\ \vdots & \vdots & \vdots & \vdots \\ d_{m1} & d_{m1} & \cdots & d_{mn} \end{bmatrix}.$$

By comparing the indicators among different evaluation objects, we can obtain the maximum indicator set U=$\{u_1, u_2, \ldots, u_n\}$ and the minimum indicator set V=$\{v_1, v_2, \ldots, v_n\}$. Identical degree a_{kp} and opposite degree c_{kp} for d_{kp} in evaluation matrix D are calculated as follows:

when there is a positive effect on the results:

$$\begin{cases} a_{kp} = \dfrac{d_{kp}}{u_p + v_p}, \\ c_{kp} = \dfrac{u_p v_p}{d_{kp}\left(u_p + v_p\right)}, \end{cases}$$

when there is a negative effect on the results:

$$\begin{cases} a_{kp} = \dfrac{u_p v_p}{d_{kp}\left(u_p + v_p\right)}, \\ c_{kp} = \dfrac{d_{kp}}{u_p + v_p}, \end{cases}$$

the connection degree (u) of set pair $\{E_k, U\}$ in the interval $[V, U]$ is

$$\begin{cases} u_{(E_k,U)} = a_k + b_k i + c_k j, \\ a_k = \sum w_p a_{kp}, \\ c_k = \sum w_p c_{kp}, \end{cases}$$

the close degree (r_k) between E_k and the maximum case is defined as

$$r_k = \frac{a_k}{a_k + c_k},$$

where r_k reflects the correlation between case E_k and the maximum case, and a higher value of r_k indicates that case E_k is closer to the maximum value. Accordingly, the exposure (r_e), sensitivity (r_s), and adaptive capacity (r_a) of coastal provinces in China can be calculated, with greater values of r_e, r_s, and r_a indicating higher levels of exposure, sensitivity, and adaptive capacity, respectively.

Using exposure, sensitivity and adaptive capacity as the basic indices, vulnerability (r_v) was calculated as the unweighted mean of the standardized values of these indices. Greater values of r_v indicate higher vulnerability among the coastal provinces. Therefore, the values of r_v were highest for the most vulnerable provinces and lowest for the least vulnerable provinces. For the purpose of presentation, the final indicator scores for exposure, sensitivity, adaptive capacity, and vulnerability were categorized into "low (0, AVG-STD)", "moderate (AVG-STD, AVG)", "high (AVG, AVG+STD)", and "very high (AVG+STD, 1)" groups based on the mean and standard deviation of the corresponding index (Wu and Yang, 2012).

3 Results

3.1 *Exploitation history of marine fisheries in China*

To examine the exploitation history of marine fisheries in China, we analyzed the changes in total marine catch in China since the early 1950s. The results showed that China's marine capture fisheries underwent an accelerated development beginning in the mid-1980s (Fig. 1). The annual marine catch, which was only 0.6 million tons in 1950, slowly increased to approximately 4 million tons in 1985. In 1985, the Chinese government introduced the No. 5 Central Document, a policy directive that aimed to accelerate marine fisheries development within Chinese waters, which resulted in a considerable increase in marine catch, reaching a peak of 12.0 million tons in 1999. In 1999, MARA proposed the "Zero Growth" policy, which led to a decline in marine catch beginning in 2000 and reached about 11.1 million tons in 2004. Marine catch were relatively stable since then (Fig. 1).

Detailed marine catch statistics began to be published annually in the mid-1980s, and this study analyzed the temporal patterns of fishing effort and %PPR during 1985–2017 in China. The results showed that the substantial increase in marine catches was mainly promoted by increasing fishing effort (Fig. 2). The total fishing effort grew substantially from 3.4 million kilowatts in 1985 to 10.8 million kilowatts in 1999. Subsequently, it increased with fluctuations and reached a peak of 12.3 million kilowatts in 2011, but slightly decreased in recent years with 11.2 million kilowatts in 2017. Figure 3 also clearly illustrates the rapid develop-

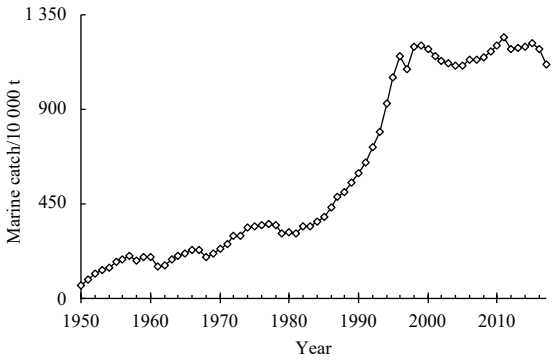

Fig. 1. Domestic marine catch in China during 1950–2017.

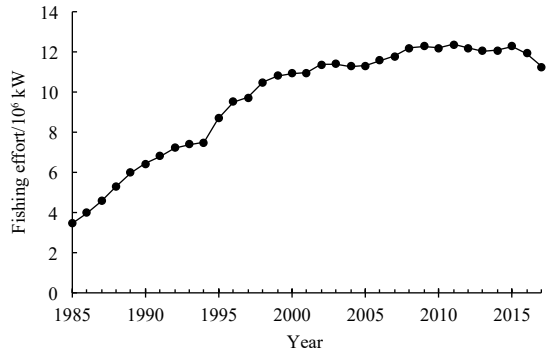

Fig. 2. Total fishing effort in China during 1985–2017.

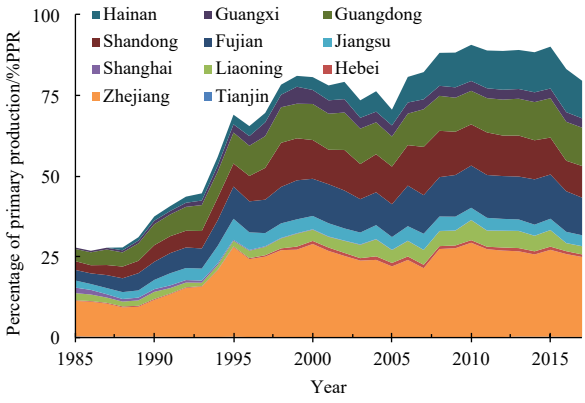

Fig. 3. Primary production required to sustain marine catches during 1985–2017 (expressed as a percentage of primary production, %PPR).

ment of marine capture fisheries since the 1980s. Specifically, the %PPR increased from 28% in 1985 to 80% in 2017. The most prominent feature of the %PPR was the period of rapid growth from the late 1980s to the end of the 20th century. Total %PPR increased throughout the time series and more than tripled from the 1980s to the 2010s but with great variability among coastal provinces (Fig. 3). Most of the growth in %PPR was driven by fleets from Zhejiang, Fujian, Shandong, Hainan, and Guangdong provinces.

To systematically quantify the historical fishing behavior of fishing fleets from different coastal provinces, we created maps of %PPR by coastal province and decade (Fig. 4). Most coastal provinces underwent the largest increase in %PPR during the 1990s. After the gradual increase in %PPR starting in the 1980s, the %PPR in Jiangsu and Guangxi provinces slightly declined and then stabilized since the end of 20th century. Furthermore, the %PPR in Liaoning, Hebei, Shandong, Zhejiang, Fujian and Guangdong provinces continued to increase and became relatively stable throughout the 2010s whereas the %PPR in Hainan Province continued to show increasing trends. In contrast, the %PPR in the municipalities of Shanghai and Tianjin had been declining since the 1980s, but Tianjin showed a sharp increase in %PPR over the last five years.

Fishing effort in China mainly came from Zhejiang, Guangdong, Fujian, Hainan and Shandong provinces. Specifically, fishing effort in the above five provinces accounted for 78% of the total in 2017. Of the 11 coastal provinces and municipalities in China, fishing effort in Shanghai showed a declining trend since the 1990s, while that in Tianjin did not show a clear trend over the past several decades. However, fishing effort in the other coastal provinces generally increased initially and then stabilized in recent years (Fig. 5).

3.2 *Vulnerability of coastal provinces to a reduction in marine catches*

In light of the considerable variability in the proportion of marine fisheries in total fishery production and the socioeconomic status of coastal provinces, this study provided an indicator-based analysis of the relative vulnerabilities of all 11 coastal provinces and municipalities to the impacts of a reduction in marine catches. The vulnerability scores varied from a low of 0.11 in the municipality of Shanghai to a high of 0.90 in Hainan Province. We categorized the final exposure, sensitivity, adaptive capacity, and vulnerability scores into “low”, “moderate”, “high” and “very high” levels based on the mean and standard deviation of the corresponding indices (Fig. 6).

Both Hainan and Guangxi provinces exhibited very high vulnerability. Hainan Province had the highest vulnerability score due to a combination of very high exposure to a reduction in marine catches, very high sensitivity and low adaptive capacity. Marine capture fisheries contributed 62% of the total production in 2017 in this province, and it showed the highest economic and nutritional dependence on fish but fewer available resources to invest in adaptation. Additionally, the low adaptive capacity score together with the high level of exposure and moderate level of sensitivity in Guangxi Province also resulted in very high vulnerability.

Both Zhejiang Province and Fujian Province had similarly high vulnerability scores, but the drivers of their high levels of vulnerability were different. Zhejiang Province had a very high exposure level; specifically, marine catches accounted for 52% of the total fishery production in this province in 2017. However, it had high levels of sensitivity and adaptive capacity. In contrast, Fujian Province was identified as having high vulnerability due to a combination of high exposure and very high sensitivity but moderate adaptive capacity.

Other coastal provinces had below-average vulnerability scores, of which, Liaoning, Hebei, Shandong, Jiangsu and Guangdong provinces had moderate vulnerability levels. Jiangsu and Guangdong provinces were generally characterized as having low or moderate levels of exposure and sensitivity and high or very high adaptive capacity. However, Hebei and Shandong provinces were the exceptions; the high level of exposure in Hebei Province was countervailed by its low sensitivity to a decrease in marine catches, while Shandong Province had high exposure, which was offset by the relatively moderate dependence on fisheries and high adaptive capacity. Therefore, these two

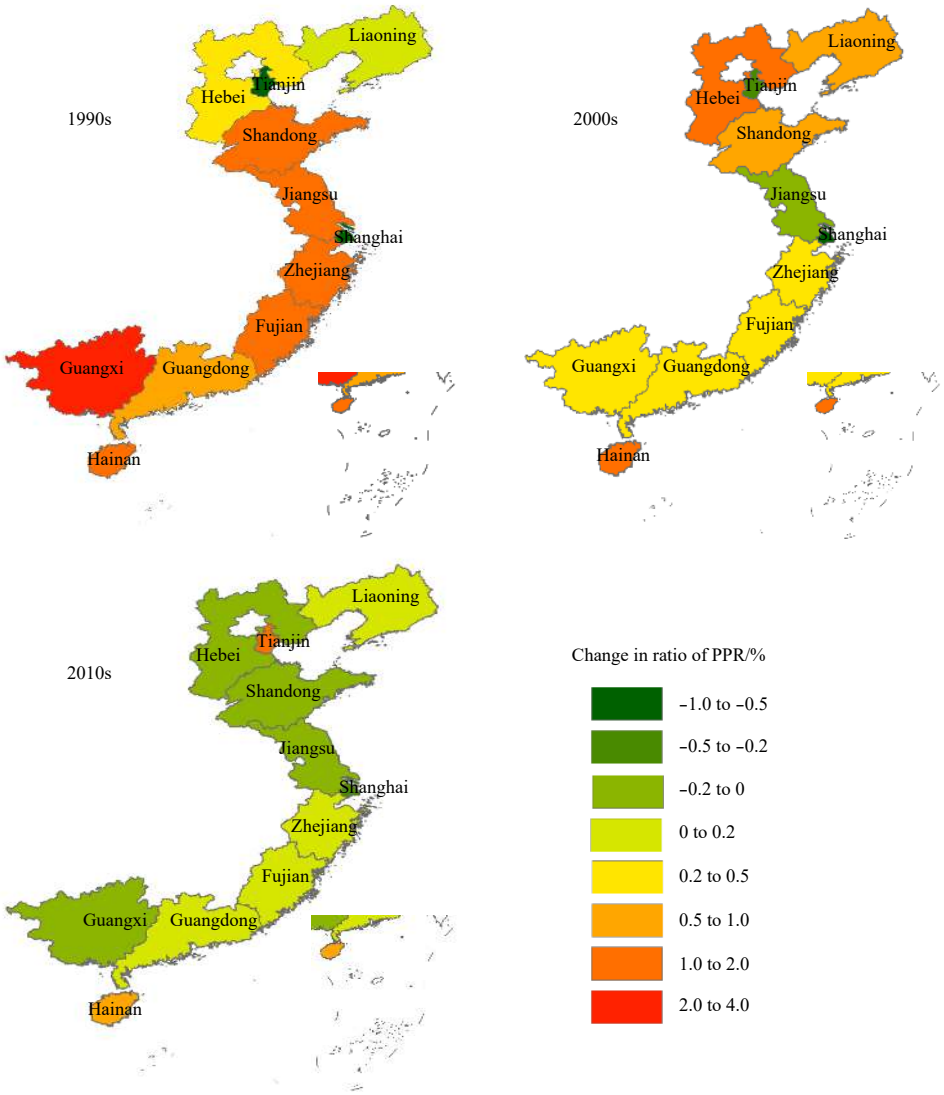

Fig. 4. Maps of the interdecadal changes in the percentage of primary production (%PPR) for the 11 coastal provinces in China.

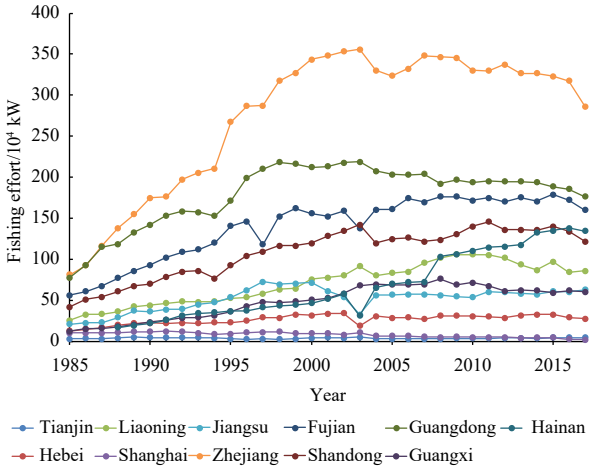

Fig. 5. Fishing effort for the 11 coastal provinces in China during 1985–2017.

provinces were also categorized as having moderate vulnerability levels. Furthermore, the high level of sensitivity in Liaoning Province was offset by its moderate levels of sensitivity exposure and adaptive capacity, which also resulted in a below-average vulnerability score.

The municipalities of Shanghai and Tianjin were ranked as having low vulnerability. Shanghai had the lowest exposure score. Specifically, marine catch only contributed 6% of the total production in 2017. In addition, this municipality exhibited low sensitivity and very high adaptive capacity. Tianjin was also identified as having low vulnerability due to its relatively low level of exposure to a reduction in marine catches, low sensitivity and very high adaptive capacity.

The component scores for each coastal province indicated that no single driver of vulnerability or single underlying mechanism made a province particularly vulnerable to declines in marine catches. Instead, coastal provinces suffered high vulnerability as the result of unique combinations of exposure, sensitivity and adaptive capacity. Our analysis revealed three different types of vulnerability: first, provinces with relatively high adaptive capacity and high levels of exposure and sensitivity, such as

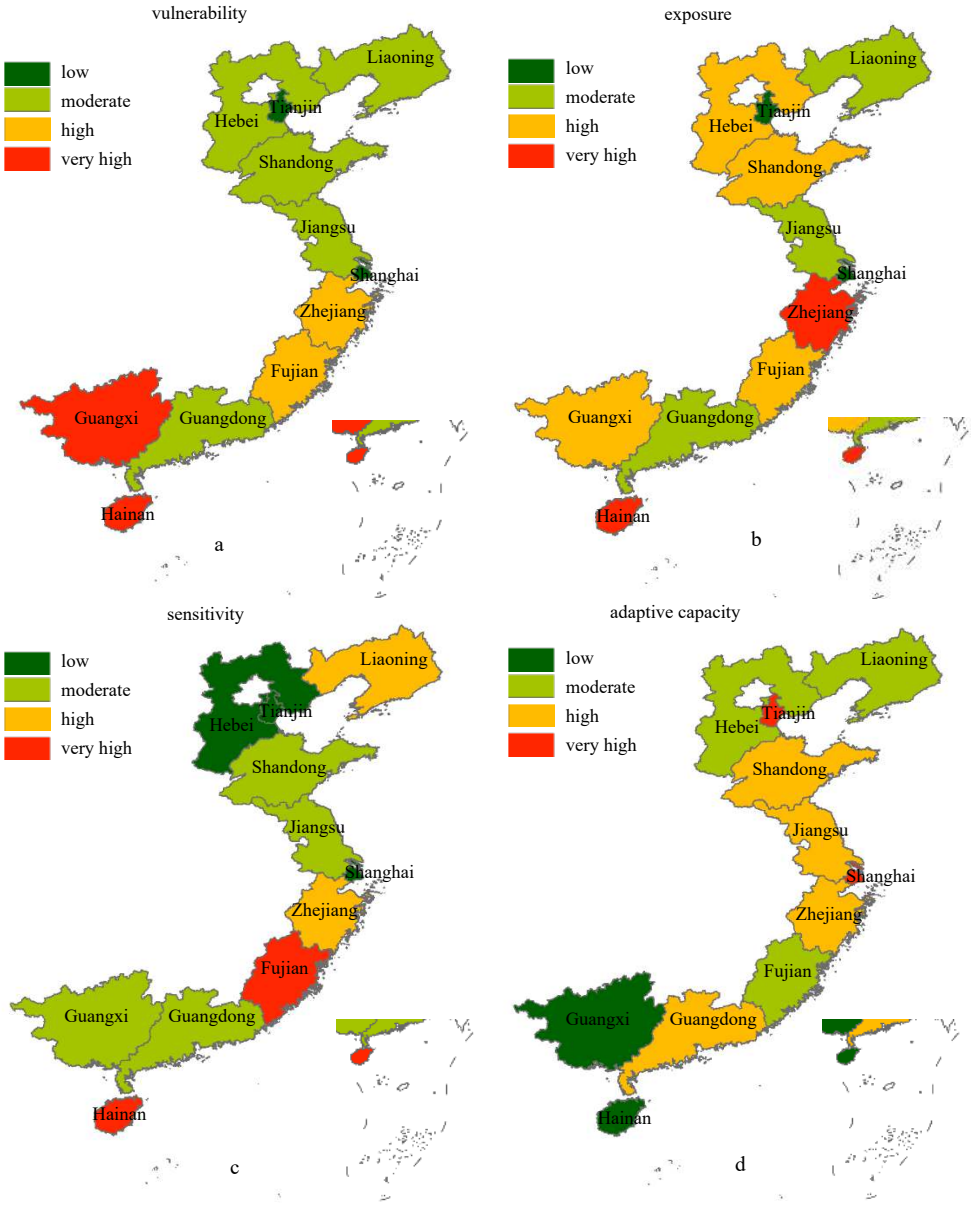

Fig. 6. Overall vulnerability (a), exposure (b), sensitivity (c), and adaptive capacity (d) of the 11 coastal provinces in China to a reduction in marine catches.

Zhejiang; second, provinces with low adaptive capacity and moderate level of sensitivity but high level of exposure, such as Guangxi; third, provinces with low or moderate adaptive capacity and high levels of exposure and sensitivity, such as Fujian and Hainan (Fig. 6).

4 Discussion

Maintaining the sustainability of marine fisheries in China is of both ecological and socioeconomic importance (Blomeyer et al., 2012; Cao et al., 2017). According to the China Fishery Statistical Yearbook, the domestic marine capture fisheries contributed RMB 198.7 billion to the national economy in 2017. In this paper, we examined the exploitation history of marine capture fisheries in China and further evaluated vulnerability to a reduction in marine fisheries at provincial level to understand the causes of such vulnerability. Our analysis suggested that the development of the Chinese marine fishing industry experienced rapid growth from the mid-1980s to the end of the 20th century and stabilized over the last few years of the time series. However, the rapid increase in marine catches was mainly promoted by increasing fishing effort. The total PPR level currently amounts to approximately 80% of the average primary productivity. Zhejiang, Fujian, Shandong, Hainan and Guangdong provinces were the main fishing provinces in China, accounting for 78% of the total marine catch in 2017. Among the 11 coastal provinces and municipalities in China, Hainan, Guangxi, Zhejiang and Fujian provinces had high or very high vulnerability to the impacts of a reduction in marine catches, while Shanghai and Tianjin were ranked as having low vulnerability.

In this study, we used the %PPR to quantify the effects of fishing on marine ecosystems. Total %PPR in China underwent the largest increase during the 1990s, and most of this growth was driven by fleets from Shandong, Zhejiang, Fujian, Guangdong and Hainan provinces. For the sustainable exploitation of wild

fish resources, the MARA introduced a "zero-growth" strategy in 1999 and a "negative-growth" strategy in 2000 for total marine catch (Shen and Heino, 2014), which resulted in a slight decline in total %PPR between 2000 and 2005. However, total %PPR continued to show a slowly increasing trend and stabilized beginning in the 2010s, and marine fishery resources still suffer from intense fishing pressure. Most of the growth in %PPR after the year 2005 was driven by fleets from Hainan, Zhejiang, Fujian and Guangdong provinces.

In response to overfishing and the steady degradation of coastal ecosystems, the Chinese government has formulated and organized a series of conservation and management regimes and measures (Yu and Yu, 2008; Shen and Heino, 2014). However, fisheries management in China mainly relies on input control measures (such as licensing systems, and the "Double Control" system) and technical measures (such as spatial and temporal closures and gear restrictions), and there is no direct control of marine catch. The poor enforcement of management measures designed to sustain fish stocks has resulted in the transfer of catch species from large, high-valued traditional fish stocks to lower-valued, small, pelagic fishes in the coastal seas of China. Although specific attention has been paid to fisheries volume control in Chinese fisheries management recently, marine fishery resource depletion is still a serious problem.

Although the total %PPR in China has significantly increased over the last three decades, the %PPR in the municipalities of Shanghai and Tianjin have shown a decreasing trend since the 1980s. This gradually declining trend of %PPR may be attributed to the following two factors. First, fishing effort in Shanghai and Tianjin has not shown a clear upward trend associated with the depletion of coastal marine fishery resources. In fact, fishing effort in Shanghai has shown a decreasing trend since the 1980s. Previous studies found that greater harvesting outside EEZs can alleviate ecosystem degradation to some extent (Clausen and York, 2008). China began to develop distant-water fisheries in the year 1985, and the distant-water fisheries have become a fast-growing seafood-producing sector (Shen and Heino, 2014). The landings from distant-water fisheries in Shanghai amounted to 129.9 thousand tons in 2017, which is over 8 times greater than the coastal marine catches for this municipality (Fisheries Bureau of the Ministry of Agriculture, 1950–2018), and the movement of fishing effort from coastal seas to more distant productive waters can relieve fishing pressure in the EEZ areas (Clausen and York, 2008). Second, aquaculture and increased fish imports can help the municipality meet its intensifying demand for fish to a certain extent. Aquaculture production accounted for approximately 86% of the total fish supply for Tianjin in 2017. In addition, as a net fish importer, the net import of seafood in Shanghai was 28 times greater than its domestic marine catch in 2017. The sharp increase in %PPR for Tianjin in the last five years is due to the increased catch of anchovy (*Engraulis japonicus*), which may relate to climate change (Niu and Wang, 2017).

With the excessive appropriation of PP, a reduction in PPR is necessary for Chinese marine fisheries to be put on a path toward sustainability. The MARA developed a Five-Year Plan for fisheries in 2017, which included at least a 23.6% reduction in marine catches for each fishing province by the year 2020 compared to the year 2015 (Cao et al., 2017). The impacts of a decrease in marine catches will vary across provinces as a result of their exposure, sensitivity and level of adaptive capacity. This study first introduced the SPA method in vulnerability assessments and evaluated the comparative magnitude and distribution of the potential impacts of a decline in marine catches for coastal provinces. Although Hainan, Guangxi, Zhejiang and Fujian provinces all exhibited high or very high vulnerability, the underlying causes of vulnerability differed among the provinces.

Vulnerability assessments have received increasing attention from policy makers and academics. Understanding these distinctions is important because specific policy tools may be required to address different dimensions of vulnerability (Allison et al., 2009; Hughes et al., 2012; Mamauag et al., 2013). In this study, three common vulnerability characterizations were recognized. Zhejiang Province belonged to the first type, Guangxi Province belonged to the second type, and Fujian and Hainan provinces belonged to the third type, respectively. For the first type, policy interventions should focus on reducing exposure and sensitivity. Nevertheless, developing context-specific measures to build adaptive capacity and further reduce exposure are likely to play a more important role in reducing the vulnerability of Guangxi Province. To reduce the vulnerability of Hainan and Fujian provinces, both decreasing exposure and sensitivity and increasing adaptive capacity are needed. This paper describes key policy actions that can help reduce vulnerability to the impacts caused by a reduction in marine catches.

Reducing fishery dependence on marine capture fisheries can help decrease exposure and sensitivity, thereby lowering the vulnerability of coastal provinces to declines in marine catches. This effect can be achieved by further strengthening the development of aquaculture and promoting the regulated and orderly development of distant-water fisheries (Cao et al., 2017). Aquaculture is expected to be a key component of a diversified fisheries production system. Aquaculture expansion can make a significant contribution to food security, and developing aquaculture can also be an efficient way to reduce fishing pressure on wild fishery resources (FAO, 2016). In fact, aquaculture accounts for approximately three-quarters of current fish supply in China. Similarly, distant-water fisheries in China have rapidly developed since 1985, with catches from distant-water fisheries accounting for approximately 18% of the total domestic marine catches in 2017. We should continue to promote sustainable aquaculture development that does not damage marine ecosystems and further enhance the competitiveness of Chinese distant-water fisheries, helping the country meet its increasing domestic demand for fish. In addition, China not only ranks as the world's leading fishing nation but also has the greatest number of people employed in the fishing sector (Cao et al., 2017). Supplemental livelihood activities and alternative livelihoods can reduce sensitivity by starting to link fishing households with new occupational sectors, and investment in new job opportunities for fishing communities is also necessary (Cinner et al., 2012).

Vulnerability can also be reduced through interventions that build adaptive capacity. Fishing provinces with high adaptive capacity are less likely to suffer from the impacts of a reduction in marine catches and are therefore better able to take advantage of the opportunities to enhance their socioeconomic resilience (McClanahan et al., 2015). The ability of fishing provinces to adapt depends on their economic strength, flexibility, education level, and social development (Hughes et al., 2012). Possible actions include developing alternative economic activities, increasing the availability of alternative income and protein sources, increasing the education and environmental literacy of fishers, reducing the economic dependence on fishing, and so on.

As a commonly used metric for the ecological footprint of fishing, the %PPR allows the quantification of fishing pressure on marine ecosystems (Swartz et al., 2010). We examined how the %PPR levels increased in China and further explored how vari-

ous fishing fleets contributed to these changes. Previous studies found that the majority of LME areas have a coefficient of inter-annual variation in PP of <5%; thus, average PP levels are representative and it is unlikely that these levels greatly deviated from the average (Watson et al., 2014). In addition, Pauly and Christensen (1995) found a range of efficiency values (3% to 18%) but suggested that these were extreme and that a rate of 10% was the most representative. Therefore, our analysis assumed a constant PP over the study period and used a fixed transfer efficiency of 10% between trophic levels in the food chain.

Studies addressing fishery vulnerability mainly focus on climate change-related impacts, while the influence of socioeconomic change is less considered. This study examined the exploitation history of Chinese marine capture fisheries since the mid-1980s and provides the first vulnerability analysis framework focused on the socioeconomic implications of a reduction in marine catches at provincial level. We found that the total %PPR in China increased from 28% in 1985 to 80% in 2017, and now, Zhejiang, Fujian, Shandong, Hainan and Guangdong provinces are the main fishing provinces. Of the 11 coastal provinces and municipalities in China, Hainan and Guangxi provinces showed very high vulnerability to a reduction in marine catches, while Zhejiang and Fujian provinces showed high vulnerability. To reduce such vulnerability to declines in marine catches, context-specific policies and actions should be developed for different economic sectors. As demand for fish continues to grow, we suggest that linked socio-ecological assessments such as the one in this study are essential tools for guiding sustainable fisheries management.

Acknowledgements

Data were obtained from the China Fisheries Statistical Yearbook, FAO, FishBase, Sea Around Us, for which we are grateful. We also thank two anonymous reviewers for constructive comments that improved this manuscript.

References

Adger W N. 2006. Vulnerability. Global Environmental Change, 16(3): 268–281, doi: 10.1016/j.gloenvcha.2006.02.006

Akpan S B, Patrick I V, Udoka S J, et al. 2013. Determinants of credit access and demand among poultry farmers in Akwa Ibom State, Nigeria. American Journal of Experimental Agriculture, 3(2): 293–307, doi: 10.9734/AJEA/2013/2810

Allison E H, Perry A L, Badjeck M C, et al. 2009. Vulnerability of national economies to the impacts of climate change on fisheries. Fish and Fisheries, 10(2): 73–196

Barange M, Merino G, Blanchard J L, et al. 2014. Impacts of climate change on marine ecosystem production in societies dependent on fisheries. Nature Climate Change, 4(3): 211–216, doi: 10.1038/nclimate2119

Bell J D, Watson R A, Ye Yimin. 2017. Global fishing capacity and fishing effort from 1950 to 2012. Fish and Fisheries, 18(3): 489–505, doi: 10.1111/faf.12187

Blomeyer R, Goulding I, Pauly D, et al. 2012. The Role of China in World Fisheries. Directorate General for Internal Policies. Policy Department B: Structural and Cohesion Policies. European Parliament

Cao Ling, Chen Yong, Dong Shuanglin, et al. 2017. Opportunity for marine fisheries reform in China. Proceedings of the National Academy of Sciences of the United States of America, 114(3): 435–442, doi: 10.1073/pnas.1616583114

Cinner J, Fuentes M M P B, Randriamahazo H. 2009. Exploring social resilience in Madagascar's marine protected areas. Ecology and Society, 14(1): 41, doi: 10.5751/ES-02881-140141

Cinner J E, Huchery C, Darling E S, et al. 2013. Evaluating social and ecological vulnerability of coral reef fisheries to climate change. PLoS One, 8(9): e74321, doi: 10.1371/journal.pone.0074321

Cinner J E, McClanahan T R, Graham N A J, et al. 2012. Vulnerability of coastal communities to key impacts of climate change on coral reef fisheries. Global Environmental Change, 22(1): 12–20, doi: 10.1016/j.gloenvcha.2011.09.018

Clausen R, York R. 2008. Economic growth and marine biodiversity: influence of human social structure on decline of marine trophic levels. Conservation Biology, 22(2): 458–466, doi: 10.1111/j.1523-1739.2007.00851.x

Coll M, Libralato S, Pitcher T J, et al. 2013. Sustainability implications of honouring the code of conduct for responsible fisheries. Global Environmental Change, 23(1): 157–166, doi: 10.1016/j.gloenvcha.2012.10.017

Cutter S L. 1996. Vulnerability to environmental hazards. Progress in Human Geography, 20(4): 529–539, doi: 10.1177/030913259602000407

Ding Qi, Chen Xinjun, Hilborn R, et al. 2017b. Vulnerability to impacts of climate change on marine fisheries and food security. Marine Policy, 83: 55–61, doi: 10.1016/j.marpol.2017.05.011

Ding Qi, Wang Yali, Chen Xinjun, et al. 2017a. Effects of economics and demographics on global fisheries sustainability. Conservation Biology, 31(4): 799–808, doi: 10.1111/cobi.12873

FAO. 2016. The state of world fisheries and aquaculture 2014. Rome: Food and Agriculture Organization of the United Nations Press

Fisheries Bureau of the Ministry of Agriculture. 1950–2018. China Fisheries Statistical Yearbook (in Chinese). Beijing: China Agricultural Press, 1–181

Huang Yunfeng, Li Fangyi, Bai Xuemei, et al. 2012. Comparing vulnerability of coastal communities to land use change: Analytical framework and a case study in China. Environmental Science & Policy, 23: 133–143

Hughes S, Yau A, Max L, et al. 2012. A framework to assess national level vulnerability from the perspective of food security: The case of coral reef fisheries. Environmental Science & Policy, 23: 95–108

Johnson J E, Welch D J. 2009. Marine fisheries management in a changing climate: a review of vulnerability and future options. Reviews in Fisheries Science, 18(1): 106–124, doi: 10.1080/10641260903434557

Liu J Y. 2013. Status of marine biodiversity of the China Seas. PLoS One, 8(1): e50719, doi: 10.1371/journal.pone.0050719

Mamauag S S, Aliño P M, Martinez R J S, et al. 2013. A framework for vulnerability assessment of coastal fisheries ecosystems to climate change-Tool for understanding resilience of fisheries (VATURF). Fisheries Research, 147: 381–393, doi: 10.1016/j.fishres.2013.07.007

McClanahan T, Allison E H, Cinner J E. 2015. Managing fisheries for human and food security. Fish and Fisheries, 16(1): 78–103, doi: 10.1111/faf.12045

Monnereau I, Mahon R, McConney P, et al. 2015. Vulnerability of the fisheries sector to climate change impacts in Small Island Developing States and the Wider Caribbean: early findings. CERMES Technical Report No 77. Barbados: University of the West Indies

Niu Mingxiang, Wang Jun. 2017. Variation in the distribution of wintering anchovy *Engraulis japonicus* and its relationship with water temperature in the central and southern Yellow Sea. Chinese Journal of Oceanology and Limnology, 35(5): 1134–1143, doi: 10.1007/s00343-017-6134-1

Pauly D, Belhabib D, Blomeyer R, et al. 2014. China's distant-water fisheries in the 21st century. Fish and Fisheries, 15(3): 474–488, doi: 10.1111/faf.12032

Pauly D, Christensen V. 1995. Primary production required to sustain global fisheries. Nature, 374(6519): 255–257, doi: 10.1038/374255a0

Pauly D, Zeller D. 2015. Sea Around Us concepts, design and data. Vancouver, B. C: Sea Around Us, University of British Columbia. http://www.seaaroundus.org/ [2018-01-12]

Pelletier N, André J, Charef A, et al. 2014. Energy prices and seafood security. Global Environmental Change, 24: 30–41, doi: 10.1016/j.gloenvcha.2013.11.014

Shen Gongming, Heino M. 2014. An overview of marine fisheries management in China. Marine Policy, 44: 265–272, doi: 10.1016/j.marpol.2013.09.012

Swartz W, Sala E, Tracey S, et al. 2010. The spatial expansion and ecological footprint of fisheries (1950 to present). PLoS One, 5(12): e15143, doi: 10.1371/journal.pone.0015143

Watson R, Zeller D, Pauly D. 2014. Primary productivity demands of global fishing fleets. Fish and Fisheries, 15(2): 231–241, doi: 10.1111/faf.12013

Watson R A, Cheung W W L, Anticamara J A, et al. 2013. Global marine yield halved as fishing intensity redoubles. Fish and Fisheries, 14(4): 493–503, doi: 10.1111/j.1467-2979.2012.00483.x

Worm B, Hilborn R, Baum J K, et al. 2009. Rebuilding global fisheries. Science, 325(5940): 578–585, doi: 10.1126/science.1173146

Wu Jian, Yang Aiting. 2012. The analysis of regional economic vulnerability and obstacle factors of Guangdong province based on set pair analysis. Economic Geography (in Chinese), 32(9): 32–38

Yu Huiguo, Yu Yunjun. 2008. Fishing capacity management in China: Theoretic and practical perspectives. Marine Policy, 32(3): 351–359, doi: 10.1016/j.marpol.2007.07.004

Zhao Keqin. 2000. Set Pair Analysis and Its Preliminary Application (in Chinese). Hangzhou: Zhejiang Science and Technology Press, 1–198

Acta Oceanol. Sin., 2020, Vol. 39, No. 4, P. 110–119
https://doi.org/10.1007/s13131-020-1585-1
http://www.hyxb.org.cn
E-mail: hyxbe@263.net

Blooms of *Prorocentrum donghaiense* reduced the species diversity of dinoflagellate community

Huan Wang[1, 3], Zhangxi Hu[1, 2, 4], Zhaoyang Chai[1, 2, 4], Yunyan Deng[1, 2, 4], Zifeng Zhan[5], Ying Zhong Tang[1, 2, 4*]

[1] CAS Key Laboratory of Marine Ecology and Environmental Sciences, Institute of Oceanology, Chinese Academy of Sciences, Qingdao 266071, China

[2] Laboratory for Marine Ecology and Environmental Science, Pilot National Laboratory for Marine Science and Technology (Qingdao), Qingdao 266237, China

[3] University of Chinese Academy of Sciences, Beijing 100049, China

[4] Center for Ocean Mega-Science, Chinese Academy of Sciences, Qingdao 266071, China

[5] Department of Marine Organism Taxonomy and Phylogeny, Institute of Oceanology, Chinese Academy of Sciences, Qingdao 266071, China

Received 24 November 2018; accepted 19 February 2019

Abstract

Most of reported harmful algal blooms (HABs) of microalgae (75%) have been caused by dinoflagellates. Studies on the negative effects of HABs have generally focused on animals, valuable organisms in particular, and environmental factors such as dissolved oxygen and nutrients, but relatively fewer on community level, particularly that using metagenomic approach. In this study, we reported an investigation on the effects of a HAB caused by the dinoflagellate *Prorocentrum donghaiense* on the species diversity and community structure of the dinoflagellate sub-community via a pyrosequencing approach for the samples taken before, during, and after the bloom season of *P. donghaiense* in the East China Sea. We sequenced partial 28S rRNA gene of dinoflagellates for the field samples and evaluated the species richness and diversity indices of the dinoflagellate community, as a sub-community of the total phytoplankton. We obtained 800 185 valid sequences (categorized into 560 operational taxonomic units, OTUs) of dinoflagellates from 50 samples and found that the biodiversity of dinoflagellate community was significantly reduced during the blooming period in comparison to that in pre- and after-blooming periods, as reflected in the four diversity indices: the species richness expressed as the number of OTUs, Chao1 index, Shannon index (evenness), and Gini-Simpson index. These four indices were all found to be negatively correlated to the cell density of the bloom species *P. donghaiense*. Correlation analyses also revealed that the *P. donghaiense* cell abundance was correlated negatively with NO_3^--N, and NO_2^--N, but positively with total nitrogen (TN) and total phosphorus (TP). Principal coordinates analysis (PCoA) showed that the community structure of dinoflagellates was markedly different among the different sampling periods, while the redundancy analysis (RDA) revealed *P. donghaiense* abundance, salinity, NO_3^--N, and SiO_3^{2-} were the most four significant factors shaping the dinoflagellate community structure. Our results together demonstrated that HABs caused by the dinoflagellate *P. donghaiense* could strongly impact the aquatic ecosystem on the sub-community level which the blooming species belongs to.

Key words: *Prorocentrum donghaiense*, dinoflagellate community, diversity, pyrosequencing, East China Sea

Citation: Wang Huan, Hu Zhangxi, Chai Zhaoyang, Deng Yunyan, Zhan Zifeng, Tang Ying Zhong. 2020. Blooms of *Prorocentrum donghaiense* reduced the species diversity of dinoflagellate community. Acta Oceanologica Sinica, 39(4): 110–119, doi: 10.1007/s13131-020-1585-1

1 Introduction

Harmful algal blooms (HABs) have been increasing globally in extension and impacts on public health, aquaculture industry, fisheries, and ecosystems such as oxygen depletion, reduction in water quality (Anderson et al., 2012, 2002; Smayda, 1990). Among all HABs-causing species, dinoflagellates are the most important contributors, as about 75% of reported HABs were caused by dinoflagellates (Smayda, 1997). Dinoflagellates have a number of characteristic features (Burkholder et al., 2006) and are one of the most important primary producers and a vital component of coral reef symbiotic system (Aranda et al., 2016; Lin et al., 2015). While HAB events may be caused by a variety of environmental

Foundation item: The National Natural Science Foundation of China under contract Nos 61533011 and 41776125; the NSFC-Shandong Joint Fund for Marine Ecology and Environmental Sciences under contract No. U1606404; the Scientific and Technological Innovation Project of the Qingdao National Laboratory for Marine Science and Technology under contract No. 2016ASKJ02; the National Key R&D Program of China under contract No. 2017YFC1404300; the Creative Team Project of the Laboratory for Marine Ecology and Environmental Science, Qingdao National Laboratory for Marine Science and Technology under contract No. LMEES-CTSP-2018-1.

*Corresponding author, E-mail: yingzhong.tang@qdio.ac.cn

and autecological factors such as illumination, water temperature, nutrients availability, growth rate, vertical migration, and special life history (Anderson et al., 2002; Xu et al., 2010), as feedbacks, HABs may cause many negative effects on the ecosystems that can be viewed from different levels (from ecosystem, community to sub-cellular and molecular levels) and aspects (physical, chemical, biological, public health, and economic). In general, previous studies on the negative effects of HABs have been mainly focused on fisheries, aquaculture, and human public health (Anderson et al., 2012; Landsberg, 2002), relatively fewer studies, however, have investigated the effects of HABs on the level of community, and even fewer using high throughput metagenomic approach, such as phytoplankton community diversity, community structure, function and stability (Cui et al., 2018; Zhou et al., 2018). This oddness was at least partly due to the limitations in how to obtain comprehensive lists of species and identify species of small sizes, simple or similar morphologies, low abundances, and to process numerous samples efficiently. Conventional methods for identifying and quantifying phytoplankton species from field samples generally involved in the use of light microscopy, and sometimes were aided with flow cytometry and alike, pigment analysis, however they all have limita-

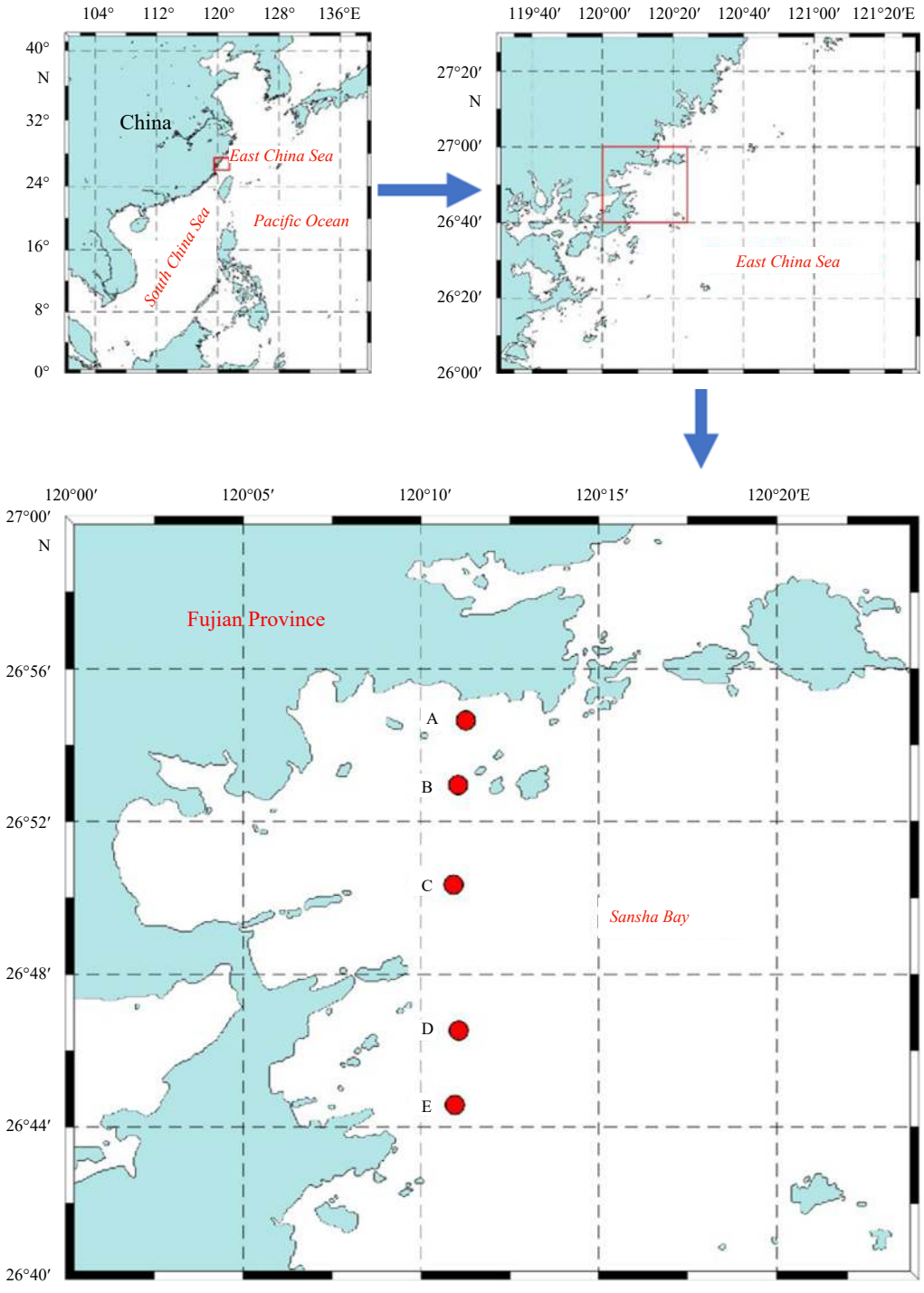

Fig. 1. Locations of sampling sites in the Sansha Bay, Ningde, China.

Table 1. Categorization of samples according to sampling timing (pre-, during, and after blooms) and locations

	0331 Non-blooming	0422 Blooming	0503 Blooming	0513 Blooming	0531 Non-bloomig	0719 Non-blooming
Sample ID	A0331a	A0422a	E0503a	A0513a	A0531a	A0719a
	A0331b	A0422b	E0503b	A0513b	A0531b	A0719b
	B0331a	B0422a	A0503a	B0513a	B0531a	B0719A
	B0331b	B0422b	A0503b	B0513b	B0531b	B0719b
	C0331a	C0422a	B0503a	C0513a	C0531a	C0719a
	C0331b	C0422b	B0503b	C0513b	C0531b	C0719b
	D0331a	D0422a	C0503a	D0513a	D0531a	D0719a
	D0331b	D0422b	C0503b	D0513b	D0531b	D0719b
			D0503a			
			D0503b			

tions in identifying and quantifying those species of highly small sizes, simple or similar morphologies, low abundances, and novel taxa that have not been described (Chai et al., 2018). With the development of molecular approaches, high-throughput gene sequencing (e.g., 18S and 28S rRNA genes) have recently been increasingly applied to environmental samples to conquer these limitations (Chai et al., 2018, 2020; Vaulot et al., 2008; Xu et al., 2017; Zhou et al., 2018). The well-developed, high-throughput sequencing allows us to deeply sequence environmental samples and to sensitively and accurately identify species, and thus detect slight changes at the community level (Miao et al., 2017; Schneider et al., 2017; Sunagawa et al., 2015).

In this study, we investigated the effects of blooms of a common HABs-causing dinoflagellate in China, *Prorocentrum donghaiense*, on the dinoflagellate sub-community level, which the bloom species belongs to, in terms of species richness and other biodiversity indices by applying a high-throughput amplicon sequencing approach. We applied a pair of particularly designed primers targeting the large subunit rRNA gene to sequencing the samples taken before, during, and after *P. donghaiense* blooming from the Sansha Bay, Fujian Province, China. We also measured other variables including cell density of *P. donghaiense*, chlorophyll content, nutrients (total nitrogen (TN), nitrate (NO_3^--N), nitrite (NO_2^--N), ammonium (NH_4^+-N), total phosphorus (TP), phosphate (PO_4^{3-}-P), silicate (SiO_3^{2-})), salinity, and temperature to examine the interactions among these variables, *P. donghaiense* blooms, and the dinoflagellates community succession.

2 Materials and methods

2.1 *Sampling sites, dates and procedures*

The study area, Sansha Bay, is located at the northeast to Ningde, Fujian Province (26°44.5′–26°54.5′N, 120°10.9′–120°11.3′E), one of Fujian Province's major aquaculture water in the East China Sea (Fig. 1), where has observed highly frequent HABs caused by *P. donghaiense*, *Karenia mikimotoi*, and, occasionally, other species (Lin et al., 2014; Lu et al., 2005; Yao et al., 2006). There were about 161 HAB incidents during 2001–2010 and 65 events between 2011 and 2015, amongst them *P. donghaiense* being the main causative species (State Oceanic Administration, 2001–2015).

From March to July, 2016, we conducted six cruises and collected a total of 50 samples, which covered pre-, during, and post-bloom periods. Four or five sampling sites were selected in the study area (Table 1). March 31 (0331) was a time prior to the bloom, the dates April 22 (0422), May 3 (0503), May 13 (0513) were categorized as during-bloom period based on cell counts of *P. donghaiense*, with May 3 observing the peak of a bloom, and May 31 (0531) and July 19 (0719) were categorized as post-bloom period. Here, we simply define a bloom according to chlorophyll *a* (Chl *a*) content and dominant specie concentration, with Chl *a* content higher than 5 μg/L when there is a dominant species (Jonsson et al., 2009) and 20 000 cells/mL of the dominant species, with an awareness of no commonly accepted standard of cell density to define a bloom. The sample IDs include sampling sites (A, B, C, D, E), sampling dates (0331, 0422, 0503, 0513, 0531, 0719), and the duplicate letters a and b. For example, the sample ID A0331a refers to the first sample taken on March 31 from Site A.

Water temperature and salinity were measured on site using a hand-held thermometer (BoBang Ltd, China) and a refractometer (Atago Ltd, Japan). Water samples were taken from 0.5 m below the surface and transferred into 5 L polyethylene bucket. Plankton samples for DNA extraction were collected by filtering 1.5 L water through a hydrophilic polycarbonate membrane (47 mm diameter, 0.4 μm pore size, Merck Millipore Ltd, Germany) with duplicates, put into an icebox and then –20°C immediately after arriving the laboratory and then stored at –80°C until DNA extraction. Water samples (1 L) were also fixed with Lugol's iodine solution (final concentration, 2%) for counting cells of *P. donghaiense* using plankton counting chamber under an inverted light microscope (IX73, Olympus, Tokyo, Japan). Samples for NO_3^--N, NO_2^--N, NH_4^+-N, PO_4^{3-}-P, and SiO_3^{2-} were filtered through Whatman GF/C filters (pore size ~1.2 μm), and added 2 drops of chloroform per 100 mL sample. Samples for TN (total nitrogen) and TP (total phosphorous) were pretreated by adding two drops of 98% sulfuric acid per 100 mL sample. Samples for Chl *a* (at least 500 mL for each sample) were filtered onto Whatman GF/F glass fiber filters (pore size ~0.7 μm) and frozen until analysis. All samples were immediately transported to the laboratory in cold conditions and subjected to measurements of the nutrients and Chl *a*.

2.2 *Measurements of nutrients and other variables*

NO_3^--N, NO_2^--N, NH_4^+-N, PO_4^{3-}-P, and SiO_3^{2-} were analyzed colorimetrically using a nutrient analyzer (Skalar Ltd, Netherland) according to the protocols of JOGFS report No. 19 (JOGFS International Project Office, 1994). For TN and TP analyses, samples were digested using potassium persulfate under high temperature (115°C, 30 min) according to the standard protocol (Valderrama, 1981), and then the treated samples were also analyzed colorimetrically using the nutrient analyzer. Chl *a* was extracted with 90% aqueous acetone, and measured fluorometrically using a Turner Designs fluorometer (Parsons et al., 1984).

2.3 *Primer design, DNA extraction, PCR amplification, and pyrosequencing*

The forward and reverse primers were designed to target the partial 28S rRNA gene (rDNA) including the highly variable D2

domain mainly for dinoflagellates. Reference sequences of 28S rDNA for microalgae of different groups and ciliates were selected and aligned with that of dinoflagellates to verify the suitability of the selected oligonucleotide sequences as primers using Primer 3 (Rozen and Skaletsky, 2000). The specificity of the generated primer candidates were checked against the GenBank sequence collection by a standard nucleotide-nucleotide BLAST search for the sake of amplifying all dinoflagellates, resulting in the primers as follows: forward primer LSU347 (5′-CAAGTACCATGAGGGAAA-3′) and reverse primer LSU929 (5′-ACGAACGATTTGCACGTCAGTA-3′).

Genomic DNA was extracted with a plant DNA extraction kit (Tiangen, Beijing, China) according to the manufacturer's protocol. PCR was then conducted in 20 μL reaction mixture containing 2 μL of deoxynucleoside triphosphate at a concentration of 2.5 mmol/L, 0.8 μL of forward and reverse primers (5 μmol/L each), respectively, 0.4 μL FastPfu Polymerase, 5× FastPfu Buffer 4 μL, and 1 μL of template DNA (final amount 10 ng) under the following PCR conditions: 94°C for 5 min, 35 cycles of 94°C for 30 s, 46°C for 30 s, and 72°C for 30 s and 72°C for 10 min extension. PCR amplicons were purified with an AxyPrep DNA gel extraction kit (Axygen, USA) and quantified using the QuantiFluor-ST Fluorescence quantitative system (Promega, USA). Amplicons from different water samples were then mixed to achieve equal mass concentrations in the final mixture, which was then pyrosequenced using a 454 Genome Sequencer (GS) FLX Titanium platform (LC-Bio Technology Co. Ltd, Hangzhou, China) as previously described (Sun et al., 2014). FASTA-formatted sequences and corresponding quality scores (QC) were extracted from the ".sff" data file using the GS Amplicon software package. Raw sequencing data of this study have been deposited in the NCBI database under Accession No. SRR8163577.

2.4 *Statistics and bioinformatic analyses*

Aligned sequences were clustered into operational taxonomic units (OTUs) defined by 97% similarity (identity) using the average neighbor algorithm. The taxonomy assignment of OTUs was done by Global Alignment for Sequence Taxonomy (GAST) process (Huse et al., 2008). Community diversity parameters ((Shannon index, Gini-Simpson index (1-λ), and Chao1 index (as an asymptotic species richness estimator)) for each sample were calculated as described in the Mothur software manual (http://www.mothur.org/). Principal coordinates analysis (PCoA) were conducted at the OTU level with the community ecology package (http://www.mothur.org/). Redundancy analysis (RDA) was performed to analyze the major environmental factors affecting the community structure using the R-vegan and R-map tools for Linux (Legendre et al., 2011). Spearman's rank correlation coeffi-

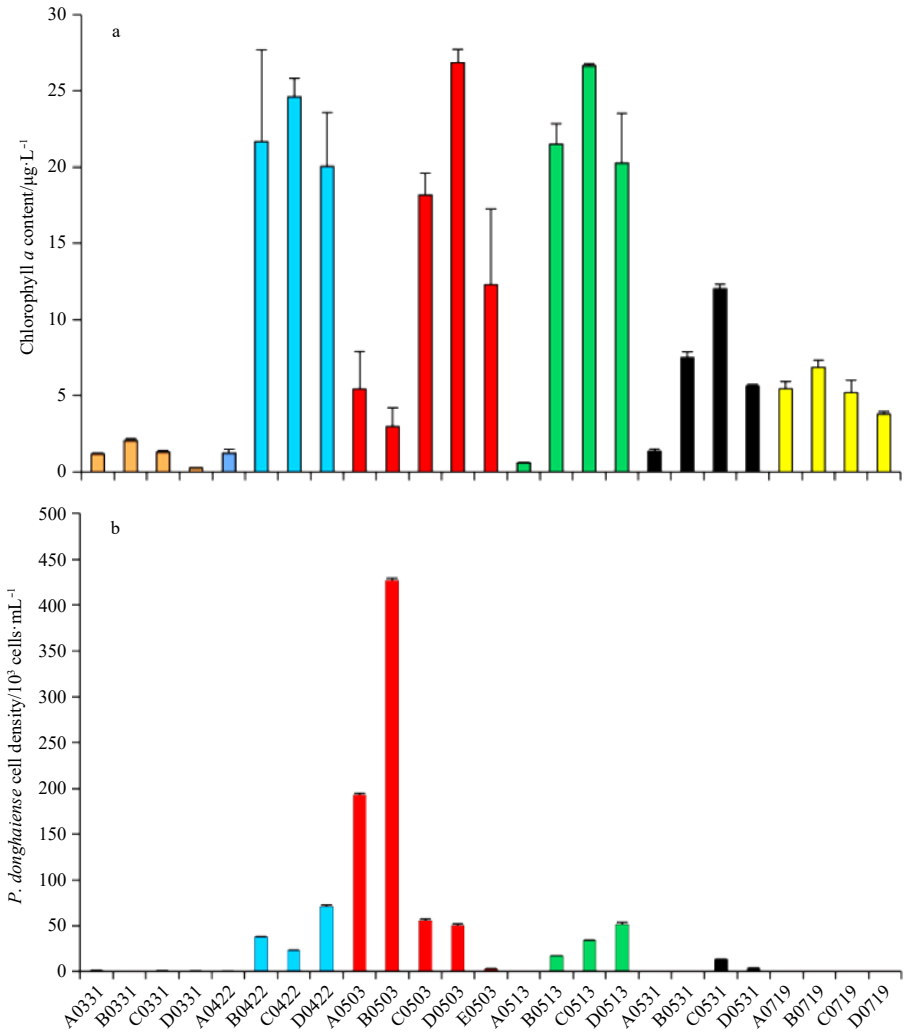

Fig. 2. The cell density of *P. donghaiense* and the chlorophyll *a* of different samples in the coastal waters of the Sansha Bay, Ningde, China. Error bars indicate ±1×SD. a. Chlorophyll *a*, and b. cell density of *P. donghaiense*.

Table 2. The ratio of dissolved inorganic nitrogen (DIN) to dissolved inorganic phosphorus (as PO_4^{3-}-P) (DIN/DIP)

Date	Max	Min	Mean±SD
0331	21.5	18.8	20.4±1.2
0422	17.8	4.0	8.3±6.4
0503	14.6	3.4	6.9±5.2
0513	5.8	3.4	4.1±1.2
0531	46.9	7.4	27.4±19.7
0719	9.9	4.7	7.0±2.2

cient (or Spearman's rho) was calculated to measure possible correlation between two variables using the software SPSS 22.0. Since the Spearman correlation evaluates the monotonic relationship between two variables that they may tend to change together but not necessarily at a constant rate, we chose to use the Spearman correlation coefficient, as we assumed that the two variables might be correlated but not necessarily correlated linearly. The significance level was set at 0.05 for all tests unless otherwise stated.

3 Results

3.1 *Variations and dynamics of P. donghaiense cell density, Chl a content, and nutrients*

During the six cruises from March to July of 2016, *P. donghaiense* reached the maximum cell density of ~4.3×10^5 cells/mL on May 3 (Fig. 2). The cell density of *P. donghaiense* was 270 cells/mL on March 31 (pre-blooming) and the lowest cell density of 83 cells/mL was on July 19 (after blooming). During the blooming period of late April to early May, *P. donghaiense* abundance ranged from 300 to ~4.3×10^5 cells/mL. However, among the sampling sites, *P. donghaiense* cell density varied significantly, with Site B or Site C having significantly higher abundance than that of Site A (p<0.05).

The Chl *a* level ranged from 0.3 to 26.8 μg/L, with the highest observed at Site D on May 3, where and when the bloom of *P. donghaiense* was observed (with a cell density of *P. donghaiense* ~5.0×10^4 cells/mL). There existed a significant positive correlation between *P. donghaiense* cell density and Chl *a* (Spearman rho=0.54, p<0.05), indicating *P. donghaiense* was one of, but not the only, major contributors of phytoplankton biomass. Strikingly, it is noteworthy that for the sample B0503, there was a discrepancy between Chl *a* and the cell abundance of *P. donghaiense* (Fig. 2), which we think was possibly due to a lower Chl *a* content per cell for *P. donghaiense* relative to that of other phytoplankton species such as diatoms and green microalgae because of the highly small-sized cells and pigment composition of *P. donghaiense*. In addition, the extremely high abundance of *P. donghaiense* during the blooming period (e.g., early May) also decreased the abundance of other phytoplankton with higher Chl *a* content per cell.

Water temperature ranged from 13.9°C to 29.5°C during the sampling period. No significant correlation was observed between water temperature and Chl *a* (Spearman rho=0.16, p > 0.05), neither between temperature and *P. donghaiense* cell density (Spearman rho=–0.19, p>0.05). Regarding the correlations between nutrients and *P. donghaiense* cell density, we observed no correlation for NH_4^+-N and PO_4^{3-}-P, but *P. donghaiense* cell density significantly correlated with NO_3^--N, NO_2^--N, TN, TP, and SiO_3^{2-}, respectively (p<0.05), with NO_3^--N and NO_2^--N being negative (Spearman rho=–0.59 and –0.60, respectively; p<0.05), and TN, TP, and SiO_3^{2-} being positive (Spearman rho=0.75, 0.84, and 0.51, respectively; p<0.05), indicating N and P as supporting or driving factors for the bloom of *P. donghaiense*. The ratios of dissolved inorganic nitrogen (DIN, the sum of NO_3^--N, NO_2^--N and NH_4^+-N) to dissolved inorganic phosphorus (DIP, as PO_4^{3-}-P) in the surface water tended to decrease along with the development and maintenance of bloom (Table 2). At the beginning of the survey (March 31), the DIN to DIP ratios in the surface layer was 18–22 on average, while, during the blooming period of *P. donghaiense*, the ratio showed a downward trend in general. On May 13, the ratio reached the minimum (3.4, Table 2). There existed a significant negative correlation between *P. donghaiense* cell density and DIN/DIP (Spearman rho=–0.64; p<0.05).

3.2 *General description for pyrosequencing results*

A total of 800 185 valid sequence reads of dinoflagellates with an average length of about 400 bp were generated from the 50 samples (Table S2). By clustering the unique sequences at 97% similarity level, these dinoflagellate sequences were grouped into 560 OTUs, with the number of OTUs ranging from 39 to 304 per sample. The highest richness was observed in the sample C0719b (after bloom) and the lowest richness was observed in A0503b (during bloom). OTU richness decreased during the blooming period from April 22 to May 13, and then increased with the disappearance of bloom from May 31 to July 17, and the Chao1 index (an indicator of total species richness) exhibited the same trend as OTU-indicated species richness.

Table 3. Correlations between *P. donghaiense* cell density and other environmental variables and diversity indices of dinoflagellate community, as measured with the rank correlation coefficient or Spearman's rho

	Number of OTUs	Shannon-Wiener index	Gini-Simpson index	Chao1 index
	Spearman rho (p-level)	Spearman rho (p-level)	Spearman rho (p-level)	Spearman rho (p-level)
P. donghaiense vs. diversity indices	–0.52 (<0.000 1***)	–0.67 (<0.000 1***)	–0.609 (0.001**)	–0.37 (0.001**)
Chl *a* vs. diversity indices	–0.43 (0.031*)	–0.51 (0.009*)	–0.56 (0.004*)	0.01 (0.007**)
Temperature vs. diversity indices	0.29 (0.156)	0.37 (0.069)	0.35 (0.088)	0.38 (0.059)
Salinity vs. diversity indices	0.16 (0.452)	0.23 (0.26)	0.22 (0.0286*)	0.37 (0.069)
Nitrite vs. diversity indices	0.62 (0.001**)	0.57 (0.003**)	0.53 (0.007**)	0.29 (0.15)
Nitrate vs. diversity indices	0.48 (0.015*)	0.48 (0.013*)	0.48 (0.014*)	0.07 (0.756)
TN vs. diversity indices	–0.62 (0.001**)	–0.72 (0.001**)	–0.76 (0.001**)	–0.43 (0.034*)
TP vs. diversity indices	–0.52 (0.007**)	–0.64 (0.001**)	–0.67 (<0.000 1***)	0.37 (0.73)
Phosphate vs. diversity indices	–0.009 (0.967)	0.01 (0.968)	–0.01 (0.971)	–0.29 (0.159)
Ammonium vs. diversity indices	0.24 (0.328)	0.03 (0.900)	–0.04 (0.85)	0.007 (0.97)

Note: The sample sizes for all were 50 (n=50). * 0.01<p<0.05; ** 0.001<p<0.01; *** p<0.001.

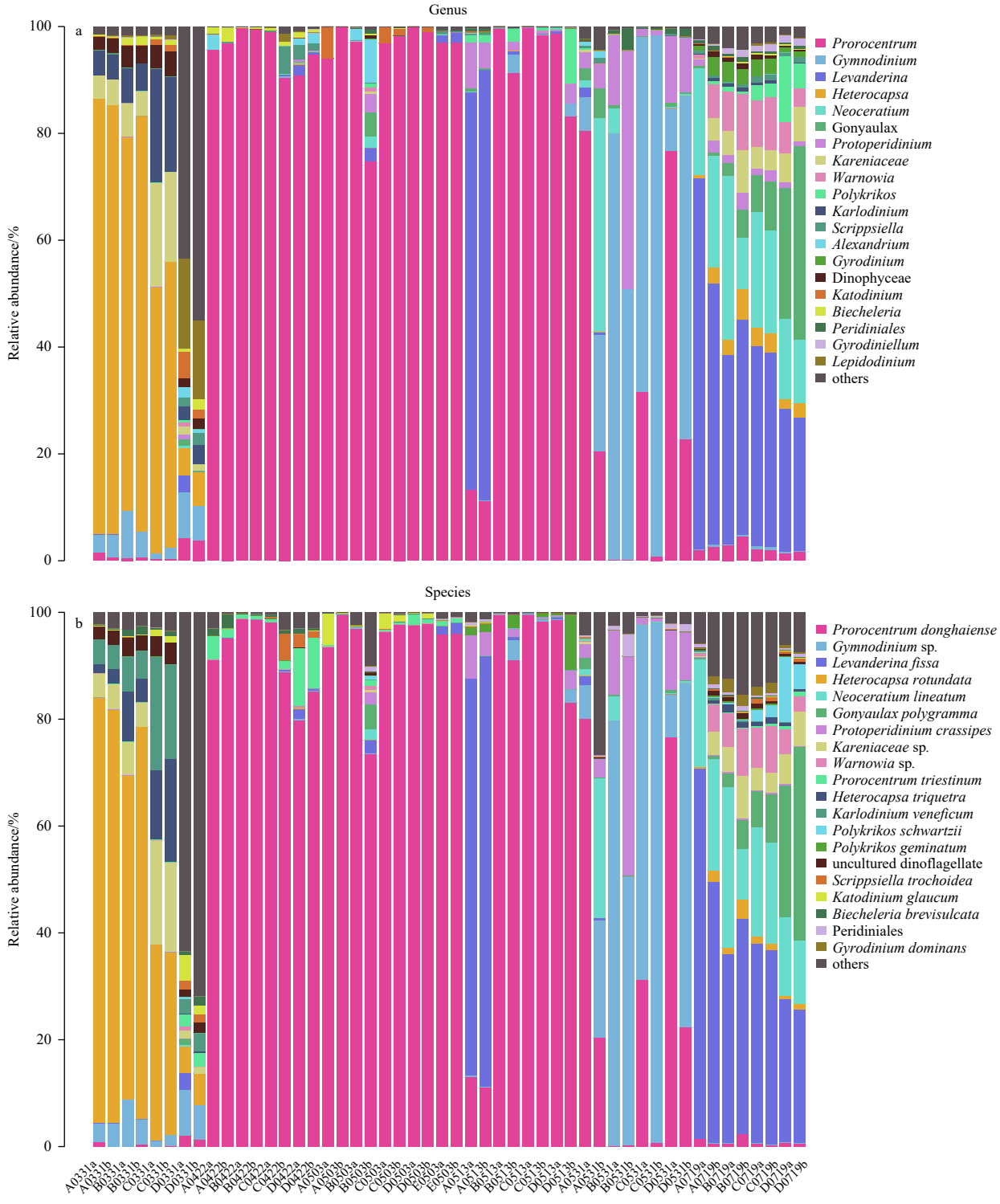

Fig. 3. Relative abundance of the top 20 genera (a) and species (b) of dinoflagellates in the 50 samples. The abundance is presented as percentage of each taxon in the total reads of valid sequences of all dinoflagellates in a sample. Note that "others" indicates the total of all other taxa except for the top 20 taxa (genera or species), which will allow a 100 percentage for all taxa. The annotations "uncultured dinofalgellate" was the original annotation of a reference sequence in the GenBank that was not convincingly identified to any particular genus or species.

3.3 *Prorocentrum donghaiense bloom negatively affected species diversity of the dinoflagellate community*

We determined if the species diversity of the dinoflagellate community was affected by the presence of *P. donghaiense* bloom using the rank correlation coefficient or Spearman's rho. Note that the alpha diversity indices here included species richness as expressed in the number of OTUs and Chao1 index, the Shannon index (indicating species evenness of community), and

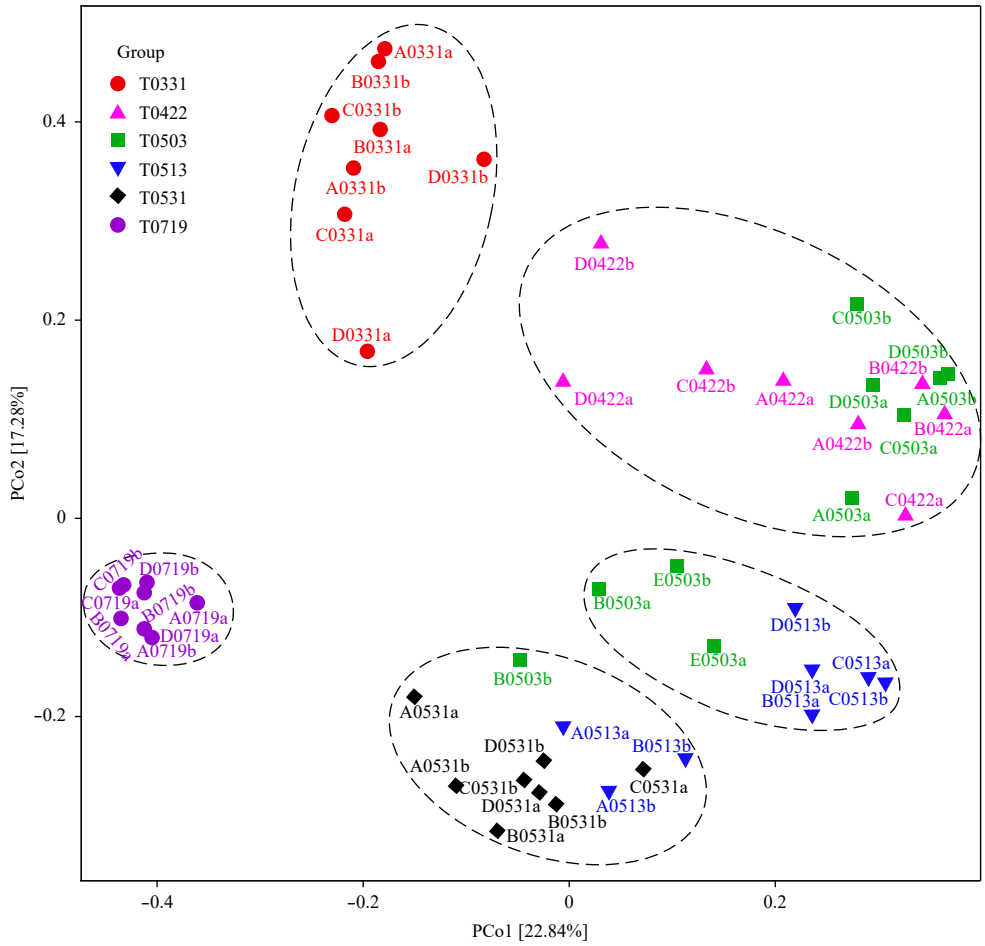

Fig. 4. Principal coordinates analysis (PCoA) plot on the Bray-Curtis distance matrix and depicting patterns of beta diversity for dinoflagellate communities of all samples. Different broken circles represent different clusters.

Gini-Simpson index (1-λ, indicating the probability that the two entities taken at random from a dataset of interest represent different species). It can be seen that all the number of OTUs, Chao1 index, Shannon-Wiener index, and Gini-Simpson index were negatively correlated with the cell density of *P. donghaiense* significantly (Table 3, Spearman's rho = –0.52, –0.67, –0.609, and –0.37, respectively; p<0.001). Because of the interactions of phytoplankton dynamics and ambient nutrients, the four indices were also significantly correlated with Chl *a*, NO_2^--N, NO_3^--N, TP, and TN, but not with PO_4^{3-}-P and NH_4^+-N (Table 3).

3.4 *Dominant dinoflagellate groups varied among pre-, during and post-blooms of P. donghaiense*

Metagenomic analysis revealed changes in the abundance of OTUs classifiable to various taxonomic levels, including shifts in dominant genera and species on date basis. The top 20 most abundant genera and species of each sample showed that 26 of the 50 samples were dominated by *Prorocentrum* (76.6%–99.6% of the top 20), while during the before-blooming period, the dinoflagellate community was dominated by *Heterocapsa_rotundata* (4.9%–79.6% dominance) that could not be well identified to any currently accepted genus of dinoflagellates (Fig. 3). All samples taken on April 22, May 3, and May 13 except for A0513a and A0513b were from blooming area and dominated by *P. donghaiense*. The samples of A0513a and A0513b were from non-blooming area and dominated by *Levanderina fissa*. After the blooming period, all samples taken on July 19 were dominated by *L. fissa* for most of the samples (25.0%–69.3% dominance; Fig. 3).

3.5 *Principal coordinates analysis (PCoA) and redundancy analysis (RDA)*

Principal coordinates analysis was conducted to evaluate similarities among different surface samples at the OTU level. The PCoA results for all samples showed that all samples formed roughly five clusters: the samples of March 31, the samples of July 19, samples were each formed a tight cluster distinctly separated from other samples, while the samples of April 22 and May 03 (except for B0503a, B0503b, E0503a and E0503b) as one, the samples of May 13 (plus samples B0503a, E0503a and E0503b, except for A0513a, A0513b and B0513b) formed one cluster and the samples of May 31 (plus samples A0513a, A0513b, B0513b and B0503b) formed one cluster, respectively (Fig. 4), corresponding to the periods of before bloom (March 31), early bloom (April 22), bloom (May 3 and 13), and postal bloom (May 31 and July 19) of *P. donghaiense*. The samples that made the clusters expanded (i.e., part of the samples taken on April 22 and May 13) represented transitions of the blooming period. The location of samples B0503b and B0513b might be caused by experimental error or the duplicated samples differing greatly. The cluster of March 31 (plus samples D0422a and D0422b) represented transitions between before bloom and early bloom, while the cluster of May 31 (plus samples A0513a and A0513b) represented transitions

between bloom and postal bloom. That the samples from 0422, 0503, 0513 and 0531 were not completely separated into three clusters (i.e., somehow mixed) represented transitions of different stages of blooms.

The results of RDA showed that the dinoflagellate community was regulated by multiple environmental variables (Fig. 5). The first axis of RDA explained 42.5% of the variation of species-environment relation, while the two axes together explained 66.3% of variation (p=0.001). *P. donghaiense* abundance, salinity, SiO_3^{2-} and NO_3^--N appeared to be the four most significant factors affecting the dinoflagellate community, compared to other factors (T, TN, TP, NO_2^--N, NH_4^+-N, PO_4^{3-}-P), and among those factors, *P. donghaiense* abundance made the greatest contribution. RDA analysis also showed that the environmental variables affected the population dynamics of some dinoflagellate species as well as *P. donghaiense* abundance. For example, *H. rotundata* and *Karlodinium veneficum* were positively correlated with NO_3^--N and PO_4^{3-}-P, while *P. triestinum* and *Katodinium glaucum* were positively correlated with TN and TP (Fig. 5).

4 Discussion

4.1 *Prorocentrum donghaiense blooms affected the bio-diversity of dinoflagellate community*

This study demonstrated that the bloom of *P. donghaiense* affected the structure of dinoflagellate sub-community of the total phytoplankton in terms of reducing the species richness and diversity estimators, as expressed in the number of OTUs, Chao1 index, Shannon index, and Gini-Simpson index. As seen from the PCoA analysis, the dinoflagellate community during the blooming period differed significantly from those before and after blooming periods. The species composition of dinoflagellate community changed with transition stages of the *P. donghaiense* bloom. For instance, the dinoflagellate community was dominated by a species that has not been well described ("uncultured dinoflagellate"), *P. donghaiense*, and *L. fissa* for the periods of before, during, and after blooming, respectively. RDA analysis revealed that *P. donghaiense* abundance affected the dinoflagellate community as the most important factor. These results well supported our hypothesis that *P. donghaiense* bloom would reduce the diversity of dinoflagellate community and alter the community structure.

Investigations on the effect of HABs on species diversity and community succession have been comparatively rare, particularly so for that using high throughput metagenomic approach. In an early study, West et al. (1996) investigated abundance and composition of phytoplankton populations during different bloom stages of *Gymnodinium breve* (=*Karenia brevis*), and found that total phytoplankton abundance increased regardless of *G. breve* abundance. Further, they discovered that the cell densities of some groups increased but others decreased, which is in contrast to our results, possibly because *K. brevis* bloom was not monospecific bloom. Besides, about 127 phytoplankton species were identified microscopically from all water samples (West et al., 1996), which was a relatively low number in comparison to our work targeting on dinoflagellates only. However, a very recent study, using high-throughput pyrosequencing approach also but targeting on a broader spectrum of microorganisms, demonstrated that microbial community structure is strongly linked to the bloom progression of *Alexandrium catenella* (Zhou et al., 2018). Multiple aspects of this study are consistent to our results presented above, such as that a decrease in diversity of the entire community of plankton during the bloom of *A. catenella* and reflects complex interactions among taxa comprising the phycosphere environment. An early study on freshwater and brackish water ecosystems has demonstrated that the diversity of

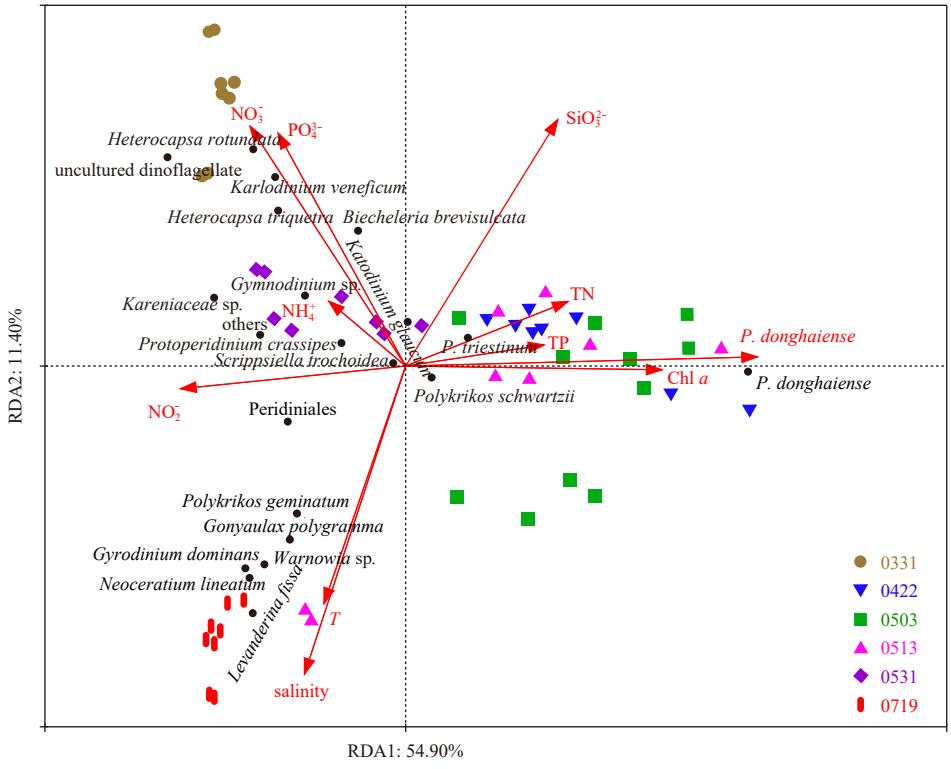

Fig. 5. Redundancy analysis (RDA) biplot for the relationship between dinoflagellate community and environmental variables.

phytoplankton communities is the best predictor for resource use efficiency (e.g., nutrients) of phytoplankton and factors reducing phytoplankton diversity may have direct detrimental effects on the amount and predictability of aquatic primary production (Ptacnik et al., 2008). While environmental variables such as temperature, turbulence, and nutrient levels are generally the primary forces shaping the community structure and driving HABs (see the discussion below), a bloom can be a vital driving force by its own for the transition of phytoplankton community structure due to the biological features of the blooming species. For example, most of HABs-causing species have been demonstrated to be allelopathic to other co-occurring phytoplankton species via releasing allelochemicals (Felpeto et al., 2018; Leão et al., 2009; Leflaive and Ten-Hage, 2007). A blooming species generally can squeeze the living space of other species via fast growth, which will consequently reduce the nutrient and space availability to competitors.

4.2 *Effects of environmental variables on the dinoflagellate community*

Our RDA results showed that *P. donghaiense* abundance, NO_3^--N, and SiO_3^{2-} were the three most important environmental factors affecting the dinoflagellate community. *Prorocentrum donghaiense* abundance was correlated negatively to NO_3^--N, NO_2^--N, PO_4^{3-}-P, NH_4^+-N, temperature and salinity, but positively to TN, TP, Chl *a* and SiO_3^{2-}. Although dinoflagellates do not need SiO_3^{2-} for growth, the RDA results showed SiO_3^{2-} appeared to be one of those important factors in shaping the dinoflagellate community, which might be indirectly caused via the effects of SiO_3^{2-} on the transition of diatom community during the sampling period. The ratio of DIN to DIP tended to decrease along with the development and maintenance of bloom, and increase along with disappearance of bloom. At the beginning of the survey (March 31), the cell density of *P. donghaiense* was comparatively low (270 cells/mL), and the DIN to DIP ratio was 18–22, which was more suitable for the growth of *P. donghaiense* (Li et al., 2009), while, during the blooming period of *P. donghaiense*, the ratio showed a downward trend in general, possibly due to the different absorption rates for different nutrients by the bloom-forming organism (Zhang et al., 2008). This trend indicates a faster absorption rate of DIN by *P. donghaiense* and consequently a larger effect of DIN on the growth of *P. donghaiense,* compared to PO_4^{3-}-P. On May 13, the ratio reached the minimum, indicating a limiting level of DIN to the *P. donghaiense* growth (Li et al., 2014; Zhang et al., 2008). Supportively, it was observed there were significant negative correlations between TP and the four diversity indices (the number of OTUs, Shannon index, Gini-Simpson index, and Chao1 index), indicating that TP also stimulated the growth or bloom of *P. donghaiense*. However, PO_4^{3-} did not exhibit a significant correlation with these four diversity indices, indicating the utilization or uptake of P by *P. donghaiens*e was not linearly correlated with the ambient concentration of PO_4^{3-}-P. Our RDA analysis revealed that, in addition to nutrients, temperature and salinity also made contributions to the transition of the dinoflagellate community, which is somehow in contrast to the recent result of Zhou et al. (2018) where temperature and salinity were two key environmental factors associated with changes in bacterial and archaeal community structure but not with variations in eukaryotic community. While it is well understandable that temperature acted as an important factor, the apparent correlation between salinity and *P. donghaiense* and the dinoflagellate community might be a good indication of nutrient input from freshwater runoff.

In summary, our investigation observed that the bloom of *P. donghaiense* negatively affected bio-diversity in the dinoflagellate sub-community level both in reducing the species richness (as expressed in the number of OTUs and Chao1 index) and diversity indices (Shannon index and Gini-Simpson index). PCoA results showed that the dinoflagellate community during the blooming period of *P. donghaiense* differed significantly from the community before and after the blooming period. RDA analyses indicated that *P. donghaiense* abundance was the most important factor affecting the dinoflagellate community, which strongly indicates that the bloom of *P. donghaiense* played a vital role in shaping the dinoflagellate community structure, possibly via processes such as allelopathy (Ens et al., 2009; Leão et al., 2012), nutrient and space competition, and fast growth itself. Although these results are not beyond our anticipation, we believe the present work provides meaningful and solid evidence for the negative effects of HABs on the plankton community and coastal ecosystem based on a comprehensive series of field sampling and high throughput pyrosequencing.

References

Anderson D M, Cembella A D, Hallegraeff G M. 2012. Progress in understanding harmful algal blooms: paradigm shifts and new technologies for research, monitoring, and management. Annual Review of Marine Science, 4: 143–176, doi: 10.1146/annurev-marine-120308-081121

Anderson D M, Glibert P M, Burkholder J M. 2002. Harmful algal blooms and eutrophication: nutrient sources, composition, and consequences. Estuaries, 25: 704–726, doi: 10.1007/BF02804901

Aranda M, Li Y, Liew Y J, et al. 2016. Genomes of coral dinoflagellate symbionts highlight evolutionary adaptations conducive to a symbiotic lifestyle. Scientific Reports, 6: 39734, doi: 10.1038/srep39734

Burkholder J M, Azanza R V, Sako Y. 2006. The ecology of harmful dinoflagellates. In: Granéli E, Turner J T, eds. Ecology of Harmful Algae. Berlin, Heidelberg: Springer, 53–66

Chai Zhaoyang, He Zhili, Deng Yunyan, et al. 2018. Cultivation of seaweed *Gracilaria lemaneiformis* enhanced biodiversity in a eukaryotic plankton community as revealed via metagenomic analyses. Molecular Ecology, 27(4): 1081–1093, doi: 10.1111/mec.14496

Chai Zhaoyang, Wang Huan, Deng Yunyan, et al. 2020. Harmful algal blooms significantly reduce the resource use efficiency in a coastal plankton community. Science of The Total Environment, 704: 135381, doi: 10.1016/j.scitotenv.2019.135381

Cui Lei, Lu Xinxin, Dong Yuelei, et al. 2018. Relationship between phytoplankton community succession and environmental parameters in Qinhuangdao coastal areas, China: a region with recurrent brown tide outbreaks. Ecotoxicology and Environmental Safety, 159: 85–93, doi: 10.1016/j.ecoenv.2018.04.043

Ens E J, French K, Bremner J B. 2009. Evidence for allelopathy as a mechanism of community composition change by an invasive exotic shrub, *Chrysanthemoides monilifera* spp. *rotundata*. Plant and Soil, 316(1–2): 125–137, doi: 10.1007/s11104-008-9765-3

Felpeto A B, Roy S, Vasconcelos V M. 2018. Allelopathy prevents competitive exclusion and promotes phytoplankton biodiversity. Oikos, 127(1): 85–98, doi: 10.1111/oik.04046

Huse S M, Dethlefsen L, Huber J A, et al. 2008. Exploring microbial diversity and taxonomy using SSU rRNA hypervariable tag sequencing. PLoS Genetics, 4(11): e1000255, doi: 10.1371/journal.pgen.1000255

JOGFS International Project Office. 1994. JGOFS report No. 19. protocols for the Joint Global Ocean Flux Studies (JGOFS) core measurements. Bergen, Norway: JGOFS International Project Office, Center for Studies of Environment and Resources

Jonsson P R, Pavia H, Toth G. 2009. Formation of harmful algal

blooms cannot be explained by allelopathic interactions. Proceedings of the National Academy of Sciences of the United States of America, 106(27): 11177–11182, doi: 10.1073/pnas.0900964106

Landsberg J H. 2002. The effects of harmful algal blooms on aquatic organisms. Reviews in Fisheries Science, 10(2): 113–390, doi: 10.1080/20026491051695

Leão P N, Ramos V, Vale M, et al. 2012. Microbial community changes elicited by exposure to cyanobacterial allelochemicals. Microbial Ecology, 63(1): 85–95, doi: 10.1007/s00248-011-9939-z

Leão P N, Vasconcelos M T S D, Vasconcelos V M. 2009. Allelopathy in freshwater cyanobacteria. Critical Reviews in Microbiology, 35(4): 271–282, doi: 10.3109/10408410902823705

Leflaive J, Ten-Hage L. 2007. Algal and cyanobacterial secondary metabolites in freshwaters: a comparison of allelopathic compounds and toxins. Freshwater Biology, 52(2): 199–214, doi: 10.1111/j.1365-2427.2006.01689.x

Legendre P, Oksanen J, ter Braak C J F. 2011. Testing the significance of canonical axes in redundancy analysis. Methods in Ecology and Evolution, 2(3): 269–277, doi: 10.1111/j.2041-210X.2010.00078.x

Li Hongmei, Tang Hongjie, Shi Xiaoyong, et al. 2014. Increased nutrient loads from the Changjiang (Yangtze) River have led to increased Harmful Algal Blooms. Harmful Algae, 39: 92–101, doi: 10.1016/j.hal.2014.07.002

Li Ji, Glibert P M, Zhou Mingjiang, et al. 2009. Relationships between nitrogen and phosphorus forms and ratios and the development of dinoflagellate blooms in the East China Sea. Marine Ecology Progress Series, 383: 11–26, doi: 10.3354/meps07975

Lin Senjie, Cheng Shifeng, Song Bo, et al. 2015. The *Symbiodinium kawagutii* genome illuminates dinoflagellate gene expression and coral symbiosis. Science, 350(6261): 691–694, doi: 10.1126/science.aad0408

Lin Jianing, Yan Tian, Zhang Qingchun, et al. 2014. *In situ* detrimental impacts of *Prorocentrum donghaiense* blooms on zooplankton in the East China Sea. Marine Pollution Bulletin, 88(1–2): 302–310, doi: 10.1016/j.marpolbul.2014.08.026

Lu Douding, Goebel J, Qi Yuzao, et al. 2005. Morphological and genetic study of *Prorocentrum donghaiense* Lu from the East China Sea, and comparison with some related *Prorocentrum* species. Harmful Algae, 4(3): 493–505, doi: 10.1016/j.hal.2004.08.015

Miao Yu, Wang Zhu, Liao Runhua, et al. 2017. Assessment of phenol effect on microbial community structure and function in an anaerobic denitrifying process treating high concentration nitrate wastewater. Chemical Engineering Journal, 330: 757–763, doi: 10.1016/j.cej.2017.08.011

Parsons T R, Maita Y, Lalli C M. 1984. A Manual of Chemical & Biological Methods for Seawater Analysis. Oxford: Pergamon Press, 423–453

Ptacnik R, Solimini A G, Andersen T, et al. 2008. Diversity predicts stability and resource use efficiency in natural phytoplankton communities. Proceedings of the National Academy of Sciences of the United States of America, 105(13): 5134–5138, doi: 10.1073/pnas.0708328105

Rozen S, Skaletsky H. 2000. Primer3 on the WWW for general users and for biologist programmers. In: Misener S, Krawetz S A, eds. Bioinformatics Methods and Protocols. Totowa: Humana Press, 365-386

Schneider A R, Gommeaux M, Duclercq J, et al. 2017. Response of bacterial communities to Pb smelter pollution in contrasting soils. Science of the Total Environment, 605-606: 436–444, doi: 10.1016/j.scitotenv.2017.06.159

Smayda T J. 1990. Novel and nuisance phytoplankton blooms in the sea: evidence for a global epidemic. In: Granéli E, Sundström B, Edler L, et al., eds. Toxic Marine Phytoplankton. New York, USA: Elsevier, 29–40

Smayda T J. 1997. Harmful algal blooms: their ecophysiology and general relevance to phytoplankton blooms in the sea. Limnology and Oceanography, 42: 1137–1153, doi: 10.4319/lo.1997.42.5_part_2.1137

State Oceanic Administration. 2001–2015. Bulletin of marine disaster of China (in Chinese). http://www.mnr.gov.cn/sj/sjfw/hy/gbgg/zghyzhgb [2019-12-03/2020-02-24]

Sun Zhen, Li Guoping, Wang Chengwei, et al. 2014. Community dynamics of prokaryotic and eukaryotic microbes in an estuary reservoir. Scientific Reports, 4: 6966

Sunagawa S, Coelho L P, Chaffron S, et al. 2015. Structure and function of the global ocean microbiome. Science, 348(6237): 1261359, doi: 10.1126/science.1261359

Valderrama J C. 1981. The simultaneous analysis of total nitrogen and total phosphorus in natural waters. Marine Chemistry, 10(2): 109–122, doi: 10.1016/0304-4203(81)90027-X

Vaulot D, Eikrem W, Viprey M, et al. 2008. The diversity of small eukaryotic phytoplankton (≤3 μm) in marine ecosystems. FEMS Microbiology Reviews, 32(5): 795–820, doi: 10.1111/j.1574-6976.2008.00121.x

West T L, Marshall H G, Tester P A. 1996. Natural phytoplankton community responses to a bloom of the toxic dinoflagellate *Gymnodinium breve Davis* off the North Carolina coast. Castanea, 61(4): 356–368

Xu Ning, Duan Shunshan, Li Aifen, et al. 2010. Effects of temperature, salinity and irradiance on the growth of the harmful dinoflagellate *Prorocentrum donghaiense* Lu. Harmful Algae, 9(1): 13–17, doi: 10.1016/j.hal.2009.06.002

Xu Xin, Yu Zhiming, Cheng Fangjin, et al. 2017. Molecular diversity and ecological characteristics of the eukaryotic phytoplankton community in the coastal waters of the Bohai Sea, China. Harmful Algae, 61: 13–22, doi: 10.1016/j.hal.2016.11.005

Yao Weiming, Li Chao, Gao Junzhang. 2006. Red tide plankton along the south coastal area in Zhejiang province. Marine Science Bulletin (in Chinese), 25(3): 87–91

Zhang Chuansong, Wang Jiangtao, Zhu Dedi, et al. 2008. The preliminary analysis of nutrients in harmful algal blooms in the East China Sea in the spring and summer of 2005. Haiyang Xuebao (in Chinese), 30(3): 153–159

Zhou Jin, Richlen M L, Sehein T R, et al. 2018. Microbial community structure and associations during a marine dinoflagellate bloom. Frontiers in Microbiology, 9: 1201, doi: 10.3389/fmicb.2018.01201

Supplementary information:

Table S1. Biological and abiotic variables in different phases of the bloom series (mean±SD).

Table S2. Number of reads and OTUs during the analysis process in the dinoflagellate community.

The supplementary information is available online at https://doi.org/10.1007/s13131-020-1585-1. The supplementary information is published as submitted, without typesetting or editing. The responsibility for scientific accuracy and content remains entirely with the authors.

Acta Oceanol. Sin., 2020, Vol. 39, No. 4, P. 120–126
https://doi.org/10.1007/s13131-019-1467-z
http://www.hyxb.org.cn
E-mail: hyxbe@263.net

Protoraphis Simonsen, a newly recorded marine epizoic diatom genus for China

Lang Li[1], Changping Chen[1, 2*], Lin Sun[3], Jiawei Zhang[1], Junrong Liang[1, 2], Yahui Gao[1, 2, 3*]

[1] School of Life Sciences, Xiamen University, Xiamen 361102, China

[2] Key Laboratory of Ministry of Education for Coastal and Wetland Ecosystems, Xiamen University, Xiamen 361102, China

[3] State Key Laboratory of Marine Environmental Science, Xiamen University, Xiamen 361102, China

Received 16 December 2018; accepted 22 April 2019

Abstract

Epizoic diatoms on marine copepods are common in nature and may have a special ecological relationship with their hosts. However, this special ecological group is not well known, and it has only rarely been studied in the China seas. To address this knowledge gap, the species diversity and classification of epizoic diatoms on planktonic copepods were studied with samples collected from the East China Sea. In the present study, a marine araphid diatom genus *Protoraphis* and its type species, *Pr. hustedtiana*, were observed and identified by light and electron microscopy, thus representing the first record of this genus and its type species in China. This genus is characterized by a median sternum strongly bent to opposite sides and terminate in two transapical grooves at the valve ends. *Protoraphis hustedtiana* was found to be epizoic on the posterior body appendages and segments of the marine calanoid copepod *Candacia bradyi*. An internal view shows a complex, ear-shaped process that is close to the apical slit field. The ecological habitats and geographical distributions of *Protoraphis* were also discussed, and, together with complementary morphological studies, our results have increased the number of records for marine epizoic diatoms to three genera with three species in China, including *Pseudohimantidium* and *Pseudofalcula*.

Key words: marine epizoic diatom, copepod, *Protoraphis*, newly recorded genus, ear-shaped process

Citation: Li Lang, Chen Changping, Sun Lin, Zhang Jiawei, Liang Junrong, Gao Yahui. 2020. *Protoraphis* Simonsen, a newly recorded marine epizoic diatom genus for China. Acta Oceanologica Sinica, 39(4): 120–126, doi: 10.1007/s13131-019-1467-z

1 Introduction

In the last few years, the term "epizoic diatom" has been prominent in the taxonomy of marine diatoms, and many articles on this special diatom group have been continuously published (Sar and Sunesen, 2014; Li et al., 2014; Majewska et al., 2017; Frankovich et al., 2018). Most of these studies were carried out on the carapace or neck skin of sea turtles and the exoskeleton of marine copepods (Fernandes and Calixto-Feres, 2012; Donadel and Torgan, 2016; Gárate-Lizárraga and Esqueda-Escárcega, 2018). According to their results, it seemed that epizoic diatoms occurred with greater abundance on vertebrates compared to invertebrates and that distinct differences existed in the morphology of epizoic diatoms on different hosts (Riaux-Gobin et al., 2017a, b). Numerous new diatom taxa, such as species of *Tursiocola* Holmes, Nagasawa & Takano, *Tripterion* Holmes, Nagasawa & Takano, *Chelonicola* Majewska, De Stefano & Van de Vijver, *Poulinea* Majewska, De Stefano & Van de Vijver and *Medlinella* Frankovich, Ashworth & Sullivan, were described from marine turtles and manatees (Frankovich et al., 2015; Majewska et al., 2015; Frankovich et al., 2016; Riaux-Gobin et al., 2017a, b; Frankovich et al., 2018). In contrast, after Hiromi et al. (1985) and Hallegraeff and McWilliam (1990) recognized only six araphid diatom taxa (*Pseudohimantidium pacificum* Hustedt & Krasske, *Falcula hyalina* Takano, *Protoraphis altantica* Gibson, *Pr. hustedtiana* var. *hustedtiana* Simonsen, *Sceptronema orientale* Takano, and *Licmophora unidenticulata* Takano) as epizoic diatoms on marine copepods, no new species or varieties specific to copepods have been reported.

All the araphid diatoms epizoic on marine copepods are highly distinctive, and most are either monotypic or species-poor genera. For example, both *Protoraphis* Simonsen and *Pseudohimantidium* Hustedt & Krasske have clearly visible sigmoid sternum and polar grooves under light microscopy (LM), but they can be easily distinguished by shapes (Simonsen, 1970). *Falcula hyalina*, which was transferred into the new genus *Pseudofalcula* Gómez, Wang & Lin in Gómez et al. (2018), shows two plate-like chloroplasts and arcuate valve views (Li et al., 2014). Although *Pseudohimantidium pacificum* possesses a sickle-like valve, it can be separated from *Pseudofalcula hyalina* (Takano) Gómez, Wang & Lin by its rostrate apices and stalk-forming colony (Rivera et al., 1986; Fernandes and Calixto-Feres, 2012).

Apart from *Pseudohimantidium pacificum* documented sixty years ago and *Pseudofalcula hyalina* found in the mariculture and mangrove waters, only sparse research on epizoic diatoms has been carried out in China (Voigt, 1959; Li et al., 2014). The present study describes a newly recorded epizoic diatom genus, *Protoraphis*, represented by *Pr. hustedtiana* var. *hustedtiana* epizoic on *Candacia bradyi* Scott collected from the East China Sea

Foundation item: The National Key Research and Development Program of China under contract No. 2016YFA0601302; the National Natural Science Foundation of China under contract Nos 41876146 and 41476116.
*Corresponding author, E-mail: chencp@xmu.edu.cn; gaoyh@xmu.edu.cn

during a survey cruise in the autumn of 2016. Morphology and ultrastructure were examined by light and scanning electron microscopy. Biogeography and ecology of *Protoraphis* taxa were also briefly described.

2 Materials and methods

2.1 *Sampling*

Copepods in this study were collected on October 1, 2016 by a standard zooplankton net (diameter 80 cm, mesh 505 μm) hauled vertically from the open waters in the East China Sea (26°23′58.194″N, 121°27′06.39″E) at a depth of 79 m. Samples were collected from the bottom of the net and immediately preserved in 5% seawater formalin. The East China Sea is located in the western North Pacific between China and Okinawa in the Ryukyu Arc. It is one of the largest continental shelf seas in the world (Jiao et al., 2005; Takayanagi et al., 2006). The area is about 7.5×10^5 km^2, and the average depth is 349 m (Takayanagi et al., 2006). Three main water systems exist in the East China Sea: fresh water input from the Changjiang (Yangtze) River in the west, the Kuroshio Current in the east, and the mixing water system between them (Jiao et al., 2005). Along the shelf, picoplankton and nanoplankton are very common, and the abundance of diatoms depends on the thickness of the mixed surface layer (Takayanagi et al., 2006).

2.2 *Methods*

Copepods with epizoic diatoms were examined under an inverted microscope (Olympus CKX41, Japan) and then transferred into a tube with Pasteur pipettes. Epizoic diatoms were removed from the infested copepods by ultrasound at 300 W for 25 s, acidized with HCl (36%–38%) at 100°C for 20 min to eliminate organic matter, and then rinsed with distilled water eight to ten times. Cleaned material was mounted on slides and coverslips for LM (Olympus BX51, Japan) and SEM (JEOL JSM-6390LV, Japan) observations, respectively. LM micrographs were taken by a digital camera (Olympus DP71, Japan). Permanent slides were made with Naphrax® and deposited in the School of Life Sciences, Xiamen University, China.

Diatom morphological terminology, as presented in Simonsen (1970), Hallegraeff and McWilliam (1990), Sullivan (1993) and Witkowski et al. (2000), was respectively referenced.

3 Results

Based on our observations and reports in the literature (Simonsen, 1970; Hallegraeff and McWilliam, 1990), the diatom of interest among our specimens was identified as *Pr. hustedtiana* var. *hustedtiana*, which was epizoic on the planktonic copepod *C. bradyi* collected from the East China Sea. This is the first record of the genus *Protoraphis* for China. Generic and specific descriptions follow.

3.1 *Protoraphis* Simonsen

Simonsen, 1970, p. 383–394, pl. 1; Gibson, 1979a, p. 109–126, Figs 1–18; Hallegraeff and McWilliam, 1990, p. 39–45, Figs 1–13; Sullivan, 1993, p. 161–167, Figs 1–8; Witkowski et al., 2000, p. 74, 75, pl. 26, Fig. 15, pl. 29, Figs 1–3.

3.1.1 *Description*

Cells attached to the hosts with mucilaginous stalks (Figs 1a–d). Chloroplasts two or four, large, positioned near the middle of the cell (Fig. 1d). Valves clavate to lanceolate, with broadly rounded apices (Figs 1d–f). Sternum narrow, but conspicuous, straight and median in the middle of the valve, abruptly bent to opposite sides at the ends, terminating in two polar grooves (Figs 1e, f). Transverse striae parallel, composed of rounded, elliptical or rectangular areolae, interrupted by the sternum (Figs 2a, b, e). Apical groove surrounded by a hyaline zone, penetrating the frustule, forming a siliceous rim (basis) and protruding as a series of specific structures internally (Figs 2b–d and 3b–d). Apical slit fields starting on the valve face and going down the mantle with unequal vertical openings (Figs 2a–d). Girdle bands several to numerous, perforated by two rows of rounded or elongate pores per band (Fig. 2f).

3.1.2 *Ecology*

Protoraphis was established by Simonsen in 1970. Up to now, only two species and one variety have been reported. All taxa inhabit marine environments and most of them are epizoic on copepods, snails or the second stage larva of a barnacle, the Cypris (Foged, 1984; Sullivan, 1993; Gómez et al., 2018).

3.2 *Protoraphis hustedtiana* var. *hustedtiana* Simonsen

Simonsen, 1970, p. 383–394, pl. 1; Hallegraeff and McWilliam, 1990, p. 39–45, Figs 1–13; Witkowski et al., 2000, p. 75, pl. 29, Figs 1 and 2; Guiry and Guiry, 2018.

3.2.1 *Description*

Chloroplasts four, large, positioned close to the middle of the cell (Figs 1b–d). Frustules in girdle view rectangular to slightly inflexed (Fig. 1d). Valves lanceolate, diagonally symmetrical, with broadly rounded apices (Figs 1d–f and 2a). Apical axis 45–129 μm, transapical axis 4–10 μm. Striae uniseriate, composed of rounded areolae (Figs 2a–e). Transverse rows 31 in 10 μm, longitudinal rows 3–4 in 1 μm. Sternum distinct, linear, lying in the median position for almost its entire length, bent to opposite sides at the apices (Figs 1e, 1f and 2a–d). A total of 12–16 vertical openings present in the apical slit fields (Figs 2b–d). A groove (1.1–1.7 μm long) penetrating the valve located in the hyaline zone at the end of sternum, exposing a siliceous structure concave to the valve pole (Figs 2a–d). Internally, margin of groove thickened and developed as an ear-shaped basis (1.3–2 μm long), with a large E-shaped lip protruding from the distal side and a small lamelliform or U-shaped lip projecting from the opposite side (Figs 3b–d). Transapical striae slightly depressed between weakly developed virgae (Fig. 3e). Girdle bands open, with two rows of rounded pores (Fig. 2f).

3.2.2 *Ecology*

In our material, *Pr. hustedtiana* var. *hustedtiana* attached to the hosts with unbranched mucilaginous stalks. They usually occurred as solitary cells or formed short chains by apex-to-apex. It seemed that this taxon preferred to infect the posterior body appendages and segments of the calanoid copepods. All three host copepods in our study were males. Hallegraeff and McWilliam (1990) also reported that the diatom taxon was only epizoic on male calanoid copepods (*C. discaudata* Scott).

3.2.3 *Distribution*

The diatom species *Pr. hustedtiana* was first found in the Arabian Sea and Persian Gulf by Simonsen in 1970. Hallegraeff and McWilliam (1990) recorded *Pr. hustedtiana*, which was recognized as var. *hustedtiana* in Sullivan (1993), from coastal waters of northwestern Australia. Our copepods infested with diatoms were sampled from open waters in the East China Sea.

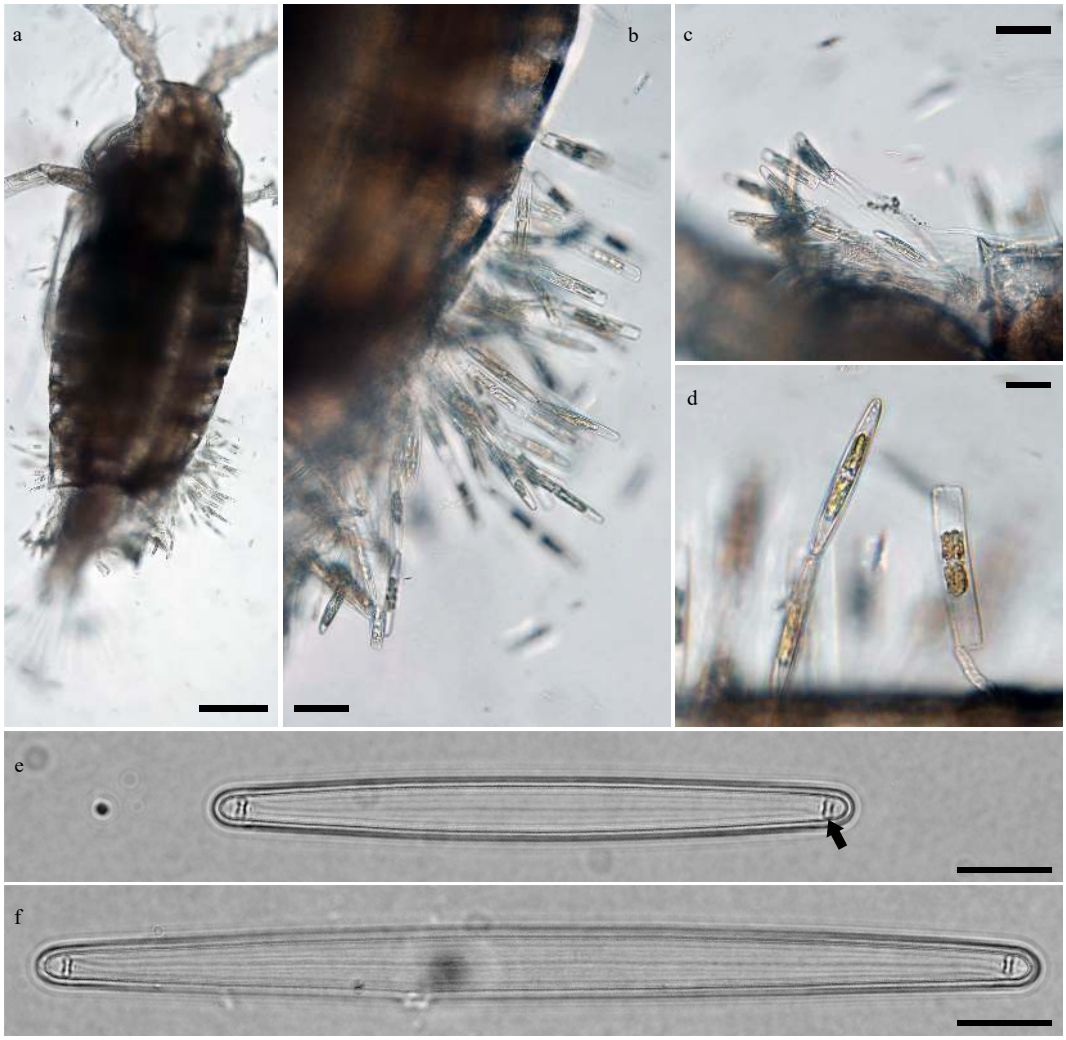

Fig. 1. *Protoraphis hustedtiana* var. *hustedtiana* Simonsen. LM. a–c. Living colonies on *Candacia bradyi* Scott; d. cells with chloroplasts, one showing girdle view; and e and f. cleaned frustules showing sternum and polar grooves (arrow). Scale bars: 200 μm (a), 50 μm (b, c); 20 μm (d), and 10 μm (e, f).

4 Discussion

Protoraphis is a distinct araphid diatom genus characterized by its linear valve, sigmoid sternum and transapical grooves at the valve ends. Its type species, *Pr. hustedtiana*, was first described in Simonsen (1970). After that, Gibson (1979a) reported a new species, *Pr. atlantica*, from the northwestern Atlantic Ocean. In addition, a variety, *Pr. hustedtiana* var. *nana* Takano, was reported from the northwestern Pacific Ocean (Takano, 1985). Results showed that its transapical groove was shorter than that in the nominate variety and that an internal Y-shaped process was positioned at the groove. The fine structure of *Pr. hustedtiana* var. *hustedtiana* was first revealed by Hallegraeff and McWilliam (1990). Considering that the ear-shaped processes located near the apices were complex and specific, the authors hypothesized that the raphe system in raphid diatoms and the grooves in *Pr. hustedtiana* var. *hustedtiana* were homologous. *Pseudohimantidium* also displays similar sternum and grooves, but it can be easily distinguished by its scythe-shaped valve and series of rimoportulae at each apex of the valve (Simonsen, 1970; Rivera et al., 1986). Based on these facts, the two genera were merged into the family Protoraphidaceae by Simonsen (1970). So far, although the significance of the groove has not been confirmed, most studies have recognized that the mucilaginous stalks in Protoraphidaceae taxa are not secreted by this structure (Gibson, 1979a, b; Sullivan, 1993).

Protoraphis has some morphological similarities with *Neosynedra* Williams & Round, *Cyclophora* Castracane and *Lucanicum* Lobban & Ashworth (Table 1). All of these diatoms share somewhat lanceolate or linear valve outlines and structureless valves when observed with light microscope. Since an apical slit field is one of their common features, several studies have reported on this feature, making respective comparisons among these genera (Round et al., 1990; Lobban and Ashworth, 2014; Gómez et al., 2018). The *Protoraphis* taxa differ mainly from *N. provincialis* (Grunow) Williams & Round by their grooves with complex labiate processes and uninterrupted apical slits (Table 1). *Cyclophora* is characterized by the central pseudosepta on the valves and the absence of polar grooves. The general shape of this genus is often constricted in the middle or below the apices (Ashworth et al., 2012). *Lucanicum* is a benthic genus with long chains, while *Protoraphis* can only form short chains or live in a solitary frustule. Like *Neosynedra* and *Cyclophora*, *Lucanicum* also bears a simple rimoportula near each apex (Table 1). The striae of *Lucanicum* are composed of transapically elongated macroareolae,

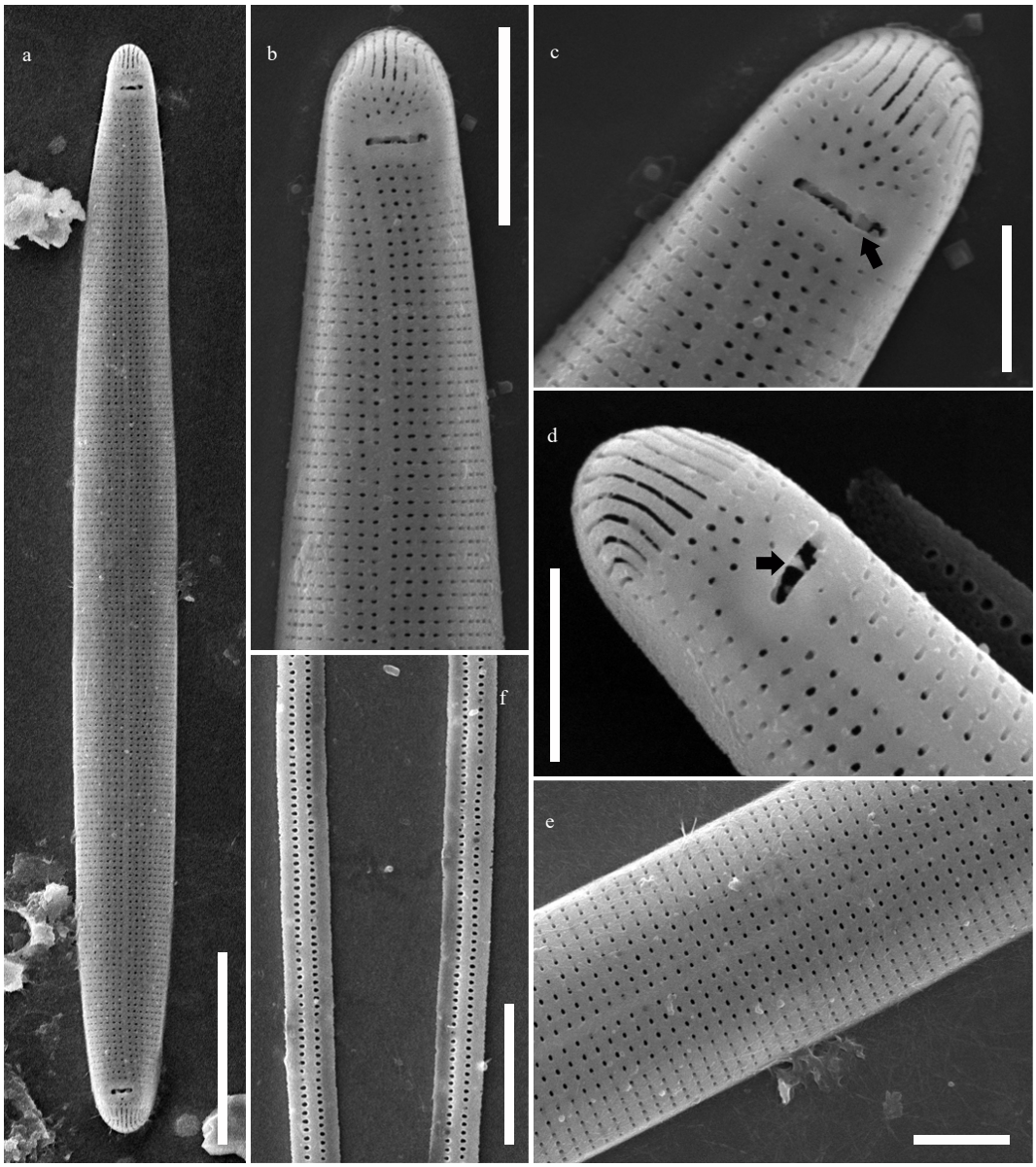

Fig. 2. *Protoraphis hustedtiana* var. *hustedtiana* Simonsen. SEM. a–e. External valve view: entire valve (a); valve ends showing apical slit fields and transapical grooves, note the siliceous structure concave to the valve pole (arrows) (b–d); mid-valve with uniseriate striae composed of rounded areolae (e). f. Detail of girdle bands. Scale bars: 10 μm (a), 5 μm (b, f), and 1 μm (c–e).

while areolae in *Protoraphis* are very small (Lobban and Ashworth, 2014). Consequently, critical features of these genera are apparent and easily to be recognized under light and electronic microscopy.

The dimensions and fine structures of the valves in our material are close to those in Hallegraeff and McWilliam (1990) (Table 2). But our SEM images revealed that the U-shaped lip combined with the groove can develop as a lamelliform structure with two spines (Fig. 3b). Compared to the complex ear-shaped labiate process in *Pr. hustedtiana* var. *hustedtiana*, a simpler Y-shaped protrusion presents in var. *nana* (Sullivan, 1993). Sullivan (1993) suggested that "all features of valve morphology appear to be identical" in the genus *Protoraphis*. In fact, some slight distinctions in valve morphology are present within the genus, except for the heteropolarity of *Pr. atlantica*. It is clear that the maximum valve lengths in both *Pr. hustedtiana* var. *nana* (57 μm) and *Pr. atlantica* (50 μm) are much shorter than valve length in *Pr. hustedtiana* var. *hustedtiana* (130 μm). According to Figs 4–8 in Sullivan (1993), the areolae in *Pr. hustedtiana* var. *nana*, which are similar to those in *Pr. atlantica*, seem to be elliptical or rectangular. However, *Pr. hustedtiana* var. *hustedtiana* only has small, rounded areolae based on our results (Figs 2b–e and 3b–e) and those of Hallegraeff and McWilliam (1990). Furthermore, both *Pr. hustedtiana* var. *nana* (Fig. 4 in Sullivan, 1993) and *Pr. atlantica* (Fig. 4 in Gibson, 1979a) have two rows of elongate pores on the girdle bands, while the bands of *Pr. hustedtiana* var. *hustedtiana* are pierced by two rows of rounded pores (Fig. 2f). Therefore, although no internal view of *Pr. hustedtiana* was shown in Gómez et al. (2018), the taxon seems rather to represent var. *nana* based on their description.

Up to now, *Protoraphis* has been reported from the Arabian and Persian Gulfs, the United States, Japan, Australia, the Carib-

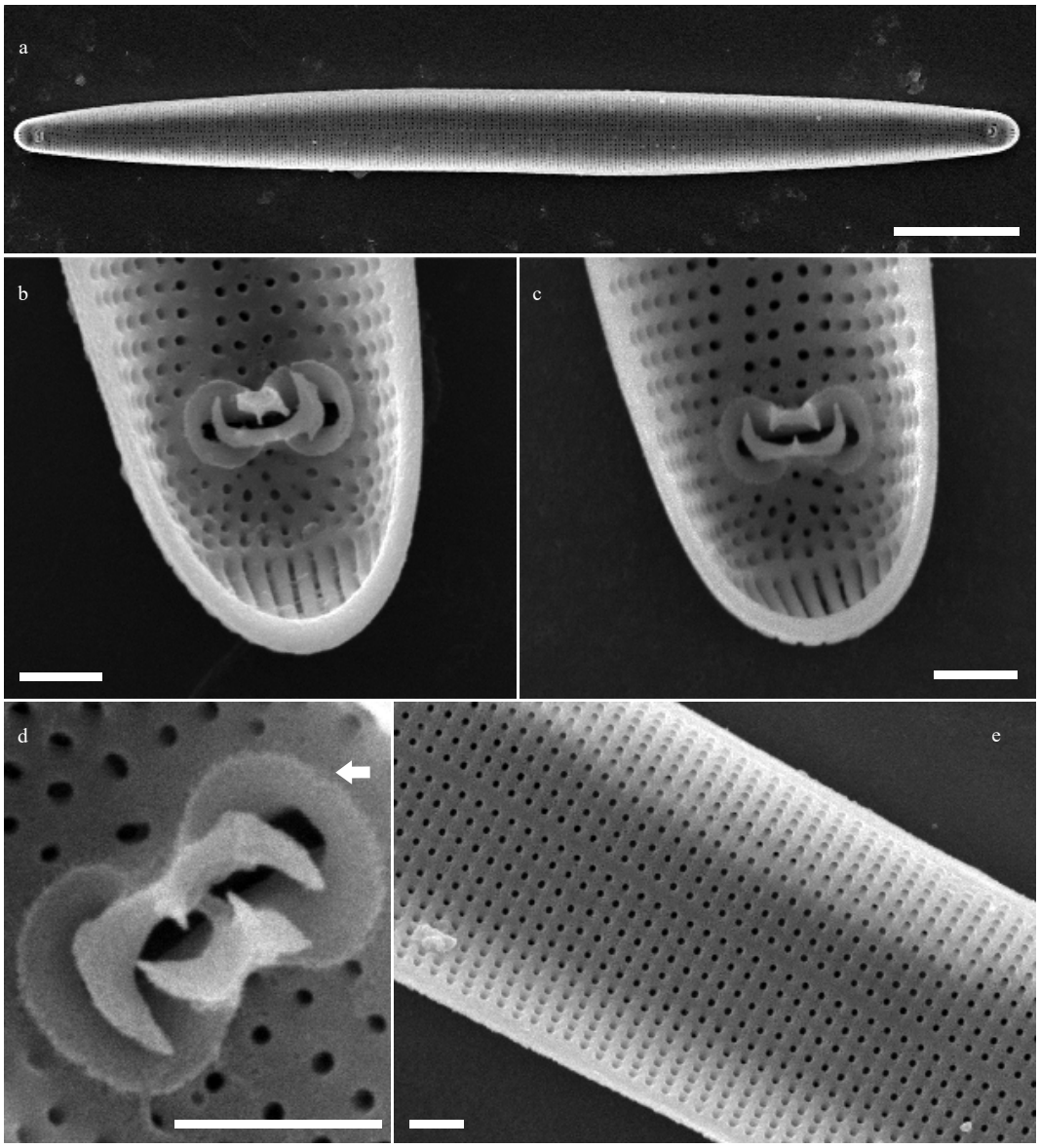

Fig. 3. *Protoraphis hustedtiana* var. *hustedtiana* Simonsen. SEM. Internal valve views. a. Entire valve; b–d. close up of ear-shaped processes located near the apices, and arrow indicating the basis; and e. close up of the valve middle, note the striae forming areolae depressed between the narrow viminae. Scale bars: 10 μm (a), 1 μm (b–e).

bean Sea, Brazil and the East China Sea (Simonsen, 1970; Gibson, 1979a; Foged, 1984; Takano, 1985; Hallegraeff and McWilliam, 1990; Sullivan, 1993; Witkowski et al., 2000; Gómez et al., 2018). This genus distributes mainly in the Indian Ocean, the West Atlantic Ocean and the North Pacific Ocean. Our result enlarges the global distribution of this genus and indicates that *Protoraphis* may be widespread in the world. In the present study, *Pr. hustedtiana* var. *hustedtiana* was observed on the posterior body appendages and segments of planktonic copepods, consistent with the results in Gibson (1979a) and Hallegraeff and McWilliam (1990). *Candacia* Dana seemed to be one of the most common copepod hosts for *Protoraphis*. The occurrence of *Protophis* taxa (except for *Pr. hustedtiana* var. *nana* and *Pr. hustedtiana* f. *latior* Foged) on specific body parts is probably related to the motion of planktonic copepods. As the main appendages for swimming, the first antennae of calanoid copepods are generally longer than those of harpacticoid families, and their strong swing may interfere with the attachment of epizoic diatoms to the anterior body appendages and segments. But harpacticoid copepods are mostly benthic and their first antennae are usually very short. The less swing range of first antennae may have no influence on the attachment diatoms. That may explain why *Pr. atlantica* can be found on the all body segments of harpacticoid copepods (Gibson, 1979a). In some ways, the infestation of *S. orientale* on the harpacticoid copepod *Euterpina acutifrons* Dana confirmed our inference of the first antennae (Skovgaard and Saiz, 2006; Sar and Sunesen, 2014). As for *Pseudofalcula hyalina*, which attaches itself to various parts of *Acartia* Dana by mucilaginous pads (Takano, 1983; Prasad et al., 1989), its smaller cell size and shorter extension may not interfere with movement of the first antennae. Gibson (1979a) insisted that the infestation of *Pr. atlantica* can be related to the mating behavior of copepod hosts. However, neither our observations nor those of Hallegraeff and McWilliam (1990) were based on finding *Pr. hustedtiana* var. *hus-*

Table 1. Comparison of *Protoraphis* with related genera

	Protoraphis 1, 2, 3, 4, 5, 6	*Pseudohimantidium* 7, 8, 9	*Neosynedra* 10, 11, 12	*Cyclophora* 12, 13	*Lucanicum* 14
Order	Protoraphidales	Protoraphidales	Fragilariales	Cyclophorales	Cyclophorales
Colony	solitary or in short chains	solitary	zig-zag	zig-zag	apex-to-apex into nearly straight chains
Frustule outline	clavate to lanceolate	sickle-shaped	linear or undulate	lanceolate to linear	linear
Chloroplasts	two or four	multiple	four	four to multiple	multiple
Sternum	straight in the middle of the valve, abruptly bent to opposite sides at the ends	principally median, or slightly off-centre, narrow, strongly curved at the apices to form a hook-like shape	straight	straight	straight
Areolae	small, rounded, elliptical or rectangular	small, elliptical or rounded	small, elliptical or somewhat quadrate	small, elliptical or rectangular	elongated macroareolae
Apical slit fields	slits uninterrupted	elongated perforations	slits intermittent	slits intermittent	slits intermittent
Pseudosepta	–	–	–	+	–
Grooves	+	+	–	–	–
Labiate processes	ear-shaped, Y-shaped processes or plicate siliceous bands	rimoportulae	rimoportulae	rimoportulae	rimoportulae
Ecology	epizoic	epizoic	epiphytic/benthic	epiphytic/benthic	benthic

Note: 1 represents Simonsen, 1970; 2 Gibson, 1979a; 3 Hallegraeff and McWilliam, 1990; 4 Sullivan, 1993; 5 Witkowski et al., 2000; 6 present study; 7 Gibson, 1979b; 8 Rivera et al., 1986; 9 Fernandes and Calixto-Feres, 2012; 10 Williams and Round, 1986; 11 Takano, 1988; 12 Round et al., 1990; 13 Ashworth et al., 2012; and 14 Lobban and Ashworth, 2014.

Table 2. Biometric data and morphological features of the *Protoraphis* taxa

	Pr. hustedtiana				*Pr. atlantica*
	var. *hustedtiana*		var. *nana*	5	6
	1	2	3, 4		
Valve length/μm	45–129	40–130	[3]19–57 / [4]32–48	46–112.5	18–50
Valve width/μm	4–10	5–8	[3]4.5–5.8 / [4]4.5	5–5.5	4–11
Transverse striae in 10 μm	31	32	[3]32 / [4]34–36	30–32	33–40
Areolae	rounded, 3–4 in 1 μm	rounded, no data	[4]elliptical or rectangular, 4 in 1 μm	–	elliptical to rectangular, no data
Number of apical silts	12–16	12–18	[3]8 / [4]12	–	60 in 10 μm
Groove length/μm	1.1–1.7	1.5	[3]ca. 0.7 / [4]0.6–0.85	–	–
Labiate processes	ear-shaped, 1.3–2 μm long	ear-shaped, 1.6–2 μm long	Y-shaped, no data	–	plicate siliceous band, no data
Girdle bands	two rows of rounded pores	two rows of rounded pores	[4]two rows of elongate pores	–	two rows of elongate pores

Note: 1 represents the present study; 2 Hallegraeff and McWilliam, 1990; 3 Takano, 1985; 4 Sullivan, 1993; 5 Simonsen, 1970; and 6 Gibson, 1979a.

tedtiana on female copepods. In our opinion, more specimens from different locations should be examined to confirm if *Pr. hustedtiana* var. *hustedtiana* is specific to male individuals, and more *in vitro* experiments should be conducted to explain the relationship between *Pr. hustedtiana* var. *hustedtiana* and *Candacia*.

Acknowledgements

We thank Caiming Wu and Luming Yao from the Electron Microscopy Laboratory, Xiamen University, for providing assistance with SEM observation. We also thank David Martin for his assistance with language editing.

References

Ashworth M P, Ruck E C, Lobban C S, et al. 2012. A revision of the genus *Cyclophora* and description of *Astrosyne* gen. nov. (Bacillariophyta), two genera with the pyrenoids contained within pseudosepta. Phycologia, 51(6): 684–699, doi: 10.2216/12–004.1

Donadel L, Torgan L C. 2016. *Falcula hyalina* (Fragilariaceae, Bacillariophyta) from a coastal lagoon, Southern Brazil: an additional approach on its morphology. Phytotaxa, 243(2): 185–189, doi: 10.11646/phytotaxa.243.2.10

Fernandes L F, Calixto-Feres M. 2012. Morphology and distribution of two epizoic diatoms (Bacillariophyta) in Brazil. Acta Botanica Brasilica, 26(4): 836–841, doi: 10.1590/S0102–33062012000400012

Foged N. 1984. Freshwater and littoral diatoms from Cuba. Bibliotheca Diatomologica, 5: 1–243

Frankovich T A, Ashworth M P, Sullivan M J, et al. 2016. *Medlinella amphoroidea gen. et sp. nov*. (Bacillariophyta) from the neck skin of Loggerhead sea turtles (*Caretta caretta*). Phytotaxa, 272(2): 101–114, doi: 10.11646/phytotaxa.272.2.1

Frankovich T A, Ashworth M P, Sullivan M J, et al. 2018. Epizoic and apochlorotic *Tursiocola* species (Bacillariophyta) from the skin of Florida manatees (*Trichechus manatus latirostris*). Protist, 169(4): 539–568, doi: 10.1016/j.protis.2018.04.002

Frankovich T A, Sullivan M J, Stacy N I. 2015. *Tursiocola denysii sp. nov*. (Bacillariophyta) from the neck skin of Loggerhead sea turtles (*Caretta caretta*). Phytotaxa, 234(3): 227–236, doi: 10.11646/phytotaxa.234.3.3

Gárate-Lizárraga I, Esqueda-Escárcega G M. 2018. *Ditrichocorycaeus*

anglicus (Copepoda; Poecilostomatoida), new basibiont of *Pseudohimantidium pacificum* (Bacillariophyceae) in Bahía de La Paz, Gulf of California. CICIMAR Oceánides (in Spanish), 33(1): 63–67

Gibson R A. 1979a. *Protoraphis atlantica* sp. nov., a new marine epizoic diatom. Bacillaria, 2: 109–126

Gibson R A. 1979b. An ultrastructure study of *Pseudohimantidium pacificum* Hust. & Krasske (Bacillariophyceae: Photoraphidaceae) with special reference to the labiate processes. Nova Hedwigia Beihefte, 64: 147–161

Gómez F, Wang Lu, Lin Senjie. 2018. Morphology and molecular phylogeny of epizoic araphid diatoms on marine zooplankton, including *Pseudofalcula hyalina* gen. & comb. nov. (Fragilariophyceae, Bacillariophyta). Journal of Phycology, 54(4): 557–570, doi: 10.1111/jpy.12760

Guiry M D, Guiry G M. 2018. AlgaeBase. World-wide electronic publication, National University of Ireland, Galway. http://www.algaebase.org [2003–09–22/2018–07–15]

Hallegraeff G M, McWilliam P S. 1990. The complex labiate process of the epizoic diatom *Protoraphis hustedtiana* Simonsen. Beihefte zur Nova Hedwigia, 100: 39–45

Hiromi J, Kadota S, Takano H. 1985. Diatom infestation of marine copepods (review). Bulletin of Tokai Regional Fisheries Research Laboratory, 117: 37–45

Jiao Nianzhi, Yang Yanhui, Hong Ning, et al. 2005. Dynamics of autotrophic picoplankton and heterotrophic bacteria in the East China Sea. Continental Shelf Research, 25(10): 1265–1279, doi: 10.1016/j.csr.2005.01.002

Li Xuesong, Chen Changping, Liang Junrong, et al. 2014. Morphology and occurrence of a marine epizoic diatom *Falcula hyalina* Takano (Bacillariophyta) in China. Algological Studies, 145–146: 169–179, doi: 10.1127/1864–1318/2014/0158

Lobban C S, Ashworth M P. 2014. *Lucanicum concatenatum*, gen. nov., sp. nov., a benthic marine diatom from Guam, and a less restrictive diagnosis for Cyclophorales (Bacillariophyta). Marine Biodiversity Records, 7: 1–8, doi: 10.1017/S1755267214000918e90

Majewska R, Kociolek J P, Thomas E W, et al. 2015. *Chelonicola* and *Poulinea*, two new gomphonemoid diatom genera (Bacillariophyta) living on marine turtles from Costa Rica. Phytotaxa, 233(3): 236–250, doi: 10.11646/phytotaxa.233.3.2

Majewska R, Van de Vijver B, Nasrolahi A, et al. 2017. Shared epizoic taxa and differences in diatom community structure between green turtles (*Chelonia mydas*) from distant habitats. Microbial Ecology, 74(4): 969–978, doi: 10.1007/s00248–017–0987–x

Prasad A K S K, Livingston R J, Ray G L. 1989. The marine epizoic diatom *Falcula hyalina* from Choctawhatchee Bay, the Northwestern Gulf of Mexico: frustule morphology and ecology. Diatom Research, 4(1): 119–129, doi: 10.1080/0269249X.1989.9705057

Riaux-Gobin C, Witkowski A, Kociolek J P, et al. 2017a. New epizoic diatom (Bacillariophyta) species from sea turtles in the Eastern Caribbean and South Pacific. Diatom Research, 32(1): 109–125, doi: 10.1080/0269249X.2017.1299042

Riaux-Gobin C, Witkowski A, Chevallier D, et al. 2017b. Two new *Tursiocola* species (Bacillariophyta) epizoic on green turtles (*Chelonia mydas*) in French Guiana and Eastern Caribbean. Fottea, 17(2): 150–163, doi: 10.5507/fot.2017.007

Rivera P S, Gonzalez H E, Barrales H L. 1986. Cingulum and valve morphology of *Pseudohimantidium* Hustedt & Krasske (Bacillariophyceae). Phycologia, 25(1): 19–27, doi: 10.2216/i0031–8884–25–1–19.1

Round F E, Crawford R M, Mann D G. 1990. The Diatoms. Biology and Morphology of the Genera. Cambridge: Cambridge University Press, 345–447

Sar E A, Sunesen I. 2014. The epizoic marine diatom *Sceptronema orientale* (Licmophoraceae, Licmophorales): epitypification and emendation of specific and generic descriptions. Phytotaxa, 177(5): 269–279, doi: 10.11646/phytotaxa.177.5.3

Simonsen R. 1970. Protoraphidaceae, eine neue Familie der Diatomeen. Nova Hedwigia Beihefte (in German), 31: 377–394

Skovgaard A, Saiz E. 2006. Seasonal occurrence and role of protistan parasites in coastal marine zooplankton. Marine Ecology Progress Series, 327: 37–49, doi: 10.3354/meps327037

Sullivan M J. 1993. The labiate process of the diatom *Protoraphis hustedtiana* var. nana Takano. Nova Hedwigia Beihefte, 106: 161–167

Takano H. 1983. New and rare diatoms from Japanese marine waters-XI. Three new species epizoic on copepods. Bulletin of Tokai Regional Fisheries Research Laboratory, 111: 23–35

Takano H. 1985. A small form of the marine diatom *Protoraphis hustediana*, epizoic on a snail. Bulletin of Tokai Regional Fisheries Research Laboratory, 117: 31–35

Takano H. 1988. A bloom of *Neosynedra provincialis* in a mariculturral tank. Diatom (in Japanese), 4: 17–19

Takayanagi K, Nishiuchi K, Yokouchi K, et al. 2006. A possible collaboration with China on marine ecosystem research in the East China Sea. Japan Agricultural Research Quarterly, 40(1): 59–64, doi: 10.6090/jarq.40.59

Voigt M. 1959. Nouvelle note concernant le genre *Pseudohimantidium*. Vie Milieu (in French), 10: 199–203

Williams D M, Round F E. 1986. Revision of the genus *Synedra* Ehrenb. Diatom Research, 1(2): 313–339, doi: 10.1080/0269249x.1986.9704976

Witkowski A, Lange-Bertalot H, Metzeltin D. 2000. Diatom flora of marine coasts I. In: Lange-Bertalot H, ed. Iconographia Diatomologica. Ruggell: A. R. G. Gantner Verlag Kommanditgesellschaft, 74–75